DOTTORATO DI RICERCA IN INGEGNERIA CIVILE

SCUOLA DOTTORALE / DOTTORATO DI RICERCA IN

VIII CYCLE

CICLO DEL CORSO DI DOTTORATO

Analysis and Modeling of a Deep-Seated Slope Movement

Titolo della tesi

Assefa Siraj Mulugeta

Nome e Cognome del dottorando firma

Prof. Alessandro Graziani

Docente Guida/Tutor: Prof. firma

Prof. Aldo Fiori

Coordinatore: Prof. firma

Collana delle tesi di Dottorato di Ricerca
In Scienze dell'Ingegneria Civile
Università degli Studi Roma Tre
Tesi n° xx

To my lovely wife Elhame and
My cute baby girl Sobrina

Abstract

Slope movements challenge the Geotechnical and Rock Mechanics engineering field since they pose immediate risks and damages to the nearby infrastructures (e.g. dams, tunnels, highways, railroads etc …). Understanding the deformation mechanism of large slopes remains a puzzling problem. The present research has attempted to give some valuable insights about this field of study.

The case history of a deep-seated slope movement in a complex rock formation (Marly- Arenaceous Formation) is analyzed. The movement, monitored for more than 20 years, was recognized after the discovery of intense cracking in the concrete lining of a hydraulic tunnel running across the slope. The time history of displacements shows that the ongoing deformation process is essentially a stationary creep phenomenon, also influenced by transient variations in pore pressure distribution

The shearing zone is formed by tectonized clay gouge and is characterized by a mobilized strength close to residual.

The peaks in piezometer levels seem reasonably correlated with the 90 days cumulative rainfall. Moreover, the peak displacement velocities are correlated in some periods with the cumulative rainfall exceeding the average values and increase of piezometer levels.

The shape of slip surface in toe part can be unambiguously traced from field investigations, while in the upper part reasonable hypotheses have been developed on the basis of slope morphology and location of the damaged tunnel section. This issue has been investigated by employing discontinuum modelling approaches.

The complex slope structure has been modelled using discontinuum modelling by including reasonable joint sets (bedding planes and crossing joints). Using the persistent and staggered joint pattern, the ongoing slope deformation mechanism has been reproduced. The pre-failure deformation mechanism depends on the type of blocky structure (staggered or persistent), while the collapse situation is less dependent on the slope structure. The mobilized friction angle of the slip surface close to the residual friction angle of the shear box test results has been evaluated and is less dependent on the slope structure. Filling of the reservoir and groundwater table increase have limited influence on the mobilized friction angle of the slip surface.

Steady state flow analysis has been carried out with the help of discontinuum model. The influence of joint aperture in different parts of the slope and boundary condition on the steady state water table has been remarked. The observed average piezometer levels can be estimated reasonably taking in to account joint inflows from the surface boundary. The influence of the filling of the reservoir on the steady state pore pressure regime and slope deformation has been studied using coupled hydromechanical analyses.

Moreover, a continuum model has been applied to assess the influence of rock mass permeability and infiltration amount on the steady state pore pressure regime. In order to describe reasonably the observed groundwater profiles, a relatively higher permeability should be considered for the toe portion including the transition zone. Contrary to the discontinuum model, the applied inflow quantity in the continuum model can be reasonably matched with the expected infiltration amount in the field.

The time dependent behaviour of the ongoing slope movement has been studied by employing elasto-visco-plastic model. The observed stationary movement (constant velocity) can be predicted reasonably using the model. A modified model, formulated on the base of Perzyna's overstress law, has been considered too. The new model allows to examine the influence of the filling of the dam and loss of friction angle on the steady state velocity of the movement.

The last part of the research deals with the role of the proposed remedial measure (a large rockfill embankment at the toe of the slope). The stabilizing embankment has been modelled as a blocky structure by including random joint pattern (voronoi polygons) to get isotropic responses during mechanical interaction with the moving slope. The remedial measure significantly reduces the displacement velocity and joint shearing especially in the toe part. However, these beneficial effects are also accompanied by diffuse yielding inside the stabilizing embankment and at the interface of the embankment with the moving slope.

Acknowledgment

I would like to express my sincere gratitude to my supervisor Prof. Alessandro Graziani for his skillful comments and his continuous attention to my work. His valuable discussions and support at every course of the study are highly appreciable. I am also thankful to Prof. Albino Lembo-Fazio for his comments and advices throughout the study.

I am grateful to Mr. Massimiliano for his sincerity to share his experiences with me since some part of my thesis is related to his work.

Many thanks to all my colleagues in the lab ("open space") where I share all my experiences with you. I would like to thank Dr. Antonio for his advices and encouragement during the organization of my thesis.

I would like to express my best thanks to all my extended families for their support, motivation and love. They gave me strength, appreciation and confidence in the difficult moments.

A special thanks and appreciation is to my beloved wife, Elhame, and my cute baby girl, Sobrina, for their emotional support, love, encouragement and endless patience. I am deeply thankful to my wife for all her sacrifices she has made on my behalf. She "shows me colors when there's none to see".

The financial support provided by the Department of Engineering, Civil Engineering section of University of ROMA TRE is gratefully acknowledged.

Table of contents

List of figures

List of tables

List of symbols

The following list shows the main symbols that appear in the chapters of the thesis.

a_o	*Initial hydraulic aperture*
a_r	*Residual hydraulic aperture*
c	*Cohesion*
E	*Young's modulus*
EPM	*Equivalet porous medium permeability*
e_{ij}	*Deviatoric shear strain*
f	*Yield function*
g	*Potential function*
G	*Shear modulus*
GSI	*Geological Strength Index*
JRC	*Joint roughness coefficient*
JCS	*Joint compression strength*
K	*Bulk modulus*
k_n	*Joint normal stiffness*
k_s	*Joint shear stiffness*
k_w	*Fluid bulk modulus*
k	*Equivalent hydraulic permeability of the rock mass*
p	*Pore pressure*
q	*Joint flow rate or Infiltration amount*

Q	*Rock mass quality*
RQD	*Rock quality designation*
S	*Joint spacing*
s_{ij}	*Deviatoric shear stress tensor*
T	*Joint transmissivity*
u_n	*Joint normal displacement*
UCS	*Uniaxial compression strength*
V_p	*P-wave velocity*
V_s	*S-wave velocity*
μ	*Dynamic viscosity of water*
ψ	*Dilation angle*
ΣQ	*Flow sum into a node*
ΔV	*Domain volume change*
Δp	*Change in pore pressure*
Δl	*Change in length*
Δt	*Timestep*
Δt_f	*Fluid timestep*
η^M, η^K	*Dynamic viscosity for Maxwell and Kelvin unit respectively*
η^{vp}	*Dynamic viscosity of the Bingham unit*
γ	*Fluidity parameter, constitutive parameter*
Φ	*Viscous nucleus*
δ_{ij}	*Kronecker's delta*

φ_p	*Peak friction angle*
φ_r	*Residual friction angle*
ρ	*Density*
ν	*Poisson's ratio*
ε_{ij}	*Strain tensor*
$\varepsilon_1, \varepsilon_2, \varepsilon_3$	*Principal strains such that* $\varepsilon_1 > \varepsilon_2 > \varepsilon_3$
σ_{ij}	*Stress tensor*
$\sigma_1, \sigma_2, \sigma_3$	*Principal stresses such that* $\sigma_1 > \sigma_2 > \sigma_3$
τ	*Shear stress*
σ_n	*Normal stress*
Δu^e_s	*Elastic shear displacement increment*
Δu_n	*Normal displacement increment*

Chapter 1

1 Introduction

1.1 Background

The presence of a slope deformation needs special attention since it causes a direct threat to life and the nearby civil structures, for instance dams, tunnels, highways, railroads. Therefore, to minimize the risks and damages posed, it is necessary to understood the possible deformation mechanisms and choose the appropriate method of analysis for evaluating the degree of stability of the slopes by taking in to account change of boundary condition.

However, problems are inevitable when tracing the boundary of the sliding mass of a large slope deformation (Forlati et al., 2001). Thus numerical analysis should be applied to validate possible hypotheses (i.e. sliding mass geometry) based on the back analysis of the observed slope deformation and mobilized friction angle of slip surface, as determined by laboratory shear tests.

Using large-scale in situ shear tests along contacts between different lithological units, the shear strength of joints can be reasonably determined (Baldovin, 1968, Oberti et al., 1986, Alonso and Pinyol, 2014).

The deformation behavior of a slope movement in a complex rock formation can be reasonably examined using discontinuum numerical modeling (DEM) techniques by introducing realistic joint sets on the base of field investigations: bedding planes, which can be continuous and gently inclined and crossing joints, which are inclined and continuous or discontinuous. The overall properties of joints or discontinuities in a rock mass determines the deformation mode of a slope failure (Brideau and Stead, 2012).

The slope deformation as a consequence of change of fluid boundary condition (e.g. filling of a nearby reservoir) could be reasonably determined by employing coupled hydromechanical analysis (Gioda and Borgonovo, 2004).

The time dependent behavior of a slow moving slope usually conveys a steady state creep behavior (i.e. constant velocity). The influence of fluid boundary condition on the creep deformation should be assessed by taking in to account viscous effects (Vulliet, 1999, Forlati et al., 2001, Puzrin, and Schmid, 2011, Oberender and Puzrin, 2016).

Remedial measures like a large rockfill embankment at the toe can significantly reduce the joint shearing and horizontal displacement

velocity, which in turn gives an increase of the safety factor. Previous studies (Gioda and Borgonovo, 2004, Corkum and Martin. 2004) remarked the effectiveness of a toe berm in reducing the rate of deformation of a slope movement using numerical analysis.

1.2 Problem statement

The deformation behavior of slow movements in a complex lithological unit requires a comprehensive study. They are characterized by a typical velocity of few centimeters per year. The shear strength of the basal slip surface may reach to the residual condition if the movement has already produced significant shearing along the basal slip surface.

The characteristics of the slope structure (joint pattern) influence the deformation mechanisms.

The pore pressure regime change, especially due to the filling of the nearby reservoir, can significantly influence the deformation behavior. To explore this behavior, a proper numerical modeling has to be employed by taking in to account the influence of fluid boundary conditions on the slope deformation.

Slow movements exhibit a time dependent phenomenon, which needs to be discussed taking in to account viscous effect in constitutive models. The movement velocities are usually influenced by the seasonal change of pore pressure regime.

Although the deformation behavior of slow movements has been widely discussed in several case histories using site investigations, laboratory tests and numerical analyses, the topic remains an open problem due to the complexity of lithological types, mechanical properties and boundary conditions encountered in each case studies.

1.3 Objectives and Scope of research

The objective of this research is to explore the deformation behavior of a slow movement in a complex rock formation (Marly-Areanceous Formation). In order to understand the overall behavior of the movement, detailed analysis of field investigations has been considered. The purpose of applying numerical models is to examine the ongoing slope deformation behavior.

The scope of the research is as follows:

1. Detailed analysis of the field investigation data, which include displacement measurements, borehole loggings, geophysical surveys, rainfall and piezometer measurements.

2. Discuss the ongoing slope deformation mechanism using discontinuum (DEM) approach taking in to account the field investigations.

3. Prediction of the observed piezometer levels using continuum and discontinuum modeling techniques. Evaluation of the effect of stepwise filling of the dam on the slope behavior using coupled hydromechanical analysis.

4. Describe the ongoing stationary movement (constant velocity) by employing suitable creep modeling methods. Implementation of a new user defined viscoplastic model in the continuum model to discuss velocity changes due to filling of the dam or reduction of friction angle.

5. Assess the influence of the proposed remedial measure (a large rockfill embankment at the toe of the slope) on the ongoing rate of deformation.

1.4 Organization of thesis

This thesis is divided in to eight chapters. The first three chapters discuss the detail discussion of field investigations. Chapter 1 presents the general introduction of the study. Chapter 2 is devoted to discussion of the discovery of the movement, geomorphological aspects, analysis and modeling of displacement measurements using statistical models.

Chapter 3 discusses the characterization of the geotechnical properties of the rock mass by referring field investigations (borehole loggings and geophysical studies). The shear strength of the slip surface is presented based on the shear box tests carried out on tectonized clay gouge. This Chapter also discuss the possible correlations between cumulative rainfall and piezometer levels. Correlation between peak velocities with intense rainfall and peak piezometer levels are presented. The slip boundary and kinematic of the movement are also discussed.

Chapter 4 presents the DEM modeling of the slope as a blocky structure by introducing reasonable joint sets: bedding planes and

crossing joints. The influence of joint patterns (staggered and persistent) on slope deformation mechanism is highlighted.

Chapter 5 is devoted to the modeling of the hydromechanical behaviors using DEM approaches. The continuum model has been also applied to explore the influence of continuum rock mass permeability and infiltration amount on the steady seepage process. This chapter also discuss the influence of stepwise filling of the dam on slope deformation behavior using coupled hydromechanical analysis.

Chapter 6 presents the analysis of the ongoing stationary slope movements using visco-elasto-plastic model. In this chapter, the influence filling of the dam or reduction of friction angle on the steady state velocity is also discussed with a new modified viscoplastic model.

Chapter 7 presents the review of rockfill behaviors by referring large-scale triaxial test. The role of the proposed remedial measure (a large rockfill embankment at the toe of the slope) on the slope safety factor has been examined.

Finally, Chapter 8 summarizes the whole work, provides some conclusions and suggestions for further studies.

Appendix A presents the formulation of the new modified viscoplastic model and Appendix B gives displacement vectors and deformed shape along a vertical measured by inclinometers installed at the toe part.

Chapter 2

2 Geomorphological characterization and displacement measurements

2.1 Introduction

The main results of analysis of geomorphological investigations and displacement measurements carried out in the last 25 years have been discussed. The discovery of the ongoing movement has been highlighted. The analysis of the observed slope displacements owing to the early filling of the reservior (1991-92) has been presented. The ongoing displacements trend has been modelled with linear regression models in order to understand the behavior the displacement velocity throughout the whole monitoring period. Moreover, the deformation behaviour of the slope has been discussed on the base of the deformed inclinometer profiles along depth.

2.2 The study site

The slope movement analyzed in this study was recognized in 1985 after the excavation of a hydraulic tunnel in the right bank of the Chiascio River (Italy) (Figure 2.1). The movement affects a large portion of a ridge which has the longitudinal direction approximately perpendicular to the river.

A rockfill dam was built in 1984 just downstream of the moving mass to create a reservoir at the toe of the slope for water supply by a diversion tunnel located on the right bank. Up to now, the reservoir behind the dam has never been impounded. The tunnel departs at the toe of the slope perpendicular to the valley and runs downstream crossing the slope in the east part. So far, the diversion tunnel has been operated only once, in 1991-1992, not for regular water conveyance but for temporary deviation of the river flow.

The first sign of the ongoing slope deformation was seen from the intense cracking of the concrete lining in a tunnel section located well inside the ridge, at a distance from the intake of some 250 m, under an average overburden depth of 50 m. The damaged tunnel stretch was soon interpreted as the place where the tunnel axis intersects a deep-seated slip surface.

The entire area of the dam reservoir, included the sliding slope and the dam foundation, is formed by an outcrop of the Marly-Arenaceous Formation, a Miocene flysch characterized by alternating sequence of marl, sandstone and calcarenite layers. As observed in many flysch formations of Italian Apennines (Angelucci et al., 1967), joints are often slickensided as a consequence of tectonic shearing and bending deformation of strata.

The presence of major discontinuity planes of low strength represents a key factor for stability analysis in slope and dam engineering and has often required specific investigations (Oberti et al., 1986, Graziani et al., 2012). Weak layers of small thickness, such as clay gouge interbeds or thin shear bands, may be easily overlooked during ordinary borehole investigations, particularly in structurally complex formations (D'Elia et al., 1998), such as flysch and layered limestone formations (Alonso and Lloret, 1993, Hatzor et al., 1997, Graziani et al., 2009).

In the present case, it is likely that most of the sliding surface is seated along an over-thrust plane gently dipping towards the Chiascio River valley. This circumstance adds further complexity to the structural setting of the slope and can explain some particular features of the sliding mass, whose overall volume has been estimated of some 18 Mm^3. The kinematic characters of the movement are essentially those of a planar-sliding (average velocity of 13-17 mm/y) presumably localized along tectonized clay interbeds.

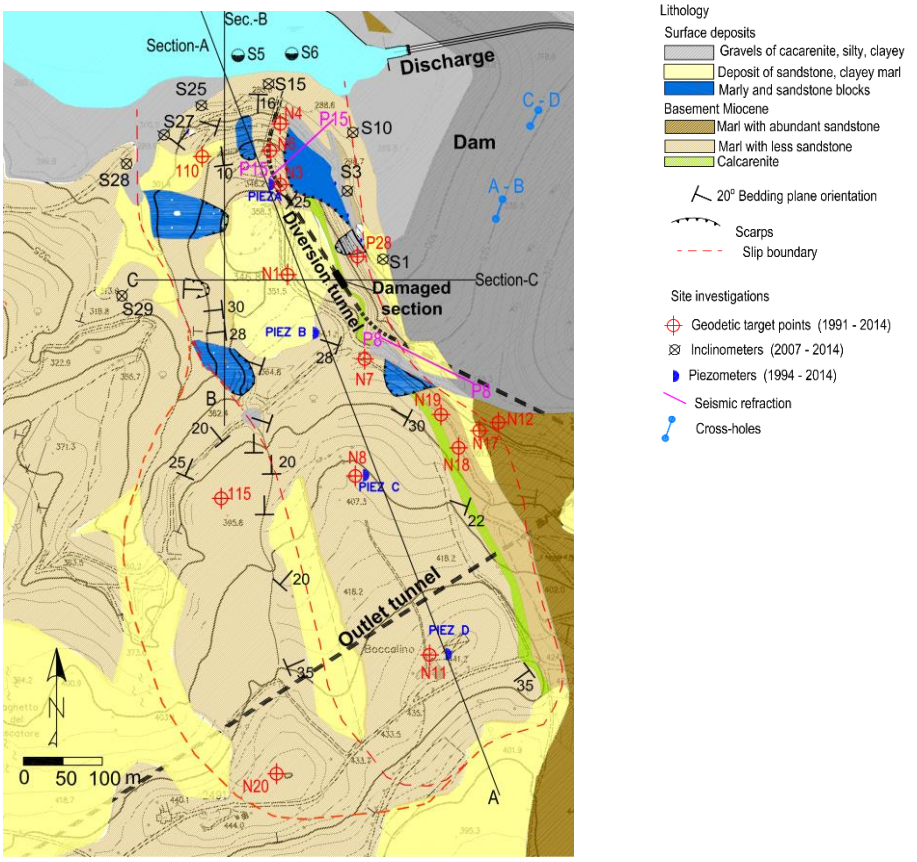

Figure 2.1: Study area

2.3 Geological setting and morphology of the slope

The stretch of Chiascio River basin considered in this study is entirely based on a thick sequence of Miocene flysch deposits (Figure 2.2). The main valley as well as the lateral gullies are carved in the same rock formation.

The Marly-Arenaceous Formation is characterized by a layered structure, at least in its less disturbed portions (Celluzzi et al., 2014, Assefa et al., 2015). The different layers can be grouped on the base of the prevailing lithological components:

a) Lower marls unit, with rare thin layers of clay shale,
b) Marly-arenaceous-calcarenitic unit,
c) Calcarenite unit, sparsely present as single layers,

d) Upper marls unit.

The lower marls are characterized by a more regular and continuous bedding. The a) unit was mostly exposed during the excavation for dam foundation, nearby the toe part of the sliding area (Figure 2.3). The excavation works, started in 1984, required the removal of debris and loosened rock up to 15 m depth below the river bed elevation.

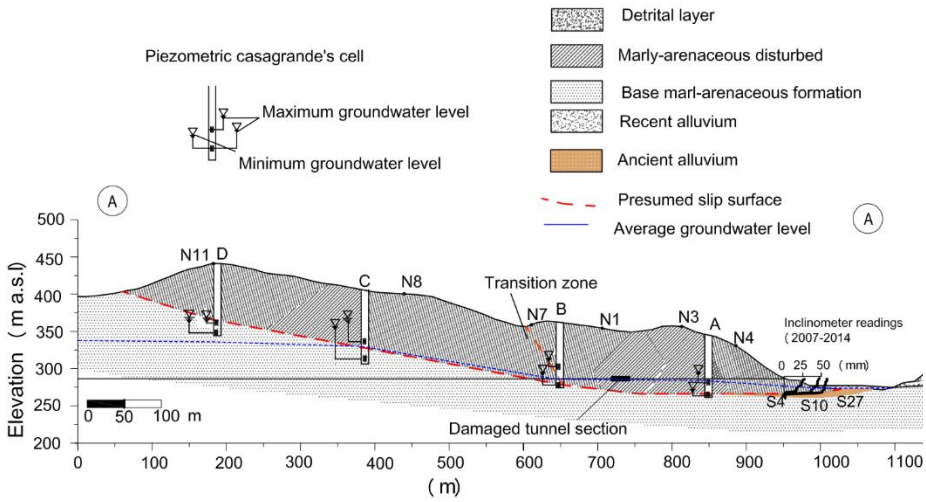

Figure 2.2: Longitudinal cross-section of the ridge with relevant geological data and location of piezometers and geodetic targets

The slope movement affects a large portion of a long ridge, upstream to the right abutment of the dam. The sliding mass is mostly composed of alternating layers (thickness, 0.1–0.2 m) of unit b) lithotypes, with the upper marls unit and some debris deposits at the top. The Calcarenite unit consists of two separate strata (each one formed by single layers of 0.1–1 m for a total thickness of 3–4 m) intermingled with the thinner layers of unit b). Moreover, the calcarenite layer was observed in several boreholes located in the east and west side of the slope which assures the lateral continuity of the rock formation.

For instance, in the west side from borehole S4/91, the calcarenite layer accounts for around 9.5m thick layer between 286-296m a.s.l and in the east part considering borehole S2/91, the same calcarenite layer accounts for 7.2m thick located in between 278.2-285.4m a.s.l (Figure 2.4).

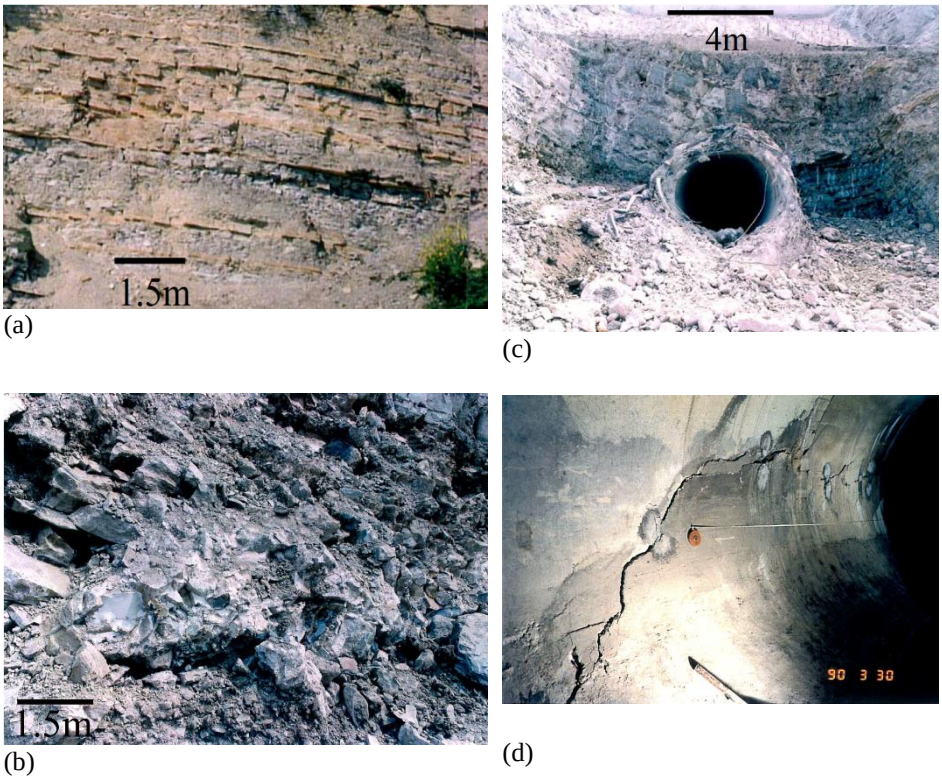

(a) (c)

(b) (d)

Figure 2.3: Regularly layered marly-arenaceous rock mass in the east side of the ridge (a); disturbed rock mass structure at the toe of slope (b); curved layers exposed during the excavation works for tunnel intake (c); main cracks and fissures seen in the concrete lining of the diversion tunnel (d)

While the upper portion of the ridge is gently dipping (10°) towards the Chiascio valley, the frontal slope and lateral flanks are steep (25-40°) and mostly covered by a talus of rock debris and remoulded clay. This situation hampers the visual detection of any trace of the slip surface at the toe of the slope (el. 280 m a.s.l.). The upper limit of the ridge (S sector) is characterized by a plateau, located at an average elevation of 395 m a.s.l.

In the east flank of the ridge a regular monocline structure (bedding dips to W, inclined 20–40°) can be clearly identified. The same structure, with remarkably continuous and consistent orientations of the bedding joints, could be observed also on the foundation surface of the dam, as reported by the construction surveys. Conversely, the west flank of the ridge (bordered by the gully called “Fosso della Torre”) is characterized by a less consistent orientation of bedding, especially in the lower part

where bedding orientation is more dispersed, although dip direction in the E to NE range seems prevailing, with dip angle of 25-50°. Therefore, the overall pattern of the bedding planes suggests the hypothesis of a syncline structure, with axial plane having N-S direction.

The N sector of the ridge could be carefully inspected during the excavation works for the intake structure of the diversion tunnel and, after the discovery of the ongoing movement, by extensive borehole investigations (Figure 2.3c). In this area the rock mass exhibits a higher degree of fracturing and local disarrangement of the bedding joints.

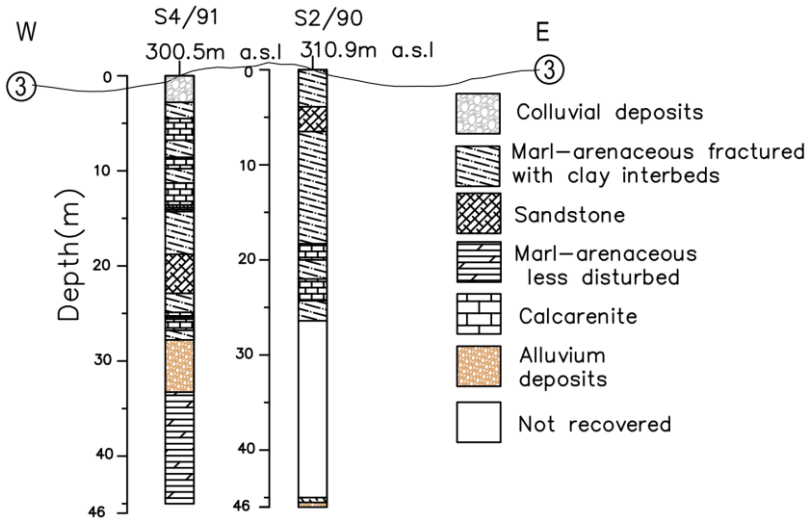

Figure 2.4: Borehole loggings which show the lateral continuity of the existing lithological formation

A fundamental evidence acquired from borehole loggings in the N sector is the presence of quaternary alluvium under the Miocene flysch forming the toe of the slope (Figure 2.5). This circumstance can be reasonably explained as the consequence of an overthrust deformation. By comparing the position of the contact between alluvium layer and marly-arenaceous formation at different boreholes, it can be argued that the basal plane of the overthrust is almost horizontal and it is located at an elevation slightly lower than the river bed. Moreover, the cumulated amount of shearing displacement would be as high as 100-150 m. If such hypothesis holds true, it is likely that also the current process of slope deformation is governed by the same shear band, i.e., by a layer of strongly tectonized clay gouge, at least for the lower portion of the slip surface.

Figure 2.5 shows the alluvium layer recovered from boreholes S1/90, S2/90 and S3/90 at an average elevation of around 265m a.s.l which also hints that the ongoing movment could have a basal plane close to this elevation, at least in the toe part.

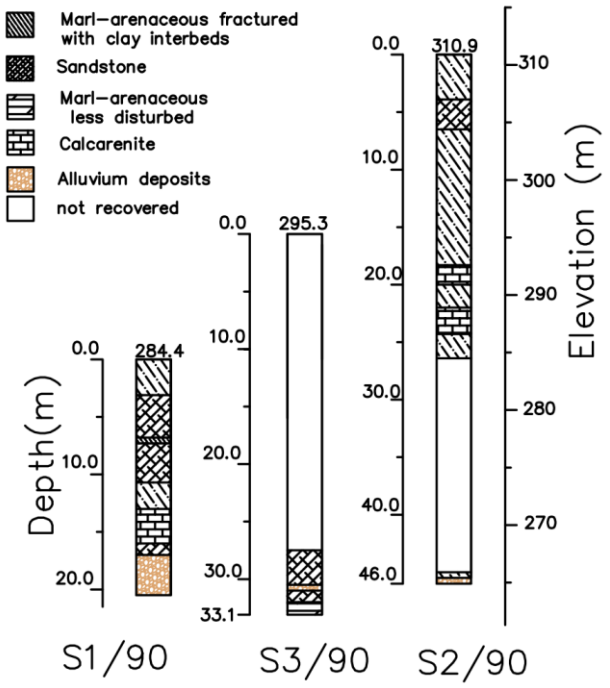

Figure 2.5: Borehole loggings which show the presence of alluvium layer under the Marly-arenaceous formation

2.4 Survey of tunnel damage and slope displacement

As already mentioned, the occurrence of a slow movement in the ridge crossed by diversion tunnel of the Casanuova dam, was recognized only after the completion of the tunnel lining. Nowadays, surface evidences of the ongoing deformation can also be detected, especially on the east boundary of the sliding area, where the pavement and curbs of some country roads appear locally displaced and fissured.

The diversion tunnel departs from the right flank of the valley, at an elevation of 287 m a.s.l., approximately 15 m higher than the toe of the slope, and runs through the long ridge with a direction almost

perpendicular to the river (Figure 2.1) for some 900 m, before turning to the W, by taking a N238° direction.

The clear evidence of a deep-seated movement came from the heavy damaging of the tunnel lining, not yet in operation, which consists of a 4.5 m diameter, 0.5 m thick cast concrete ring. Cracking and opening of the construction joints were localized in a 23 m long stretch of tunnel, between chainage 235 and 258 m from the intake section. The limited width of the damaged stretch is strongly suggestive of a deep movement with localized shearing. The damaged section of the tunnel is under an average overburden of 50 m and is located, in plan, some 40 m inside the lateral boundary of the movement, as successively demonstrated by the geodetic survey of surface displacements.

The fissures in the lining were repeatedly sealed but formed again, then four 4 couples of crack-meters were installed across the main cracks (Figure 2.6).

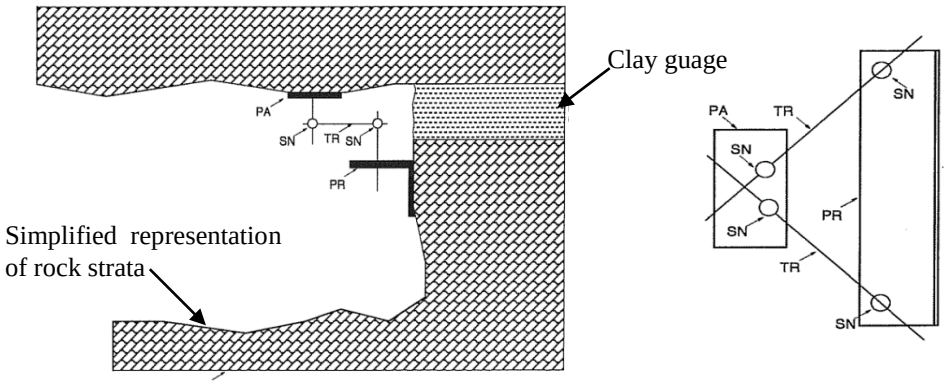

(a) (b)

Figure 2.6: Schematic representation of section (a) and plan (b) which show the position of crack-meters assembled for measuring the displacement of the crack opening

A clear picture of the relative displacement trend was obtained in 1991-1992, during a short-time operation of the diversion tunnel as temporary discharge tunnel in order to allow the completion works of the dam bottom outlet.

2.5 Investigation conducted in 1991-92

This investigation has been discussed separately herein since it gives us some useful insights about the response of the slope during temporary

filling of the dam. In 1991, the river discharge was stopped for few periods due to the construction of sluice gate. The reservoir level before the closure of the sluice gate was around 267m a.s.l on 27/05/91 and around 287.3m when it was reopened latter on 22/07/92 (Figure 2.7).

On those periods, the average reservoir level was approximately 287.4m a.s.l. Moreover, two peak levels were recorded between November-December 1991 and April 1992, with corresponding levels of 296.50m and 291.40m a.s.l. respectively (Figure 2.7). The diversion tunnel operated with its full discharge capacity (i.e. pressurized flow) for about 3 months. Peak reservoir levels are reasonably correlated to cumulative precipitation on those periods (Figure 2.7).

The rainfall data were recorded in 15 days cumulative value, then 30days cumulative and 90days cumulative rainfall values were evaluated latter for correlation analyses.

Four boreholes (S5, S6, S7, and S8) each with two Casagrande piezometric cells with depth between 35-45m were installed on the Chiascio river valley to monitor pore pressure regime. These piezometers started working in April 1991 one month earlier than the sluice gate closure and the measurements were lasted only for 18 months period (i.e. April 1991 - September 1992).

The difference in piezometer cells at borehole S5 (PC1 and PC2) as depicted in Figure 2.7 could arise most likely from undrained loadings developed when reservoir level increased instantaneously due to closure of sluice gate .The stationary flow occurring in the rock strata could also contribute for this pore pressure change.

The correlation analysis shows that 30days cumulative rainfall gives reasonable correlation with the piezometer levels.

The time lag observed between rainfall, piezometer and reservoir level plots could arise from time of concentration associated with surface and groundwater flow. The recorded peak reservoir levels are reasonably correlated with 30 days peak cumulative rainfall (Figure 2.7).

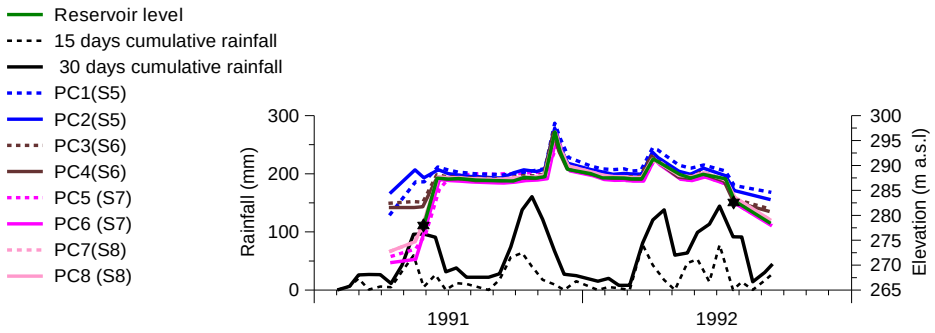

Figure 2.7: Correlation between piezometer levels, reservoir level and cumulative rainfall

Crack-meters

The maximum stroke (50 mm) of the displacement gauges was achieved from the crack-meters (Figure 2.8a) during the short operation of the hydraulic tunnel. The relative displacement vectors (Figure 2.8c) measured across the cracks exhibit a negligible plunge and a direction close to the tunnel axis (i.e. between N and N67°W). Average velocity of 0.6mm/day and maximum velocity of 1.6mm/day were evaluated (Figure 2.8b).

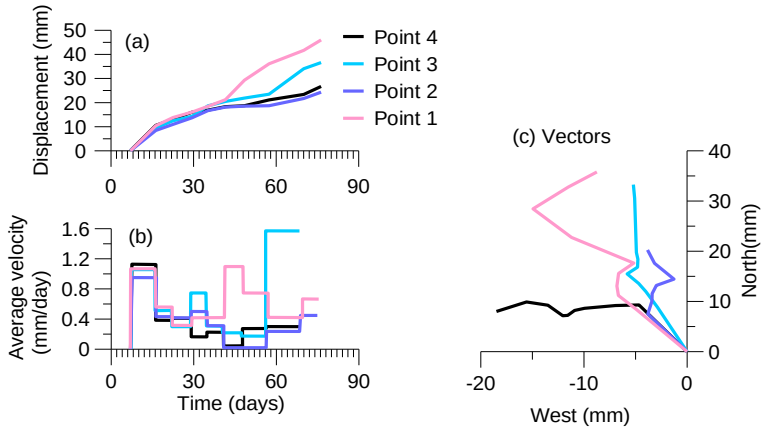

Figure 2.8: Crack-meter measurements conducted from 7/5/1991 to 14/7/1991 during early filling of the dam. (a) displacement, (b) average velocity and (c) vectors

Target points

A maximum velocity of 20mm/month has been obtained for target points during temporary operation of the dam in 1991/92 (Figure 2.9). Moreover

the peak velocities of the target points (N1-- N11) are well correlated with the peak reservoir levels, cumulative rainfall and piezometer levels (Figure 2.9). Particularly, the effect of reservoir level increase on peak velocities was significant when the diversion tunnel was operating at pressurized flow (i.e. when the reservoir level is in between 290 and 296m a.s.l). These observations illustrate how the slope movement is sensitive to pore pressure regime change developed due to filling of the reservoir.

Therefore, the observed higher displacement velocities in those limited operation of the diversion tunnel, as it was confirmed from both geodetic and crack-meter measurements, further reinforce the ongoing deep seated slope movement is sensitive to reservoir filling.

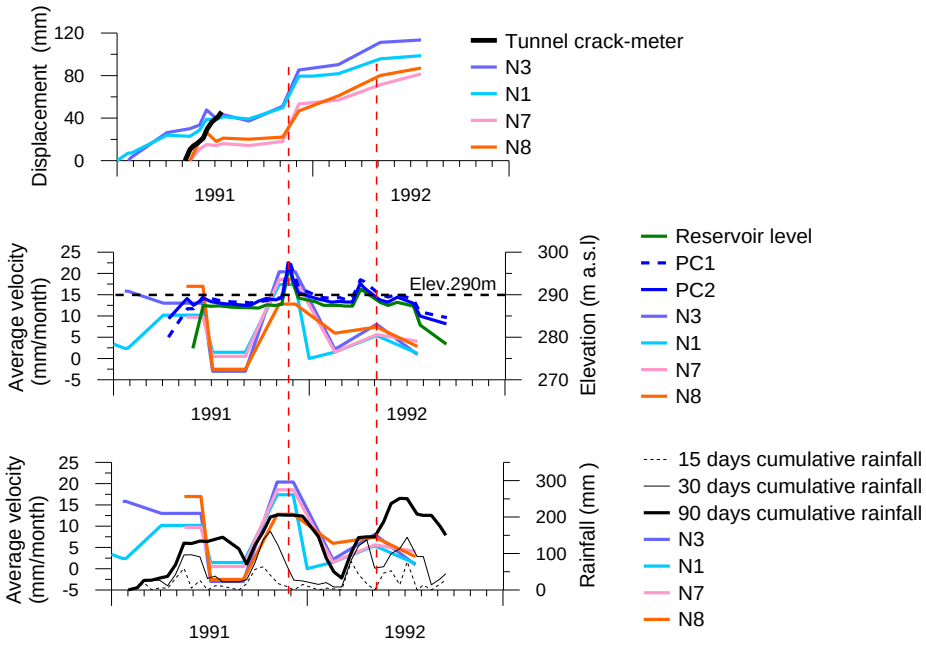

Figure 2.9: Target point displacement, velocity and their corresponding correlation with reservoir level and cumulative rainfall

2.6 Displacement monitoring

Displacement measurements have been carried out since the discovery of the movement using surface displacement measurement (geodetic surveys), inclinometers (mostly located in the toe part) and tunnel extensometer in the damaged section of the tunnel.

2.6.1 Geodetic displacements

A first network of targets (N1-N11) for the geodetic survey of surface displacements, restricted to the frontal slope of the ridge (N sector), was implemented to integrate the crack-meters installed in the damaged section of the tunnel, before starting the temporary filling of the dam pool. The geodetic network was thereafter extended to the S and W areas, with targets (N12-N20) at greater distances from the N slope, in order to estimate areal distribution and limits of the movement (Figure 2.1).

Since then, all the targets have been continuously monitored by a total station installed, on the opposite side of the valley, at the top of the concrete walls of the dam spillway. Measurements are performed regularly once a month. The prevailing components of displacement are in the horizontal plane; the vertical components are much smaller and usually are not processed.

2.6.2 Tunnel extensometer

In 1994, it was decided to install a steel lining within the damaged section of the tunnel (Figure 2.10). The annular gap between the extrados of the steel pipe was not sealed but endowed with a “telescopic joint”, in order to accommodate differential axial displacements between the two tunnel stretches separated by the cracked zone and, therefore, hosted, respectively, inside and outside the sliding rock mass. The telescopic joint was supplemented by an electric dial gauge, thereafter referred to as “tunnel extensometer”.

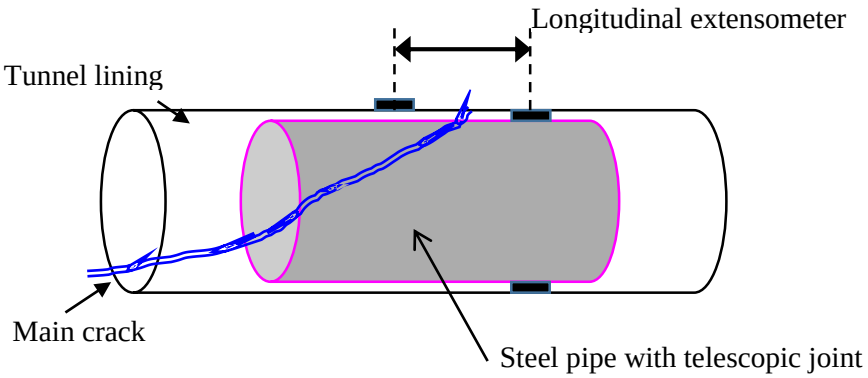

Figure 2.10: Installation of steel pipe with a telescopic joint inside the damaged concrete lining to measure longitudinal displacement

2.6.3 Inclinometer measurements

The displacement data available after some years of geodetic monitoring were instrumental to trace the approximate boundaries of the slide surface. The lateral limit of the movement along the E flank of ridge were considered with particular attention due to proximity of the right abutment of the dam. Therefore, it was decided to refine the survey by installing a set of inclinometer tubes (Figure 2.1). Taking advantage of the shallow depth of the slip surface in this peripheral zone of the movement, the length of the boreholes (S1…S29 series in Figure 2.1) is comprised in the 20-45 m range. The boreholes were drilled in 2006-2008, since then, readings have been carried every two months by removable sliding inclinometer probe.

To analyze inclinometer data which were recoded as of 2007 onwards, a reference date of 05/02/2007 is taken for all boreholes except for Inclinometer I1 which has one less data as compared to others since the measurement was started one year later. While for S1, S3, and S15 inclinometers their consecutive readings are calculated with respect to their measurement at the reference year (05/02/2007). Thus, the displacement profiles trend can be compared easily with the reference year.

The observed profile of inclinometers (S3, S28 and S4) showed a distinct shearing zone where a monotonic block movement is undergoing over the sheared surface. Other inclinometers (S1, I1 and S29) also depicted a tilted inclinometer profile along depth suggesting strong internal deformation occurs without a clear shearing plane (see Appendix B).

Deformed profile of S10 inclinometer started from the bottom end of the borehole which could indicate that the borehole would be probably too short to intercept the slip surface.

The inclinometer profiles have been employed so as to trace the shape of the slip surface at least in the toe part (refer Chapter 3).

Moreover, the displacement magnitudes recorded at different years of the deformed inclinometer profiles depicts that the ongoing sliding is probably characterized by a ‘stick-slip’ type of movement.

Table 2.1: Summary of boreholes with inclinometers installed with some remarks

Borehole Id	Date of zero reading	Depth (m)	Depth to slip surface (m)	Cumulative disp.(mm)*	Azimuth (degree)	Deformation mode/shape
S1	12/09/2006	25	not clear	15	40	smeared /linear
I1	02/04/2008	43.5	not clear	8.4	75	smeared/ linear
S3	12/09/2006	34	28	46	30	
S4	05/02/2007	25	22	54.4	14	
S10	05/03/2007	21	not clear	64.9	74	rigid block
S15	06/10/2006	25	15	62.9	20	
S25	05/02/2007	25	16	65.6	35	
S27	05/02/2007	26	18	29.8	330	
S28	05/02/2007	28	20	19.2	60	
S29	05/03/2007	45	not clear	19.7	not clear	smeared/linear

*Refers to cumulative displacement up to 14/11/2014 at the ground surface.

The direction of displacements measured by inclinometers, is between N30º-75ºE (see Appendix B). This is also consistent with the orientation of displacements measured by target points located in the toe part, which shows that the ongoing movement is directed generally towards the east side at least in the toe part where inclinometers were installed.

2.6.4 Time history of displacements

The time history of measured displacements (Figure 2.11) shows that the ongoing deformations are characterized by stationary velocity (i.e. constant velocity). Apart from the much higher velocities recorded in 1991, during the temporary operation of the diversion tunnel, the average velocity of the targets lies in the 13-17 mm/y range in the period 1992-2001 and tends to decrease in the following years. However, an increase in velocity was observed recently after the last measurements. The tunnel extensometer exhibits a similar trend and consistent magnitude of displacement.

A secondary fluctuation of velocity is also observed. This behavior is likely a consequence of transient seasonal variations in pore pressure distribution. Some targets also show alternated phases of negative and positive velocity, which may be tentatively explained as the combined effect of "stick-slip" phenomena and/or temperature variations. Additional difficulty in analyzing the velocity trend (Figure 2.11) stems from the low frequency of measurements.

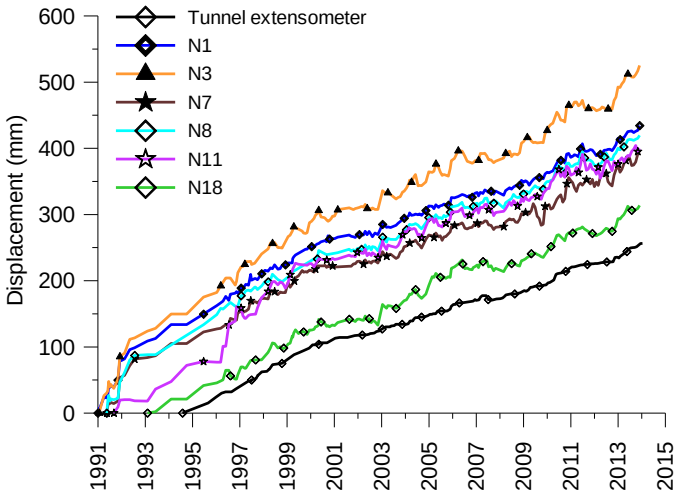

Figure 2.11: Displacement of the geodetic targets and deformation of the telescopic joint of the tunnel; the time of first measurement is not the same for all monitoring points

2.7 Statistical modeling of displacements

The measured displacement in the field by target points and tunnel extensometer with time has been modelled with the help of simple linear regression models. The models consist a time dependent component associated with creeping behavior and a seasonal component which accounts for effect of pore pressure regime fluctuations on displacement trends. By taking in to account the displacement magnitude, target points can be clustered in two groups: stable targets, those which show small displacements mainly due to seasonal changes and have negligible velocity. While the other groups are unstable targets, which show mainly a constant velocity movement, and some peak values which are related to seasonal pore pressure regime changes (Figure 2.11).

Figure 2.12 illustrates the magnitude of displacements measured by stable targets, which comprises between 10-20mm fluctuations of

displacements or sometimes it tends to be around 2mm for some stable targets. As it can be referred from Figure 2.13 (e.g. point N3), the displacement of the unstable target points shows negligible seasonal behaviors, rather they convey mainly a constant velocity movement.

Moreover, the ongoing velocity of the movement can be clustered reasonably in two four time periods. In the first period, between 1991-1992 we have seen high velocities up to 77 mm/y, obviously this is the consequence of early filling of the dam as mentioned earlier. The second period, which is between 1992-2000, the velocities are in the range of 20-24 mm/y and the third period, which is in between 2000-2008, has velocities in between 10-15 mm/y and the last period which covers from 2009-2014 has a velocity of 15-19 mm/y. On average, the unstable targets show velocity between 13-17 mm/y, which is typical value for a slow moving mass.

A number of possible regression models have been considered and discussed as follows (Table 2.2). Firstly, by modeling the observed displacement of the stable target points, with the help of only sinusoidal functions (Table 2.2), the contribution of the seasonal displacement magnitude on the unstable target points could be reasonably approximated.

Secondly, preliminary linear models have been studied in order to obtain the most plausible linear fitting models (Table 2.2) by taking in to account the displacement history of N3.

Therefore, four statistical models which have time dependent components (linear functions of time with coefficients d_1 --- d_5) and seasonal components (sinusoidal functions of time with coefficients a_1--- a_2) have been considered as shown in Table 2.2.

Table 2.2: Models implemented for analysis of displacements measured by unstable target points and extensometer

Description	Statistical models
Model_I	$disp(t) = d_1 * t_1 + d_2 * t_2 + a_1 \sin(2\pi * t) + a_2 \cos(2\pi * t)$
Model_II	$disp(t) = d_1 * t_1 + d_2 * t_2 + d_3 * t_3 + a_1 \sin(2\pi * t) + a_2 \cos(2\pi * t)$
Model_III	$disp(t) = d_1 * t_1 + d_2 * t_2 + d_3 * t_3 + d_4 * t_4 + d_5 * t_5 + a_1 \sin(2\pi * t) + a_2 \cos(2\pi * t)$
Model_IV*	$disp(t) = d_1 * t_1 + d_2 * t_2 + d_3 * t_3 + d_4 * t_4 + a_1 \sin(2\pi * t) + a_2 \cos(2\pi * t)$

*Based on the regression coefficient, R, this mode fitted the observed displacements reasonably.

Figure 2.12 depicts the approximation of the displacement trend of the stable targets, dominated by seasonal component. Preliminary analyses have shown that Model-IV gives good approximation for displacement trend of the unstable target points as compared to other models. However if we consider Model-I (Figure 2.13), the observed displacement histories are not well reproduced by the adopted functions.

Thus, Model-IV has been implemented to all the unstable targets including the tunnel extensometer (Figure 2.15). As it is shown in Figure 2.15, the trend of the ongoing movement (target points and tunnel extensometer) has been well represented by the same model (Model-IV), which confirms that there exists some sort of rigid type of movement.

In further analyses, a moving regression function has been also implemented for the period between 1998 to 2014, since more data has been recorded as compared to other periods. Results from this model are effective in describing the peak displacements as compared to the previous models (Figure 2.16).

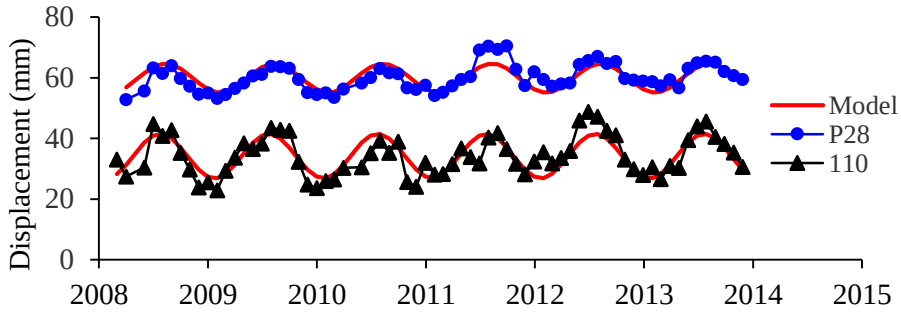

Figure 2.12: Displacement vs time for stable targets showing mainly seasonal component

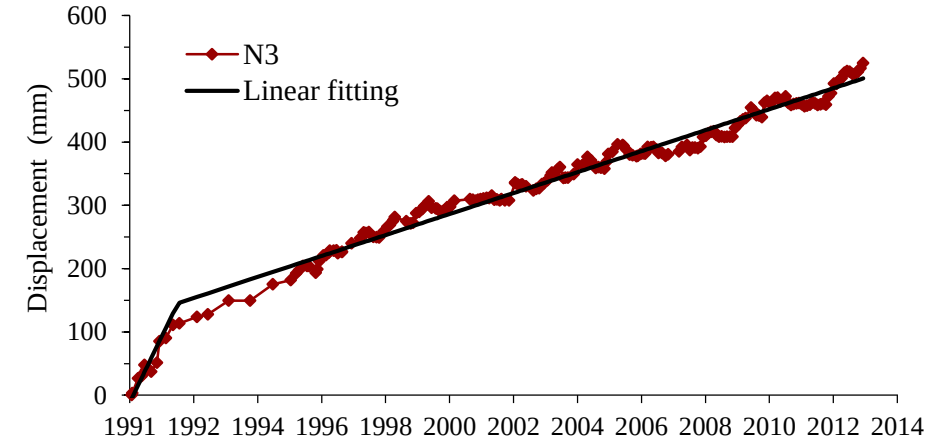

(a)

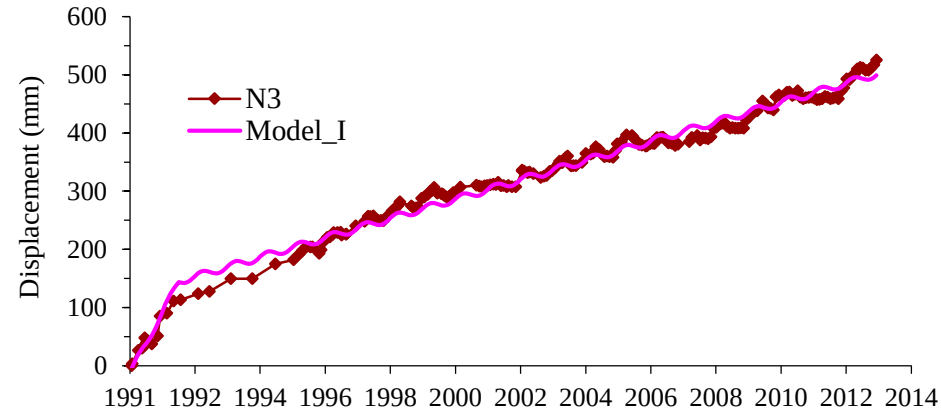

(b)

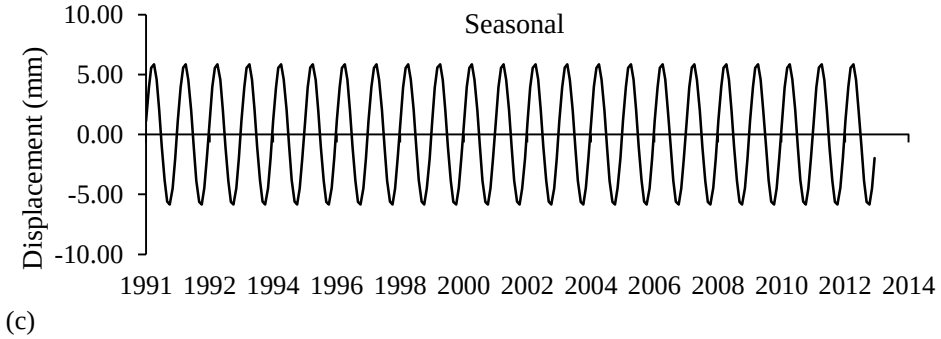

(c)

Figure 2.13: Displacement vs time (a) using linear fitting (b) using Model-I and (c) seasonal component

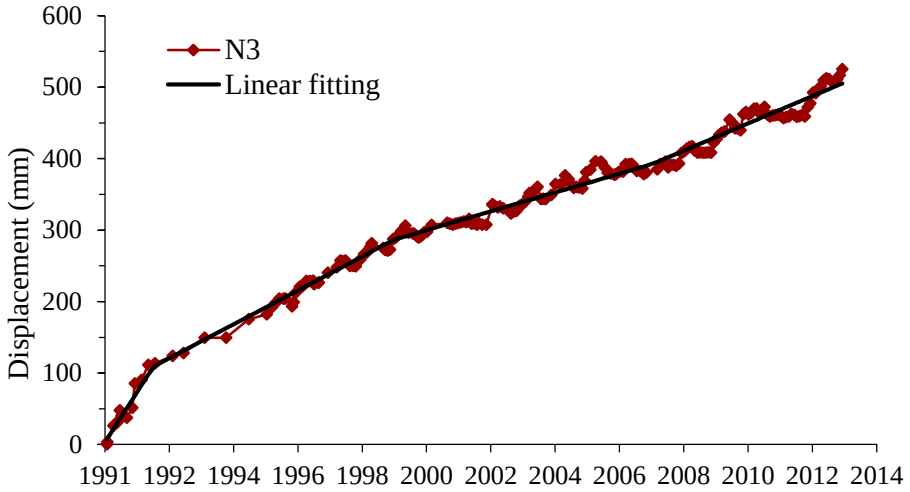

(a)

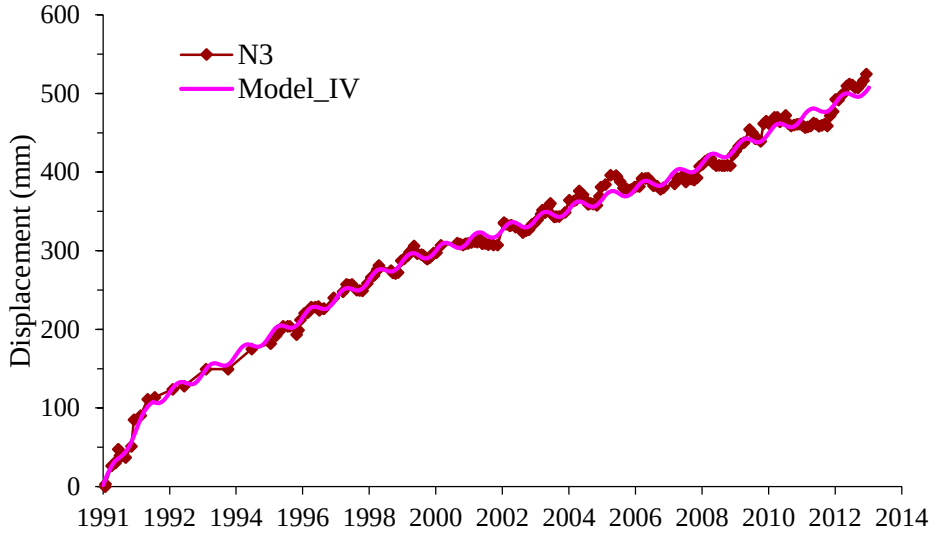

(b)

Figure 2.14: Displacement vs time (a) linear fitting and (b) using Model_IV

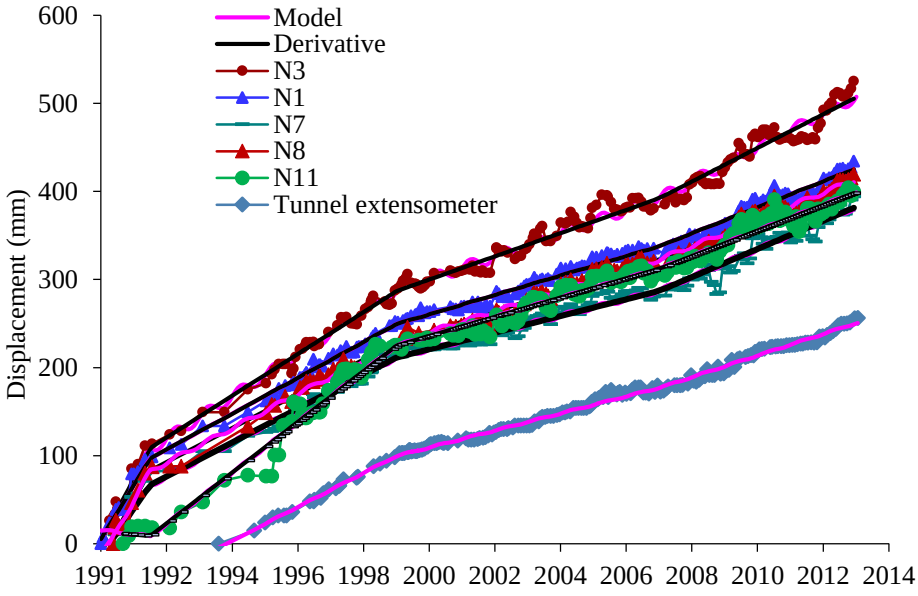

Figure 2.15: Displacement vs time for target points applying Model_IV

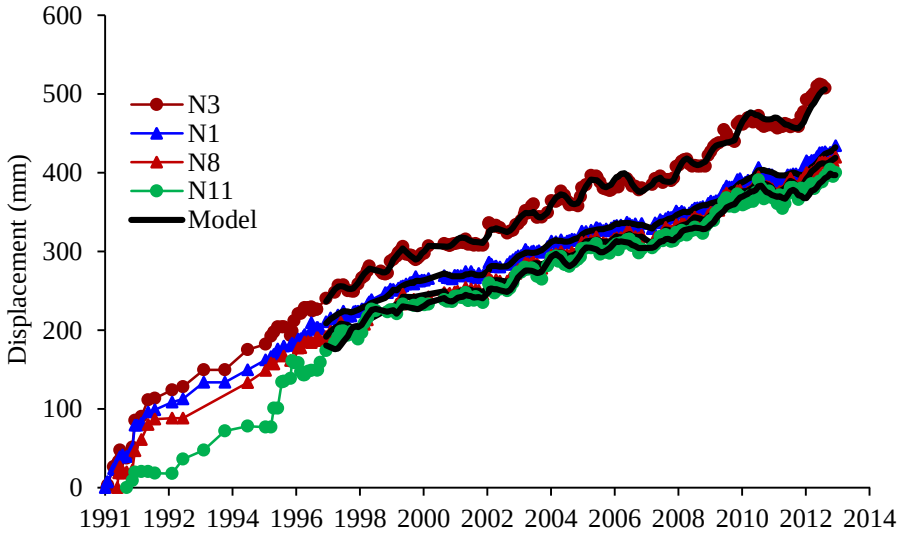

Figure 2.16: Displacement vs time for targets using a moving linear fitting

2.8 Conclusions

On the basis of the field investigations, the overall geomorphological behavior of the slope has been discussed.

The first sign of the ongoing movement has been discussed from the intensified cracks seen in the concrete lining section of the hydraulic tunnel. The clear picture of the ongoing movement has been evidenced from the remarked displacement trend observed during the early fillings of the dam.

Some interesting correlations between the early filling of the reservoir and the velocity of the ongoing movement are discussed.

The degree of fracturing of the slope has been highlighted: the toe part is more disturbed, as it was observed during the construction of intake structure. The base rock shows a regular bedded formation as it was evident during the excavation works of the dam foundation.

The measured displacement trend (targets and tunnel extensometer) has been modelled using simple linear regression models. Though some velocity changes occur throughout the monitoring period, average velocity between 13-17mm/y is prevalent which is a typical velocity of a slow moving mass.

Chapter 3

3 Geotechnical investigations, pore pressure regime and kinematic of the movement

3.1 Introduction

The characterization of the rock mass properties of the moving slope has been presented on the base of field investigations. Data from borehole loggings, geophysical studies have been employed to estimate the rock mass deformability.

The shear strength of discontinuities has been discussed by referring previous in situ and lab tests carried out on similar lithological contacts. While the shear strength of the basal sliding surface can be referred from the result of direct shear box tests, carried out on clay gouge recovered from sheared interbeds behind the damaged tunnel section.

Some reasonable correlations have been obtained between 3months (90days) cumulative rainfall and piezometer levels. Further analyses have shown that the 3months (90 days) cumulative rainfall exceeding the average rainfall correlates with the increase in piezometer levels. Finally, correlation between peak displacement velocities (i.e. target points and tunnel extensometer) with piezometer and cumulative rainfall data has been highlighted. Finally, the slip boundary and kinematics of the movement have been discussed from inclinometer profiles and displacement vectors.

3.2 Review of rock mass characterization

The deformation behavior of a given rock mass depends on the elastic properties of the intact block (deformation modulus, E, and poisson's ratio, v) and the elastic properties of joints (normal stiffness, k_n, and shear stiffness, k_s). The rock deformability can be evaluated from laboratory compression tests or field tests (Plate-bearing test, Flat-jack tests etc ….).

For instance, if a rock mass which contains a single joint set with spacing, S is subjected to shear and normal loading, the equivalent continuum moduli (Figure 3.1) can be evaluated from Equations (3.1) and (3.2). These equations highlight the rock mass deformation depends on the joint spacing or degree of fracturing. Moreover, the rock mass deformation can be estimated with the help of rock mass classification indices (Rock mass rating, RMR, Rock mass quality, Q, Geological

Strength Index, GSI, and Geophysical studies). These aspects will be discussed in the next section by referring previous studies.

The joint stiffness values for typical rock joints with soft clay infillings can be in the range of 10-100MPa/m. Published data concerning the stiffness of rock joints is limited. Previous studies (Bandis, 1980, Bandis et al., 1983) can offer some valuable data values. Barton (2007) revised some previous studies and provided range of values for the ratio of k_n/k_s.

The joint stiffness can be approximated from the back-analyses using information related to: the deformability of the intact rock, joint structure and rock mass deformability. In other words, the values of k_n and k_s can be estimated from Equations (3.1) and (3.2) provided that the intact rock (E, G) and rock mass (E_m, G_m) properties; and spacing, S, are known.

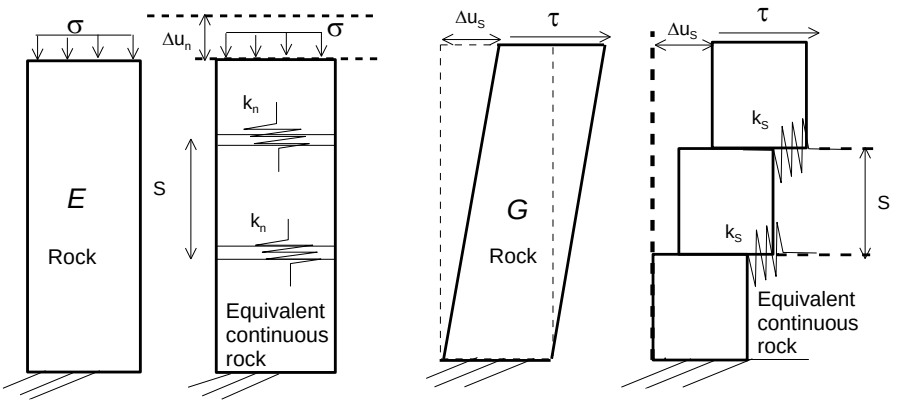

Figure 3.1: Idealization of a regularly jointed rock with an "equivalent" transversely isotropic material

$$\frac{1}{E_m} = \frac{1}{E} + \frac{1}{S * k_n} \tag{3.1}$$

$$\frac{1}{G_m} = \frac{1}{G} + \frac{1}{S * k_s} \tag{3.2}$$

where E, G are the intact rock Young's and shear moduli respectively, E_m, G_m are the rock mass Young's and shear moduli respectively, k_n and k_s are the fracture normal and shear stiffness respectively and S is joint spacing.

3.2.1 Estimation of deformation modulus

The Q-value method

The rock mass quality, Q value (Barton, 2002) can be approximated as

$$Q = \frac{RQD}{J_n} * \frac{J_r}{J_a} * \frac{J_w}{SRF} \tag{3.3}$$

where RQD is the percentage of core segments ≥100mm in length in a selected domain, J_r is the rating for joint surface roughness (of least favorable joint set or discontinuity), J_a is the rating for joint alteration, discontinuity filling, J_n is the rating for number of joint sets, J_w is the rating for water softening, inflow and pressure effects, SRF (Stress reduction factor) is the rating for faulting, strength/stress ratios, squeezing, swelling.

To include the influence of uniaxial compression strength, σ_c (MPa), to rock mass quality a new parameter, Q_c (Barton, 2002) is defined by Equation (3.4):

$$Qc = Q * \frac{\sigma_c}{100} \tag{3.4}$$

The value of Q varies from 0.001 to 1000 as shown in Figure 3.2. For example if we consider the value of Q to be 0.001 (i.e. for poor quality rock mass) and on the limit range of weak rocks uniaxial compression strength 0.25-1 MPa, the estimated value of E will be between 0.14-0.22GPa.

Then the rock mass deformation modulus E (in Gpa) can be estimated from Equation (3.5):

$$E = 10 * Q_c^{1/3} \tag{3.5}$$

Barton (2002) proposed the relationship between the Q-value of the rock mass and the Lugeon value (L) as follows after analyzing several data sets. Those previous results indicated a potential linkage between Lugeon value, L and Q_c-value, at least where permeability is caused by different degree of joint connectivity. Equation (3.6) can be used for approximating the permeability parameter of a rock mass.

$$L = \frac{1}{Q_c} \tag{3.6}$$

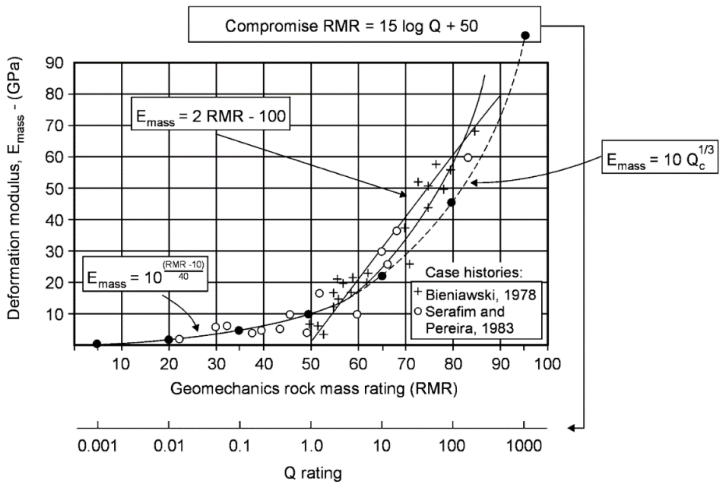

Figure 3.2: Static deformation modulus E_{mass}, Q and RMR and some empirical inter-relationships (after Barton, 2002). Note that rock mass quality varies from 0.001-1000 values for poor and excellent quality rock mass

The GSI-value method

For poor quality rock mass with $\sigma_{ci} < 100$MPa, the modified Serafim and Pereira's equation can give good results for estimating deformation modulus based on Geological Strength Index (GSI).

$$E = \sqrt{\frac{\sigma_{ci}}{100}} * 100\left(\frac{GSI - 10}{40}\right) \tag{3.7}$$

The GSI which is introduced by Hoek (1994) assists to characterize the rock mass deformation and strength. The rock mass characterization can be performed by referring the blocky structure, the surface condition of the discontinuities described by joint roughness and alteration. Combining these parameters, tables provided by Hoek and Brown (1998) can be referred to select the appropriate GSI value. However the choice of parameter values needs extensive experience to get reliable estimation.

The deformation modulus can also be approximated from the GSI value and uniaxial compression strength (σ_c) (Figure 3.3). Table 3.1 shows the deformation modulus of very weak and sheared rock masses as reported by Hoek et al. (1998).

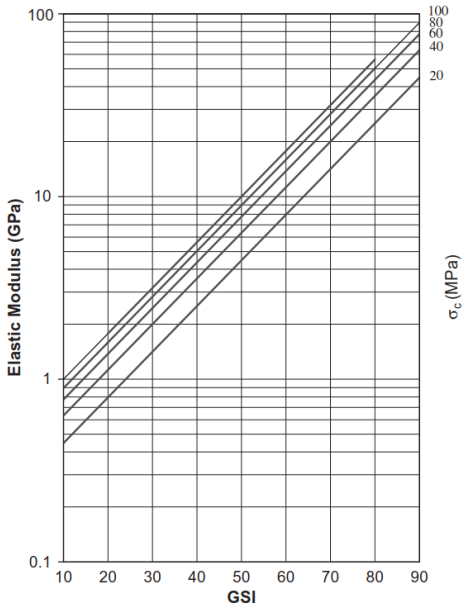

Figure 3.3: Elastic modulus vs GSI for various σ_c values (after Cai et al., 2004)

Table 3.1: Estimated deformation modulus values (in GPa) for various rock types of the Athens Schist Formation which is classified between A^+ to C^- (after Hoek et al., 1998)

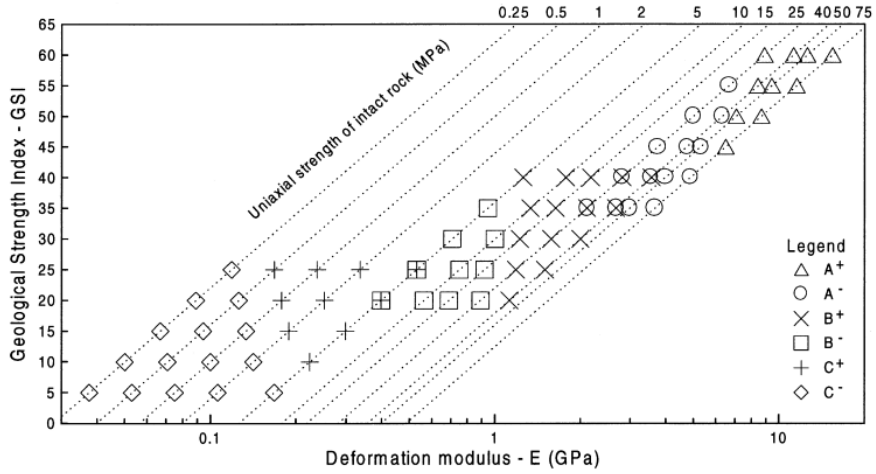

A⁺	Medium strong to strong metasandstone or limestone rock mass, interlocked, with angular block formed by four or more discontinuity sets with rough and MW to SW surface condition.
A⁻	The lower E_m values of this field derive either from lower σ_{ci} values due to weathering-tectoni weakening of the intact rock material, or from lower GSI values reflecting the decreased surfac quality due to shearing / mylonitization and weathering.
B⁺	Medium strong to weak, thinly foliated sericite sandstone / schist or greywacke, with occasiona boudins of quartz.
B⁻	The lower E_m values may derive either from lower σ_{ci} values due to weathering-tectonic weakenin of the intact rock material, or from lower GSI values reflecting the decreased surface quality due t shearing / mylonitization and weathering.
C⁺	Weak to very weak, laminated argillaceous shale or phyllite, with boudins of quartz or lenticula blocks of intact rock in a soft rock environment.
C⁻	The lower E_m values bottom left derive either from lower σ_{ci} values due to weathering-weakening o the intact rock material, or to lower GSI values reflecting the absence of blockiness and th decreased surface quality due to shearing / mylonitization and weathering.

Estimation of GSI value

The GSI value can be determined more precisely if there is a possibility to employ some quantitative input parameters. Previous studies (Palmström, 1995, Cai et al., 2004) discussed the importance of volumetric joint count (J_v) and block volume (V_b) values, which can be determined on the base of field investigations. A study by Cai et al. (2004) emphasized the importance of these quantitative values (J_v and V_b) in order to obtain reliable GSI values, more helpful for the less experienced experts.

Block volume

The block size which is evaluated from the joint spacing, joint orientation, number of joint sets and joint persistency is often applied to describe the rock mass quality. If three or more persistent joints are present (Figure 3.4), the block volume, V_b can be calculated as

$$V_b = \frac{s_1 * s_2 * s_3}{\sin(\gamma_1) * \sin(\gamma_2) * \sin(\gamma_3)} \tag{3.8}$$

where s_i and γ_i are the joint spacing and the angle between the joint sets respectively. Moreover the above expression could be further simplified so as to obtain a more practical expression for block volume as

$$V_b = s_1 * s_2 * s_3 \tag{3.9}$$

and the volumetric joint count, J_v can be determined from

$$J_V = \frac{1}{s1} + \frac{1}{s2} + \frac{1}{s3} + ... + \frac{N_r}{5} \tag{3.10}$$

where N_r is the number of random joints in the observation area

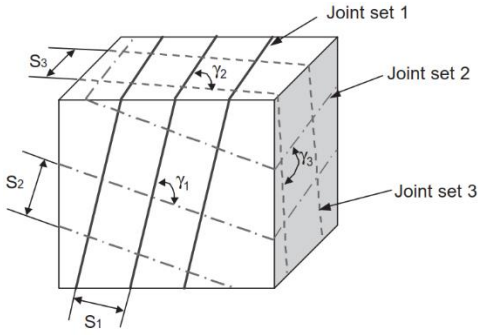

Figure 3.4: Block formed by three joint sets (after Cai et al., 2004)

However, if irregular jointing is encountered in the rock mass, it becomes more difficult to trace three or more joint sets. In such circumstances, it is advisable to measure the dimension of representative block volume in the field. Otherwise methods proposed by Palmström (1995) can be adopted using the value of RQD, volumetric joint count, J_v and weighted joint density.

Therefore, the block size V_b can be evaluated from the RQD from Equation (3.11).

$$V_b = \beta * \left(\frac{115 - RQD}{3.3} \right)^{-3} \tag{3.11}$$

where β is the block shape factor which ranges from 27 to 100. For equal dimension blocks, β = 27-35 with an average value of β = 31. If not known the value of β = 36 is recommended.

Joint condition factor

The joint condition factor which describe the roughness, weathering and infilling condition. According to previous studies (Palmström, 1995, Cai et al., 2004) the joint condition factor, J_C is given as:

$$J_C = \frac{J_W * J_S}{J_A} \tag{3.12}$$

where J_W is the large scale waviness in meters between 1 to 10 m and J_S is the small scale smoothness in centimeter from 1 to 20 cm and J_A is the joint alteration factor. The value of the parameters can be approximated from tables provided by previous authors (Palmström, 1995 and others).

3.2.2 Roughness of discontinuities

In practice the friction angle of the rock joint could include two components: the base friction angle of the rock material plus the contribution from the irregularities or asperities of the rough surface.

The value of joint roughness coefficient (*JRC)* can be estimated from tilt test, measurement of surface amplitude of roughness from a straight edge or visually comparing joint profiles with the standard profiles provided by Barton and Choubey (1977). Its value varies from 0 – 20 for smooth and very rough profiles respectively (Figure 3.5). The roughness of the surface, *i* can be related to the *JRC* as

$$i = JRC * \log\left(\frac{JCS}{\sigma_n^{'}}\right) \tag{3.13}$$

where *JCS* is joint compressive strength and σ'_n is the effective normal stress on the surface due to the weight of the overlying rock mass. *JCS* is equal to the unconfined compressive strength of the intact rock, if the discontinuity is clean and unweathered, otherwise it can be estimated by performing Schmidt rebound hammer test.

For instance, Bandis (1980) reported *JCS* = 64 - 58 MPa for siltstone while *JCS* = 67 for a moderately weathered rock joint in sandstone. Moreover weathered joints of siltstone and sandstone can have *JCS* = 44 MPa and 22 MPa respectively.

These parameters (*JRC* and *JCS*) depend on the scale (i.e. length of the joint). As the size of the discontinuity decreases there is a corresponding decrease of *JRC* and *JCS* values. Detailed analyses of the scale effects can be referred from previous studies (Barton and Choubey, 1977, Bandis et al., 1981).

Higher values are expected for less persistent and rough joint sets while low values for persistent and mineralized joint sets.

Considering the above rock joint parameters, *JRC* and *JCS*, the shear strength of a rock joint can be evaluated as:

$$\tau = \sigma_n * \tan\left[JRC * \log\left(\frac{JCS}{\sigma_n^{'}} \right) + \varphi_r \right]; \qquad i = \varphi_p - \varphi_r \tag{3.14}$$

where τ is peak shear strength, *JRC* is joint roughness coefficient, *JCS* is the joint wall compression strength , φ_p is the peak friction angle, φ_r is the residual friction angle and i is the roughness angle, which can be evaluated from Equation (3.13). A comprehensive discussion on the shear strength of discontinuities has been provided in Section 3.3.3 by referring several in situ and laboratory investigation results.

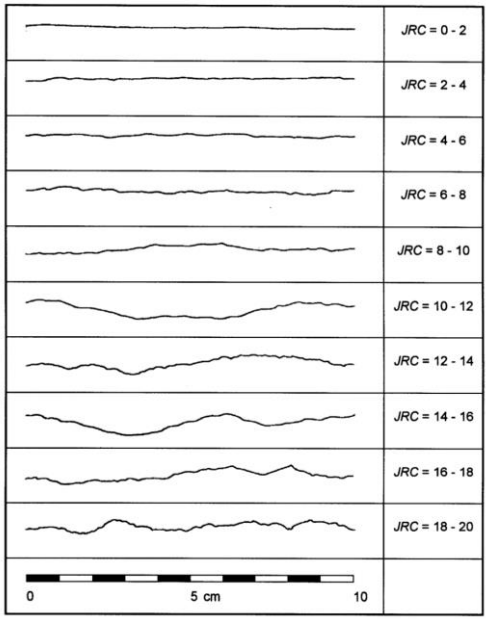

Figure 3.5: Typical roughness values for *JRC* range based on peak shear strength criterion (after Barton and Choubey, 1977)

In addition to the mechanical property, the hydraulic properties of discontinuities depend by the morphology of the fracture surfaces (roughness parameters).

For a clean rock joint, when fracture undergoes shear displacement, the fracture will dilate and the transmissivity of the joint will increase.

Previous studies (Bandis, 1980, Barton et al., 1985) discussed in detail the behavior of coupling occurred between rock joint conductivity and shearing. They remarked that smooth joints (with slickensided surface) often found in soft rocks have limited coupling between conductivity and shearing. While the rough rock joints found in strong rocks have limited closure of aperture during compression but the joints experienced strong coupling between shearing and conductivity.

In contrary to a clean rock joint, the characteristics of infilling material should be considered so as to predict the behavior of the discontinuity of a filled rock joint (Indraratna et al., 1998). Joint dilation would be limited if the infill thickness is substantial, instead compression of the infill material occurs.

3.2.3 Rock mass strength properties

Hoek-Brown non-linear criterion

The rock mass strength can be estimated from the most commonly used Hoek-Brown (1980) non-linear criterion which is given by:

$$\sigma'_1 = \sigma'_3 + \sigma_{ci}\left(m_i \frac{\sigma_3'}{\sigma_{ci}} + s\right)^{0.5}$$
$$m_b = m_i \exp\left(\frac{GSI - 100}{28}\right) \qquad (3.15)$$

where σ'_1 is the major principal effective stress at failure, σ'_3 is the minor principal effective stress (confining pressure). And m_b, m_i are material constants for rock mass and intact rock respectively.

From the equation of Hoek-Brown, the principal stresses at failure for an intact rock depend on parameters i.e. uniaxial compression strength, σ_{ci} and constants, m_i and s. The value of m_i, varies from 0.001 for a highly disturbed rock mass to 25 for hard intact rock while the value of s, ranges from 0 for jointed rock mass and 1 for intact rock material.

Basically these parameters should be evaluated using statistical analysis of data obtained from a series of triaxial tests on a carefully recovered core samples. Hoek and Brown (1980) recommended to use a range of minor principal stresses, $0 < \sigma_3' < 0.5 * \sigma_{ci}$ in laboratory tests to get reasonable estimate of σ_{ci} and m_i since the choice of minor principal stress affect to get reliable results.

Tables, which are already prepared based on a range of values taken from tests conducted in typical rocks, can be consulted to approximate the required parameters whenever lab tests are not possible. Moreover, the Hoek-Brown failure criteria assumes an isotropic rock mass behavior where there are significant number of discontinuities.

Knowing the GSI value together with the intact rock parameters (σ_{ci} and m_i), the rock mass strength properties can be estimated (Hoek, 1998) as shown in Figure 3.6.

For GSI > 25 and rock masses of good quality, the original Hoek-Brown criterion can be applicable with parameters (s and a) defined below.

$$s = \exp\left(\frac{GSI - 100}{9}\right);\ \text{a} = 0.5 \tag{3.16}$$

For poor quality rock mass with GSI < 25, modified Hoek-Brown criterion can be referred with parameters (s and a) expressed as follows.

$$\text{s} = 0 \text{ and } a = 0.65 - \frac{GSI}{200}$$

$$\sigma'_1 = \sigma'_3 + \sigma_{ci}\left(m_i \frac{\sigma_3'}{\sigma_{ci}}\right)^{0.5} \tag{3.17}$$

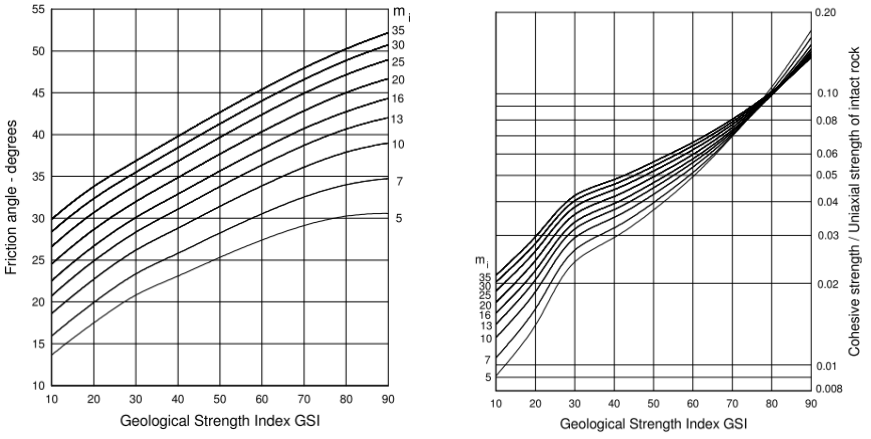

(a) (b)

Figure 3.6: Relationship between (a) friction angle and GSI and (b) cohesion strength and GSI for various m_i values (after Hoek et al., 1998)

Influence of joint orientation on strength of rock mass

In anisotropic condition the failure condition is favored by property of weak planes. Thus the above Hoek-Brown criterion cannot be employed. In such cases failure occurs on the along discontinuities.

Uniaxial and triaxial tests on marl and sandstone lithotypes were performed by Oberti et al. (1986) to understand the influence of orientation of specimen axis in relation to the bedding plane on deformability and strength characteristics. As the orientation angle, α increases from 0º to 45º using confining pressures 0, 2.5, 5, 10 and 15MPa, a marked decrease of strength was evidenced particularly from low confining pressures (Figure 3.7).

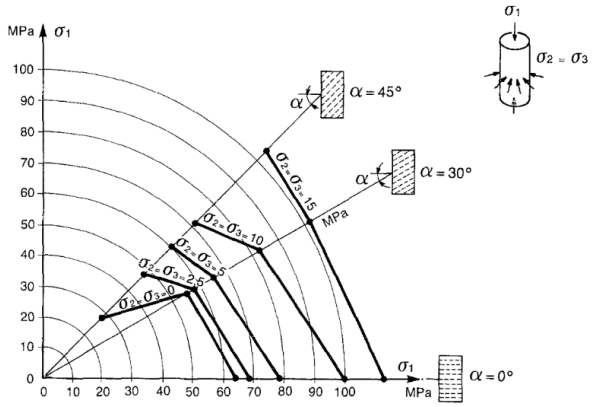

Figure 3.7: Triaxial test on marl specimens (after Oberti.et al.1986)

3.3 Rock mass properties of the slope

By referring borehole loggings some remarks have been made regarding the RQD value, the joint spacing and dip angle of the joint sets. In addition, the deformation modulus of the rock mass has been evaluated by employing GSI, Q-value method and geophysical studies.

3.3.1 Borehole loggings

The complex structure of the rock mass, as expected from the geological investigations, is clearly confirmed by a comprehensive analysis of borehole loggings. Borehole investigations have been focused on the N sector of the ridge, particularly, in the zone of the tunnel intake.

Bedding joints have discordant orientation in the upper and lower portion of the ridge, especially on the W flank, as already recognized

from field surveys. This situation suggests that the entire body of the ridge can be divided in different zones, characterized by a variable degree of fracturing and disarrangement of the rock mass. Figure 3.8 depicts the typical borehole (S3) logging recovered from site investigation which confirms the variability of the degree of fracturing along depth. Sheared surfaces can also be visually seen as a consequence of block shear deformation (Figure 3.8 a and c).

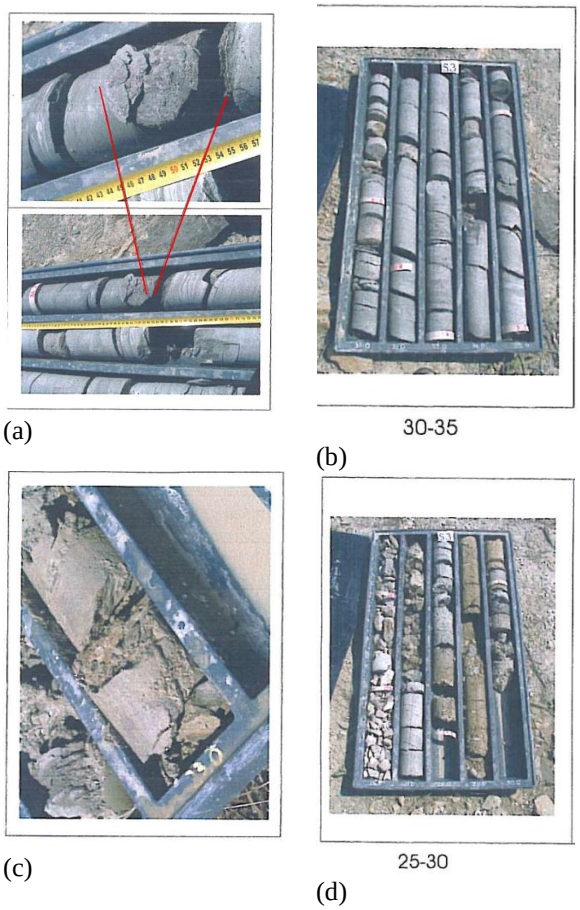

Figure 3.8: Typical borehole (S3) logging recovered during investigation with particular sheared surfaces at 34.5m (a); and 24.9m (c) depth from the surface

Though results obtained from borehole loggings are sparse, chaotic formation typically accounts for 10 to 40% of total borehole logging data (Figure 3.9). Comprehensive analysis of joint dips from borehole

loggings shows that sub-horizontal strata and steep joints are inclined, respectively, between 5-20° and 30– 60° or 80º (Figure 3.10). Likewise field spacing of the joints lies in the range of 0.05-0.5m as shown in (Figure 3.11). The upper marly–arenaceous formation has joints with spacing in between 0.05-0.2m while the lower undisturbed formation has 0.05-0.4m joint spacing.

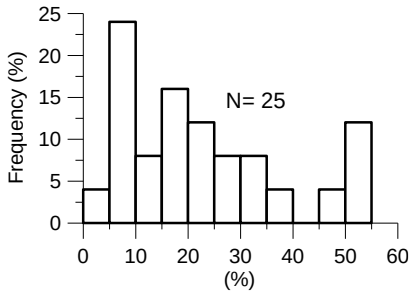

Figure 3.9: Frequency distribution of the percentage of chaotic formation observed in 25 boreholes

For instance, the S3 borehole (Figure 3.8), drilled through the toe of the N slope of the ridge, shows that the base marly-arenacoues-calcarenitic unit has RQD value in the 40-70% range with discontinuities dipping between 18-20° while the upper layer of disturbed marl RQD value is from 15-40% with discontinuity inclined at 12-20°. Lower RQD values between 10–40 % and even null values were obtained in the more disturbed zones, presumably the zones of higher shearing deformation.

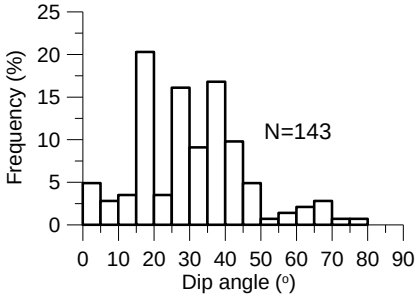

Figure 3.10: Frequency distribution of joint dip angles (from 143 local measurements in different boreholes)

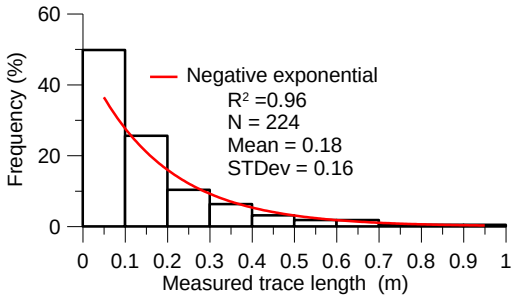

Figure 3.11: Frequency distribution of joint spacing obtained from an overall borehole length of 78m

Borehole S27 (Figure 3.12), located in the NW side of the ridge, shows RQD values of 50-70% for the undisturbed marly-arenaceous-calcarenitic unit and RQD of 15-30% at the depth of the sheared zone.

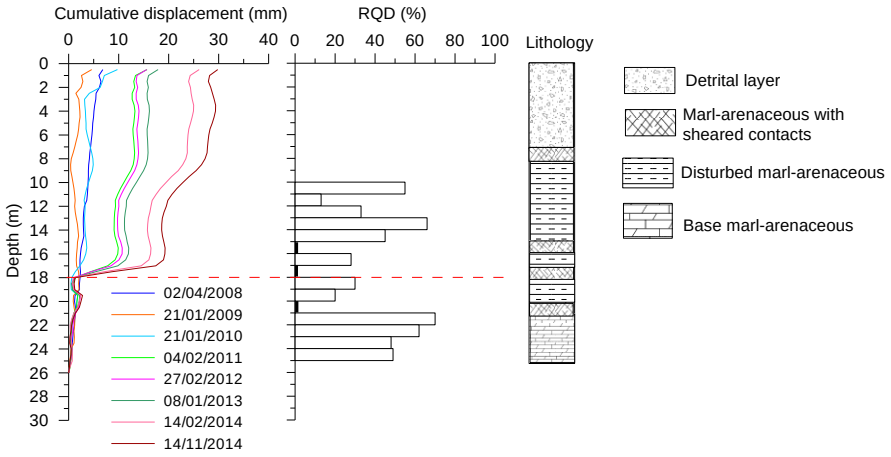

Figure 3.12: Displacement vs. depth arranged at yearly interval and its relation stratigraphy and RQD of the inclinometric borehole, S27. Zero reading starts on 5/2/2007

3.3.2 Application of rock mass characterizations

The deformation modulus of the rock mass in the more disturbed and less disturbed portion of the slope has been estimated using the Q and GSI values. The shear strength of rock mass can be approximated with the help of Hoek-Brown parameters.

The Q-value method

The Q-value method (Barton, 2002) has been applied here to estimate the deformation modulus of the upper disturbed rock mass and the lower base rock (less disturbed) marly-arenaceous formation.

In the previous discussion of borehole data analyses, the disturbed marly-arenaceous formation has RQD values in between 10-40 % while the less disturbed formation has RQD between 40-75%. Thus, for instance if we consider the following parameters for the disturbed marly-arenaceous formation (i.e. RQD = 10-40%, J_n =15, J_r = 1.5, J_a =8, σ_{ci} = 50MPa, SRF = 1). Then Q_c-value between 0.05-0.2 can be estimated from Equation (3.4).

Therefore, the rock mass deformation modulus E= 3-5GPa has been evaluated (Equation (3.5**)**. Similarly, for the less disturbed rock mass adopting the following parameters, RQD = 40-80%, J_n =6, J_r = 1.5, J_a =2, σ_{ci} =75MPa, then Q_c=2.5- 4.7 will be evaluated. Therefore, E=13-17GPa has been obtained.

Estimation of GSI value

The concepts of block volume and volumetric joint count has been adopted herein to characterize the rock mass deformation.

The block volume, V_b has been estimated from Equation (3.11) as it is more advisable method when there is difficulty to trace clearly the join sets found in the rock mass, i.e. more sparse joint sets.

With regard to the joint condition factor, J_C, the rating of parameters J_W, J_S and J_A has been carried out from borehole loggings and by consulting previously prepared tables (Palmström, 1995).

Therefore, joint condition factor, J_C = 0.25-0.67 and V_b =0.5-5*10^3 cm^3 is estimated (Equations (3.11) and (3.12)) by taking in to account RQD = 10-40 % and β = 36. Using the above values of J_C and V_b in the GSI system, the disturbed rock mass GSI = 25-35.

While for the base marly-arenaceous formation J_C = 0.67- 1.7 and V_b =5-30 x$10^3$$cm^3$ by considering RQD = 40-80%. Thus, GSI = 40-55 seems appropriate for the less disturbed rock mass formation.

Deformation modulus using GSI value

With the help of the GSI estimated earlier, the deformation modulus could be evaluated from the modified Serafim and Pereira's equation (Equation (3.7)), which is a recommended approach for rock masses with UCS < 100 MPa value ranges.

Moreover, plate load tests and uniaxial compression tests were performed during the construction of the new river discharge tunnel in the upstream reach to characterize marly–arenaceous formation.

Thus, for the marly lithological unit, the UCS (unconfined compression strength) obtained from uniaxial tests lies in between 22-88 MPa. A similar result for UCS between 26-118 MPa were obtained from plate load tests. This dispersion of UCS values arises from presence of discontinuity in the rock mass and a typical value of UCS between 25 - 75 MPa can be assumed. Similarly, in the formation of arenaceous-calcarenite unit the uniaxial test results showed that UCS is in between 73 -140 MPa.

Therefore, UCS = 50 MPa for the disturbed portion and UCS = 75 MPa, for the base rock deformation modulus can be taken as representative average values. Recalling the GSI value ranges for disturbed and the base rock marly-arenaceous formation, deformation modulus, E can be estimated easily from the modified Serafim and Pereira's equation.

Therefore, the estimated deformation modulus, E, for the disturbed part of the slope lies in between 1-5GPa.While for the base rock, E, could be in the range of 5-10GPa. Moreover, the deformation modulus estimated from the GSI value are lower as compared to the values calculated earlier using the Q-value method.

Shear strength of the rock mass

Once the GSI value is estimated, together with the values of m_i and σ_{ci}, the shear strength properties of the rock mass could be estimated.

The shear strength has been estimated considering the intact rock Hoek-Brown parameter, m_i = 7-10 and the uniaxial compression strength, σ_{ci}, equals to 50 and 75 MPa for the disturbed and less disturbed rock mass respectively.

Thus, the friction angle, φ, of the disturbed rock mass could be in the range of 25-27^o and cohesion, c, would be between 0.5-1MPa (Figure 3.6). While the less disturbed rock mass, shear strength properties would be φ = 27-30^o and cohesion in the range of 1-2.3 MPa.

3.3.3 Mechanical properties of discontinuities

Slickensided joints are frequently found in borehole cores (Figure 3.13), mainly at the contact between marly and arenaceous layers but also within

claystone beds. Based on field observations, rock joints can be characterized by JCS = 30-40MPa and JRC = 3-5.

In situ shear tests were performed by Baldovin (1968) on laminated bedding joints of marly arenaceous formation using blocks (90 x 90 cm) assembled together. Figure 3.14 depicts the friction angle between 12-13^o determined from the in situ test of the slickensided discontinuities present in the marly-arenaceous formation.

In a similar fashion, Oberti et al. (1986) also performed in situ shear tests on blocks (0.5x0.5x0.35 cm) assembled in a layer of sandstone. The results of the shear tests (Figure 3.14) showed φ =13^o for contacts between sandstone and laminated–clayey marlstone. A higher friction angle between 26-35^o was obtained for contacts between sandstone and marl.

Laboratory shear strength tests between inclined clay filling and limestone contacts were also conducted by Hatzor et al. (1997); φ_r = 13.5-18° was obtained. A relatively higher friction angle between 32-35^o was determined from the clay–limestone contacts.

In addition, from in situ and laboratory direct shear tests, Alonso and Pinyol (2014) obtained peak and residual strength of 14° for sandstone – sandstone contacts and φ_p = 19°; φ_r = 13-18° for sandstone–claystone contacts.

A report by Grana and Tommasi (2013) shows φ_r in the range of 10-26° after several ring shear test performed on specimens from an outcrop of the same Marly-Arenaceous in a nearby site, also containing thick clay interbeds. Ring shear tests from Tommasi et al. (2009) show that φ_p = 13-27° and φ_r = 10-15° for different types of clay-rich interbeds.

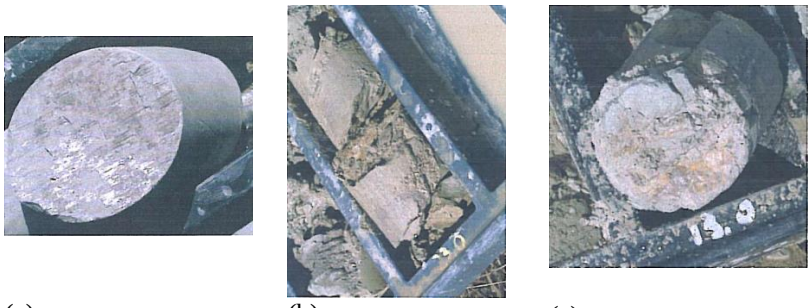

(a) (b) (c)

Figure 3.13: Typical aspect of joint surfaces: joint surface recovered from borehole S27 at depth of 7.4m (a), from borehole S3 at depth of 24.9m (b), presumably close to the depth of the slip surface, and from borehole S23 at depth 13m (c)

Direct shear tests (Lembo Fazio et al., 1990) conducted on 60x60x25mm samples of clayey interbeds show φ_p = 15-27^o and φ_r = 12-15^o according to the structural conditions of the interbeds and their softening condition.

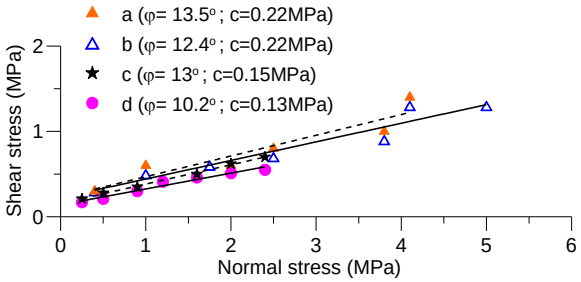

Figure 3.14: In situ shear tests performed on joints between sandstone and laminated clayey marlstone. a and b, data from Oberti et al. (1986), c and d, data from Baldovin (1968)

Mechanical properties of slip surface

The intense shearing deformation occurred along the basal zone of the slope strongly suggests that the mobilized strength is likely to be close to residual conditions for most of the sliding surface.

Figure 3.13 depicts the typical slickensided joint surface recovered from several boreholes located in the toe part.

The properties of the sheared material (clay gouge) were examined from exploratory window opened at the damaged portion of the tunnel section, where the slip surface could intersect the tunnel. The core of the shear zone consists of a 0.15 - 0.20m thick band of clay gouge (Figure 3.15) entrapping fragments formed by shear grinding of the rock materials (mainly marl and sandstone). Index properties of the clay gouge samples are: Clay = 46%, Silt = 45%, Sand = 9%, γ_s = 27.2 kN/m3, w_L = 72.6%, w_P = 40.2 %, I_p =32.4%, CaCO3 = 20.1%. This material possesses high plasticity and its grain size composition is dominated by a high silt-clay proportion and less coarse materials. The results of the lab tests in drained condition are: peak, c_p =21.5 kPa and φ_p = 15° and residual, φ_r = 7.7° (Figure 3.16).

(a) (b)

Figure 3.15: Clay gouge interbed with thickness of 0.1-0.2 m exposed at the damaged tunnel section (a), detail with deformed steel set (b)

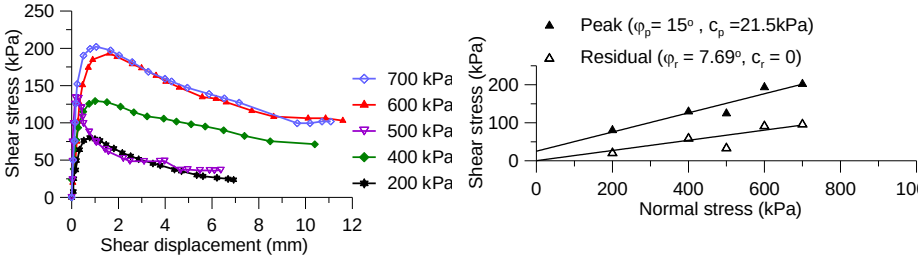

Figure 3.16: Results of direct shear tests on clay gouge sample

3.3.4 Geophysical surveys

In this section a detailed discussion of the geophysical studies conducted in the dam site and slope has been provided. The geophysical surveys have been referred to investigate the deformation modulus and permeability of the rock mass.

Previous study by Oberti.et al. (1986) showed good correlation between sonic velocity and deformation modulus (Figure 3.17). They determined the deformability of the rock mass using hydraulic pressure chamber test, plate bearing test performed parallel and perpendicular to the stratification of marl and sandstone. Moreover, their test results showed deformation moduli E=18-24GPa and 16-18 GPa for tests conducted parallel and perpendicular to the stratification respectively.

A comprehensive study by Ribacchi (1987) on several dam sites in Italy also showed good correlation between plate loading tests and sonic measurements.

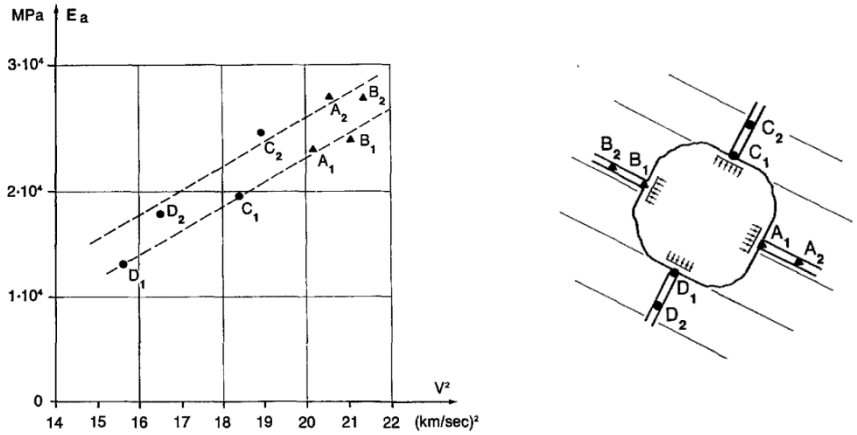

(a) (b)

Figure 3.17: (a) Correlation between deformation moduli and square of velocity of elastic waves measured at different depths from the loading surface (0.07m, 0.5m) and (b) Plate bearing tests on a section of right bank exploratory adit (after Oberti.et al.1986)

Seismic refraction tests conducted in the slope (earlier investigations)

A geophysical study was conducted on Chiascio River valley covering around 0.85km^2 area in 1971. The scope of investigation in the vertical includes: upper detrital cover, disturbed and less disturbed Marly-arenaceous formation.

In the upper detrital cover, which accounts for a depth of 4-5 m, lower P-wave velocities in the range 0.3-0.7 km/sec, were obtained. The disturbed Marly-arenaceous formation, which is identified to be altered and with discontinuities, P-wave velocities between 1.1-1.9 km/sec were recorded. Relatively higher P-wave velocities between 2.5-3 km/s were obtained in the less disturbed Marly-arenaceous formation. The contrast of the P-wave velocities inside the rock mass along a vertical below the detrital layer cover is low lying in the range of 1.1-3 km/s. So it is not straightforward to differentiate clearly the disturbed rock mass from the undisturbed formation from these seismic refraction tests.

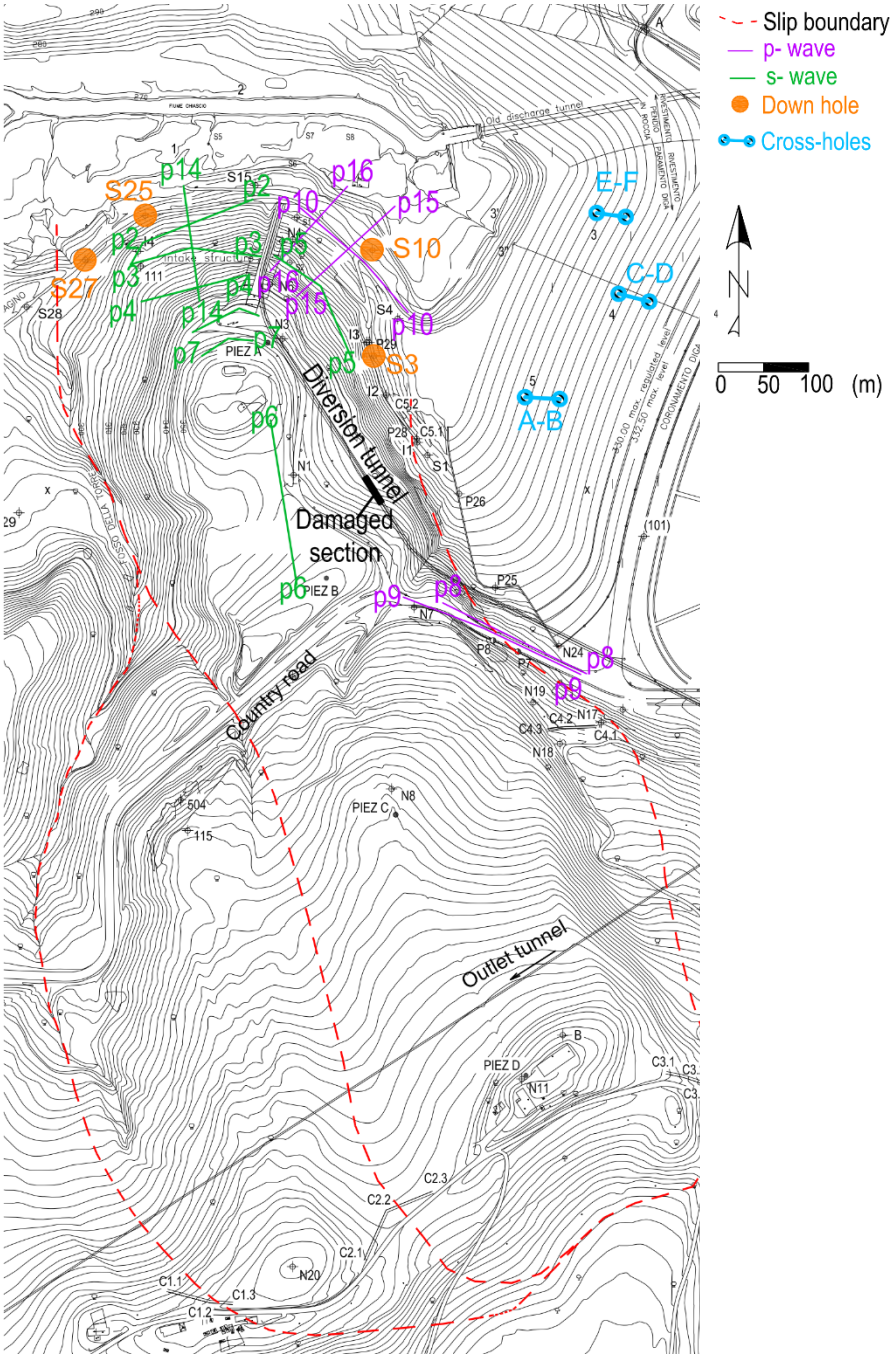

Figure 3.18: Locations of geophysical studies

The corresponding dynamic moduli of elasticity, which have been estimated using (Equation (3.18)) from seismic P-wave velocities for each layer, are presented in Table 3.2 assuming, $v = 0.25$. Similar results will be reported latter from geophysical studies conducted on the slope site.

Table 3.2: Estimated rock modulus from seismic refractions (V_p)

Velocity ranges V_p (km/s)	Dynamic modulus E_d (GPa)	Lithological remarks
1.1- 1.9	2.2 - 6.6	Disturbed Marly-arenaceous
2.1- 3.0	8.1- 16.5	Less fractured Marly-arenaceous formation
3.0-3.5	16.5 - 22.5	Base Marly-arenaceous-calcarenite formation

Cross hole

Cross-hole tests were employed in the excavated zone of the dam site using compressional (V_p) and shear wave velocities (V_s). Three sets of cross-holes tests (i.e. A-B, C-D, E-F) were installed up to 30m depth intersecting the Marly-arenaceous-calcarenite dam foundation (Figure 3.18). Measurements were recorded at 1.5 m intervals.

From the cross-hole tests (A-B, C-D, and E-F), V_s is in between 1.2-2km/s while the value V_p is in the range of 3.2-4.2 km/s.

Assuming the rock mass to be homogeneous, isotropic and elastic the following calculations can be made to estimate the deformation moduli (Equations (3.18), (3.19) and (3.20)). Figure 3.19 depicts the elastic properties (E_d, v_d) estimated from cross-hole tests. The deformation modulus lies between 10-15GPa. These estimated elastic properties (E_d, v_d) are higher as compared to results estimated earlier based on GSI values.

$$E_d = \rho V_p^2 \left(\frac{(1+v_d)(1-2v_d)}{1-v_d}\right) \tag{3.18}$$

where the dynamic poisson's ration v_d is given by:

$$v_d = \frac{\left(\frac{v_p}{v_s}\right)^2 - 2}{2\left(\frac{v_p}{v_s}\right)^2 - 1} \tag{3.19}$$

and dynamic shear modulus, G and the dynamic bulk modulus, K_{bulk} can be evaluated from velocities V_p and V_s as follows: -

$$G = \rho V_s^{\,2} = \frac{E_d}{2 + 2v_d}$$
$$K_{bulk} = \rho(V_p^{\,2} - \frac{4}{3}V_s^{\,2}) = \frac{E_d}{3 - 6v_d} \tag{3.20}$$

where G is shear modulus, ρ is density and V_s is seismic velocity in transversal direction and V_p is seismic velocity in longitudinal direction.

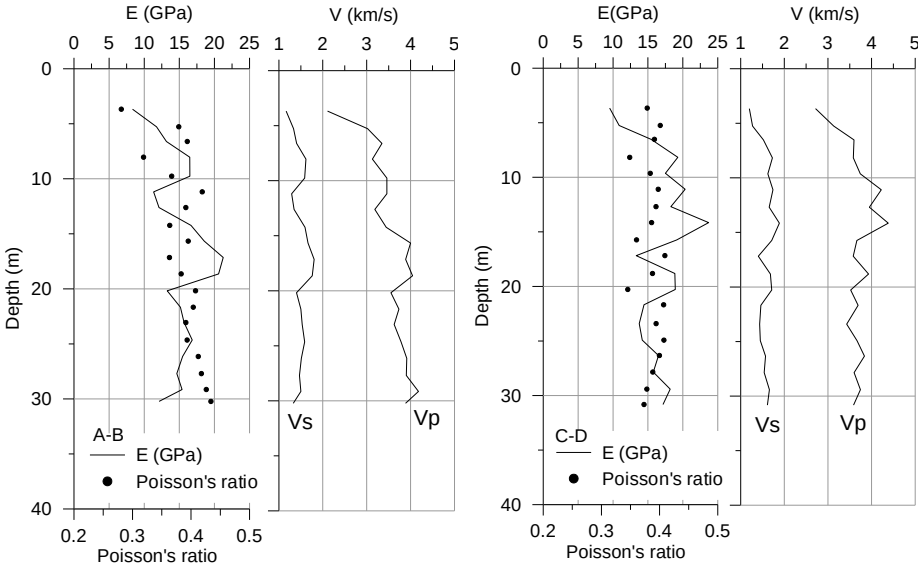

Figure 3.19: Estimated rock mass modulus and poisson's ratio using cross-hole test results

Geophysical studies conducted on the slope site (recent investigations)

Downhole tests mainly in the toe part of the slope were carried out at boreholes S10, S3, S27 and S25 in 2007. Besides this, seismic refractions using P and S waves were conducted on the slope site (Figure 3.18). Some attempts were made to match P and S wave velocity profile with the lithological formations. The first few meters composed of loose detrital layers (i.e. silt and gravel deposits) gives lower values between 0.1-0.6km/s while velocities between 0.5-1.5km/s were achieved for the disturbed marly-arenaceous formation with RQD between15-30%. A relatively higher velocity in the range of 1.5-3.2 km/s was reported for the less disturbed marly-arenaceous-calcarenite matrix with RQD in the range of 40-70%. Figure 3.20 depicts the vertical profile of P-wave velocities at different locations (P15, P16, P8 and P9).

The recorded low velocities are associated with the high density of open fractures which cause low P-wave velocity and rock mass cohesion (Jeanne et al., 2013). The values of P-wave velocity measurements are correlated with the volumetric stiffness of the rock mass and the quality or degree of weathering of the rock mass; and lower P-wave velocity values are related to the lack of confining stress (Alonso et al., 2014).

The corresponding dynamic modulus of elasticity could be estimated from seismic P-wave velocity for each layer assuming, ν = 0.25. Therefore, the upper more disturbed rock mass could have deformation modulus between 0.5-1.3GPa. While for the less disturbed rock mass, E will be in between 1.3-4.5GPa. Higher value of E= 16-22 GPa is obtained for base rock. Moreover, the values of E evaluated from geophysical studies are comparable with the previous estimations obtained using GSI value.

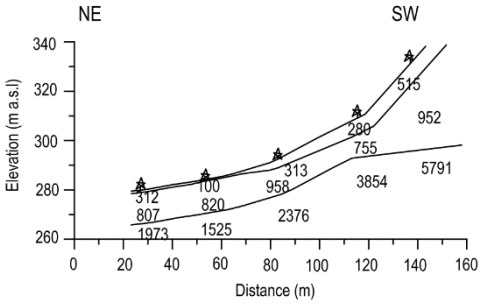

(a) P15

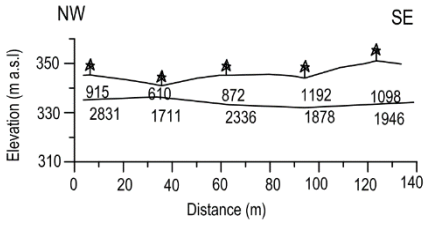

(b) P8

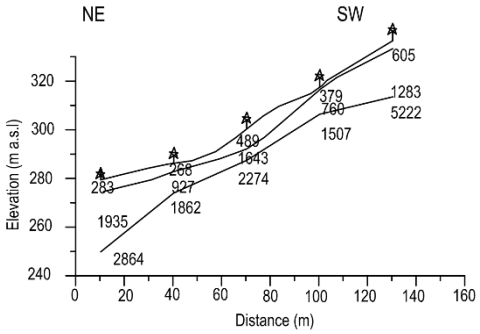

(c) P16

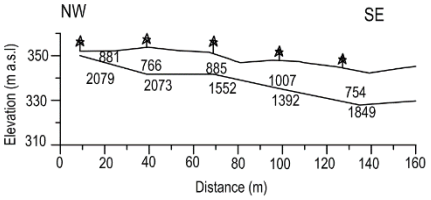

(d) P9

Figure 3.20: P-wave velocities (m/s) obtained from geophysical investigations performed on the sliding mass

3.3.5 Permeability tests

Lugeon tests were conducted in the area of the dam foundation. The permeability of the rock mass lies between $1x10^{-7}$–$3x10^{-7}$ m/s (Figure 3.21). Moreover, from the Lugeon test results it has been observed that higher Lugeon values were frequently associated with the more disturbed and loosened marly-arenaceous formation while the lower values were obtained in the clay rich bedding layers.

Similar results were obtained by Oberti et al. (1986) in the area of Ridracoli dam of similar lithology, average permeability of $1x10^{-7}$–$4x10^{-7}$ m/s at high and shallow depths, respectively.

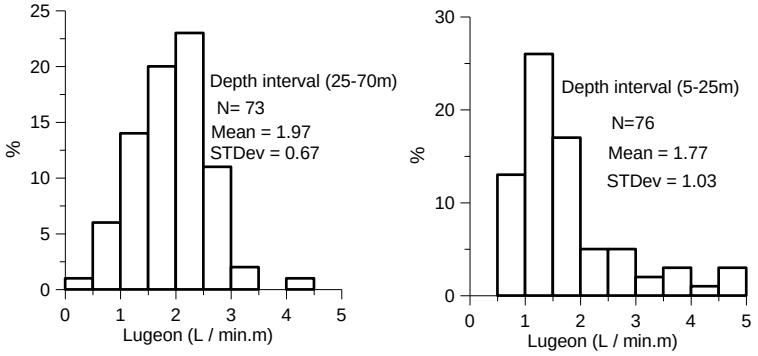

Figure 3.21: Frequency distribution of Lugeon values for a test conducted at the valley

It is worthwhile to remark that the marly-arenaceous formation may exhibit higher hydraulic transmissivity in the direction of strata, with seepage paths limited to discontinuities planes and involving almost exclusively the more fractured sandstone strata, while the clay-rich layers represent low-permeability barriers.

Permeability estimates using Q and Vp

Using the Q_c values estimated before, it is also possible to relate it qualitatively with the expected rock mass permeability. Thus, if we consider the Q_c value between 1 to 10 for the base rock marly arenaceous formation and Q_c between 0.01-0.1 for the moving rock mass. Therefore, the Lugeon value for the base rock could be in between 0.1-1 Lugeon while the moving rock mass coud have a relatively higher Lugeon value between 10-100.

Moreover, for the base rock the estimated Lugeon values by the Q_c method can also be contrasted with the already measured Lugeon test results which cover a range of 1-2 Lugeon.

In addition, it is also possible to relate the magnitude of P-wave velocity, V_p with the Lugeon values. Therefore, considering the magnitude of velocities between 3.2-4 km/s which were obtained from cross-hole test at the dam foundation, the Lugeon values could be between 0.3-2 Lugeon which is not a bad approximation as compared to the measured Lugeon values (i.e. 1-2 Lugeon).

While for the disturbed marly-arenaceous formation with lower P-wave velocity in between 0.5-1km/s, permeability in the range of $1x10^{-6}$-$1x10^{-5}$ m/s can be approximated by relating the Lugeon value with the P-wave velocity and rock mass quality based on Barton (2002) suggestions. This estimated higher permeability value could be expected in the disturbed, fractured marly-arenaceous formation.

These approaches can only help us to understand partially the permeability of the sliding mass. Moreover, it might be reasonable to hypothesize the permeability of the sliding mass could be a bit higher than the permeability of the bed rock in the dam foundation area by taking in to account the slope morphology and the already undergoing slope deformation.

Some reasonable permeability values between $1\text{-}3x10^{-5}$ m/s which are not far from these estimates will be employed for the moving mass in the flow analyses section of this research (Chapter 5). While a relatively lower value in the order of $1x10^{-6}$ m/s will be assigned for the bed rock

and slip surface permeability. Further refinement of the above estimates will be discussed latter based on reasonable simulation of the observed piezometer levels by numerical models (Chapter 5).

3.4 Rainfall and piezometer analysis

In this section, possible correlations between piezometer levels and cumulative rainfall have been discussed in detail. Some attempts have been made to correlate the peak displacement velocities with both the excess cumulative rainfall and piezometer level increase.

3.4.1 Rainfall analysis

The rainfall data obtained from nearby two pluviometer stations (i.e. Casa Nuova and Casa Castalda, which are around 3km apart) have been considered. The recorded rainfall data found at Casa Nuova station are on monthly scale for the 1991-2013 period; and daily rainfall data are also available for 2009-2013 period.

At Casa Castalda station, daily rainfall data are available for 2000-2013 period. The rainfall regime of the study area can be understood well by utilizing data from the two stations. Figure 3.22 shows the daily and average rainfall at Casa Nuova station.

The rainfall regime in the study area has minimum precipitation mostly in between June – August. While peak precipitation values occur in two periods i.e. between September-February, with higher peak value, as compared to March- May periods as shown in Figure 3.23. The mean annual rainfall of 931mm has been calculated for the period 1991-2013 (Figure 3.24) . Minimum precipitation of 534mm was recorded in 2011.

Cumulative rainfall has been evaluated with Equation (3.21). The parameter N (no of days or months) was investigated carefully so that reliable correlation can be found with piezometer levels. In Equation (3.21), $P_{i,N}^{cumu}$ stands for the cumulative rainfall for N days or months while p_j is the recorded daily or monthly rainfall. Figure 3.25 shows the cumulative rainfall evaluated using monthly rainfall data.

$$P_{i,N}^{cumu} = \sum_{j=i-N}^{i} p_j \tag{3.21}$$

Moreover, the excess rainfall has been evaluated by deducting the measured rainfall value from the seasonal average rainfall. The excess

rainfall with respect to the seasonal average value can be easily observed from the shaded area in Figure 3.26

Comparisons of annual and monthly rainfall data from the two pluviometers have been provided in Figure 3.27, Figure 3.28 respectively. Figure 3.29 shows the double mass curve analyses result and it demonstrates that a good correlation (R^2=0.994) has been obtained. Moreover, Figure 3.30 depicts the 90 days cumulative rainfall and excess cumulative rainfall evaluated from the two stations are consistent.

Exhaustive correlation analyses with piezometer level have been discussed in next section by referring rainfall data (daily and monthly) from both pluviometer stations.

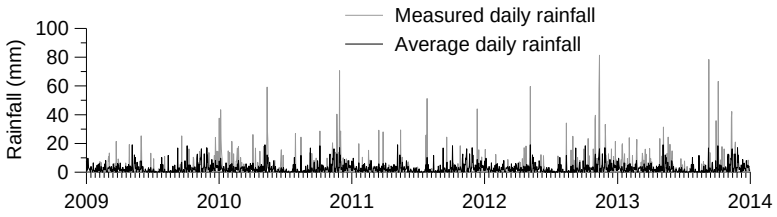

Figure 3.22: Observed and average daily rainfall for 2009-2013 period at Casa Nuova station

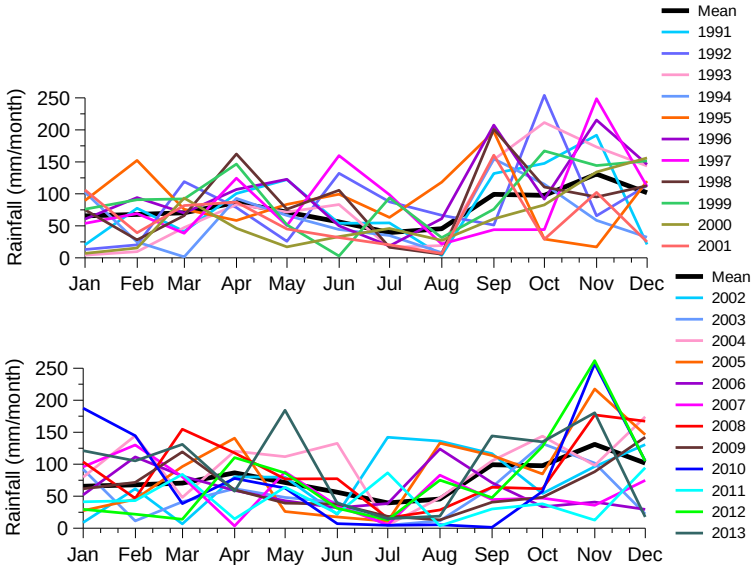

Figure 3.23: Monthly rainfall and mean value computed in the period 1991-2013 from Casa Nuova station

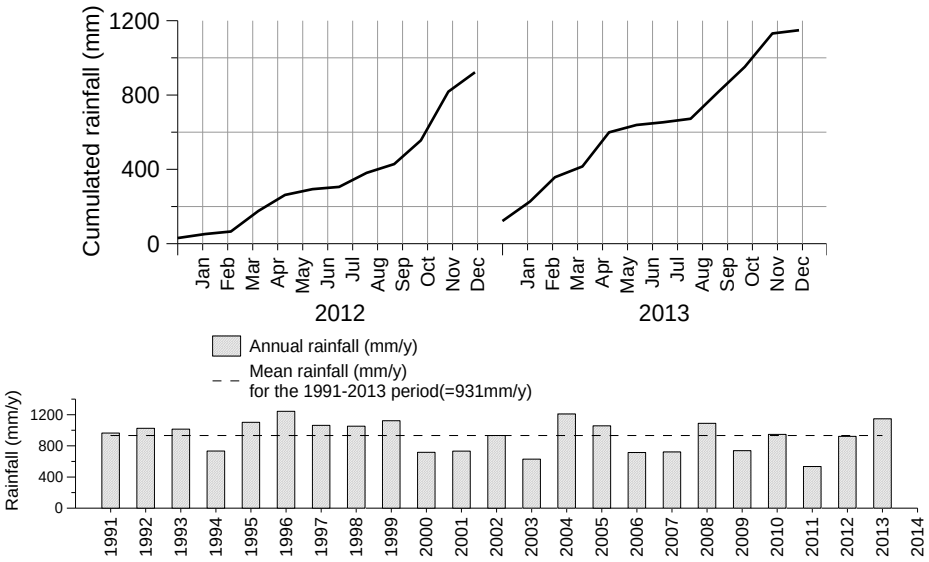

Figure 3.24: Yearly cumulative rainfall for 2012 and 2013 (upper figure), Annual and average annual rainfall value evaluated for the period 1991-2013 (lower figure)

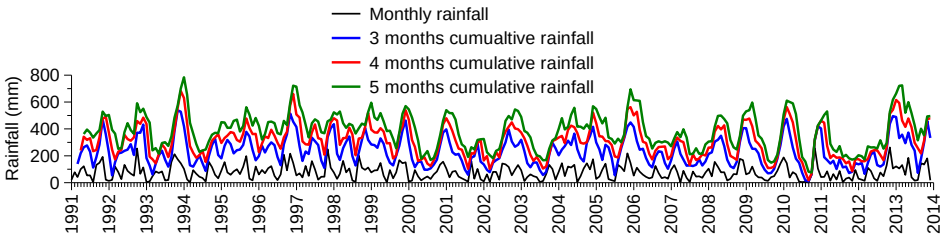

Figure 3.25: Cumulative rainfall evaluated from Casa Nuova station

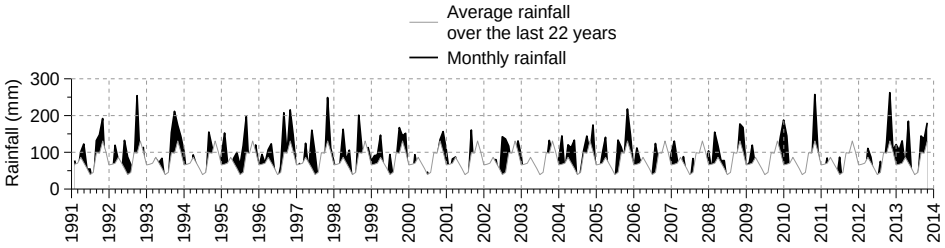

Figure 3.26: Monthly rainfall and excess rainfall (shaded area) from the average monthly value calculated for the period 1991-2013 at Casa Nuova station

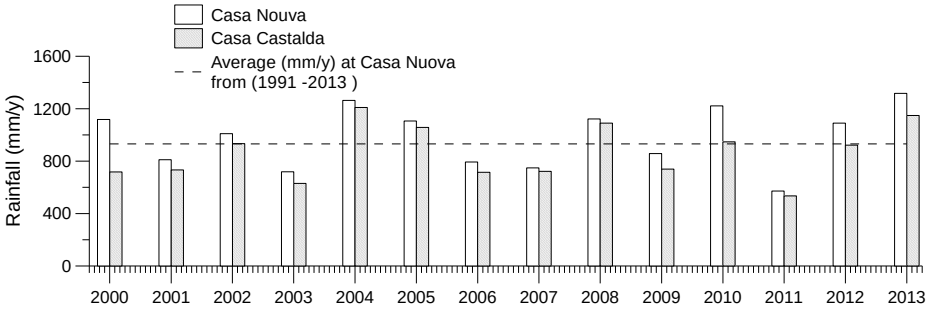

Figure 3.27: Annual rainfall at the nearby pluviometers (Casa-Castalda and Casa Nuova)

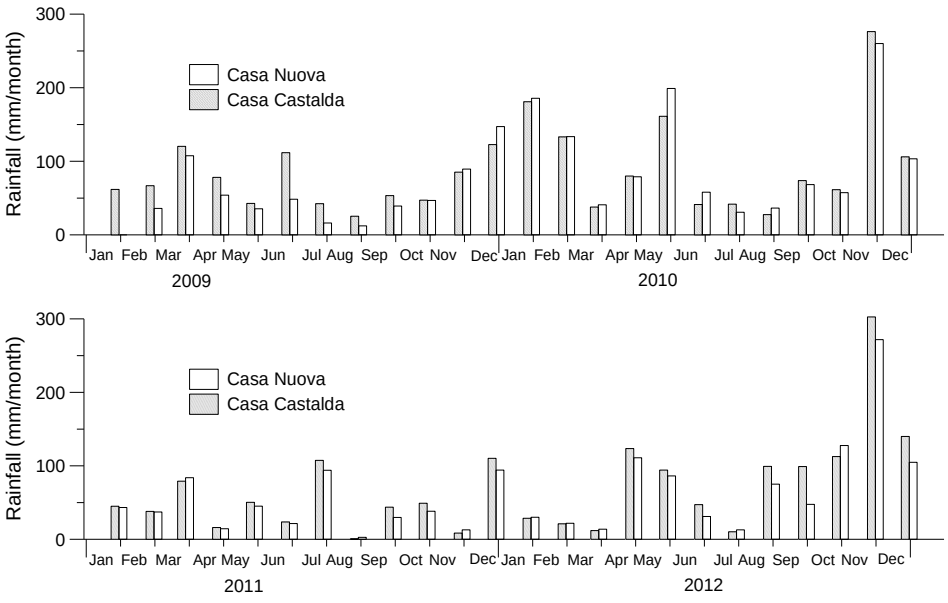

Figure 3.28: Comparison of average monthly rainfall data recorded at Casa Nuova and Casa Castalda

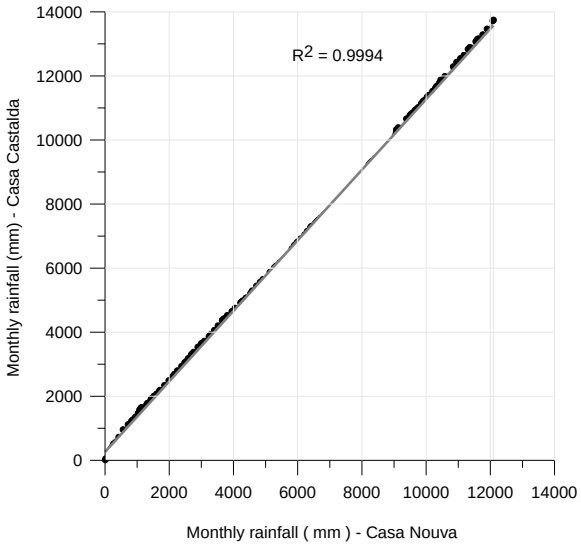

Figure 3.29: Double mass curve analysis of monthly rainfall from Casa Nuova and Casa Castalda from 2000 – 2013

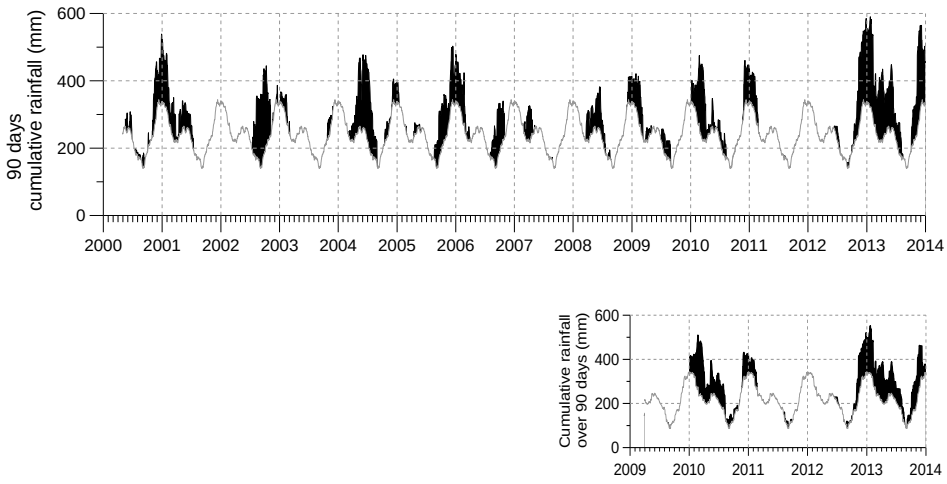

Figure 3.30: Cumulative rainfall (90 days) evaluated from Casa Castalda (upper figure) and from Casa Nuova (lower figure). The shaded area represent the cumulative rainfall exceeding the seasonal average cumulative rainfall

3.4.2 Pore pressure regime

Pore pressure in the slope has been monitored by four deep boreholes (A, B, C, D) each accompanied with two piezometric cells installed below

and above the presumed slip surface since 1994 (Figure 3.31). The piezometer cells located in the upper most part (cell C1, D2) recorded few pore pressures values (Figure 3.31). Cells B1 and D1 were not able to record any data since they were damaged immediately after being installed. The observed fluctuations in piezometric readings within the same borehole are attributed to the complex infiltration process. This can be further verified from the Marly-arenaceous geological formation where flow occurs through less permeable clay interbeds and crossing joints thereby induce hydraulic discontinuity between cells. The peak readings in upper and lower piezometric cells occur at similar instants for most of the observed data as shown in (Figure 3.31). The significant difference in readings between cells does not stem from hydrostatic condition rather by a complex flow process.

Reservoir level, which never exceeded El.282m a.s.l during the monitoring period, have limited influence on hydraulic condition at the toe of the slope. Thus, groundwater profile inside the slope is governed mainly by rainfall infiltration and seepage processes. Moreover, the groundwater profile shows a downward gradient towards the toe and a local depression has been observed near the transition zone, which is as a result of drainage process fostered by lateral steep morphology and loosening of the rock mass (Figure 3.32). This issue has been discussed in detail in fluid flow analyses part of the research (Chapter 5).

A constant average piezometer level, which is computed over the full time series, has been evaluated. The increase in piezometer level above this constant average level has been calculated and correlated with cumulative excess rainfall and displacement velocities.

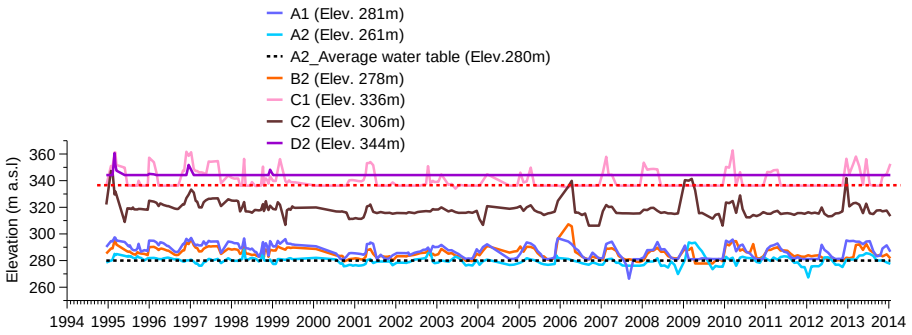

Figure 3.31: Observed piezometric levels.

The transient groundwater regime inside the slope cannot be discussed herein at all from the piezometric measurements since they are recorded with low frequency.

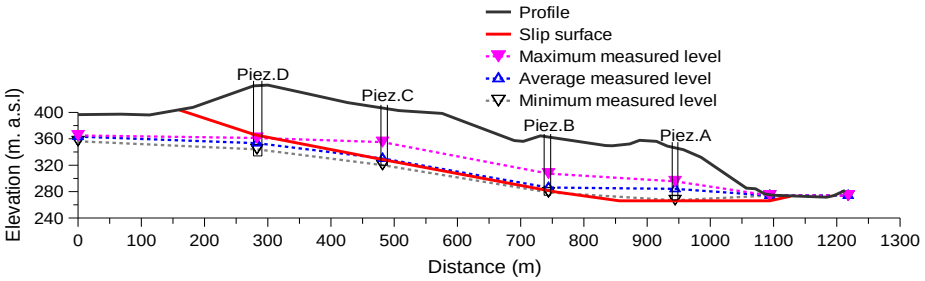

Figure 3.32: Groundwater profiles plotted from piezometer readings

3.4.3 Correlation with cumulative rainfall

In order to understand the possible correlations between rainfall and piezometer levels, various attempts have been made taking to account cumulative rainfall over various time periods. After comparing various correlation analyses between cumulative rainfall (i.e. 30 days, 60 days, 90 days and 150 days) with observed piezometer levels, 90 days cumulative rainfall gives reasonable correlations (Figure 3.33 and Figure 3.34). The time lag (i.e. around 90 days) between the heavy rainfall and the peak piezometer level could come from both surface and subsurface flow process.

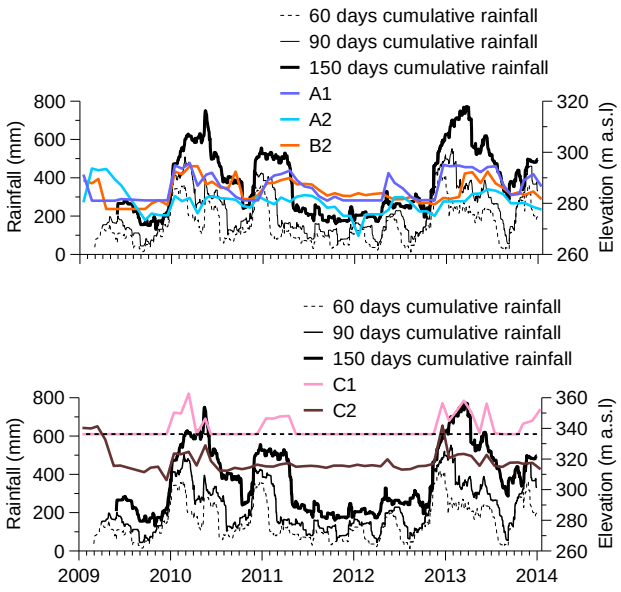

Figure 3.33: Correlation between cumulative rainfall and piezometer level

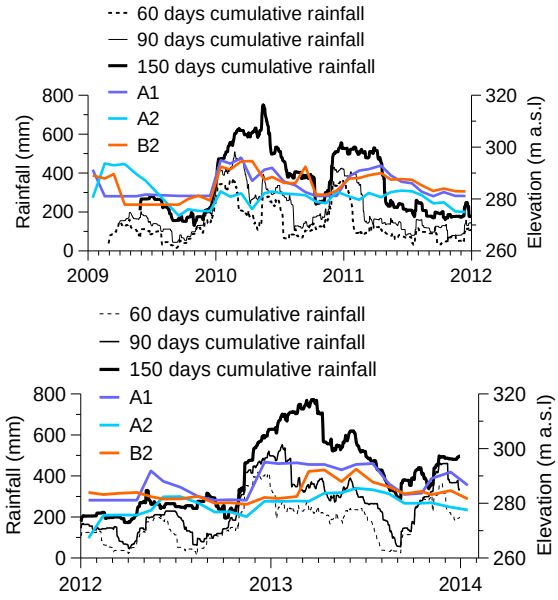

Figure 3.34: Detailed plots, which shows correlation with cumulative rainfall

Comparison of correlation analysis with daily and monthly rainfall data

Correlations carried out between piezometeric levels and cumulative rainfall, evaluated based on daily rainfall data show better match with the the peak piezometeric levels (Figure 3.35 and Figure 3.36). Thus, results obtained based on daily rainfall data are more detail and reasonable.

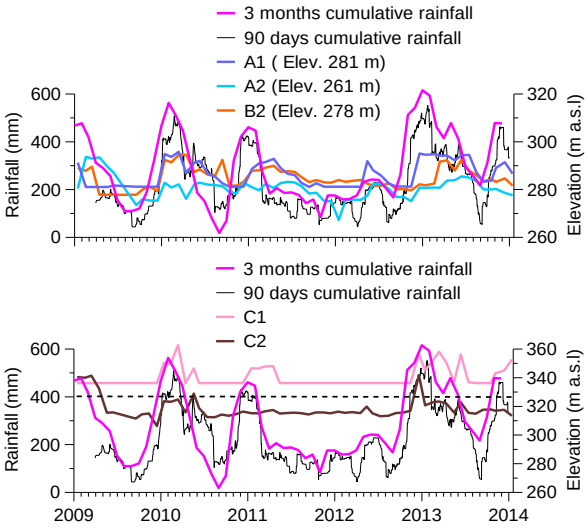

Figure 3.35: Comparison of correlation between piezometer levels with cumulative rainfall at Casa Nuova station

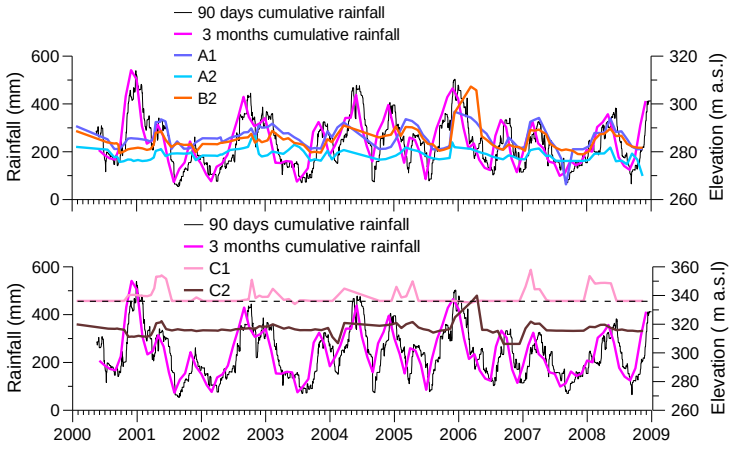

Figure 3.36: Comparison of correlations between piezometer levels and cumulative rainfall at Casa Castalda station

3.4.4 Correlation between increase in piezometer levels with excess rainfall

Figure 3.37 shows some reasonable correlations between the three months cumulative rainfall exceeding the average rainfall with the peak increase in piezometer levels (Figure 3.37). In addition, the groundwater fluctuation which accounts on average ±10 m head match with the excess rainfall in most cases throughout the last 25 years monitoring period. Figure 3.38 shows a similar behavior evaluated at Casa Castalda station.

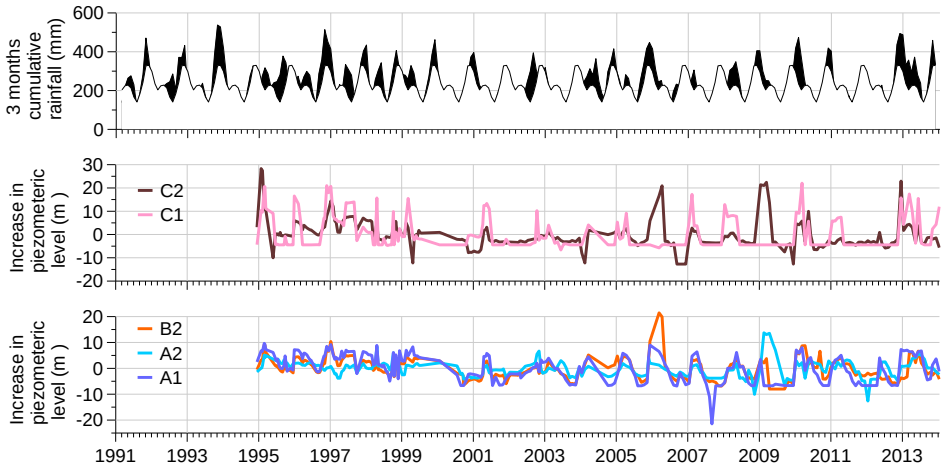

Figure 3.37: Correlation between excess rainfall with increase in piezometer levels during 1991-2014 (rainfall data from Casa Nuova station)

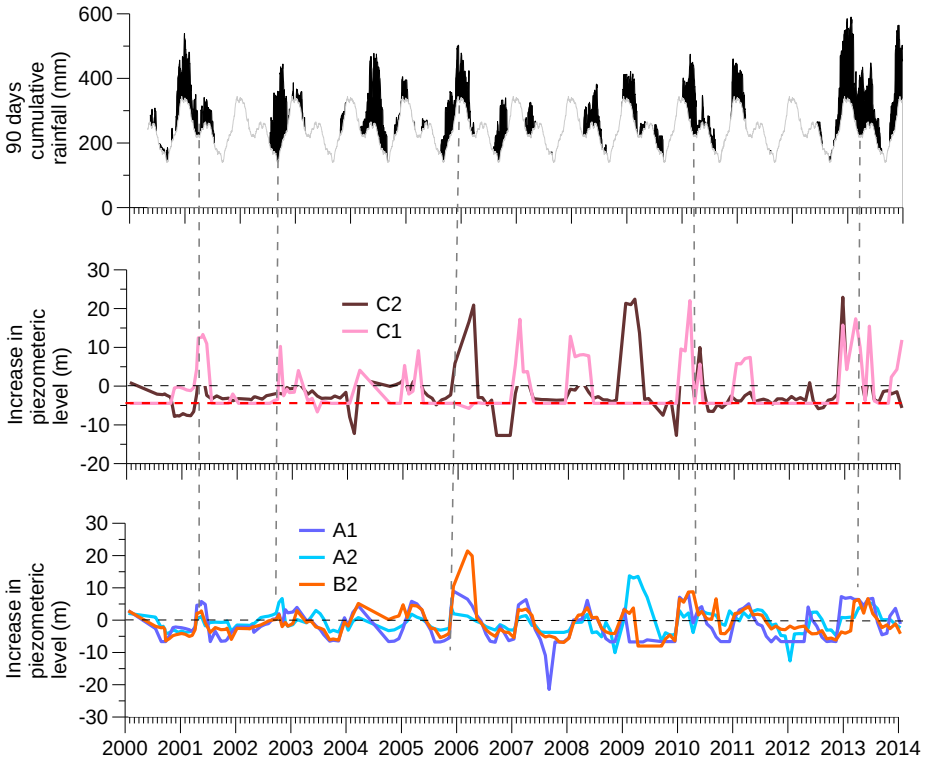

Figure 3.38: Correlation between excess rainfall with the increase in piezometer levels during 2000-2014 (rainfall data from Casa Castalda station)

3.4.5 Correlation with displacement velocity

Target displacement velocity: The average velocity of the target points have been evaluated from the displacement records. The peak velocities show some correlations with the three months cumulative rainfall (Figure 3.39). Besides this, the excess cumulative rainfall and increase in piezometer levels are correlated with peak velocities in some periods (Figure 3.40). However, the higher excess rainfall amount and piezometer level increase do not always necessarily produce higher peak velocities for some years (e.g. 2013-2014).

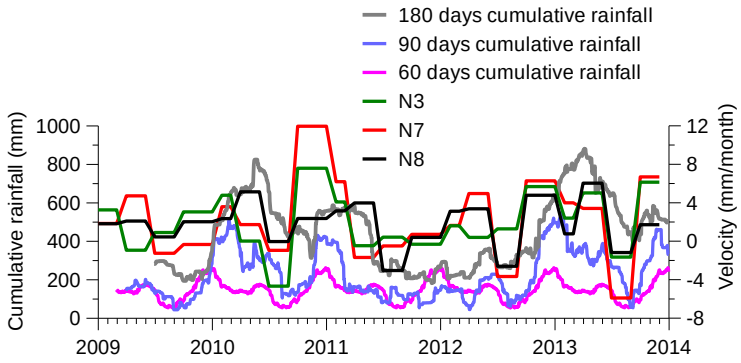

Figure 3.39: Correlation between cumulative rainfall and displacement velocities

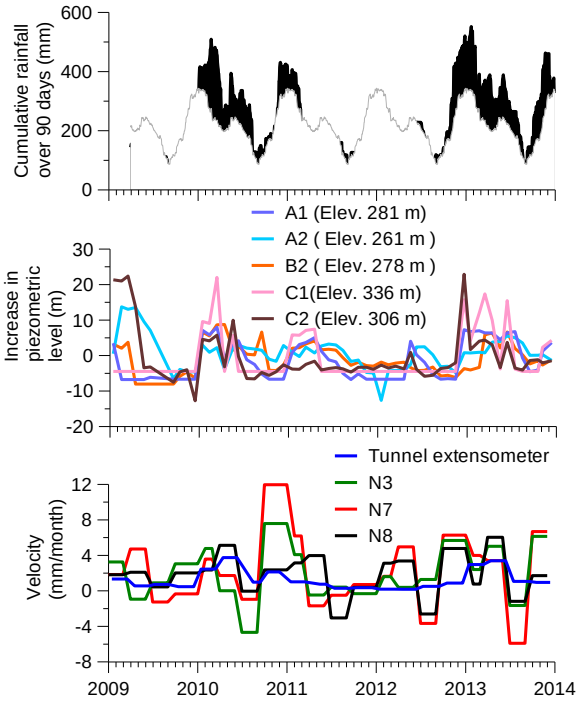

Figure 3.40: Correlation between excess rainfall and increase in piezometer levels with velocities

Tunnel extensometer: Figure 3.41 shows that three months cumulative rainfall and especially the excess three cumulative rainfall has been correlated sufficiently with the peak velocities, evaluated for the period 2002-2014. Besides this, the increase in piezometer head has been sufficiently correlated with the tunnel peak velocities (Figure 3.42).

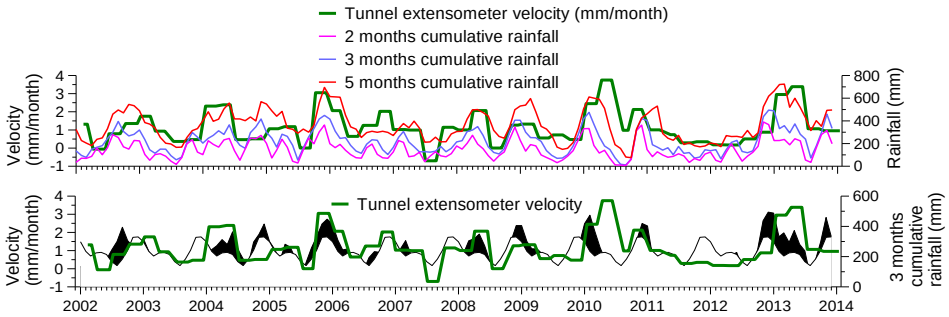

Figure 3.41: Correlation between velocity of tunnel extensometer and cumulative rainfall (upper figure) and excess rainfall, represented by shaded area (lower figure)

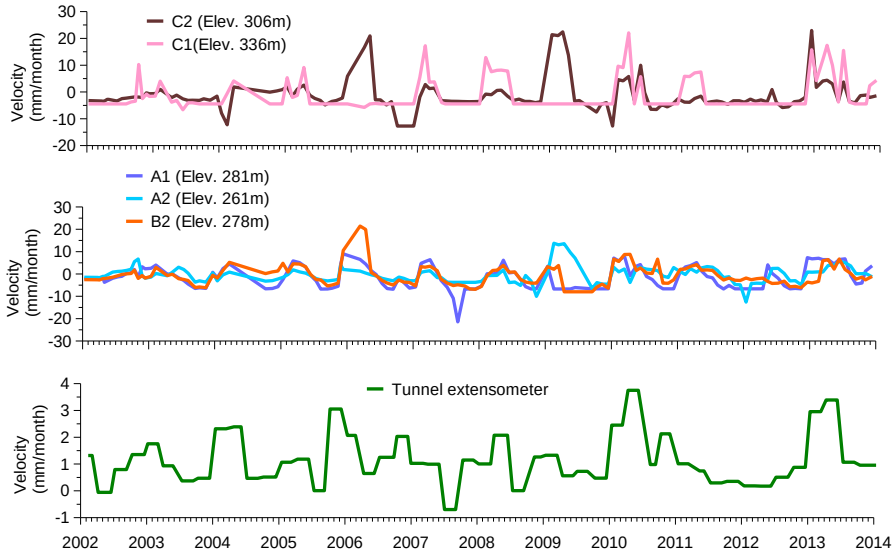

Figure 3.42: Correlation between increase in piezometer levels and velocity of tunnel extensometer

3.5 Slip boundary and kinematic of the movement

On the base of field investigations (e.g. borehole loggings, inclinometers, and geodetic targets) the slip boundary can be defined approximately, especially in the toe part. Some reasonable hypotheses developed on the base of location of the damaged tunnel section and slope morphology will be discussed with the help of DEM modeling (Chapter 4). The lateral boundaries of the ongoing movement can be traced confidently in the east part, while in the west part, it is diffused over large part of the valley.

3.5.1 General hypotheses and kinematic characters of the movement

Borehole investigations and survey of the N sector of the ridge have shown that a basal slip plane can be reasonably assumed at the top of the buried alluvium layer. Inclinometer profiles and target displacement vectors can give further support to this assumption.

Although the density of measurement points decreases in the S sector, at greater distance from the river bed, magnitude and direction of horizontal displacements measured at different points are generally consistent. The overall direction of displacement is approximately parallel to the longitudinal direction of the ridge, with some eastward rotation at the toe of the slope. The basic hypothesis of a planar sliding with some internal shearing of the moving body seems therefore reasonable.

The position of the damaged tunnel section represents a further restraint to trace a likely longitudinal profile of the slip surface (Figure 3.43). Finally, the upper limit (S boundary) of the movement can be located mainly on the base of the morphology of the ridge, i.e., by observing the presence of a plateau with some deformation traces at elevation 400 m a.s.l. The distance from this plateau to the river bed, measured along the longitudinal axis of the ridge, is approximately 1000 m.

The slip surface can be reasonably drawn as a near horizontal plane in the toe part. The slip surface is certainly more inclined in the upper part but the effective geometry cannot the defined in detail. This aspect will be further investigated by comparing different DEM models in order to identify the most likely slip surface profile.

The lateral boundary of the movement can be traced easily on the E side, on the base of displacement measurements, while on the W side the separation line between stable and unstable zone fades away (Figure 3.44). The slide boundary is close to the top of the dam but the movement does not affect the abutment zone, as demonstrated by the null displacement of targets N12 and N19.

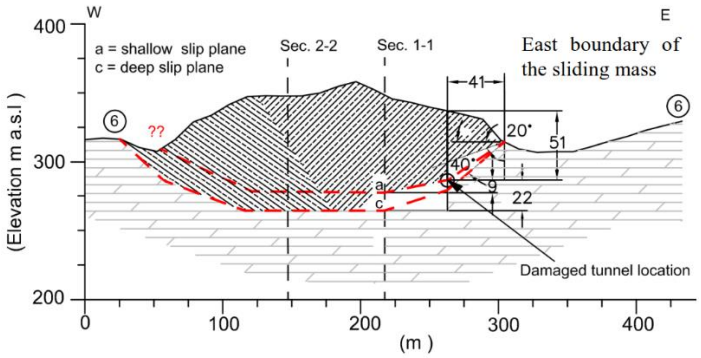

Figure 3.43: Slip surface reconstructed at section x-x considering the position of damaged tunnel section and typical dip angles (20-40º) of layers at the East side of the ridge, as evidenced from field investigations (all dimensions are in m)

The current kinematics of the movement can be outlined as a compound mechanism in which a blocky system is sliding on a low inclination basal plane. The depression along the upper profile of the ridge, between the targets N7 and N8, may represent a morphological evidence of past inter-block deformation.

Figure 3.45 depicts the shape of the slip surface constructed by taking in to account the inclinometer profiles. It is apparent that most of the inclinometers display a flat basal shearing surface around at the same elevation of 267m a.s.l. The slip surface near the toe part can also be further assessed from the lateral section plots (Figure 3.46).

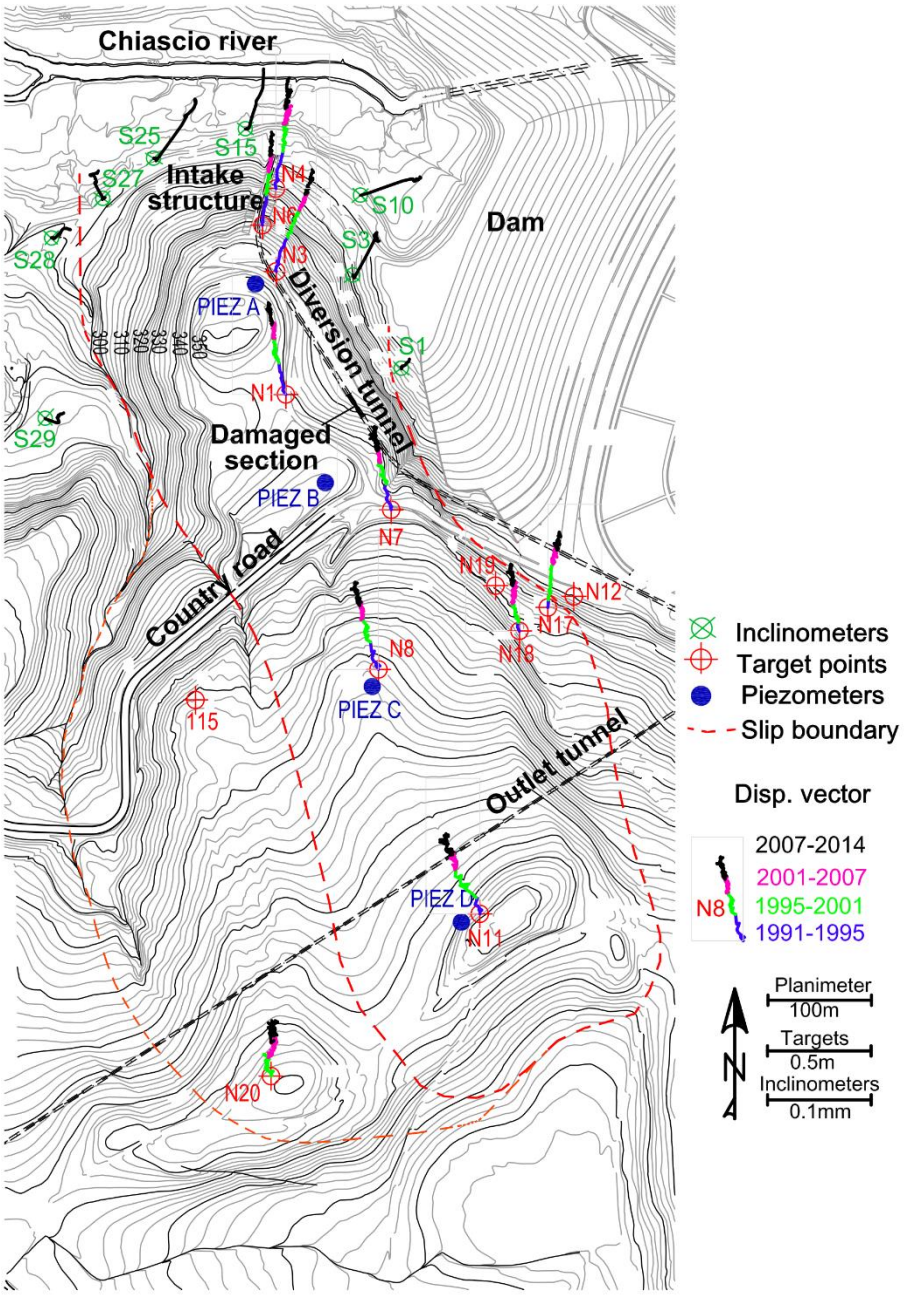

Figure 3.44: Displacement vectors plots and movement boundary

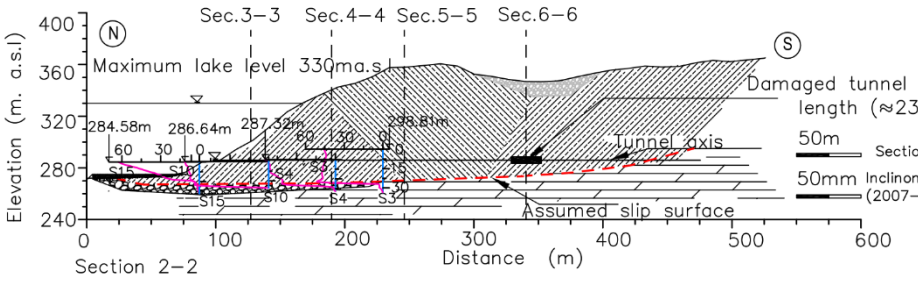

Figure 3.45: Shape of the slip surface traced at the toe part on the base of inclinometer profiles

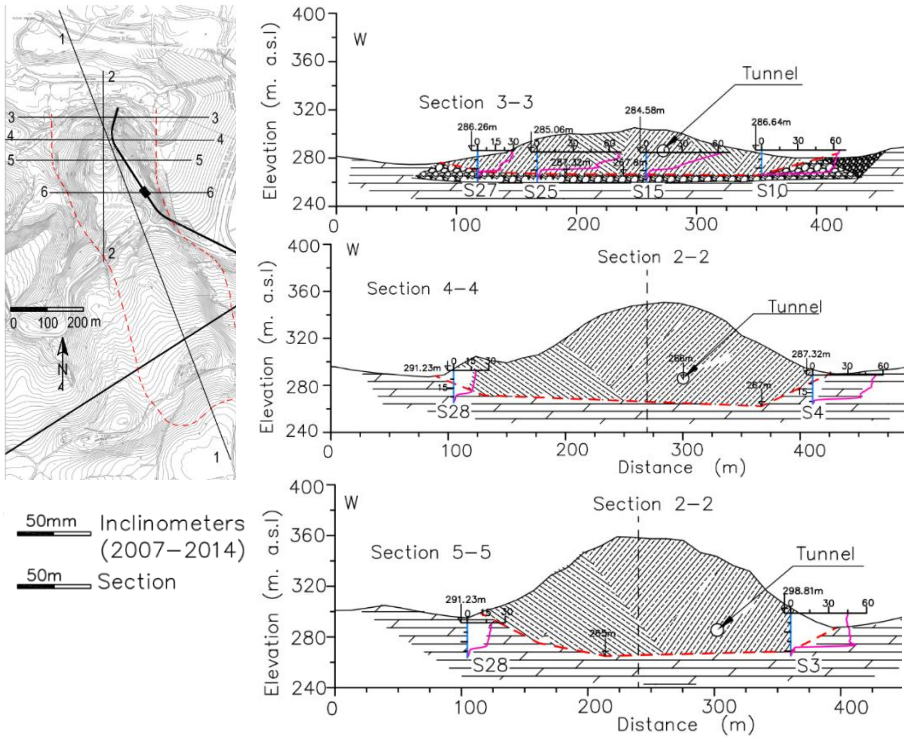

Figure 3.46: Lateral cross-sections with inclinometer profiles which assist for reconstruction of the slip surface

3.6 Conclusions

The rock mass characterization of the complex rock slope has been attempted by employing previous suggested methods (i.e. Q- value

method, GSI, and others). Site investigations, which include borehole loggings, geophysical surveys, have been considered in the rock mass characterization course. Thus, the deformation modulus of the rock mass has been estimated from the geophysical studies, GSI and Q-value method.

The friction angle of the basal sliding surface (peak, c_p =21.5 kPa and φ_p = 15° and residual, φ_r = 7.7°) has been obtained from the shear box test conducted on the clay gouge recovered from the damaged section of the tunnel.

With the aim of understanding the possible correlations between the piezometer levels with the cumulative rainfall, several analyses have been performed. Then, the 3 months or 90 days cumulative rainfall is reasonably correlated with the piezometer levels.

Further relevant information can be obtained by correlating the fluctuation of groundwater level, which accounts between ±10 from the average water table, with the cumulative rainfall exceeding the average rainfall values. The analyses results show that the rise in piezometer levels are usually correlated with the three months or 90 days cumulative excess rainfall.

Some good correlations between displacement velocities with piezometer levels increase and cumulative rainfall exceeding the average values have been reported too.

The kinematics of the movement can be characterized by mainly translational one, along a low inclination basal slip surface with limited block shearing as confirmed by some morphological depressions. The displacement vectors consistently display that the ridge movement is directed towards the valley with some rotation to east in the toe part.

Moreover, most of the deformed inclinometer profiles mainly located in the toe part demonstrate clearly a flat slip surface.

Chapter 4

4 Numerical modeling using DEM

4.1 Introduction

This chapter discusses the DEM modeling of the complex blocky structure. In the first part, a review of the basic conceptual formulations of the UDEC code has been discussed. Particular attention has been given to mechanical behavior of a discontinuous system: (a) behavior of discontinuities or joints; and (b) behavior of the solid (intact) material. Some numerical exercises have been presented to clarify some of these aspects.

The complex blocky structure of the slope has been modelled by incorporating reasonable joint sets (bedding and sub-vertical joint sets). The influence of slope structure (i.e. block size, joint pattern, joint stiffness, joint friction angle, shape of slip surface) on slope deformation and mobilized friction angle of the slip surface has been investigated. Finally, the effect of water table increase and filling of the dam on the limit friction angle has been assessed too.

4.1.1 UDEC code

The Universal Distinct Element Code (UDEC) is a two dimensional program used for discontinuum modeling based on the concept of distinct element method. A discrete element method allows finite displacements and rotations of discrete bodies, including complete detachment and recognizes new contacts automatically as the calculation progresses. UDEC is best suited to explore the behavior of jointed rock mass or blocky structure under static or dynamic loading. The individual blocks can be rigid or deformable; contacts are deformable (Itasca, 2011).

The calculations performed in the distinct element method alternate between application of a force-displacement law at all contacts and Newton's second law at all blocks (Figure 4.1). Figure 4.2 shows the numerical calculation cycle employed in the DEM formulation. Thus the dynamic equation of equilibrium for each blocks is formulated and repeatedly solved taking in to account the boundary condition and contact laws.

A rock joint is represented numerically as a contact surface (composed of individual point contacts) formed between two block edges. In UDEC

adjacent blocks can touch along a common edge segment, or at discrete points where a corner meets an edge or another corner. In the case of ridge blocks, a contact is created at each corner interacting with a corner or an edge of an opposing block (Figure 4.3a). For deformable block, contacts are created at all gridpoints located on the block edge in contact (Figure 4.3b). Therefore, the number of contact points is directly related to the internal zoning of the adjacent blocks.

Corner rounding is included for each block by specifying a circular arc for each block corner. Corner rounding applies only to the contact mechanics calculation in UDEC. Moreover, corner rounding can introduce inaccuracy to the solution if too large rounding parameter is considered. It is recommended to keep the rounding length approximately 1% of the representative block edge length in the model in order to obtain good accuracy to the solution.

Domains are void spaces formed between blocks, which are defined by the contact points (see D1 and D2 in Figure 4.3b). Contact updating is triggered by a significant relative motion within a domain. For instance, if the relative shear displacement at a contact exceeds two times the rounding length, a new contact is formed. For block motions involving large shear displacement, contact updating must ensure that contact forces are preserved when contacts are added or deleted such that a smooth transition will exist between neighboring states.

Moreover, UDEC operates in large-strain mode by default, thus block coordinates and gridpoint coordinates are updated at each step, according to computed displacements. UDEC can also be run in small-strain mode, in which case coordinates are not changed, even if computed displacements are large.

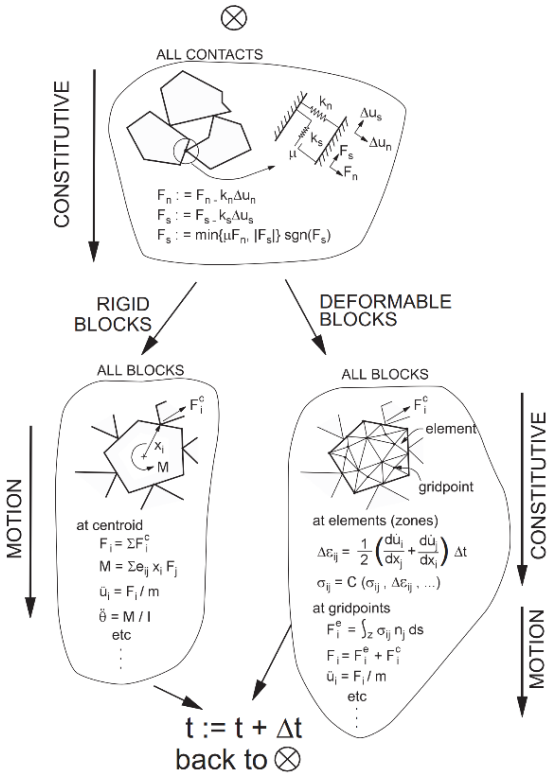

Figure 4.1: Calculation cycle for the distinct element method (after Itasca, 2011)

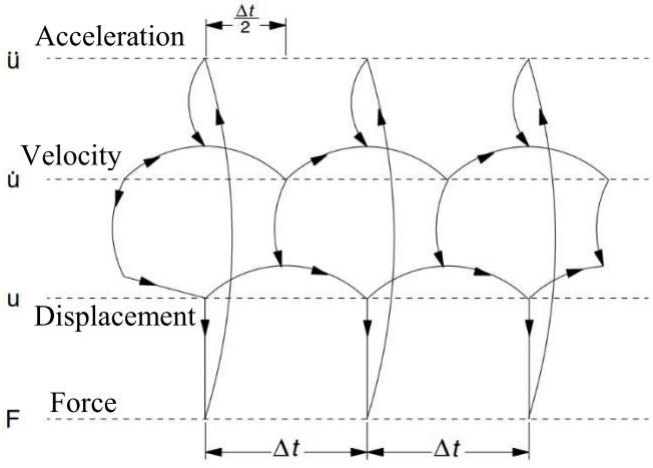

Figure 4.2: Solution stages used in the Explicit method (after Itasca, 2011)

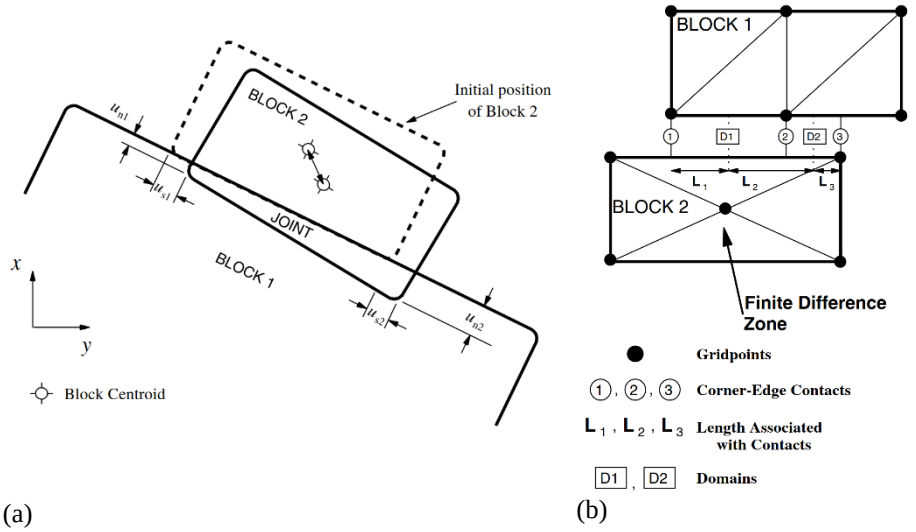

(a) (b)

Figure 4.3: Contact representation between rigid blocks (a); contact and domains between two deformable blocks (b) (after Itasca, 2011)

Block deformability

The deformable blocks are subdivided in to mesh of finite difference triangular elements, a constant strain zones (Figure 4.4). In the case of a deformable block, motion is evaluated at the gridpoints of the triangular finite-strain elements within the blocks. Then the zone strain rates are computed from the nodal point velocities. The applied constitutive models give new stresses within the zones. Mohr-Coulomb failure criterion with a non-associated flow rule is usually adopted for zones. Other non-linear plasticity models can also be employed to zones: Drucker-Prager failure criterion, the ubiquitous joint model and strain-softening models for both shear and volumetric yield.

Even though UDEC is primarily intended to simulate mechanisms related to movement along discrete features (such as joints and faults) within a rock mass, however in many cases the failure and collapse of the intact rock material (e.g. roof collapse or sloughing of sidewalls of excavations) should be considered in the model.

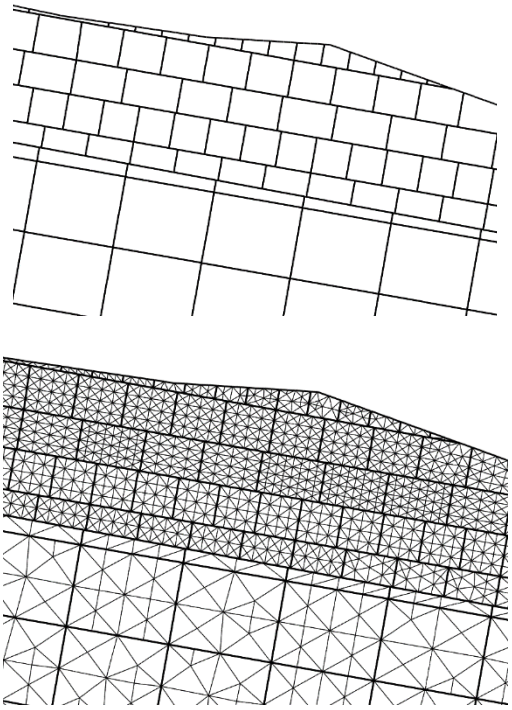

Figure 4.4: Zones in a blocky structure model which contains persistent and staggered joint sets

Mechanical damping

The mechanical damping in the DEM modeling is devised into the equations of motion to evaluate static and dynamic solutions. The damping force is proportional to the unbalanced force at a node and its direction is aligned so that energy is always dissipated. The equations of motion for deformable blocks are rewritten by including local damping (Equation (4.1), (4.2)).

$$\dot{u}_i^{(t+\Delta t/2)} = \dot{u}_i^{(t-\Delta t/2)} + \left\{ \sum F_i^{(t)} - F_{di}^{(t)} \right\} \frac{\Delta t}{m_n} \tag{4.1}$$

where $\sum F_i^{(t)}$ is the net nodal force, m_n is the total nodal mass, and $F_{di}^{(t)}$ is the applied damping force which is given by:

$$F_{di}^{(t)} = \alpha \left| \sum F_i^{(t)} \right| \mathrm{sgn}\left(\dot{u}_i^{(t-\Delta t/2)} \right) \tag{4.2}$$

where α is the damping value. For static analyses, the local damping (i.e. damping value of α = 0.8) is the default option.

The timestep in a deformable blocky system depends on the zone size, the stiffness of the overall system which include contributions from both the intact rock modulus and stiffness at the contacts.

Moreover, the convergence to a solution becomes slower if there is contrast in stiffness in block materials or joint materials or block versus joint materials or if there are large contrast in block or zone sizes. For instance for mechanical only calculations, joint normal and shear stiffness should be governed by Equation (4.3) to avoid long computation time.

$$k_n \text{ and } k_s \leq 10\left[\max\left(\frac{K+4/3G}{\Delta z_{\min}}\right)\right] \tag{4.3}$$

where K and G are bulk and shear moduli, respectively, of the block material, and Δz_{min} is the smallest width of the zone adjoining the joint in the normal direction.

Modeling joint behavior

The joint models adopted in UDEC are capable of describing the behavior of physical joints in normal and shear responses. Joint shearing, closing or opening during mechanical deformation can be modelled.

In the normal direction, the stress-displacement relation is assumed to be linear and governed by the stiffness k_n such that

$$\Delta\sigma_n = -k_n \Delta u_n \tag{4.4}$$

where $\Delta\sigma_n$ is the effective normal stress increment, Δu_n is the normal displacement increment. In a similar fashion, the shear response is controlled by a constant shear stiffness, k_s. The shear stress, τ_s, is limited by the Mohr-Coulomb yield line.

Thus, if $\tau_s \leq c + \sigma_n \tan\varphi$

Then $\Delta\tau_s = -k_s * \Delta u_s^e$ (4.5)

where Δu_s^e is the elastic component of the incremental shear displacement, c is the cohesion and φ is the friction angle.

The amount of joint dilation observed during shearing depends on a constant joint dilation angle in Mohr-Coulomb model. Moreover, the magnitude of dilation is limited by the high normal stress or total shear displacement experienced by the joint, that is when there is sufficient shearing of asperities, dilation will be no more manifested by the joints.

A more comprehensive displacement-weakening model is also available in UDEC. The continuously yielding (CY) joint model is able to reproduce the progressive damage of joint asperities under shear. The Barton-Bandis joint model (Barton et al., 1985) is also available as an option to UDEC.

4.2 Numerical tests

Direct shear test

In this numerical test, comparisons between the Mohr-Coulomb slip and CY joint models have been carried out considering a simple direct shear test (Figure 4.5). The model is formed by two deformable blocks separated by a single joint. Keeping a given normal force, a horizontal velocity is applied to the upper block to introduce a shearing load. The average joint shear stress and shear displacements have been evaluated with the help of user defined internal programming language (FISH). The adopted parameters listed in Table 4.1 may not have any physical meaning since the aim of these exercises is only to explore the behavior of the joint models by employing simple shear test.

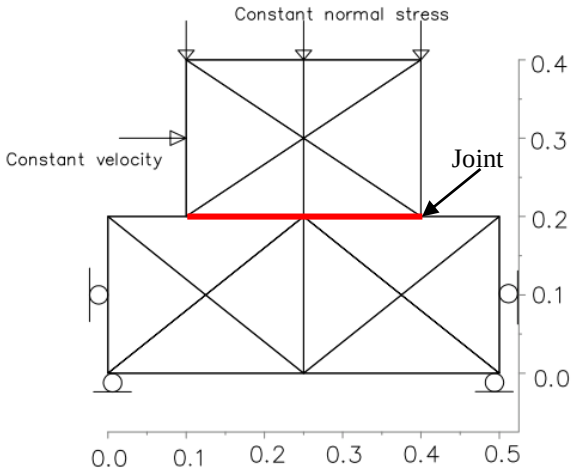

Figure 4.5: Model used for direct shear test (Dimensions are in m)

Table 4.1: Model parameters considered for the study of CY joint model

Parameters	Values
Elastic modulus of shearing block , *E*	10GPa
Poisson's Ratio, *v*	0.20
Joint normal stiffness, k_n	100GPa/m
Joint shear stiffness, k_s	100GPa/m
joint shear stiffness exponent, e_s	0.0
joint normal stiffness exponent, e_n	0.0
Joint intrinsic friction angle, φ	8^o
Joint initial friction angle, φ_m	16^o
Joint roughness parameter, R*	0.1mm

*The value of R is latter changed to assess its influence on CY joint model

The CY joint model shows a peak strength and then enters to a softening regime (Figure 4.6). This behavior cannot be reproduced by the Coulomb slip model (Figure 4.7). The CY model is able to describe the gradual decrease of joint dilation during shearing (Figure 4.7 and Figure 4.8).

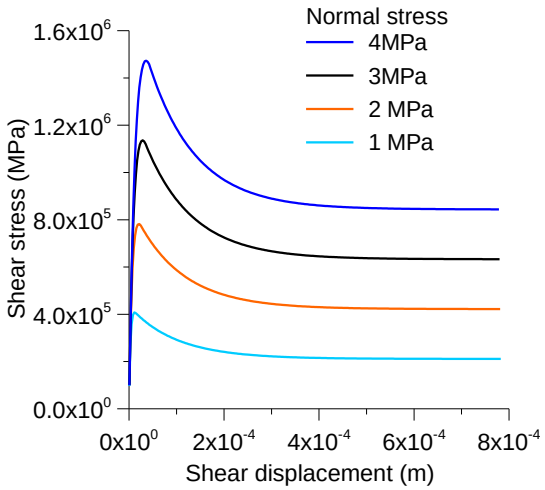

Figure 4.6: Shear stress vs shear displacement curves when CY model is considered for the rock joint

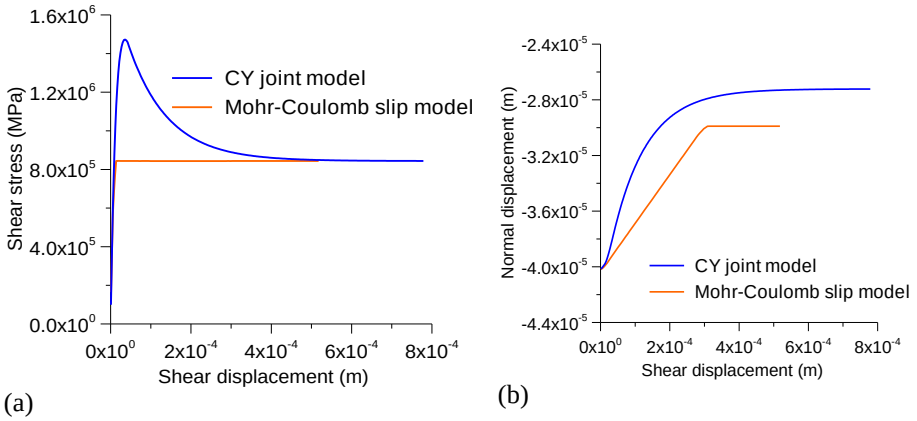

Figure 4.7: Comparison between CY joint model and Coulomb slip model on joint shear stress vs shear displacement response (a) and joint dilation responses (b). Note that the normal force is 4MPa

Besides this, the effect of the joint surface roughness parameter, *R*, on the behavior of CY joint model can be appreciated from Figure 4.8. The peak stress and the post-peak response of the joint differs clearly by this parameter (Figure 4.8). Higher value of R increases the peak stress and causes slower decay of φ_m. Moreover, the dilation effect continues for a higher shear displacement if the value of R is high (Figure 4.8b).

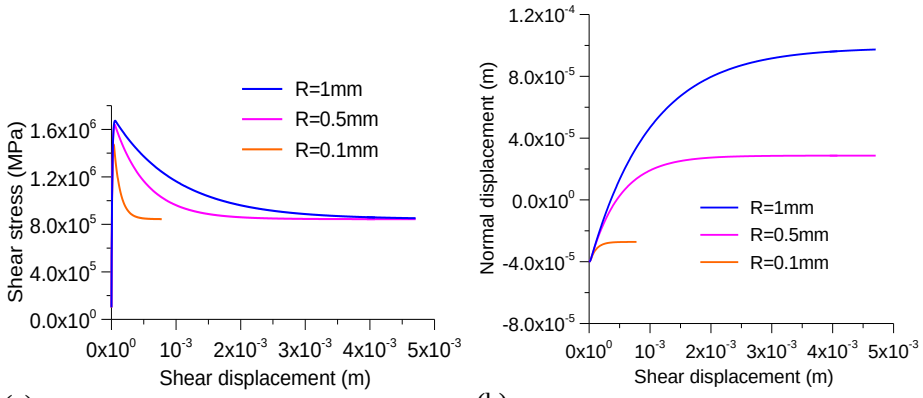

Figure 4.8: Influence of the roughness parameter (R) in the CY joint model on the shear stress vs shear displacement curves (a) and joint dilation (b). Note that normal stress = 4MPa

Influence of anisotropy on rock mass strength

In order to examine the influence of joint orientation on the rock mass strength, biaxial compression tests have been worked out on a simplified model, considering two continuous joint sets (Figure 4.9). The joints obey Mohr-Coulomb yield criterion with friction angle, $\varphi = 35^o$, assigned for both joint sets. The joint stiffness k_n = 6GPa/m and k_s = 3GPa/m are considered. The blocks have elastic properties (E =20GPa, $\nu = 0.25$). The model has size of 1m x 1m (Figure 4.10). In the simulation, the dip angle of the joint set2 has been kept to 10^o while the dip angle of the joint set1 has been changed in order to assess the influence of joint orientation on the model responses.

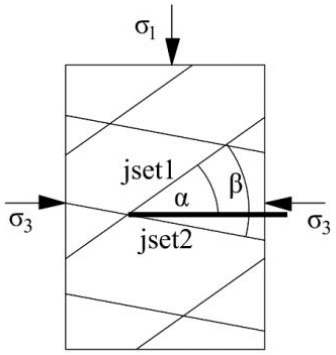

Figure 4.9: Joint sets (jset1 and jset2) considered for numerical study

A typical plot of shear displacement can be observed from Figure 4.10 when jointset1 are inclined at 76°. Figure 4.11 illustrates the anisotropy behavior of the rock mass, the bottom part of the concave curves (low axial strength) shows the orientation of joint set1 leading to shear failure along the discontinuity. Obviously higher axial strength is obtained when failure occurs through the rock mass rather than through discontinuities.

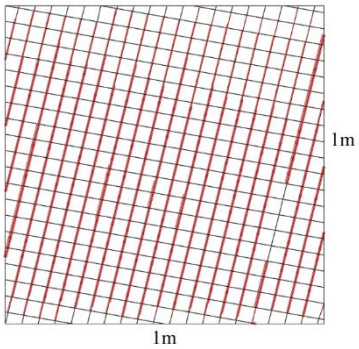

each line thick =0.8mm

Figure 4.10: Joint shear displacement when α= 76° when confining stress, σ3 = 2MPa

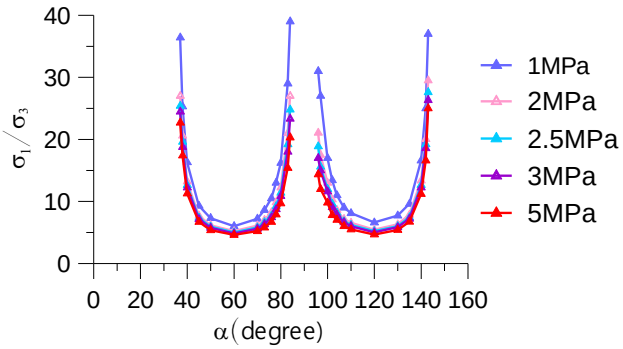

Figure 4.11: Ratio of σ_1/σ_3 vs joint inclination angle, α

The influence of confining stress on the axial strength has been illustrated in Figure 4.12. Besides this, the plot of axial stress vs confining stress shows a linear strength envelop similar to the Mohr-Coulomb criterion (Figure 4.12).

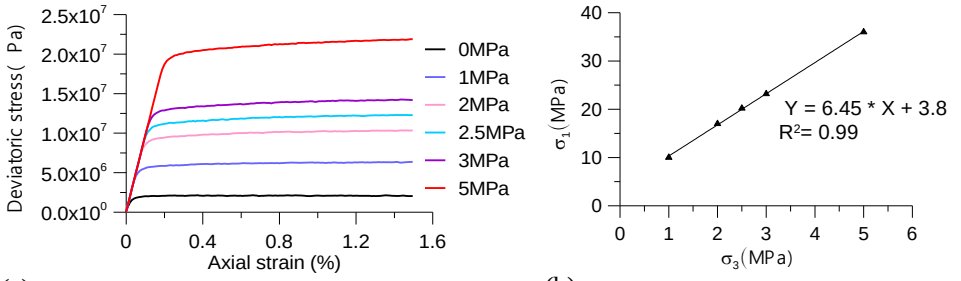

(a) (b)

Figure 4.12: (a) Deviatoric stress vs axial strain evaluated when $\alpha = 50^o$ at different confining stress σ_3= 0-5MPa and (b) strength envelop drawn when the discontinuity angle $\alpha = 143^o$

Comments

The previous numerical exercises can give some hints about the behavior of the DEM model. Concerning the joint models, although the CY joint model seems more reasonable to reproduce the actual joint shear behaviors, the Mohr-Coulomb model is common for large scale analyses since the strength parameters can be assessed with less difficulty as compared to CY joint model. Thus, the CY joint model will not be considered for our case history. The study of rock mass strength behavior considering anisotropic conditions can be used to get some insights about the joint set orientations which favor failure along discontinuities.

4.3 DEM modeling of the slope

The aim of this DEM modeling is to investigate the influence of the structure of the moving mass (i.e. block size, shape of slip surface, and joint pattern) on model deformation and mobilized friction angle of the slip surface. A 2D discontinuum modeling approach was adopted via the UDEC code (Itasca, 2011). Block materials have been assumed linearly elastic while joints are ideal elasto-plastic and obey the Mohr–Coulomb strength criterion.

The following analyses are primarily a back analysis of the slope deformation observed in more than 20 years of field monitoring, which allowed to categorize the movement as a “slow” process. Dynamics aspects often related to catastrophic slope failures (e.g. Alonso and Pinyol 2010, Kveldsvik et al., 2009) are not essential for the present case. Therefore, local damping has been applied, as customary in UDEC code

for static or quasi-static processes. In addition, all the numerical analyses are carried out considering large-strain mode, which is the default mode.

The slope has been modelled as a complex blocky structure defined by several joint sets. Bedding planes, gently inclined and markedly continuous are crossed by steeper and sub-vertical joints. Frequency and number of joint sets have been increased in the more disturbed portions of the slope, i.e., at the toe and in the transition zone, i.e., where the dip angle of the slip surface changes. The plane section considered in the model is parallel to the longitudinal axis of the ridge (Figure 4.13).

The mechanical properties of the joint sets are illustrated in Table 4.2. All the joint sets have the same stiffness properties (k_n and $k_s = 0.1k_n$) and purely frictional strength. The normal stiffness of the joints has been calibrated so that the equivalent rock mass modulus is in agreement with the elastic modulus suggested by the GSI approach, Q-value method and using other geophysical investigations (see Section 3.3).

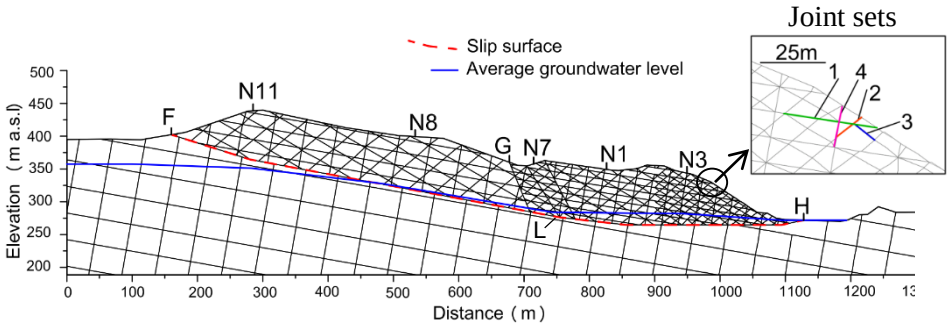

Figure 4.13: Model A with continuous joint pattern

The present morphology of the slope has been formed by simulating an "erosion" process, starting from an ideal situation with horizontal ground surface and in situ stress condition with horizontal-to-vertical stress ratio K_0 = 0.5. The reference groundwater table (stationary conditions) considered in the following analyses represents the average profile obtained from piezometer measurements (vertical boreholes A, B, C and D).

The influence of rock mass structure on the mobilized friction angle of the basal slip surface has been investigated. The shear strength reduction method was employed to calculate the failure condition for a given joint pattern. Equilibrium conditions have been satisfied for each step of reduction in basal friction angle. To this aim, an unbalanced forces ratio (Itasca, 2011) of 10^{-6} has been adopted as a convergence criterion.

Normally, a progressively higher number of calculation steps is required as the model approaches the plastic collapse. Additionally, the displacement histories of some grid points were monitored. The selected control points correspond to the position of specific geodetic targets (N1-N11), located at the toe of the slope as well as in the transition and upper zone of the ridge.

As highlighted by previous studies (Boon et al., 2014), the problem of finding the strength corresponding to the onset of collapse involves computational difficulties and ambiguous results are likely to be obtained. The expedient of progressively decreasing the step-size of the strength reduction as the system approaches the stability limit proved to be useful but not decisive.

Finally, for the present analyses, it was decided to adopt the following empirical approach. The limit friction angle has been identified by inspecting the displacement vs mobilized friction curves, i.e., it corresponds to the point of maximum curvature, where the displacement exhibits a sharp increase (e.g. Figure 4.16 and Figure 4.17). The aforementioned criterion may not be fully satisfactory, in general, but seems effective in order to compare the responses of the different models.

Moreover, a safety factor (S.F) can be easily calculated as the ratio of the tangent of the actual friction angle to the tangent of the failure friction angle, as suggested in Dawson et al. (1999). The shear strength assumed for the bedding planes corresponds to the typical properties determined for the contact planes between marly and arenaceous layers (see Chapter 3). The pattern of cross joints included in the model represents an idealized picture of the blocky structure of the marly-arenaceous formation. Persistent or discontinuous joints can be considered (Figure 4.18), as shown in the following sections.

A particular remark concerns the shear strength of the cross joints (joint sets 3 and 4). A minimum friction angle of 30° and 18° is required for the cross joints of Model A and B, respectively, in order to mobilize a translational movement of the rock mass along the basal plane. For lower friction angles, a different collapse mechanism is obtained, i.e., the slip failure of a steep wedge of rock mass in the frontal zone of the slope (between points N3 and H in Figure 4.13). This local failure mode was to be avoided since it is not in agreement with the observed characters of the real movement.

The aforementioned difference in the friction angle required for cross joints can represent a measure of the interlocking contribution to shear strength due to the non-persistent joints.

Table 4.2: Joint properties adopted in UDEC simulations

Description	S[a] (m)	ψ (°)	φ (°)	k_n (GPa/m)	k_s (GPa/m)
Bedding planes (1)	8-16	10	14-18	2.3	0.23
Joint set (2)	12-24	40	30	2.3	0.23
Joint set (3)	10-20	30	30	2.3	0.23
Joint set (4)	20-40	80	30	2.3	0.23
Slip surface	-	0-10.5[b]	Varies[c]	2.3	0.23

where :S = joint spacing, ψ = dip angle, φ= friction angle, k_n= normal stiffness, k_s = shear stiffness

[a]Spacing is different for the upper and lower (transition and toe) portions of the slope.

[b]Range of dip angles of the slip surface (c) assumed for the model in Figure 4.13

[c]Friction angle of slip surface is varied according to the strength reduction method.

4.3.1 Effect of blocky structure

Block size

Since the actual joint spacing in the field cannot be represented by the model, it is worthwhile to assess the influence of block size on model response (Boon et al., 2014, Zangerl et al., 2003). To this aim, a simplified model with two joints sets i.e. bedding planes (joint set 1) and sub-vertical joints (joint set 4) has been considered with spacing, S and 0.5*S respectively as depicted in Figure 4.14. Figure 4.14 illustrates that block scaling affects the overall stiffness of the rock mass (Goodman, 1989) but does not change the mobilized friction angle. Further analyses have been performed by employing 1/3*S of block size of Figure 4.14. Similarly, the limit friction angle does not change apart from an increased in displacement magnitude. Moreover, as the number of blocks increases the model exhibits a toppling mechanism in the frontal part (Figure 4.15). This feature is not in agreement with the observed mainly translational movement.

Boon et al. (2014) obtained similar results, in which the failure friction angle was found to be progressively less sensitive to block size as the number of blocks becomes sufficiently higher.

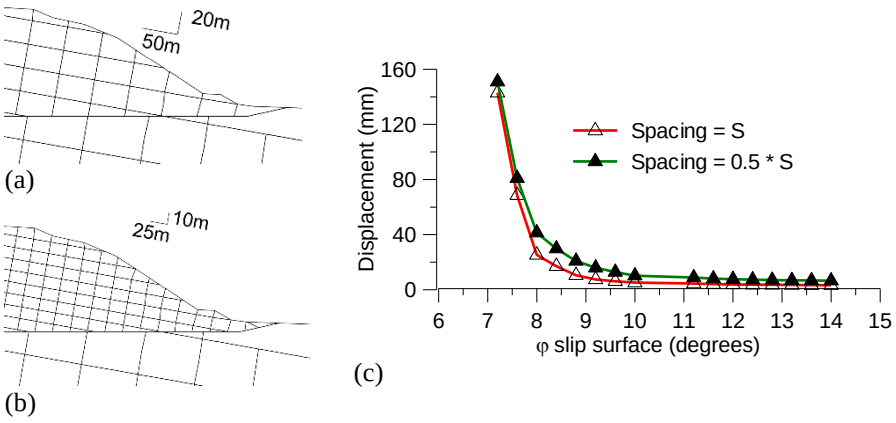

Figure 4.14: Models with joint spacing S (a) and 0.5*S (b); calculated displacement of point N3 vs mobilized friction angle of the slip surface (c)

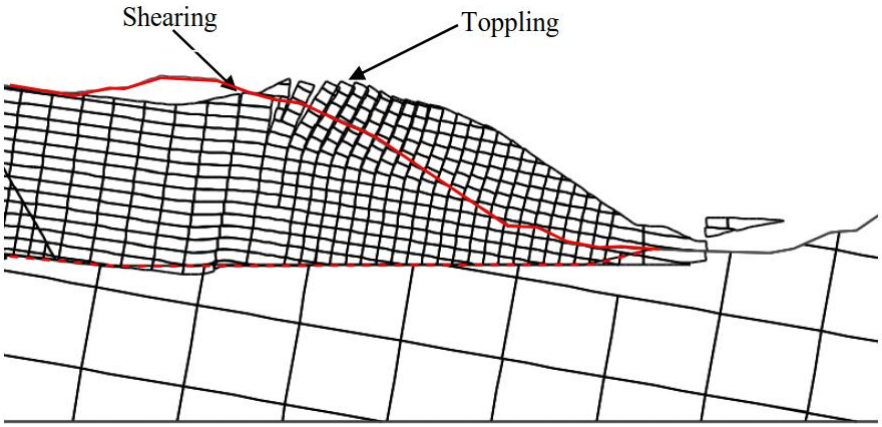

Figure 4.15: Deformed shape (x300) when the basal friction is equal to 8o which shows shearing and toppling failures

Internal joint friction angle

The influence of friction angle of the internal joint sets on the mobilized friction angle of the slip surface has been studied herein using model shown in Figure 4.14. Figure 4.16 illustrates that the friction angle of the persistent sub-vertical joints has no influence on the mobilized friction angle of the basal slip surface. However, the displacements are relatively

higher when we consider low friction angle for sub-vertical joint sets especially in the elastic shear displacement stages.

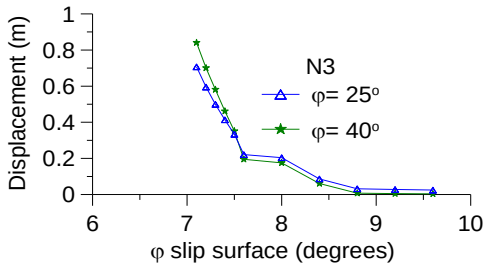

Figure 4.16: Influence of friction angle of the persistent sub-vertical joints on the collapse limit

Joint shear stiffness

The shear stiffness of the slip surface joint varies between 0.01GPa/m to 2.3GPa/m. Figure 4.17 shows that the collapse limit is not sensitive to the shear stiffness of the basal surface except some minor displacement increase when the shear stiffness decreases. Previous study by Boon et al. (2014) also discussed the collapse limit is not dependent on the shear stiffness of the sliding surface.

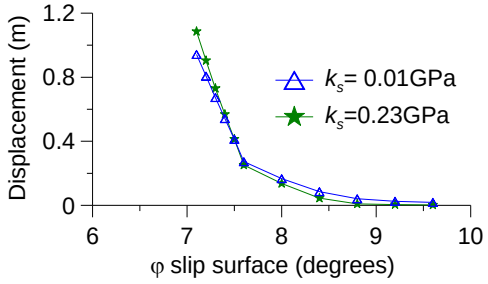

Figure 4.17: Mobilized friction angle vs displacement for N3 at two shear stiffness values of the basal surface

Joint pattern

After the preliminary studies, two refined joint patterns are prepared for further study of the slope behavior (Figure 4.18). In Model A, all the joint sets are continuous, on the base of field survey and borehole data, a staggered joint pattern has been also implemented (Model B in Figure

4.18), in order to analyze the influence of non-persistent joints and interlocking. Thus, these two joint patterns can give us detail information about the ongoing slope deformation behavior.

The model with staggered joints exhibits less internal shearing of the rock mass and a uniform distribution of horizontal displacements (Figure 4.18). The deformation mode of Model (A) is more complex especially in the elastic phases: the lower portion of the slope, particularly N1 and N3 points, displaces more than the upper portion, where shearing deformations along the joints dipping towards S (joint set 2) are also activated.

Both models demonstrate mainly a basal sliding, with intensified deformations localized around the transition zone and the position where the slip surface changes its dip angle. Similar influences of joint pattern on the deformation mechanism of rock slopes have been reported by previous studies (Hammah et al., 2009, Brideau and Stead, 2012).

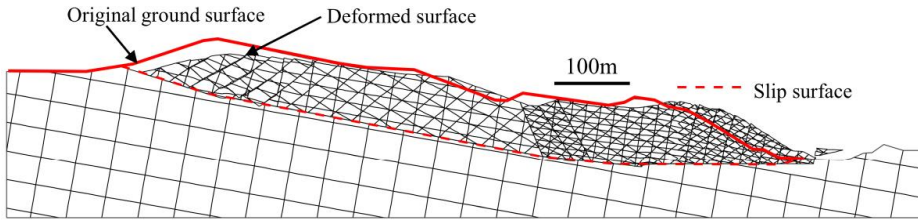

(a) Model A

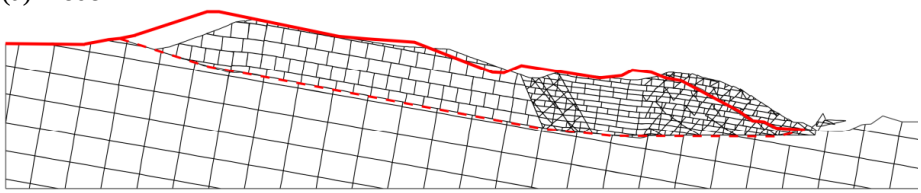

(b) Model B

Figure 4.18: Deformed shape (x200) of Model A (a) and Model B (b) for a mobilized friction angle $\varphi = 8^{o}$ on the basal slip surface

Figure 4.19 illustrates both models experience plastic deformation when φ approaches to 8.4^{o} and then a marked displacement increase occur when the friction angle is close to 7.6^{o}.

At collapse, Model-B shows less internal shearing and bending type of deformation is evidenced at the lower part where the slip surface changes its geometry (Figure 4.20a) While the deformation mode of Model-A at collapse situation is characterized by intensified shearing along the sub-vertical joint sets (Figure 4.20b). These mechanisms are

more visualized at the transition zone, location of change of shape of slip surface and the south part of the model (i.e. around N11).

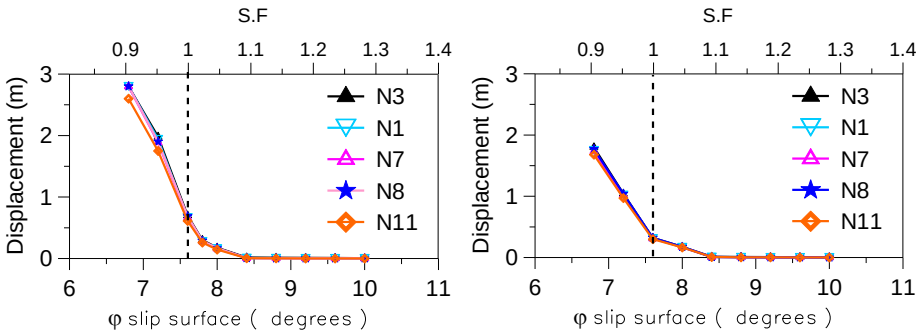

(a) Model-A (b) Model-B

Figure 4.19: Calculated displacement vs mobilized friction angle of basal slip surface for Model A (a) and Model B. (b)

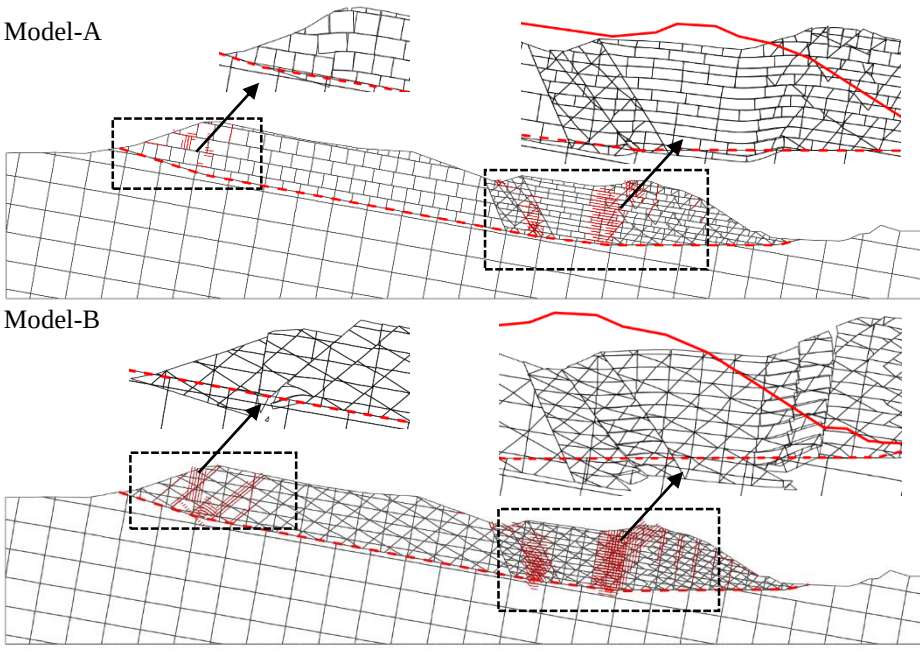

each line thick = 4mm joint shear displacement

Figure 4.20: Comparison of the shear displacement along joints in Model A and B for a mobilized friction angle φ =7.2º on the basal slip surface; details of the local deformation mechanism (magnification factor: x100) in the zones of intense shearing.

Depth and shape of slip surface

As already discussed in Chapter 3, depth and shape of the slip surface can be unambiguously defined only in the toe portion of the slope. However, for the upper part of the slope some reasonable hypotheses have been formulated, taking into account the location of the damaged tunnel section and the slope morphology. Figure 4.21 shows the set of four different hypotheses (a, b, c and d) which have been considered and implemented in Model A (model with continuous joints). Thus, the four models have identical joint pattern and spacing of joints, but a different slip surface is included as continuous series of cracks in each cases. Accordingly, the dip angle and depth of the upper portion of the slip surface vary reasonably between 7–13^o and 54–100 m, respectively.

The slip surface (c) is identical to the adopted slip surface for both Model-A and Model-B as depicted in Figure 4.18. The plastic collapse in slip surface (c) begins for a friction angle of φ= 8.4^o and the conventional collapse limit is close to φ=7.6^o.

The slip surfaces (a) and (b) exhibit plastic deformations since the friction angle is reduced to φ = 9.4^o and 8.8^o, respectively. A sharp increase in displacement (failure limit) occurs when φ =7.6^o for both the slip surfaces (a) and (b). The hypothesis (a), specifically, is in agreement with the minimum expected inclination of the slip surface in the transversal cross section and intersects the damaged tunnel section (Figure 3.43).

The slip surface (d) behaves differently where the plastic deformations occur at a lower friction angle close to 7.6^o, a value significantly lower than the other cases. Further reduction of the mobilized friction angle shows a sharp increase of displacement around φ =7^o.

Basically, the three profiles, (a), (b) and (c) differ in the extent of the horizontal portion of the slip surface. In the case (c), the limit of the horizontal slip reaches corresponds to the boundary of the “transition zone”, formerly identified on the base of morphological evidences on the ground surface.

Therefore, hypothesis (c) has been selected for the rest of modeling works of the research.

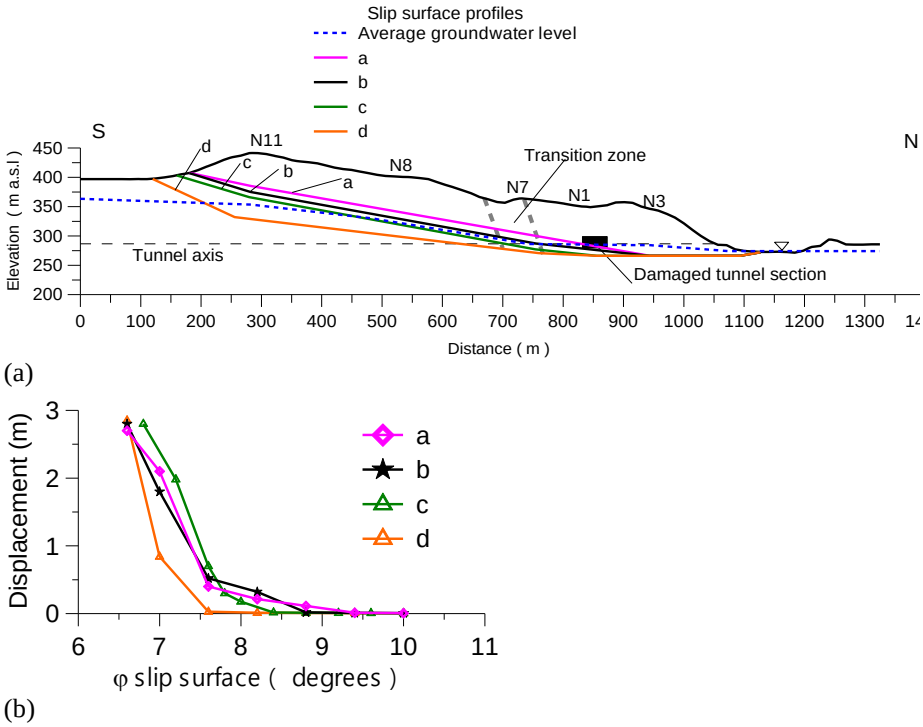

Figure 4.21: Considered slip surface profiles (a) and their limit condition (b)

The influence of the shape of the slip surface on the slope deformation can also be appreciated by looking at the intensified joint shearing at the interface zone where the dip angle of the slip surface changes from mild slope (around 10^{o}) in the upper portion to zero in the lower part (Figure 4.20).

Previous studies (Alonso and Pinyol, 2010, Yerro et al., 2015) highlighted significant internal shearing at the interface region where the upper steep slip surface meets the lower flat surface. Figure 4.20 also depicts a similar tendency of shearing at the interface zone even though in this case the change of inclination of the slip surface is not as such critical as that of Vajoint case. Moreover, Figure 4.20 illustrates in detail the joint shearing and block deformation observed at various parts of the model.

4.3.2 Influence of groundwater table rise and stepwise reservoir filling

In the first set of analyses, the water level of the reservoir was kept constant at 274m a.s.l., while the groundwater table inside the slope rises from the average conditions (AGW) to the maximum groundwater table (MGW) recorded throughout the monitoring period. Figure 4.22 depicts that the displacement increase during friction reduction steps is significantly dependent on the groundwater level. Obviously, the displacement increase is higher when the maximum groundwater table is considered inside the slope. Moreover, the abrupt increase in displacement has been observed at φ equals to 7.6^o and 8.2^o when the groundwater table increases from the average to the maximum water table respectively.

In separate analyses, the influence of reservoir filling on model deformation has been considered. Here a horizontal water table is introduced inside the slope till the intersection point with the average groundwater table profile. In addition, the model responses during the stepwise filling of the dam will be discussed in Section 5.5.5 and 5.6.3 by taking in to account flow analyses in order to obtain a more reasonable pore pressure distribution.

The effect of reservoir level increase, up to the maximum project level of 330 m a.s.l, has been analyzed by keeping constant the friction angle of the slip surface (9^o) for the entire slip surface. In other analyses, the friction angle equals to 9^o is assigned to upper slip surface (between F-L) and 7.6^o to the lower slip surface (between L-H) in order to compare to the previous results.

Figure 4.22 shows the "rate" of increase in displacement (displacement increment divided by the increase in reservoir level) obtained for different water pool elevation.

As it is shown from Figure 4.22, the maximum rate of displacement has been obtained when the reservoir level is between 320 to 325 m a.s.l. The upper portion of the slope, N8 point, experiences a slightly higher displacement as compared to the lower zone.

The slope deforms differently in the upper part, between points F and G, where effective stress is less affected by filling. Vertical displacements are directed upwards between G and H and downwards in the upper zone of the ridge. Figure 4.23 depicts the horizontal displacement obtained when the reservoir level is 330m a.s.l. The mechanical pressure from the reservoir seems to provide some restraint to the toe of the slope, even

when it is mostly submerged. Several numerical analyses showed that the filling of the dam induces higher displacement in the front part (i.e. N3) when the reservoir level is approximately lower than 310m a.s.l. While for higher levels, in between 310-325m a.s.l, the upper part of the slope (N8) is displacing more as compared to the lower part. Obviously, this is due to the change of pore pressure distribution.

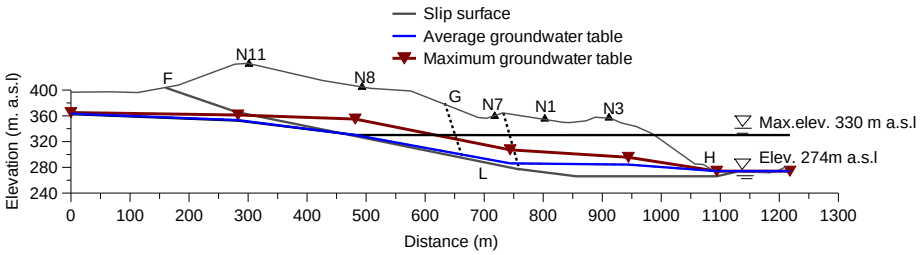

(a) Note that the groundwater tables are drawn from average and maximum piezometer levels.

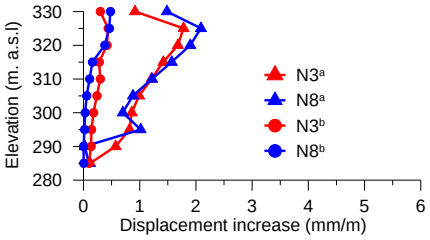

(b)

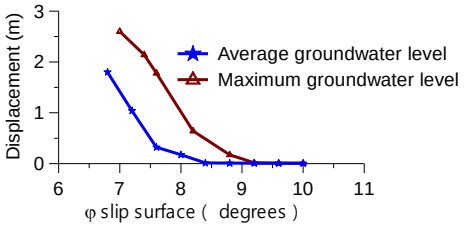

(c)

[a] displacement rate when the friction angle is equal to 9 and 7.6° for the upper part (F-L) and lower part (L-H) of the slip surface respectively.
[b] displacement rate when the friction angle is equal to 9° for the whole slip surface.

Figure 4.22: Average and maximum elevation of groundwater table, maximum level of reservoir considered in DEM modelling (a); horizontal displacement increases calculated for progressive reservoir filling (b); horizontal displacements vs mobilized friction angle curves calculated for average and maximum groundwater profiles keeping empty reservoir level (i.e. 274m a.s.l) (c)

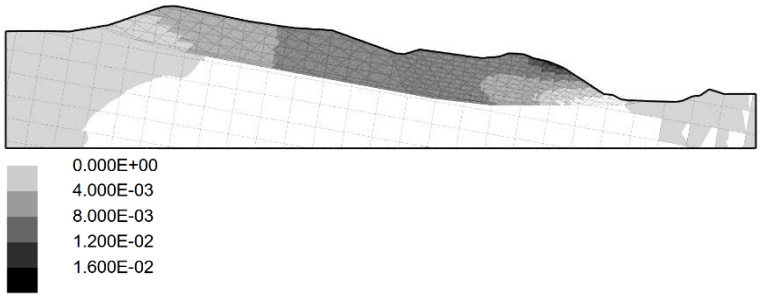

Figure 4.23: Horizontal displacement contour when the reservoir level is equals to the maximum design level (i.e. Elev. 330m a.s.l) keeping friction angle of 9º for the entire basal slip surface

4.4 Conclusions

On the base of the numerical models conducted in this section, some lessons regarding the deformation mechanisms and influence of the slope structure on mobilized friction have been learned. The observed slope deformation behavior has been reproduced reasonably with the DEM model by introducing reasonable joint pattern and joint set properties. The joint pattern (staggered or persistence) influences the model deformation mechanisms.

The mobilized friction angle of the basal slip surface is independent of the slope structure (i.e. block size, internal joint friction angle, shear stiffness of the slip surface and joint pattern). Some limited influences have been observed with regard to depth of slip surface. The mobilized friction angle ($\varphi = 7.6^{o}$) close to residual friction angle of direct shear box tests (clay gouge) has been evaluated.

The groundwater table rise and reservoir level increase have limited effect on the mobilized friction angel of the slip surface. The groundwater table inside the slope significantly controls the displacements during shear strength reduction steps, keeping empty reservoir (elev. 274m a.s.l).

The increase of the reservoir level causes limited displacement increases. Moreover, the mechanical pressure at higher reservoir elevations tries to slow down the slope displacement in toe part, but the upper part experiences higher deformation.

Chapter 5

5 Hydromechanical analysis

5.1 Introduction

This chapter focuses on the hydromechanical analyses of the ongoing slope movement using numerical modeling approaches. In the first part, the hydromechanical behavior of the DEM model has been revised and discussed with the help of numerical experiments. In the second part, the discontinuum modeling of the hydromechanical behavior of the slope has been presented. The influence of joint pattern, joint properties and hydraulic boundary condition on the steady state groundwater profile has been examined. In the third part, the continuum modeling has been introduced to describe the flow process. The influence of infiltration amount, keeping reasonable rock mass permeability, on the steady state groundwater profile has been assessed. Lastly, the effect of the stepwise filling of the dam on pore pressure regime and slope deformation behaviors has been investigated.

5.2 Review on hydromechanical analysis using DEM

Flow in a rock mass occurs mainly through the discontinuities since the permeability of intact rocks is relatively lower. Previous studies (Barla et al., 2004, Farinha et al., 2012, Bretas et al., 2013) discussed the seepage process in a dam through a jointed rock mass foundation, where flow mainly occurs through discontinuities. In the hydromechanical analyses using DEM, the permeability is influenced by the stress state. The mechanical deformation changes the joint conductivity and the overall rock mass permeability will be altered consequently. Cammarata et al. (2007) discussed the hydromechanical-coupled transient responses by injecting fluid in a single fracture.

Barla et al. (2004) presented hydromechanical analysis in jointed granitic rock mass foundation of a dam by considering random and deterministic joint patterns. Zengerl et al. (2003) also carried out hydromechanical analyses in order to evaluate the ground displacements in a fractured rock mass using DEM. A study by Cappa, et al. (2006) discussed the hydromechanical analysis of a large moving rock slope using DEM. Bonzanigo et al. (2007) studied the influence of deep

drainage works on the displacements of a creeping slope in a complex rock formation using hydromechanical analyses.

A study by Zhang et al. (1996) discussed the influence of joint orientation on the overall permeability of a fractured media. He remarked that maximum permeability is obtained when the joints have higher connectivity, which depends on the joint orientation. Similar study by Indraratna et al. (1999) also showed the influence of joint network on the flow rate to a cavity using different orientation of joints. He discussed that vertical joints carry more flow rate as compared to other joint sets since effect of gravity is more dominant.

Liao and Hencher (1997) studied the influence of horizontal stress to vertical stress ratio. Their study showed that the overall permeability decreases with the increase in horizontal stress to vertical stress ratio. Indraratna et al. (1999) also discussed that horizontal stresses are more dominant for joint closure as compared to vertical stress influencing joint conductivity, hence flow decreases when the horizontal stress to vertical stress ratio increases for a given joint pattern and boundary condition.

Basic fluid flow formulations

The flow rate, q (m^3/s. m) is given by using cubic law equation, which is derived for laminar flow between two parallel plates with smooth surfaces (Witherspoon et al., 1980).

$$q = \frac{a^3}{12\mu} * \frac{\Delta p}{\Delta l} \tag{5.1}$$

where $\Delta p/\Delta$l is the hydraulic gradient of a fracture with unit width (Pa/m), a is hydraulic aperture (m), μ is dynamic viscosity of water ($1x10^{-3}$ Pa.s). The rate of fluid flow depends on the cubic power of aperture. Flow estimated from cubic law gives higher value but widely used in numerical models. Witherspoon et al. (1980) tested both open and closed joints and concluded that the cubic law is still valid for the closed joints, if the actual mechanical aperture is used.

The transmissivity of a joint, T (m^2/s) is directly proportional to the cubic of hydraulic aperture and it is defined as follows

$$T = \frac{\rho g a^3}{12\mu} \tag{5.2}$$

Then the equivalent hydraulic permeability of the rock mass, k (m/s) in the plane of the fracture is given by dividing the joint transmissivity by the spacing, S as

$$k = \frac{\rho g a^3}{12 \mu S} \tag{5.3}$$

where ρ is the density of water (kg/m^3) is g is the acceleration due to gravity (m/s^2), S is the spacing between joints (m).

In coupled analysis, hydraulic conductivity depends on mechanical deformation and vice versa. Thus, the joint hydraulic aperture changes due to mechanical closure, opening or dilation, which is given by the following expression:

$$a = a_o + u_n \tag{5.4}$$

where a is hydraulic aperture, a_o is initial hydraulic aperture, u_n is the joint normal displacement which depend on normal effective stress and normal stiffness. A minimum value, residual aperture, a_{res} is kept below which mechanical deformation does not affect contact conductivity. Joint conductivity depends on mainly on residual aperture, a_{res} once a critical load is exceeded (Indraratna et al., 1999).

Pore pressure, p in domains or joints is evaluated as:

$$\Delta p = \frac{k_w}{V}\left(\sum Q \Delta t - \Delta V\right) \tag{5.5}$$

where Δp is change in pore pressure, k_w fluid bulk modulus, ΔV is mechanical volume change, ΣQ is flow into node, Δt is the timestep and V is average volume between timesteps.

For fully coupled hydro-mechanical transient analysis, the timestep is given by

$$\Delta t_f = \min\left\{\left[\frac{V_i}{k_w \sum_{j=1}^{N_c} k_{cj}}\right]\right\}; i = 1, 2, ...N_d \tag{5.6}$$

where K_w is the fluid bulk modulus, N_d is the total number of domains and V_i is the volume of the i_{th} domain, and N_c is the number of contacts connected to the i$_{th}$ domain and k_c is the permeability of the j_{th} contact of domain i, where its value is can be found as k_c or k_j depending on the type of contact.

From the above expression, the hydraulic timestep depends on the minimum domain volume, which is computed from the residual hydraulic apertures for transient flow analysis. Moreover, transient analysis becomes time consuming and convergence is usually too difficult when there are small domain volumes with large contact apertures. Besides this, fluid filling the joint increase the apparent joint stiffness by (K_w/a) and it reduces the mechanical timestep.

This behavior has also been observed by our numerical experiments (Section 5.3) in which the fluid timestep for transient analysis depends on the residual hydraulic apertures as well as on model discretization. Therefore, it is advisable to control both the residual aperture and model discretization till satisfactory fluid timestep is obtained.

In the steady state flow algorithm, only the final steady state solutions are correct, even though some transient behaviors might be observed. For a steady flow analysis, the hydraulic timestep is equal to the mechanical timestep. Steady state solution does not involve domain volumes in pore pressure variations. By assigning a given volume, *V*, the same timestep can be obtained (Equation (5.6)) for all domains so that it can give good convergence to a final solution. Therefore, the computation is faster than other transient analyses. The steady state condition can be recognized from the history of domain pore pressure or flow balance.

5.3 Numerical flow tests

With the intention of exploring the influence of several joint properties (joint apertures, joint stiffness) on pore pressure histories, coupled hydromechanical analyses have been carried out via UDEC code on a simple mode of size L = 50m and H = 17.5m (Figure 5.1). In the modeling, two continuous joint sets: sub-vertical, (jset1) and sub-horizontal, (jset2) have been employed as shown in Figure 5.1. Blocks are elastic while joints are elasto-plastic and obey Mohr-Coulomb failure criterion. Elastic properties, (v=0.25) and Young modulus, E =15 and 10 GPa are considered for the base rock and upper sliding wedge respectively.

In the modeling, the incompressible transient fluid flow analysis has been carried out. Table 5.1 shows data pertaining to joint properties used for the analysis.

In order to take in to account the effect of infiltration two approaches were realized i.e. applying directly point inflows to the boundary domains or applying a given low boundary pore pressure (e.g. boundary pore

pressure 0.1-1kPa) to trigger inflow from the boundary domains towards the interior domains.

The applied inflows to single joint, with magnitude around $7.5x10^{-5}$ $m^3/s.$ m, are appropriate without inducing any local joint failures (slip, opening of joints). Therefore, theses applied joint inflows have been considered in order to take in to account the effect of water infiltration volume on pore pressure history.

While studying the effect of several joint parameters (Table 5.1), the hydraulic boundary condition has been kept constant. However, in the last part of these numerical simulations, separate numerical analyses have been carried out just to examine the influence of applied inflows to the steady pore pressure distribution keeping other model parameters constant.

Table 5.1: Joint properties utilized for flow numerical tests

Joints	*k_n (GPa/m)	k_s (GPa/m)	φ (°)	c (kPa)	ψ (°)	S (m)	*a_o (mm)	*a_{res} (mm)
Jset1	10	0.1	40	40	75	5	0.32	0.09
Jset2	4.5	0.45	25	20	7	5	0.68	0.1
Slip plane	4.5	0.45	20	10	14	---	---	---

*Parametes considered to examine their influence on pore pressure history.
where: k_n=normal stiffness, k_s= shear stiffness, φ= friction angle, c= chohesion, ψ =dip angle, S= spacing, a_o= initial aperture, a_{res} = residual aperture.

5.3.1 Modeling procedure

Firstly, the model mechanical deformation has been calculated in dry condition only by applying gravity load. Secondly, keeping boundary pore pressure of magnitude 130kPa and 110kPa to the left and right boundary respectively, steady flow analysis has been performed (Figure 5.1). In this stage, both the mechanical and flow analyses have reached to equilibrium.

In the third step, fully coupled transient calculations have been performed using incompressible flow analysis taking in to account the water infiltration in the surface boundary. In order to simulate the effect of inflows on the model pore pressure history, joint inflows, $q_j = 7.5e^{-5}$ $m^3/s.m$ have been applied directly to the boundary domains.

The following results discuss separately the influence of joint stiffness (k_n), initial hydraulic aperture (a_o) and residual aperture parameters (a_{res})

on pore pressure history. Besides this, the change in water table profile owing to initial and residual hydraulic aperture values has been included.

To monitor time history of pore pressure in the transient coupled analyses, points 9,10,11,12 shown in Figure 5.1 have been considered.

As discussed above the model discretization influences the timestep for coupled analyses, therefore the mesh depicted in Figure 5.1 has been applied in the analyses which is a bit coarser so that computational time could be reduced. It has been understood that a finner mesh size decrease significanly the timestep and computational time will be longer.

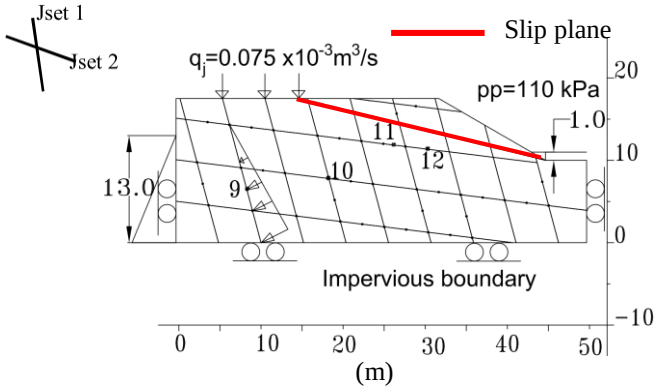

(a)

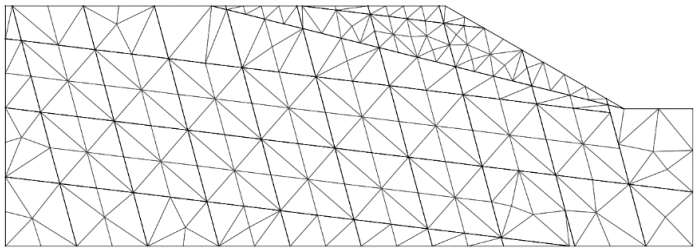

(b)

Figure 5.1: Model geometry applied for parameter study (a); and (b) zoning utilized for the transient flow analyses

Table 5.2: Values of joint parameters considered for each flow simulations

Parameters	Case 1	Case 2	Case 3	Case 4
Joint stiffness, k_n (GPa/m)	10	4.1	1.1	0.44
Initial aperture, a_o (mm)	0.35	0.40	0.45	0.50
Residual aperture, a_{res} (mm)	0.082	0.092	0.10	0.20

5.3.2 Effect of joint parameters

Joint stiffness (k_n)

In the first set of analyses, the influence of joint stiffness, k_n on the time history of pore pressure during coupled analyses have been examined. It is assumed that $k_s = k_n/10$. The joint aperture a_o =1mm and a_{res} = 0.1mm has been kept constant for all the model joints.

As it has been depicted in Figure 5.2, joint stiffness affects only the transient pore pressure values of the model while the steady state solution is almost the same at different joint stiffness values. Moreover, as the stiffness increases, the peak pore pressure in the transient period increases. It seems that as the joint stiffness is higher, the joint aperture does not change much to allow the pore pressure variation due to volume change. While for low joint stiffness, the domain volume can change easily, consequently the pore pressure inside the domains can be affected by the mechanical deformation.

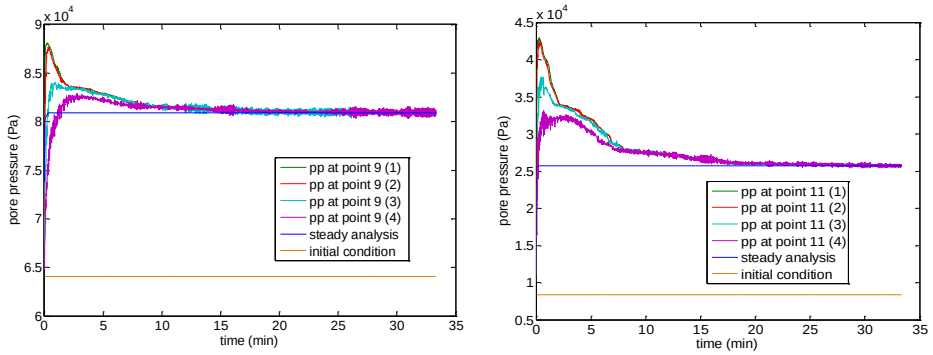

(a) (b)

Figure 5.2: Pore pressure (pp) vs time at (a) point 9 and (b) point 11 during coupled transient flow analyses

Initial hydraulic aperture (a_o)

Keeping the residual aperture, a_r =0.1mm and joint stiffness k_n= 1.1GPa for all joints, the influence of initial joint aperture a_o on the time history of pore pressure was studied.

Contrary to joint stiffness parameter, initial hydraulic aperture of the joints affects both the steady and transient responses of the model. Besides this, lower initial apertures cause an increasing pore pressure developed in the domains. For instance, when initial aperture of joints

reduced from 0.5mm to 0.35mm, pore pressure developed at point 9 increases by around 5kpa (Figure 5.3).

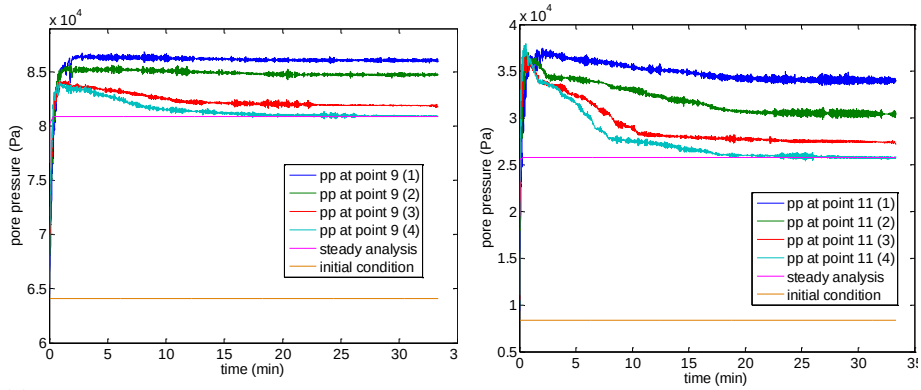

(a) (b)

Figure 5.3: Pore pressure (pp) vs time (a) at point 9 and (b) at point 11. The steady state condition clearly influenced by the initial joint aperture

Residual hydraulic aperture (a_{res})

In a similar fashion, keeping the initial joint aperture a_o = 1mm and joint stiffness k_n = 1.1GPa/m constant, the influence of residual joint aperture on the pore pressure history has been examined.

The residual hydraulic aperture also affects pore pressure history both in steady and transient phase. Moreover, the pore pressure increased by around 23kPa at point 9 when we decrease residual aperture from 0.2mm to 0.082mm (Figure 5.4). A similar change has been also observed in other control points.

Furthermore, the influence of initial and residual aperture on the water table has been depicted in Figure 5.5 considering pore pressure along a sub-vertical joint passing through point 9. Thus, the initial and residual aperture can cause only minor change in water table.

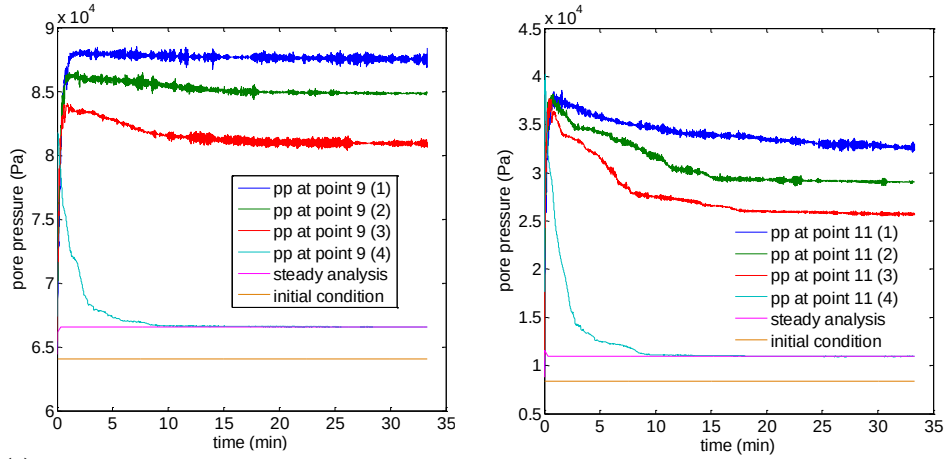

(a) (b)

Figure 5.4: Pore pressure (pp) vs time (a) at point 9 and (b) at point 11. The residual aperture also affect the steady state pore pressure regime

Boundary condition

Separate transient analyses have been carried out to explore the influence of infiltration amount on the steady state pore pressure distribution. Figure 5.5 c and d depicts the pore pressure profiles along a vertical through point 9 analyzed at different boundary conditions. It has been apparent that the infiltration amount from the surface affects the steady state pore pressure value inside the joints.

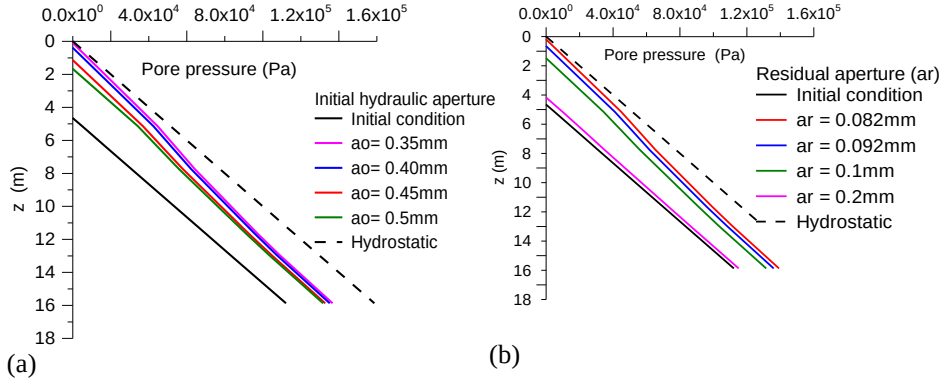

(a) (b)

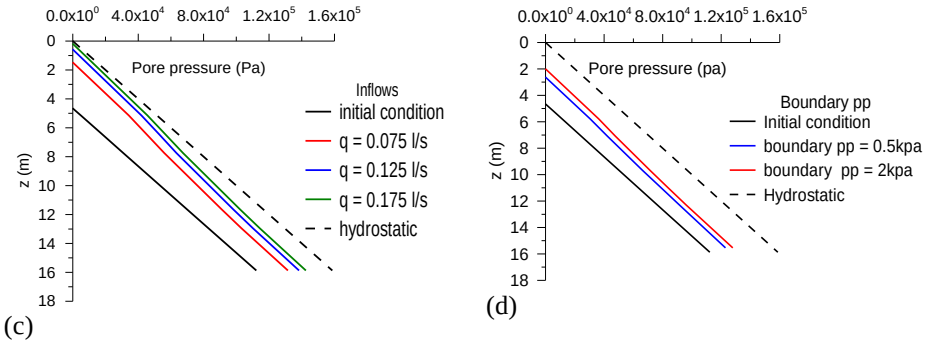

Figure 5.5: Influence of joint parameters (a and b) and boundary conditions (c and d) on pore pressure vs depth profile along a sub-vertical joint at point 9

5.4 Fluid flow inside the slope

In the following sections, some attempts have been made to reproduce the observed average and maximum piezometer levels using discontinuum and continuum approaches. These analyses have been carried out considering empty reservoir (elev. 274m a.s.l), which represent the current situation of the dam. In separate analyses, the effect of stepwise filling of the reservoir on the hydromechanical behavior of the slope has been analyzed. These last analyses have given us some insights about the slope behavior when the dam will start operation. The modeling protocol and results in the two modeling approaches have been discussed and compared.

5.4.1 Considerations related to permeability and infiltration amount

The permeability of the bedrock can be recalled by referring Lugeon tests conducted in the area of the dam foundation, which is in between $1x10^{-7}$-$3x10^{-7}$ m/s. The permeability of the sliding mass can be partially understood from geophysical investigations (e.g. P-wave velocities). Therefore, for the disturbed marly-arenaceous formation, permeability values in the range of $1x10^{-6}$-$1x10^{-5}$ m/s has been evaluated by relating the P-wave velocities, rock mass quality (Q-values) and Lugeon (L) values based on Barton (2002) suggestions. Moreover, it might be reasonable to consider the permeability of the sliding mass could be a bit higher than the permeability of the bedrock in the dam foundation area by taking in to account the ongoing slope deformation and morphological aspects.

It is more likely that the seepage process might be limited mainly to the discontinuity planes as compared to the less permeable clay-rich layers. The flow process inside the slope could also be affected by the lateral steep morphology which favors the lateral drainage of water, this influence seems dominant in the east side where the steep morphology is clearly defined as compared to the west side.

Moreover, different permeability values can be expected to various slope regions (i.e. the transition zone, upper sliding mass and lower disturbed toe part).

Therefore, the lower disturbed rock mass and the transition zone can exhibit higher permeability as compared to the upper sliding mass. The basal slip surface can have similar permeability with the bedrock. The alluvium layer in the toe part can have a bit higher permeability.

The above hypotheses of differing permeability for various slope regions will be examined using the continuum and discontinuum models.

Some reasonable permeability values between 1-3x10^{-5} m/s, which are not far from previous tentative estimates have been employed for the moving mass while a relatively reduced value in the order of 1x10^{-6} m/s has been considered for the bedrock and slip surface permeability and discussed based on simulation of the observed piezometer levels.

The infiltration quantity, q has been estimated by deducting evapotranspiration using Turc method (Turc, 1961) and the runoff amount. Infiltration amount, q =1.4 x10^{-8} m/s has been calculated which is around 50% of the average rainfall amount. Similar quantity has been also evaluated by employing the Soil Conservation Service Curve Number method (SCS-CN). The estimated quantity has been applied in the numerical simulations with the continuum modeling approaches (Section 5.5).

5.5 Flow analysis using DEM

Hydromechanical modeling using DEM has been introduced to assess the influence of joint pattern and joint properties on the steady state groundwater profile. The effect of infiltrated water volume on the estimated groundwater profile has also been examined. Since the data recorded by piezometers were not available with sufficient frequency to conduct transient analyses, it has been decided herein to estimate only the steady groundwater profile as observed in the piezometers. Therefore, a steady analysis has been carried out via UDEC code.

The influence of joint pattern on the steady state water table has been evaluated by considering staggered and persistent joint patterns.

Moreover, the joint hydraulic apertures at different parts of the model (i.e. upper, transition and lower portion) are calibrated on the base of the observed piezometer levels using preliminary analyses. Then keeping those joint properties, the influence of infiltration volume on the steady state water table has been examined.

In the first part of the model analyses, the reservoir level is kept to 274m a.s.l (empty reservoir) since the focus was to predict reasonably the observed average and maximum groundwater levels in the last 25 years.

While in the second part, the influence of stepwise filling of the dam until the design pool level (i.e. 330m a.s.l) on the steady state pore pressure distribution and slope deformation has been examined.

5.5.1 Joint pattern and model parameters

The influence of joint pattern on permeability of the rock mass needs special attention in flow analyses using DEM. Therefore, three different model structures (Model-I, Model-II and Model-II) were considered herein as shown in Figure 5.6. Models II and I have persistence joint pattern with identical spacing. Moreover, in Model-I the dip angle of the bedding planes has been kept between 9-11^o both in the upper and the lower part of the slope. While in Model-II the dip angle of the bedding planes is reduced from 11^o (upper part, F-L) to 5^o (lower part, L-H) exhibiting similar behavior as the shape of the basal slip surface. Model-III has staggered joint pattern and dip of bedding planes which is in between 9-11^o both in the upper and lower part of the model.

In addition, the size of blocks considered in both Model-I and II has not been varied significantly since the spacing of joints considered in both models are the same. Limited difference on block sizes can be seen in Model-III as compared to others.

The apertures of the joint settings considered in the model have been determined by conducting several preliminary analyses. The initial aperture of bedding planes varied between $0.5x10^{-3}$-$1x10^{-3}$m while the initial aperture of the crossing joints varied between $1x10^{-3}$-$2x10^{-3}$m.

The apertures values that gives the best-fitted value to the observed average piezometer levels have been reported in Table 5.3 for the slope portion between F and G.

In addition, in order to take in to account the presence of low permeability of clay rich interbeds inside the rock mass, a constant

aperture of 0.5mm has been considered for bedding planes between points F and G. The idea of keeping constant aperture for the bedding joints (F-G) could represent a typical clay-filled joint which exhibit less change in aperture during shear deformation. Moreover, it may not be right to consider bedding planes like clean rough rock joints, in which the changes of aperture due to joint closure, opening or shearing influence joint conductivity. The sub- vertical joints have been assigned with a relatively higher joint aperture (see Table 5.3).

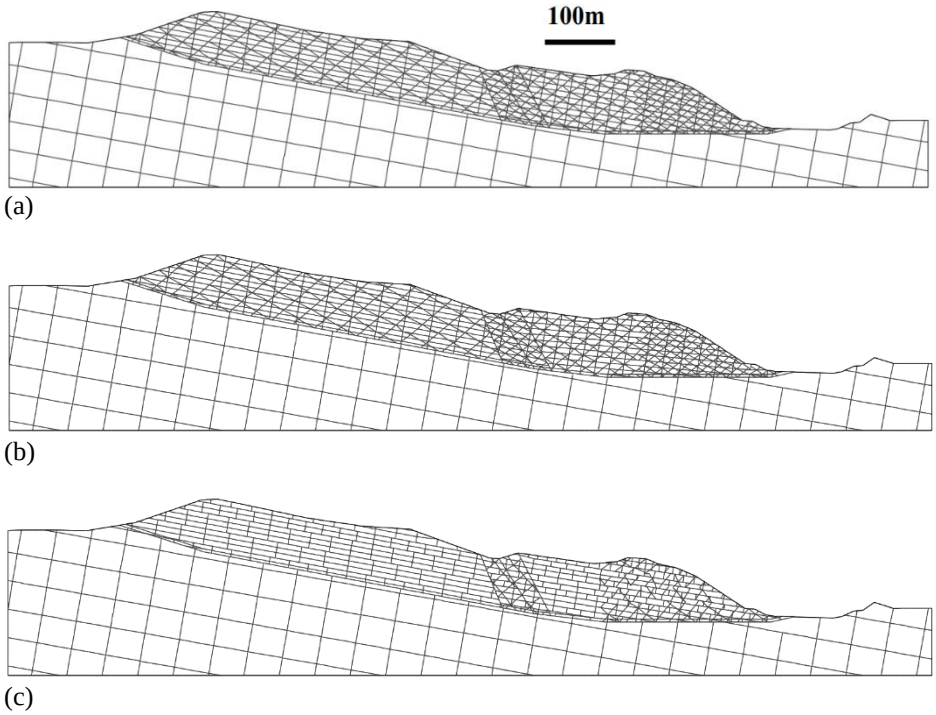

Figure 5.6: Joint patterns employed for the DEM modeling (a) Model –I ; (b) Model –II and (c) Model-III

The influence of drainage process facilitated by the lateral steep morphology of the slope between points G and H on the groundwater table has been understood from piezometric readings at B where a fall in water table was observed. Therefore in order to account this effect a relatively higher joint aperture (i.e. a_o=1.5mm and a_{res}= 0.5mm) has been adopted for both bedding and crossing joints of the model between point G and H (Figure 5.7). This assumption of higher permeability of the rock mass (i.e. between G-H) was found to give best-fit predictions as

observed from the piezometers. Initial aperture (a_o =1mm) and residual aperture (a_{res} = 0.5mm) have been assigned for all the rock joints located inside the bedrock and the slip surface. In all the analyses, the joint permeability factor k_j is held constant to 83.3$Pa^{-1}s^{-1}$ for each joints.

In the first set of flow analyses, the friction angle of the basal slip surface was kept constant to $\varphi = 9.5^o$. However, the influence of further block movement on groundwater profile was explored latter by considering a reduced value of the friction angle for the slip surfaces especially in the lower part, L-H.

Table 5.3: Hydraulic properties of joints considered for the moving rock mass between points F and G.

Joint sets	S (m)	EPM[a] (m/s)	a_o (mm)	a_{res} (mm)
Bedding planes (1)	8-16	$1.31x10^{-5}$	0.5	0.5
Joint set (2)	12-24	$4.34x10^{-6}$-$3.47x10^{-5}$	1	0.5
Joint set (3)	10-20	$5.21x10^{-6}$-$4.17x10^{-5}$	1	0.5
Join set (4)	20-40	$2.6x10^{-6}$-$2.08x10^{-5}$	1	0.5
Slip surface	----	----	1	0.5

where S= Spacing, a_o = initial aperture, a_{res}= Residual aperture,
[a] EPM refers Equivalent porous medium hydraulic permeability.

5.5.2 Hydraulic boundary conditions

Concerning the boundary conditions, special attention has been paid to the infiltration amount, and two possibilities will be discussed. In the first case (boundary condition A), a low boundary pore pressure of 0.1 and 0.2kPa is applied on the surface boundary between points E and H (Figure 5.7) in order to account for low and high infiltrated volumes respectively. The boundary pore pressure of 0.1kPa is kept on the surface (E-H) to predict the observed average piezometric level. While boundary pore pressure of 0.2kPa was considered on the same boundary to estimate the maximum groundwater level profile. In boundary condition-A, the joint pattern and magnitude of the imposed boundary pore pressure on the slope surface control infiltration magnitude and then the predicted groundwater table. Previous study conducted by Zangerl et al. (2003) applied a low boundary pore pressure 0.1kPa on the surface boundary to account for water infiltration effect to a fractured rock mass.

In the second case (boundary condition B), low flow rates between $0.1x10^{-5}$ - $2x10^{-5}$ m^3/s.m were applied directly to each boundary joint domains to account for water infiltration volumes (Figure 5.7). The magnitude of these low inflows (in the order of 10^{-5}) which has been

applied to a single joint had similar magnitude with the joint flow rate magnitude at steady state. Moreover, the applied inflow to a joint should not cause overpressure, which leads to local joint slip or opening so that the overall equilibrium condition of the model will be respected. In this boundary condition, the amount of total infiltration volume in the slope body depends on the number of domains associated with the joints lying in the boundary blocks and on the assigned flow rate magnitude to each joints.

Previous study by Cappa et al. (2004) also applied point inflow at a single joint domain in the range of 0.4-0.8x$10^{-3}$$m^3$/s.m in a complex less permeable slope formation to account for low infiltration volume concentrated in faults of the slope. However, in this study point inflows have been applied to each boundary domains so that a distributed infiltration volume can be accounted on the entire slope surface.

The magnitude of applied inflows also has been varied reasonably. Therefore, between E-D relatively lower inflows have been applied as compared to portion of the slope which runs from location of piezometer D to point H) so that good agreement between model predictions and observed piezometric readings can be obtained. It is most likely that the water table at piezometer cell D2 was located at lower depth since only few data were available by the piezometer. Thus, this is the reason for applying lower inflow volumes around the piezometer D.

It is worthwhile to remind that the total infiltrated volume evaluated by the DEM model, with the already scaled joint spacing does not give reasonable values, which can be directly compared with the expected infiltrated volume in the slope surface.

Therefore, the main target of the following sets of analyses is to reproduce the observed groundwater profile reasonably by employing acceptable values of hydraulic properties for the joint settings considered in the model. It is most likely that the infiltrated quantity employed to the model does not match with the expected physical infiltration volume.

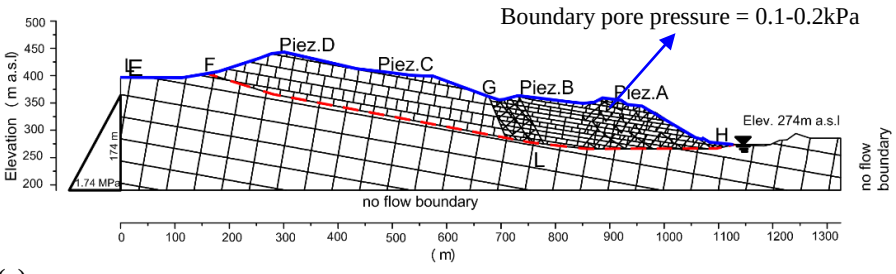

(a)

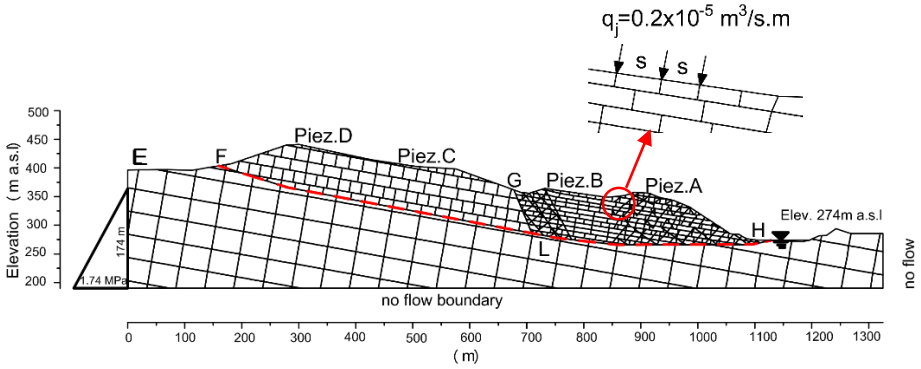

(b)

Figure 5.7: Considered boundary conditions for the flow analysis

5.5.3 Modeling protocol

In the modeling process, mechanical equilibrium was achieved first only by activating gravitational force in dry condition. Then to account for groundwater condition, a hydrostatic pore pressure distribution equal to groundwater table (363m a.s.l) is kept in the left boundary, obtained after extrapolating the observed piezometer levels at C and D. While in the valley, the reservoir level of 274 m a.s.l (empty reservoir) has been considered (Figure 5.7). Then, hydro-mechanical analysis has been performed under steady state flow condition keeping the above flow boundary conditions. At this phase of the analyses, the observed minimum piezometric readings have been predicted reasonably.

Then seepage process was activated from the surface to the model in two ways (i.e. using boundary condition A or boundary condition B) as already described previously to estimate maximum and average piezometric levels.

In the calibration process, the joint apertures at various regions of the model (upper, transition and toe part) have been determined by conducting preliminary analyses. Then the influence of the boundary condition especially the infiltration amount on the average and maximum predicted groundwater profile has been examined. The flow analyses have been evaluated considering Models-I, II and III to examine the influence of joint pattern on the estimated groundwater profiles.

Finally, the influence of further block movement, which was initiated by shear strength reduction of the basal slip surface (lower part), on the steady state pore pressure has been investigated. These last set of analyses

can simulate a special case when the increased aperture during block movement can cause further increment of infiltrated volume and consequently could alter the pore pressure regime inside the moving rock mass.

5.5.4 Estimation of groundwater profiles by DEM

Here the two different ways of applying inflow magnitude to a DEM model will be presented. The methods will be discussed by comparing predicted groundwater tables with the observed piezometric levels.

Boundary condition-A

Using model shown in Figure 5.7, infiltrated volumes of $1.7x10^{-3}$ $m^3/s.m$ have been calculated at steady state when a boundary pore pressure of 0.1kPa has been applied on the surface boundary. As it was expected, significant pore pressure increase was observed in the joints even from these low inflows (Figure 5.8). The model has predicted a higher water table between points G and H as compared to the observed average groundwater elevation. At piezometer C, the predicted water table has been relatively close to the average groundwater elevation.

When a relatively higher boundary pp of 0.2kPa was considered on the same surface boundary, infiltrated volumes of $2.9x10^{-3}$ $m^3/s.m$ have been evaluated. The water table predicted by the model keeping boundary pore pressure of 0.2kPa on the surface has been close to the maximum observed piezometric levels at piezometers A and B (Figure 5.8).

In the upper part (F-G), the model has underestimated the observed groundwater table (i.e. at piezometer C) as depicted in Figure 5.8. The predicted pore pressure distribution has been associated with the flow regime; higher water table has been obtained in the lower portion of the slope where flow distribution is higher (Figure 5.9). This is a result of higher hydraulic aperture and joint connectivity imposed to the lower part of the model.

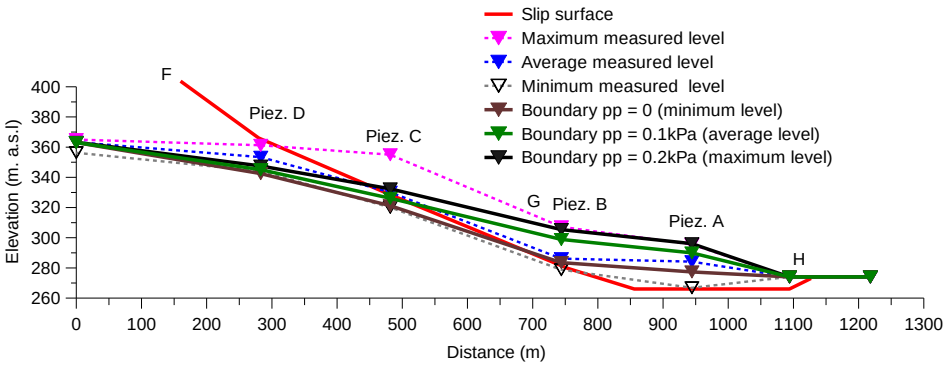

Figure 5.8: Water table profiles predicted by the model when boundary condition A is considered. Note that solid lines represent water tables estimated by the model considering boundary pore pressure of zero, 0.1kPa and 0.2kPa

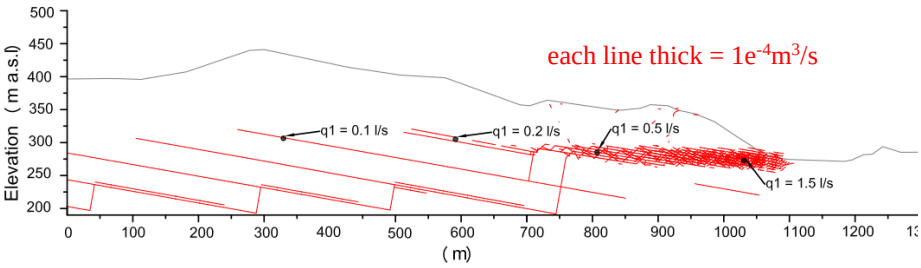

Figure 5.9: Flow distribution when boundary pp = 0.1kPa is applied on the surface boundary

Effect of joint patterns

The influence of joint patterns (i.e. Model-I, Model-II and Model-III) on the predicted water tables has been assessed. Infiltrated volumes of $2.09x10^{-3}$, $1.88x10^{-3}$ and $1.67x10^{-3}$ $m^3/s.m$ have been calculated respectively at steady state for Model-I, Model-II and Model-III when a boundary pore pressure of 0.1kPa has been applied on the surface boundary. It has been understood that the influence of the joint patters (Model-I, Model-II and Model-III) on the predicted water table keeping boundary pore pressure of 0.1kPa was negligible (Figure 5.10a). Though the influence of joint pattern on water table profile has also been still limited when a higher boundary pore pressure of 0.2kPa is considered, Model-I has showed slightly higher water table profile by around 5m and

10m at piezometers B and C respectively as compared to the other models (Figure 5.10b).

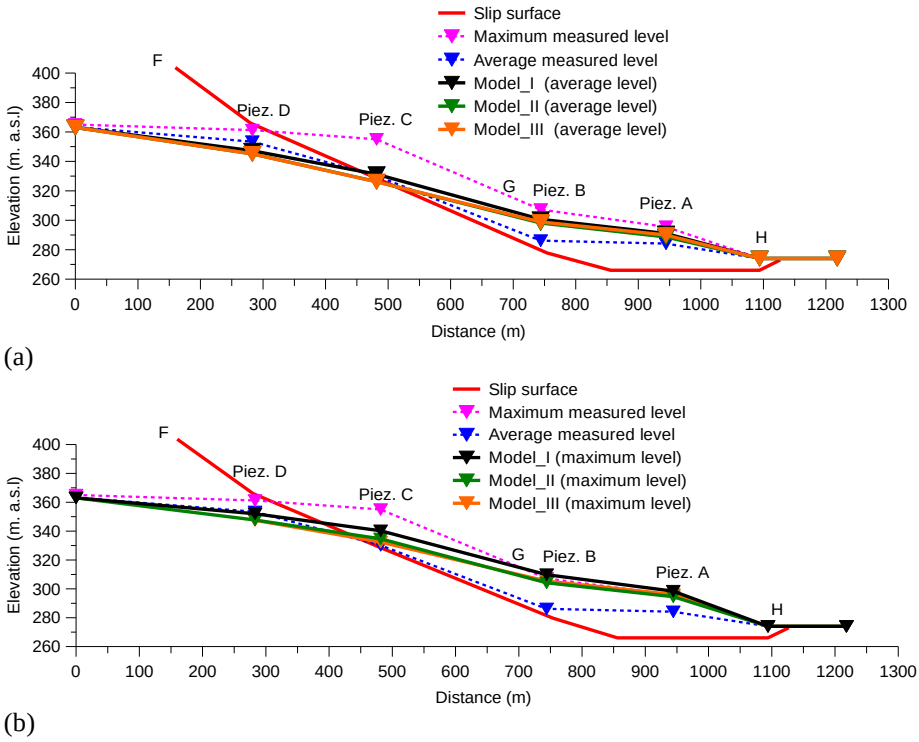

Figure 5.10: Influence of joint pattern on the estimated groundwater profiles (a) when boundary pore pressure of 0.1kPa is considered and (b) when boundary pp = 0.2kPa. Note that solid lines represent model estimations

Influence of joint apertures

The actual joint hydraulic aperture calculated by the model have been slightly higher than the initial hydraulic aperture for most of the joints located in the disturbed lower portion of the slope particularly near the slip surface. This increase of joint hydraulic aperture has been attributed to block movement and pore pressure developed inside joints. While in the upper portion of the slope, the hydraulic aperture of joints was slightly lower than the initial aperture because of limited closure. Since the closure of joint aperture up to the residual joint aperture value due to high effective stress has been limited, the influence of the residual joint aperture on permeability of the rock mass has been understood to be negligible. In addition, the applied joint stiffness also has direct influence on the magnitude of joint normal closure or opening.

The influence of joint apertures on the estimated groundwater tables has been explored further by considering three cases for the model portion between G and H (i.e. lower disturbed portion). Case-I with apertures (a_o = 2mm and a_{res} = 1mm), Case-II (a_o = 1.5mm and a_{res} = 0.5mm) and Case-III (a_o = 1.25mm and a_{res} = 0.625mm). The analyses have been performed by considering Model-I with persistent joint pattern and applying a low boundary pore pressure of 0.1kPa on the surface boundary between F and H. As it has been depicted in Figure 5.11, the predicted water table elevation has increased approximately by 5m as the aperture values has been reduced from Case II to Case-III. This highlights that the aperture values influence substantially the steady state groundwater profile. Case-I gives reasonable groundwater profile close to the observed average piezometer level (Figure 5.11).

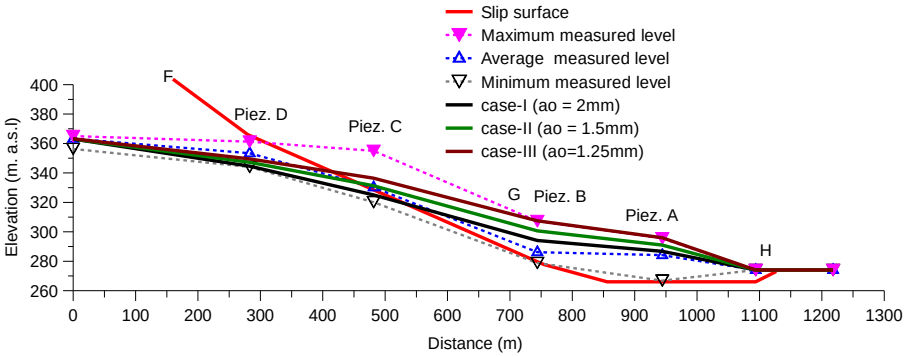

Figure 5.11: Influence of joint apertures on predicted groundwater profile. Boundary pp = 0.1kPa has been considered

Boundary condition-B

As it has been discussed before, joint inflows between $0.1x10^{-5}$-$3x10^{-5}$ $m^3/s.m$ have been applied to each boundary joints in the case of boundary condition-B. The magnitude of joint inflows has been varied accordingly to predict the observed water table profiles reasonably. In each of the joint patterns (Model-I, II and III) considered for the analyses, the predicted water table profile by the model has been controlled in two ways (i.e. using the inflow magnitude considered in a single joint and the location on the surface boundary where these joint inflows have been imposed). Therefore, the magnitude of inflow applied to the boundary joints was not equal.

For instance, in order to estimate the observed average water table, inflow magnitude of $0.1x10^{-5}m^3/s.m$ and $0.75x10^{-5}m^3/s.m$ has been applied at each boundary joints between points L-D and D-H respectively. Except in the lower part of the slope (G-H), the water table profile estimated by the model during this boundary condition has been close to the observed average water table (Figure 5.12). The maximum observed water table has been predicted reasonably by the model when inflow of $0.1x10^{-5}$ $m^3/s.m$ and $1.5x10^{-5}m^3/s.m$ has been applied between points (L-D) and (D-H) at each boundary joints respectively (Figure 5.12b).

Keeping the same hydraulic boundary condition, the influence of joint pattern on predicted water table profiles is still limited here too (Figure 5.12) as it has been understood by considering three DEM models with different joint patterns (Model-I, Model-II and Model-III).

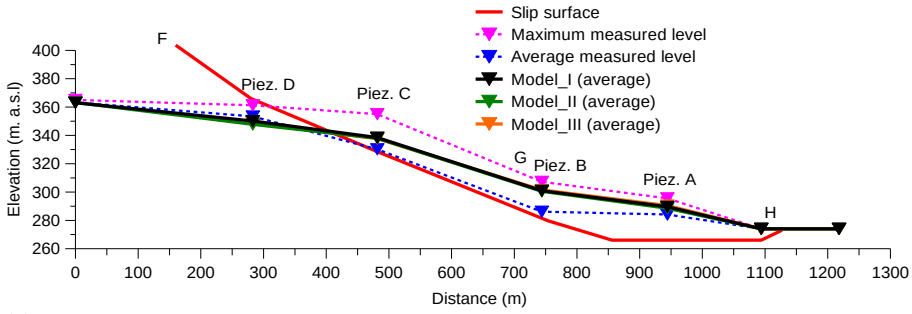

(a)

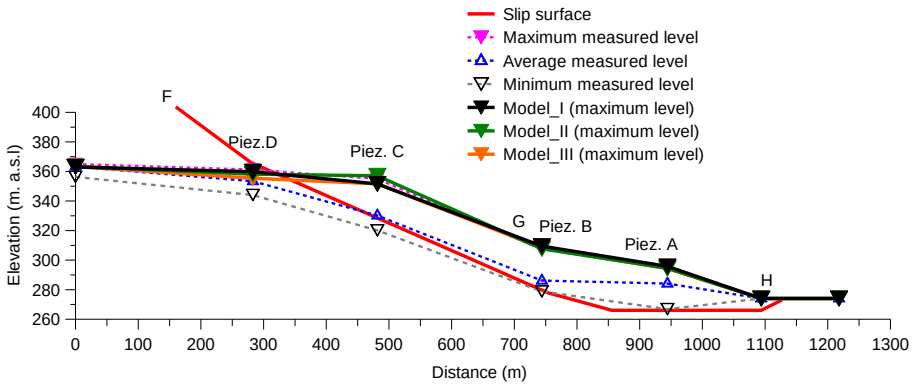

(b)

Figure 5.12: Predicted water table profiles when boundary condition B is considered (a) when total inflow of 1.37x10-3 m3/s m and (b) inflow of 2.7x10-3 m3/s m is applied on the model

Joint aperture in the disturbed slope portion (i.e. between G-H)

Further analyses have been carried out to enhance the previous model prediction of the observed groundwater profiles considering boundary condition-B. In these set of analyses, only the aperture of all the rock joints (i.e. bedding joints and crossing joints) found in lower moving rock mass (between G and H) has been increased to a_o = 2mm and a_{res} = 1mm. While the apertures of the joint sets found in the upper moving mass (i.e. between F and G) were kept identical to the previous analyses (Table 5.3).

Inflow quantities of $0.1x10^{-5}$ and $0.2x10^{-5}$ $m^3/s.m$ have been applied to the boundary joints lying between E-D and D-H slope portions respectively. The estimated groundwater profile after steady state considering this boundary condition is close to the observed average groundwater table (Figure 5.13). This is a good approximation as compared to the previous results shown in Figure 5.12.

The maximum piezometer level (Figure 5.13) has been estimated by employing higher flow rates, $0.1x10^{-5}$ $m^3/s.m$ and $2x10^{-5}$ $m^3/s.m$ for joints located in between L-D and D-H respectively.

Moreover, after steady state condition, the model has evaluated the total inflow of $3.60x10^{-3}$ $m^3/s.m$ and $0.38x10^{-3}$ $m^3/s.m$ during the average and maximum flow situations respectively. Figure 5.14 illustrates the flow rate distribution evaluated by the model at the average and maximum seepage conditions. The pore pressure distribution inside the joint at different parts of the model match with the flow rate distribution (Figure 5.15).

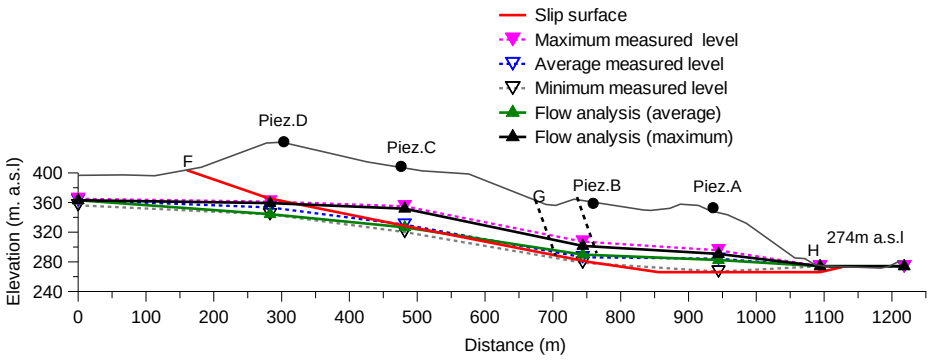

Figure 5.13: Predicted groundwater profiles estimated by employing high aperture (a_o=2mm and a_{res} = 1mm) for the slope portion between G-H)

Therefore, the best fit to the observed piezometer values can be obtained by employing a_o=2mm and a_{res}=1mm for the same region which covers the transition zone and the more disturbed portion of the moving rock mass.

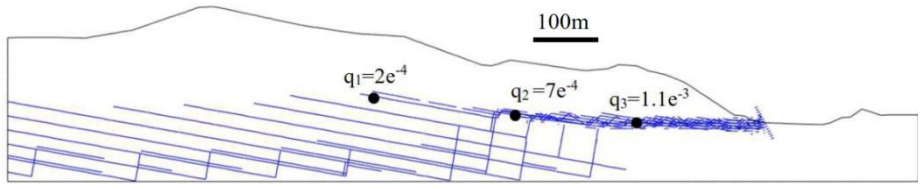

(a)

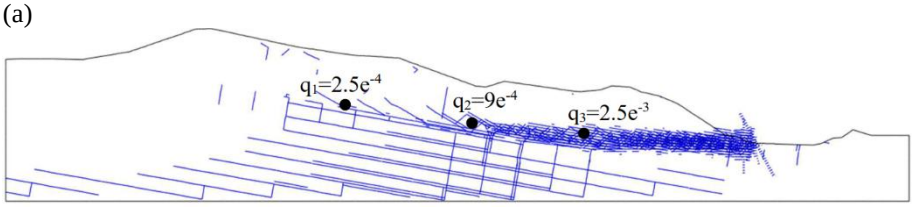

(b)

Figure 5.14: Flow rate distribution (units in m^3/s) obtained by the model. (a) when average piezometer level is estimated and (b) maximum piezometer level is predicted. Note that each line thick stands for $1x10^{-4}$ m^3/s

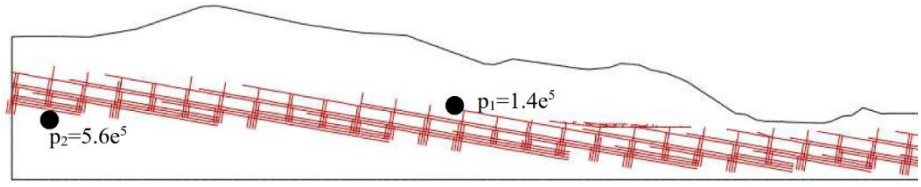

(a)

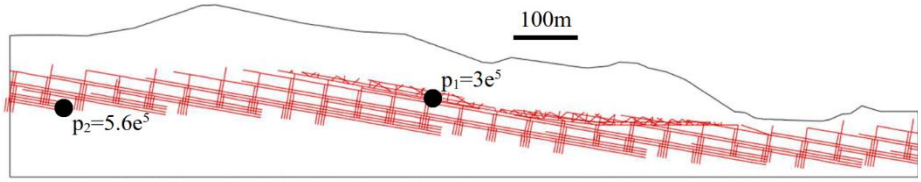

(b)

Figure 5.15: Pore pressure distribution (units in Pa) obtained by the model (a) when the average piezometer is predicted and (b) the maximum piezometer level is estimated. Each line thick stands for $1.4x10^5$ Pa. Note that pore pressures greater than $7x10^5$ Pa are not plotted here since they belong to the bedrock which are less important

Based on the above analyses, boundary condition-B can be preferred to predict the observed pore pressure though boundary condition-A should also be considered.

In general, after steady sate condition using the above boundary conditions applied on the surface of the model, a total of small infiltration volume in between 1.32-2.1x$10^{-3}$$m^3$/s.m on the slope surface has been evaluated. The water table predicted by the model considering the above small infiltration volumes has been close to the observed average groundwater table. Similarly, when total surface infiltration volumes between 2.6-3.7x$10^{-3}$$m^3$/s.m have been considered on the model the predicted water table by the model was close to the maximum observed piezometer level.

Besides this, the groundwater table evaluated by the model at piezometers B has been relatively higher as compared to the observed piezometer level (Figure 5.8, Figure 5.10). This local fall of the observed water table profile at piezometer B can be attributed to the influence of loosened rock mass and lateral steep slope morphology particularly in the lower portion of the slope which favors drainage process. Obviously, this cannot be accounted in 2D–analysis.

Previous studies showed that in less permeable joint networks small infiltration volume can induce significant pore pressure increases (Bonzanigo et al., 2001, Cappa et al., 2004).

Effect of block movements on boundary inflow

Further analyses were carried out to explore the influence of block movement on the steady pore pressure distribution. The friction angle of the lower slip surface (L-H) is further reduced from 8º to 7º by applying progressive shear strength reduction method keeping the same fluid boundary condition. The influence of further block movement on pore pressure distribution is limited when boundary condition-B is considered.

However, the predicted steady groundwater table changes slightly due to further block movements when boundary condition-A has been considered. In the staggered joint pattern (Model-III), the predicted groundwater table has increased by around 10m when friction angle of the basal slip surface gradually reduced from 8º to 7º. This rise of groundwater table has been attributed to the increase of infiltrated volume from 2.9x$10^{-3}$$m^3$/s.m to 3.8x$10^{-3}$$m^3$/s.m due to permeability increase caused by the joint shearing. It is worthwhile to remark that a small

aperture change affects significantly the flow magnitude due to the adopted cubic law.

The assumed staggered and chaotic joint pattern at the toe of the model (Model-III) favors an increase of joint aperture during mechanical deformation (Figure 5.17). A similar behavior was also observed in Model-II, but Model-I showed relatively lower pore pressure increases as compared to the other two model structures, which is obviously the consequence of joint pattern.

These model results showed that considering boundary pore pressure of 0.2kPa on the slope surface, the steady state pore pressure inside the slope can be changed as the friction angle of the lower part of basal slip surface (L-H) is reduced from 8 to 7^o keeping $\varphi = 9.5^o$ in the upper portion (F-L).

The model deformation (Figure 5.17), characterized mainly by block rotation is consistent with the developed pore pressure distribution due to the high recharge amount from the surface.

However, when a lower boundary pore pressure of 0.1kpa has been applied, the pore pressure increase because of further block movements has been limited. This is because of relatively low inflows, which have been generated on the surface from the assumed low boundary pore pressure.

The above model results can be essentially related only to the possibility of rise of groundwater table due to high increase of infiltration volume during slope deformation. The block movement has caused an increased in hydraulic aperture and consequently higher inflows have been generated from the surface.

However, the model has not reproduced the decrease in pore pressure due to domain volume increase during block movement since the considered boundary pore pressure of 0.2kPa on the surface provides continuous recharge to the slope depending on the model joint aperture. Besides this, pore pressure evaluated by the steady state mode of calculation is not sensitive to block volume change rather it is highly dependent on imposed fluid boundary condition.

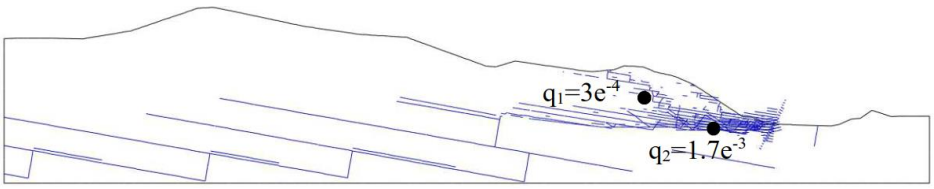

(a)

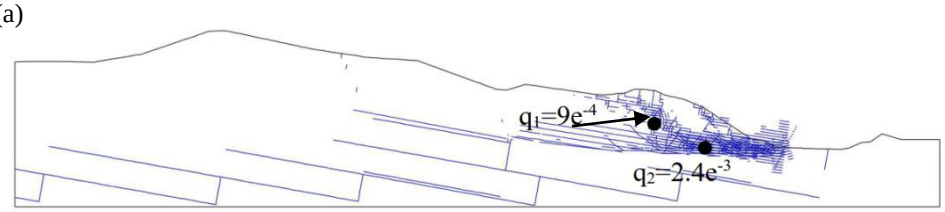

(b)

Figure 5.16: Flow rate distribution (a) when the basal friction angle, φ= 8° and (b) when φ =7°

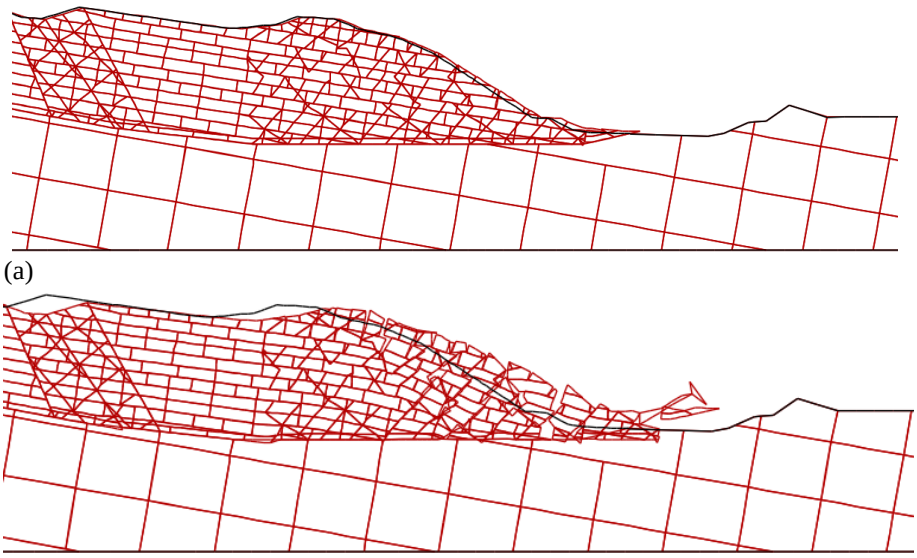

(a)

(b)

Figure 5.17: Model deformed shape (x400) (a) when φ=8° and (b) φ=7° to the lower slip surface

5.5.5 Stepwise filling of the reservoir

Previous flow analyses have been carried out keeping the reservoir level at 274m a.s.l (i.e. empty reservoir). Thus, it is worthwhile to explore the influence of stepwise filling of the reservoir level to pore pressure distribution and slope deformation.

The analyses can be carried out in two ways. On one hand, a horizontal water table can be assigned until the intersection of the average water table corresponding to a given reservoir level. On the other hand, flow analysis has been carried at each reservoir levels in order to obtain a

reasonable pore pressure distribution at steady state condition. In these two ways, subsequent filling of the dam has been performed until the maximum design level (i.e. 330m a.s.l) is reached. Comparisons could be easily made on the model response due to the two pressure regimes. In all the analyses, the basal friction angle of the slip surface is 9^{o}, which is a bit higher than the collapse limit evaluated in Chapter 4. In further studies, the limit friction angle has been evaluated at each reservoir levels by keeping the steady state pore pressure regime evaluated from flow calculation constant. These analyses will give us some useful insights about the influence of the filling of the reservoir on the mobilized friction angle of the slip surface.

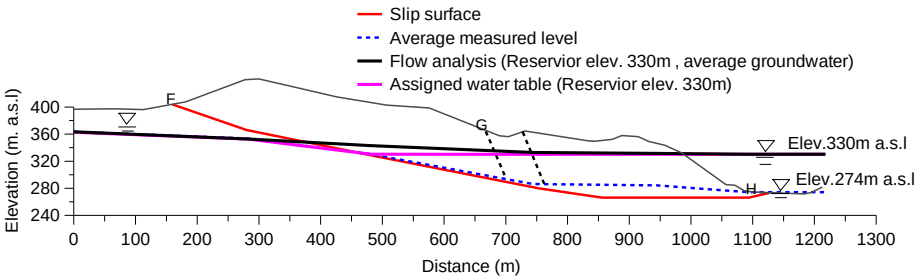

Figure 5.18: Groundwater levels corresponding to reservoir elevation of 330m a.s.l

The groundwater table predicted by the hydromechanical analyses is higher by around 10m near piezometer C, compared with the assigned water table (Figure 5.18). Obviously, the model with flow analyses gives more reasonable pore pressure distribution.

The “rate” of displacement increase (mm/m) due to a stepwise rise of the reservoir level has been evaluated. When the assigned water table is considered, the displacement rate started increasing since the assigned reservoir level is around 305m a.s.l and it becomes maximum when the filling is around elev. 325m a.s.l (Figure 5.19a).

While in the other case (i.e. considering pore pressure distribution evaluated by seepage analyses), the displacement rate starts continuously increasing as the reservoir level rises from 300m a.s.l till the maximum level (Figure 5.19).

Moreover, in both analyses (i.e. with flow and no flow analyses), the upper part (N8) moves quicker during high reservoir fillings as compared to the lower part (N3). This is obviously due to a reduction of effective stress in the upper portion (i.e. with a relatively steep slip surface); while

in the lower portion the mechanical pressure creates some restraint to the slope movement especially at the maximum design elevation.

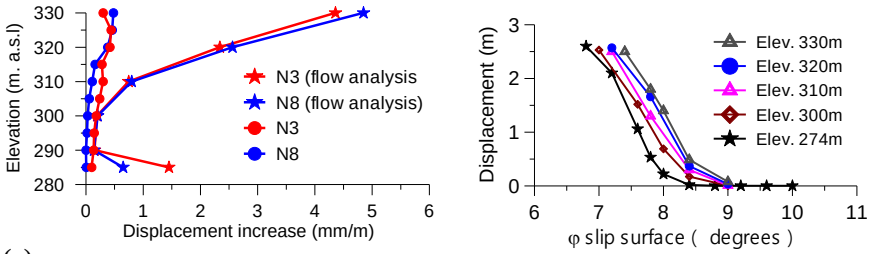

Figure 5.19: Horizontal displacement increase calculated for progressive increase of reservoir level keeping φ=9º for the slip surface (a) and horizontal displacement (N3) vs mobilized friction angle evaluated from hydromechanical analysis (b)

Figure 5.20 depicts the x-displacement evaluated in both cases taking in to account the reservoir level of 330m a.s.l., keeping φ =9º. Relatively higher displacements have been obtained when hydromechanical analyses is considered as compared to model displacements obtained by assigning a given water table. Certainly, this is the consequence of different pore pressure distribution in the two cases.

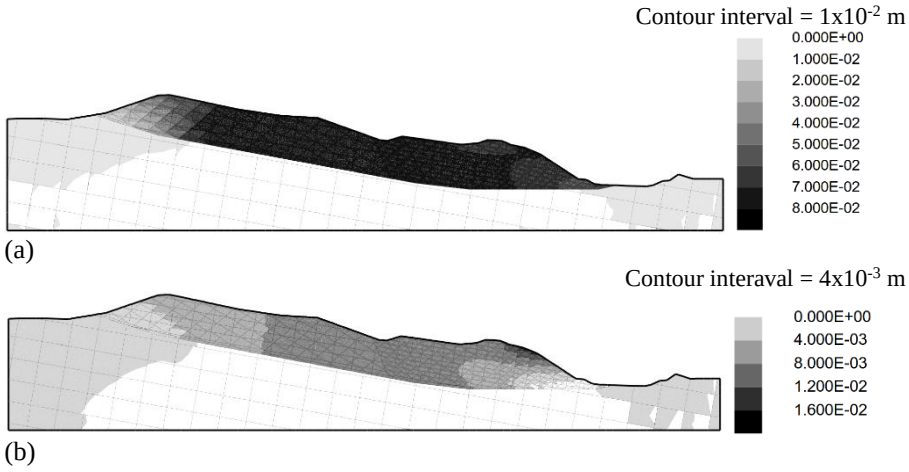

Figure 5.20: X-displacement (in m) at the filling level of 330m a.s.l when flow analyses is considered (a), when assigned water table is considered to the model (b) keeping φ = 9º for the entire slip surface.

In a separate study, keeping the already evaluated steady state pore pressure distribution during the step-wise filling of the dam, further

mechanical analyses have been carried out. These calculations are aimed to evaluate the effect of reservoir levels on the mobilized friction angle of the slip surface by employing the usual shear strength reduction steps. In fact, these type of analyses are similar to those presented in Chapter 4; however, hydromechanical analyses have been employed here.

Figure 5.19b illustrates that the reservoir level influences the horizontal displacement magnitude during shear strength reduction steps. When empty reservoir (elev. 274m a.s.l) has been considered, the plastic shear displacement occurs since $\varphi = 8.4^o$ while for the higher reservoir levels it occurs at $\varphi = 9^o$. The limit condition varies form $\varphi = 7.6^o$ to $\varphi = 8.4^o$ as the reservoir level changes from 274 to 330m a.s.l.

This results suggest that the mobilized friction angle changes in a narrow range which is around 0.8^o as the reservoir level increases from 274m to 330 m a.s.l. Similar study by Boon et al. (2014) also highlighted that the mobilized friction angle is less sensitive to reservoir level.

5.6 Flow analysis using continuum model

A continuum model using FLAC code has been developed to estimate the observed groundwater tables using steady flow analysis. Though such analyses have been performed earlier in a discontinuum medium, by UDEC code, thus the aim of the analyses herein is to discuss the continuum permeability of the rock mass and calibrate infiltration amount on the base of the observed water tables.

Moreover, the characterization of the rock mass permeability will be discussed reasonably by referring the outcomes of both continuum and discontinuum models.

In the following analyses, the influence of the permeability and fluid boundary conditions on the steady state groundwater table has been investigated.

Similar to the previous DEM analyses, in the first part of our flow analyses the reservoir level was kept empty (i.e. 274m a.s.l. see Figure 5.21) since our main target is to predict reasonably the observed groundwater profiles as measured by piezometer cells.

Then further flow analyses have been worked out by considering stepwise filling of the dam until the design level (i.e. 330m a.s.l) in order to predict the slope deformation responses due to the filling of the dam in the future operation period.

Modeling protocol

A hydrostatic boundary pore pressure has been kept in the left side with water table (elev. 363m a.s.l), obtained by extrapolating piezometer levels at C and D. While in the right side, the empty reservoir (elev. 274m a.s.l) has been considered. Moreover, the bottom boundary has been assumed impermeable.

Then, in order to account for the effect of water infiltration on pore pressure distribution inside the slope, infiltration amount in the range of $1\text{-}5.6\text{x}10^{-8}$ m/s has been applied to the boundary surface (i.e. between points F-H).

In the modeling procedure, steady state condition was recognized from flow balance at the boundaries of the model and the history of pore pressure at different parts of the model (i.e. toe, transition and upper parts). Some numerical difficulties were faced with regard to the computational time to reach a steady state solution. The elapsed time becomes higher when lower permeability and porosity values have been considered. Moreover, the calculation time is prolonged especially when the mesh size is reduced or the mode has high contrast in permeability. In order to overcome this difficulty, the fluid bulk modulus has been reduced reasonably to $2\text{x}10^{6}$ Pa.

In addition, the considered permeability of zones should be realistic (i.e. greater that the imposed inflow amount) so that the flow process can take place without inducing excessive pore pressure to the boundary zones.

Using preliminary analyses, the influence of permeability of the rock mass on the pore pressure distribution has been investigated by taking to account a given infiltration amount (i.e. $q = 1\text{x}10^{-8}$ m/s). Then keeping a reasonable permeability values at various slope regions, only the infiltration amount has been calibrated reasonably on the base of measured average and maximum piezometer levels.

5.6.1 Effect of rock mass permeability and infiltration amount

Before estimating the observed piezometric levels, some preliminary analyses have been carried out which are dedicated to explore the influence of rock mass permeability, k and infiltration amount, q on the steady state groundwater profile.

Considering infiltration rate of $1\text{x}10^{-8}$ m/s on the slope surface, three cases (i.e. case-1, case-2 and case-3) have been developed in order to assess the influence of the rock mass permeability on the steady state

groundwater table profile. The permeability of the base rock mass was kept in between $1x10^{-7}$ -$3x10^{-7}$ m/s.

In case-1, the permeability of the rock mass shown in Figure 5.21 has been considered. Here different permeability values for various slope regions has been applied. While a uniform permeability of $6x10^{-7}$ m/s and $8x10^{-7}$ m/s has been assumed for the entire moving mass for case-2 and case-3 respectively.

As it is expected in case-2 and case-3 (i.e. cases with uniform permeability), an increase of groundwater level was observed between F and H for most of the slope regions (Figure 5.22). In both cases (i.e. case-2 and case-3) the predicted groundwater level exceeds the observed maximum piezometeric level (Figure 5.22). The gradient of the water table change is lower than the observed value as we move between piezometer C and A (Figure 5.22). However, the water table predicted by the model considering case-1 has more or less similar gradient with the observed water tables (Figure 5.22). Therefore, it seems that if we adopt a uniform permeability for the entire moving mass (i.e. case-2 and case-3), the predicted water table profile is not realistic.

In a separate set of analyses, the influence of the permeability of the slope region between F-G on the estimated water table has been studied. In a similar fashion three cases (i.e. case-a, case-b and case-c) were considered. Therefore, keeping permeability of $3x10^{-6}$ m/s between G and H (i.e. disturbed portion), low permeability values of $6x10^{-7}$ m/s and $2x10^{-7}$ m/s has been implemented for the upper less disturbed portion (i.e. between F and G) in case-b and case-c respectively as shown in Figure 5.23. Case-a is identical to case-1 of the previous discussion.

Obviously, the estimated groundwater table increased only in the upper region when we apply a marked decrease of permeability (i.e. $2x10^{-7}$ m/s in case-c) (Figure 5.23). However, when permeability of $6x10^{-7}$ m/s (i.e. case-b) has been considered between F and G, the model does not show significant increase in groundwater profile (Figure 5.23).

Therefore, the groundwater profiles obtained by employing different permeability for various slope regions gives a realistic water table profiles with gradients similar to the observed profiles.

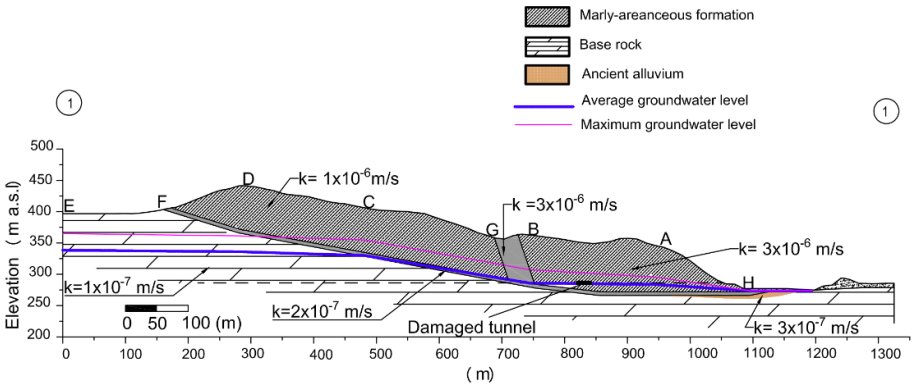

Figure 5.21: Considered permeability values for flow analyses in case1

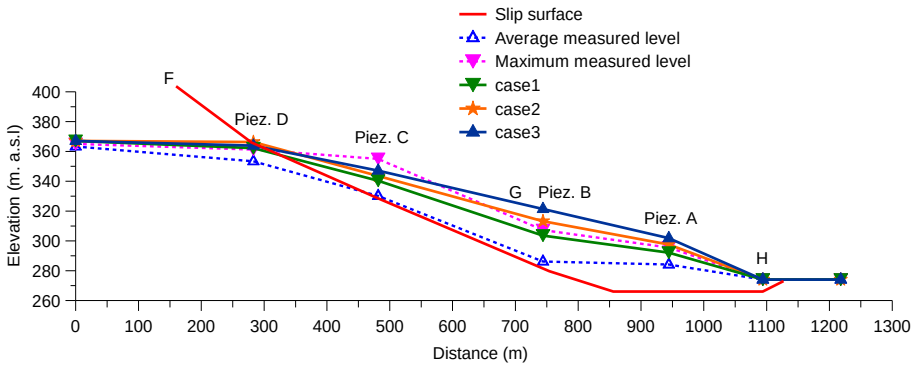

Figure 5.22: Influence of permeability on the estimated water table profiles

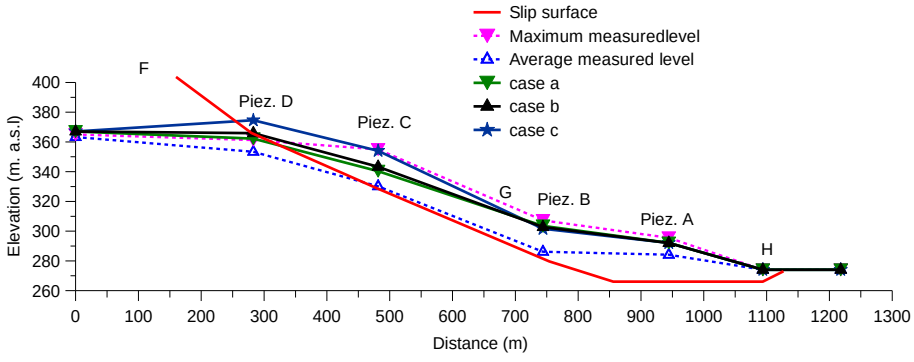

Figure 5.23: Effect of permeability of the upper region (between F and G) on the estimated groundwater tables

Infiltration amount

In a further parameter study, the influence of boundary condition (infiltration rate, q) on the steady state groundwater table profiles has been also studied using the permeability values shown in Figure 5.21. The groundwater table has increased significantly when a relatively higher infiltration rate of $1.5x10^{-8}$ m/s has been considered (Figure 5.24). Therefore, the predicted profiles are dependent on the imposed inflow amount.

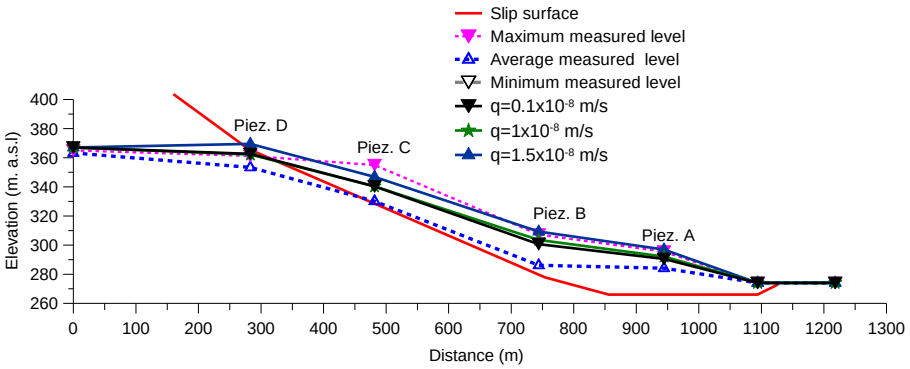

Figure 5.24: Influence of infiltration rate, q on the steady state groundwater profiles

5.6.2 Estimation of the observed piezometer levels

In this section, the observed groundwater profiles have been estimated considering reasonable rock mass permeability and infiltration rate, q.

From the previous preliminary analyses, it has been understood that permeability should be varied for different regions of the slope in order to obtain a reasonable groundwater profile. Thus, in the upper less disturbed portion (between points F and G) permeability value of $1x10^{-5}$ m/s has been considered while for the lower disturbed rock mass (between G and H) a relatively higher permeability value $3x10^{-5}$ m/s has been implemented. The slip surface and the bedrock have identical permeability of $2x10^{-6}$ m/s. The transition zone has permeability of $3x10^{-6}$ m/s.

Then keeping the above permeability values, a more reasonable infiltration rate of $1.4x10^{-8}$ m/s, which is about 50% of the average rainfall, has been applied on the slope surface.

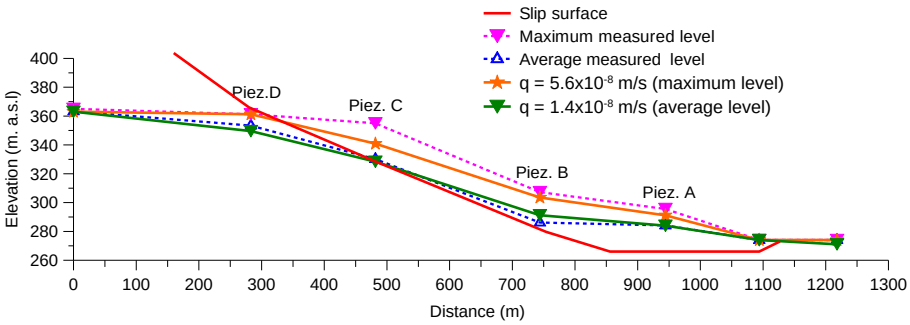

Figure 5.25: Maximum and average groundwater profiles predicted by the model at infiltration quantity, q = $5.6x10^{-8}$ m/s and q = $1.4x10^{-8}$ m/s respectively

After steady state condition, the predicted groundwater profile is close to the observed average groundwater profile (Figure 5.25). Then further analyses have been carried out considering higher infiltration rate in order to reproduce the observed maximum groundwater profile. Thus, infiltration amount of 5.6 $x10^{-8}$ m/s, which corresponds to 50% increase from the average rainfall amount, has been considered. Figure 5.25 shows that the predicted groundwater profile matches with the observed maximum piezometer level except for piezometer C, where the predicted water table is lower than the observed piezometer level.

Therefore, in order to improve the estimated maximum water table, a second set of analyses have been performed by changing only the permeability of the upper slope region (i.e. between F-G). Figure 5.26 depicts that the maximum groundwater profile has been predicted well when a lower permeability of $4x10^{-6}$ m/s has been implemented in the upper portion of the slope (i.e. between F and G). Figure 5.27 shows the pore pressure distributions during average and maximum flow conditions. Moreover, the flow rate distribution is higher in the lower disturbed portion of the slope (Figure 5.28).

Further analyses have carried out to assess the influence of the permeability of the transition zone on the predicted water table especially during high infiltration amount. In other words, the transition zone could create a barrier between the less disturbed upper slope portion (between F-G) and the more disturbed lower portion (between G-H) during flow process. Therefore, a lower permeability has been assigned to the transition zone when higher infiltration volume is considered. A limited influence on the pore pressure at piezometer C has been observed (Figure 5.29). However the pore pressure profile close to the upper side of the transition zone has been altered (Figure 5.30a). The influence of

permeability of the transition zone on pore pressure at piezometer C becomes negligible when lower infiltration volume has been considered (Figure 5.30b).

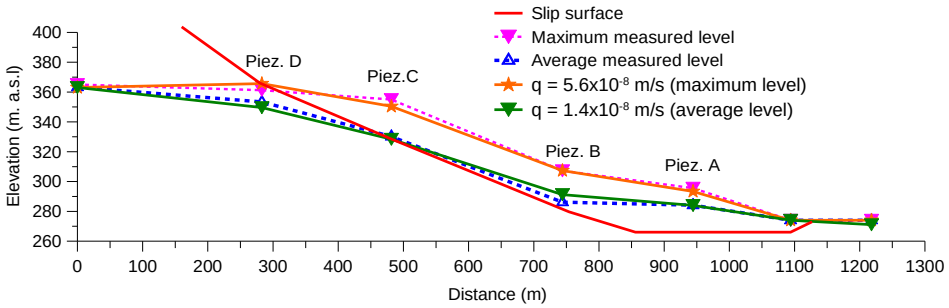

Figure 5.26: Water tables (average and maximum) estimated by the model considering a relatively lower permeability between F-G keeping the same boundary condition

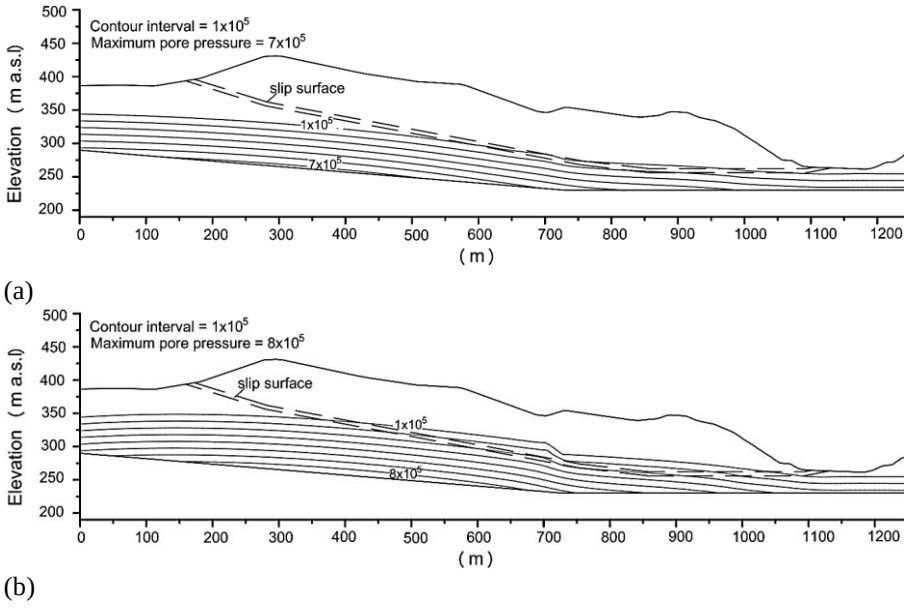

(a)

(b)

Figure 5.27: Pore pressure distribution (Pa) obtained by the model when the observed average groundwater level (a) and maximum groundwater level (b) has been estimated

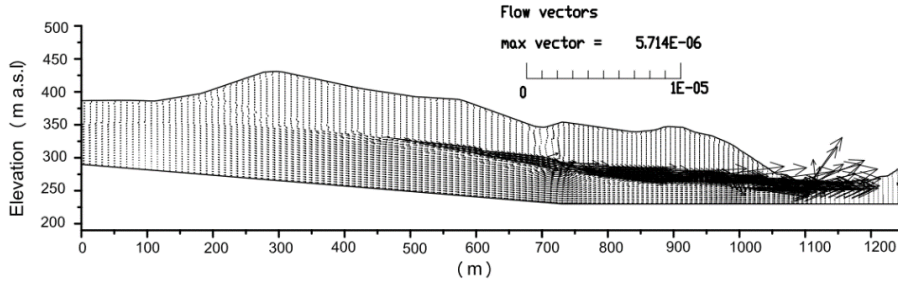

Figure 5.28: Flow rate distribution (in m^3/s) when the average groundwater is simulated by the model

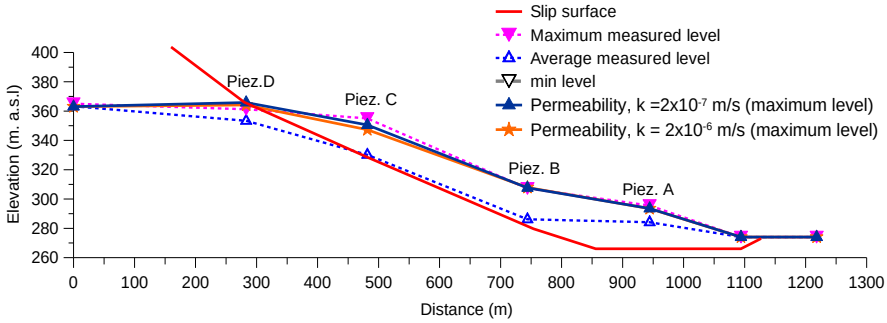

Figure 5.29: Influence of permeability of transition zone on the groundwater profile considering two cases (i.e. $k=2x10^{-7}$ m/s and $k= 2x10^{-6}$ m/s)

In general, after the above set of analyses using the continuum approach, a range of permeability values for different slope regions (i.e. upper, lower and slip surface) of the moving rock mass has been identified based on the estimated groundwater profiles. Thus, for the slope region between points F and G permeability in between $4x10^{-6}$ - $1x10^{-5}$ m/s seems reasonable. While for the more disturbed slope region (i.e. between G and H) permeability in between $6x10^{-6}$-$3x10^{-5}$ m/s and for the slip surfaces permeability in the range of $1x10^{-6}$-$2x10^{-6}$ m/s are admissible.

Moreover, infiltration rate of $1.4x10^{-8}$ m/s, which corresponds to about 50% of the average rainfall amount (i.e. 50% of $2.95x10^{-8}$ m/s), gives reasonable average groundwater table profile as it was observed from piezometric measurements; while higher infiltration rate, $5.6x10^{-8}$ m/s, which is 50% higher than the average rainfall, gives the observed maximum piezometer level.

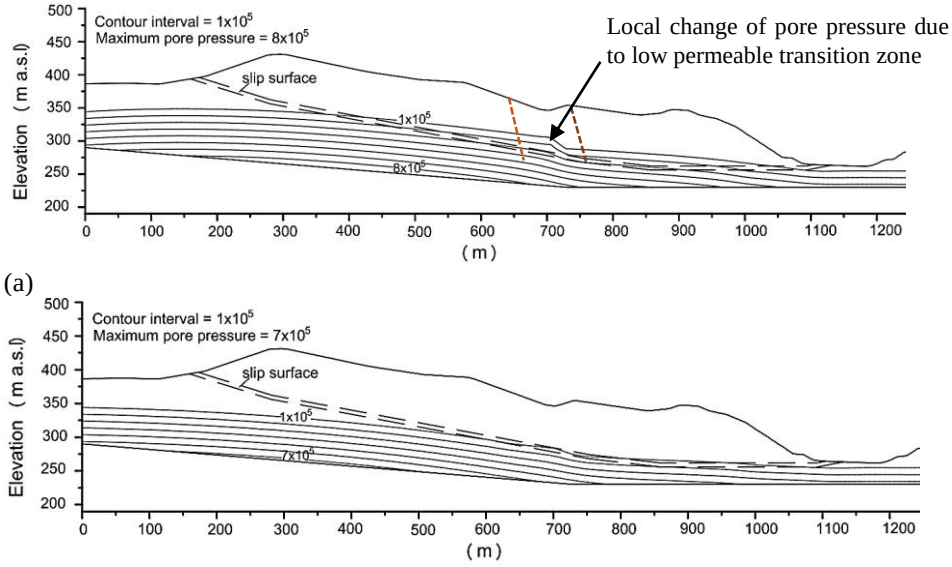

Figure 5.30: Pore pressure distribution (Pa) obtained when the permeability of the transition zone is reduced to $2x10^{-7}$ m/s keeping inflow of $5.6x10^{-8}$ m/s (a) and inflow of $1.4x10^{-8}$ m/s (b)

5.6.3 Progressive filling of the reservoir

Since in the previous analyses the reservoir level has been kept low (i.e. 274m a.s.l.), it is worthwhile to predict the influence of the progressive filling of the dam until the maximum design level (i.e. 330m a.s.l) on the pore pressure distribution and slope deformation responses. Thus, theses analyses will give us some useful insights about the slope behavior when the dam will begin operation. In fact, these analyses have been performed with the DEM approach (see Section 5.4.5). Moreover, the influence of reservoir filling on the mobilized friction angle of the slip surface has been investigated here too.

In the calculation steps, keeping the already estimated average water table inside the slope from previous flow analysis, the stepwise filling of the dam has been carried out by employing hydromechanical analysis. Thus, at each new reservoir level seepage analysis has been performed until steady state condition is reached.

It seems that once the level of 295m a.s.l has reached the displacement increase becomes significant and latter slows down when the maximum level (elev. 330m) becomes effective (Figure 5.32b).

In order to identify the collapse friction angle of the basal slip surface for a given reservoir level, only mechanical calculation have been carried out employing the usual strength reduction method keeping the pore pressure distribution evaluated from the flow analyses constant. The mobilized friction angle changes in a narrow range from 8.45 to 8.7° as the reservoir level increases from 285m to 330 m a.s.l (Figure 5.32).

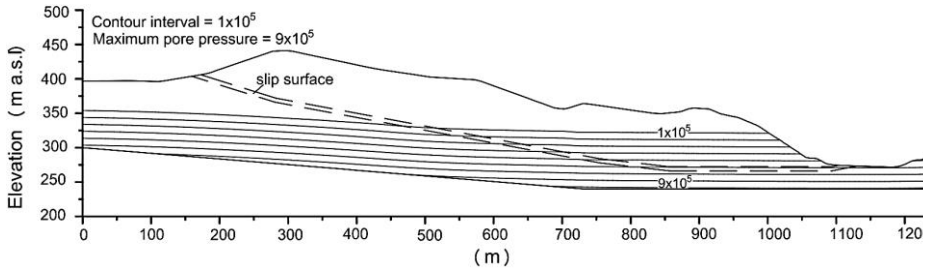

Figure 5.31: Pore pressure distribution (Pa) at steady state condition when a maximum filling level of 330m a.s.l has been considered

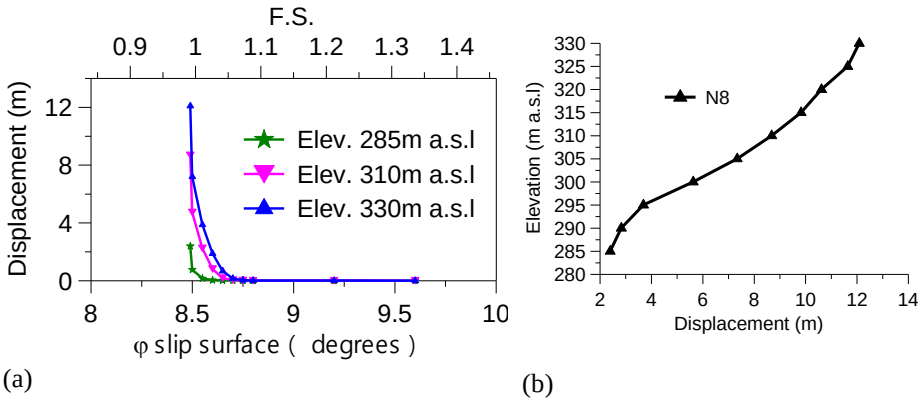

Figure 5.32: (a) Horizontal displacement (N8) vs basal friction angle obtained using shear strength reduction at different reservoir levels and (b) reservoir elevation vs displacement considering φ=8.45° (i.e. collapse friction angle)

Figure 5.33 depicts the horizontal slope displacement induced by the filling of the reservoir at different friction angle of the basal slip surface. It has been understood that if the friction angle of the basal slip surface is lower than 8.7°, the rise of the reservoir level induces a marked displacement increase. Moreover, it is worthwhile to remark the rise of the dam level causes significant displacement (i.e. collapse) at lower mobilized friction angle close to the collapse limit (8.45°).

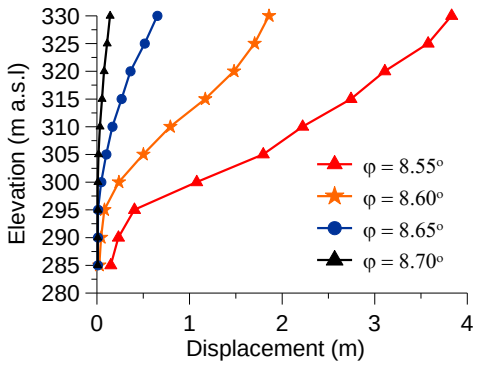

Figure 5.33: Reservoir level vs displacement for N3 when the friction angle of the basal slip surface changes

Stress path during filling of the dam

The stress-state changes during filling of the reservoir has been studied by considering several controlling points located in the upper, transition and lower part of the sliding mass (Figure 5.34). Since the filling of the dam has been performed after the shear strength of the basal slip surface is reduced close to its residual strength (φ=8.8°). Thus, it is obvious that most of the points located on inclined part of the slip surface are close to the plastic yield limit (Figure 5.35). Points 11 is slightly going towards the elastic zone as the reservoir level increases and similar behavior was also observed at point 14. However, points lying in the upper slip surface remain close to the plastic yield limit. In fact, during filling of the dam, the upper part displaces more as compared to the lower part.

Figure 5.36 shows the deformed shape of the slope when the reservoir level reaches to 300m a.s.l. The upper part deforms parallel to the slip surface while the lower part tends to show also upward deformation due to the higher pore pressure developed by the filling.

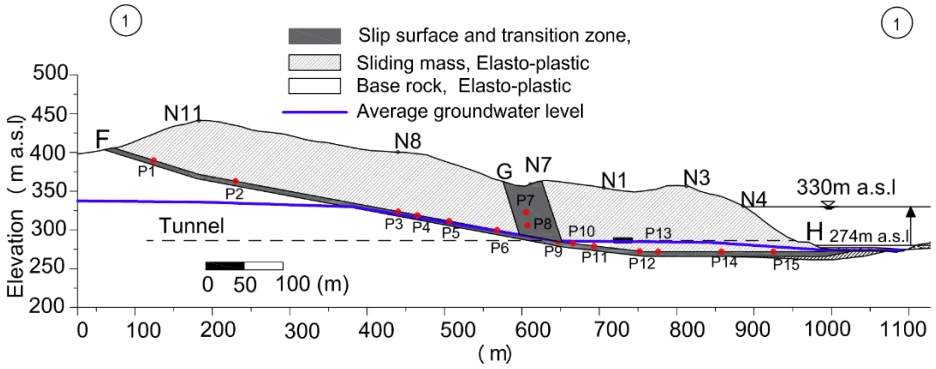

Figure 5.34: Location of points (P1---P15) along the basal slip surface used to examine the stress changes during gradual filling of the dam from 280m a.s.l to maximum design level of 330m a.s.l

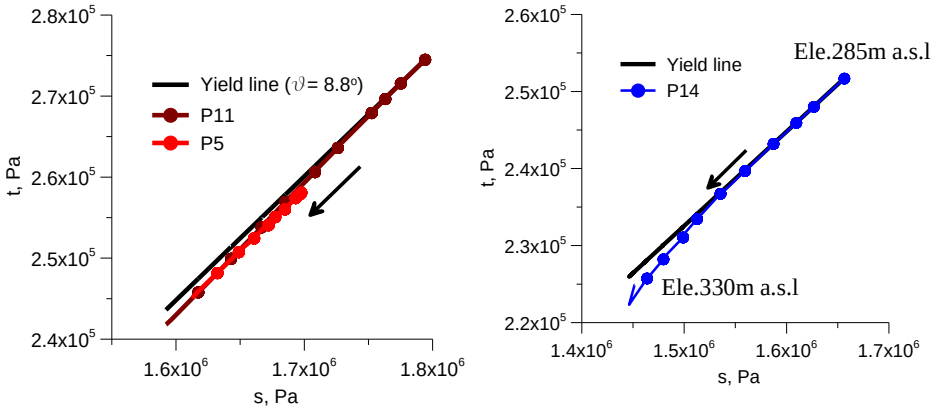

Figure 5.35: Stress-path plots in the t-s stress space during gradual filling of the dam. Note that the arrow shows the stress-path during the gradual filling of the dam from 285m a.s.l to 330m a s.l

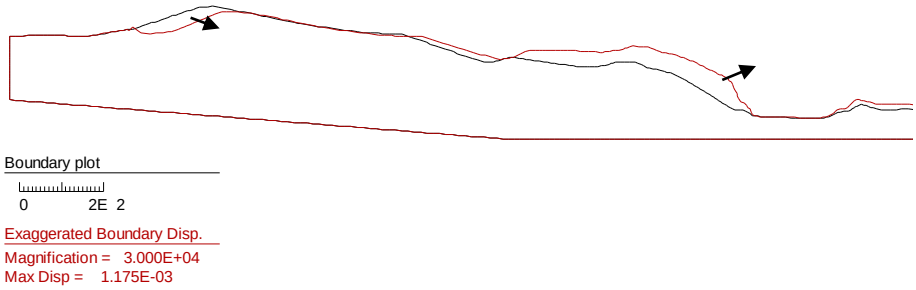

Figure 5.36: Deformed shape of the slope during filling level of 300m a.s.l, the red line shows magnified shape of the deformed slope and the arrows indicate the direction of the deformation keeping the basal friction angle equals 8.8^{o}

5.7 Conclusions

Based on the above sets of numerical analyses, some useful insights about the hydro-mechanical behavior of the slope have been understood using the continuum and discontinuum models.

Though the employed joint patterns (staggered or persistent) have limited influence on the estimated groundwater profiles, the joint hydraulic apertures have significant effect on model results.

Moreover, the joint apertures should vary in various model regions (upper, transition and lower parts). Therefore, in order to describe better the observed piezometer levels, the lower disturbed portion including the transition zone (G-H) need to have higher apertures as compared to the upper moving mass (F-G). This higher permeability between G-H seems in agreement with the expected rock mass behavior, which is loosened by the ongoing deformation, as understood from borehole loggings and geophysical investigations. Besides this, the higher aperture employed between G-H also accounts the influence of drainage favored by the lateral steep E and W flanks on the observed piezometer level, particularly at B.

The influence of the infiltration amount to steady state pore pressure has been considered in two ways: by employing low boundary pore pressure on the surface (Boundary condition-A) to trigger inflows or applying directly joint inflows to the boundary joints (Boundary condition-B), results from this boundary condition are relatively reasonable. Certainly, the applied total inflow in the DEM model would not match with the expected total inflow quantity since the model considers only few of the actual joints expected in the field. The observed

maximum and average piezometer levels are reasonably estimated by calibrating the joint inflows (Boundary condition-B) or imposed boundary pore pressure (Boundary condition-A) keeping a given model structure and joint apertures.

In a separate numerical modeling, the continuum model via FLAC code has been considered to complement the previous DEM results.

Contrary to the discontinuum model, the infiltration amount employed to the slope surface using continuum model could be related to the expected infiltration amount. Using empirical models, infiltration rate of $1.4x10^{-8}$ m/s, which is 50% of average rainfall, has been evaluated. By applying this inflow amount, the observed average water level has been reproduced reasonably. The maximum observed piezometer level can be easily estimated just by considering 50% increase of the average rainfall amount (i.e. $5.6x10^{-8}$ m/s).

In further analyses, the influence of progressive filling of the dam on the groundwater profile and slope deformation response has been discussed in both continuum and discontinuum approaches. The upper moving part shows higher deformation as compared to the lower part especially at high reservoir levels due to the reduction of effective stress by the filling process. The mechanical pressure tries to slow down the lower part of the model especially at the maximum reservior level. Moreover, the mobilized friction angle is less influenced by reservoir level.

Chapter 6

6 Analysis of time dependent behavior

6.1 Introduction

In the first part of this chapter, a review of creep models suitable for describing the time dependent behavior of a slow movement has been presented.

The time dependent behavior of the moving slope has been studied using the Burgers –Mohr Coulomb model (CVISC). The creep effect has been considered only to the basal shearing surface and the transition zone. On the basis of displacement trends recorded in the field, the creep model parameters have been calibrated.

In separate numerical analyses, a user defined viscoplastic model formulated on the base of the Perzyna's overstress law has been considered too. To this aim, modifications of the existing creep models have been carried out using the internal programming language, FISH. The new model allows to assess the influence of loading changes (e.g. reservoir level increase) and reduction of friction angle on the steady state velocity.

6.2 Review on creep behaviors

6.2.1 Characteristics of slope movement

Slope movement is a complex phenomenon, which depends on geology, geomorphology, hydrology, hydrogeology, and soil or rock mechanics of the study area. The interaction of these factors also determines the movement behavior. Slopes evolve through time and, the deformation field is a direct consequence of changes of static and hydraulic boundary conditions.

Many natural or man-made slopes show continuous movements with time at different deformation rates, (movement could be sometimes stationary, with constant velocity, accelerating or decelerating). However, most of these movements are attributed to creep or secondary consolidation, in which a visco-plastic flow of the soil or rock materials occurs under constant stresses. According to Cruden and Varnes (1996) classification, the velocity of slow moving slopes is around 16mm/y.

Deformation of deep-seated slopes affects lifelines (e.g. tunnels, dams, roads etc…) located near the moving slope. Some particular study (Lembo- Fazio et al., 1997) showed the influence of slow deformation of high rock slopes to hydraulic structures by considering two hydropower plants (i.e. Lanzanda and Grosotto) in the Adda valley, northern Italy.

Monitoring data, (for instance, inclinometer profiles) may assist to understand the deformation behavior of creeping slopes. Hence, the slope movement may occur mainly along a localized shearing zone, which exhibits creeping behavior while the rock mass above it moves like a rigid body (Figure 6.1). In this aspect, the deformation is concentrated along a limited thickness of interface located between the moving rigid rock mass and the underlying base rock. Thus, in the modeling of the slope movement it is more reasonable to allocate the viscous behavior only to the creeping zone (Ter-Stepanian, 1963). Chan (1999) discussed slope movements which occur as consequence of creep, strain rate effects and degradation of shear strength by considering some case histories.

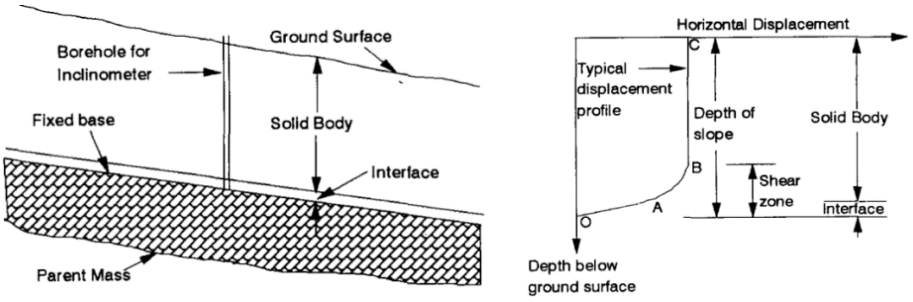

(a) (b)

Figure 6.1: Schematic representation of an idealized creeping slope (a) and deformation profile (b) (after Desai et al., 1995)

Slow moving slopes exhibit creeping behavior and a set of suitable models for analyzing slow moving slopes were revised by previous study (Vulliet and Hutter, 1988). Desai et al. (1995) discussed viscoplastic modeling of slowly moving landslides using an interface material Figure 6.1).

Previous studies (Corominas et al., 2005, Fernández-Merodo et al., 2012) showed that the observed slope creep movements can be well reproduced using numerical models by taking in to account the viscous effect.

Several studies discussed the influence of groundwater fluctuations on the viscous behaviour of slow moving slopes using visco-plastic models formulated on the base of Bingham body (Angeli et al., 1996, Forlati et al., 2001, Corominas et al., 2005, Maugeri et al., 2006, van Asch et al., 2007, Conte and Troncone 2011).

The evolution of a constrained creeping slopes was studied by Puzrin and Schmid (2011).

6.2.2 Deformation behavior during creep

Creep is peculiar form of deformation to soft and jointed rocks under significant in situ stresses. The creep response of most rocks or rock masses showed that under sustained load they yield excessively if they are subjected to a load beyond a certain threshold. Usually the time dependent behavior can include primary (stage I), secondary (steady state) creep (stage II) and tertiary creep (stage III) as shown in (Figure 6.2).

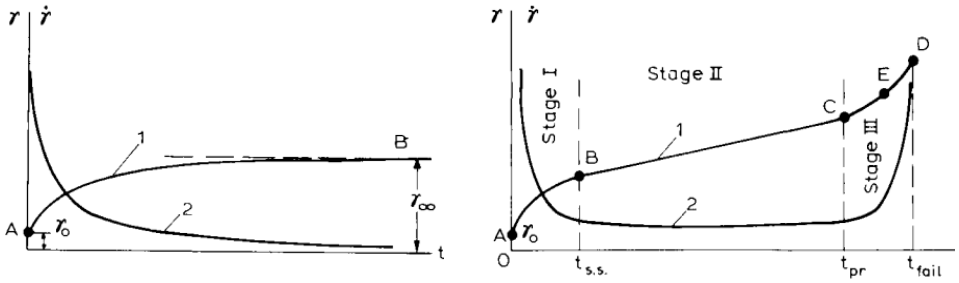

Figure 6.2: Deformation versus time (a) attenuating creep; (b) non-attenuating creep (after Vyalov, 1986)

The primary creep is characterized by decreasing strain rate and secondary (steady state) creep is characterized by a constant strain rate. While the tertiary creep is characterized by an increasing strain rate and it progressively approaches to collapse or creep failure. The viscoelastic strains in primary creep can be recovered fully while the strains in the steady state creep (stage II) and tertiary creep (stage III) are plastic and totally irrecoverable (Figure 6.3).

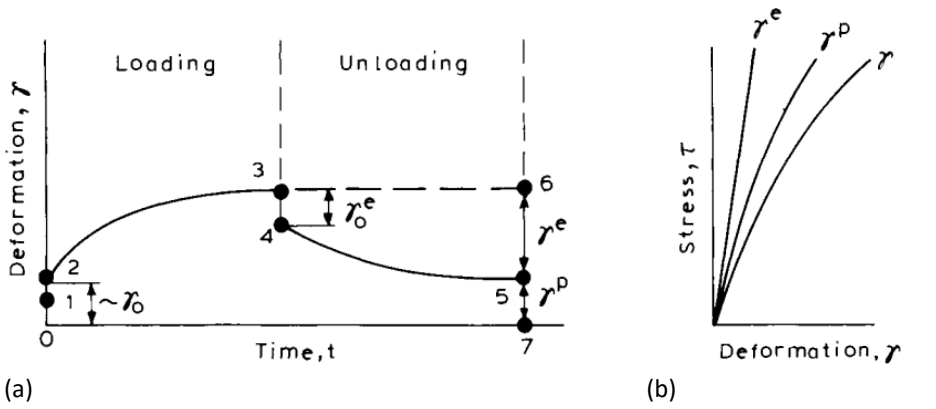

Figure 6.3: Deformation vs time which includes recoverable (γ^e), residual (γ^p) and (a) and stress vs deformation curve (b) (after Vyalov, 1986)

Figure 6.4 shows experimental results associated to creep of plastic clays and soft rocks reported by Vyalov (1986). As we can see easily the three stages of the creep process were reproduced. At low stress levels the primary creep persists while for high stress levels close to the yield limit the steady and tertiary creep phases have been manifested.

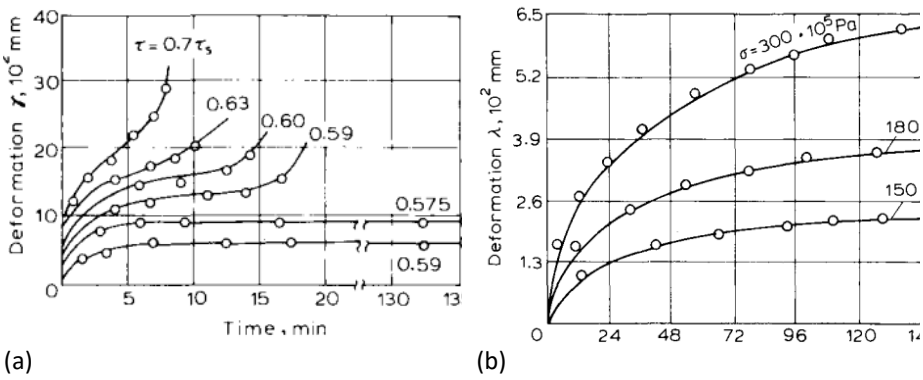

Figure 6.4: Creep curves of (a) plastic clays (b) uniaxial compression test of a fine grained sandstone in saturated condition (Vyalov, 1986)

6.3 Models for creep analysis

6.3.1 Rheological models

In this section, the concept of the rheological models and their parameters has been discussed by considering a uniaxial loading condition and then

extended to the general stress state condition. Rheological models are formulated by combining the basic elements such as Hookean element (spring), Newtonian element (viscous dashpot) and Saint-Venant's (slider) element.

The Hookean element (Figure 6.5), in which stress-strain obey the Hook law, represent the elastic response of the medium being studied. If we consider that the spring has shear modulus *G* and subjected to a shear stress τ the following relation can be easily formed from Hook's law.

$$\tau = G\gamma \tag{6.1}$$

where G is the constant of proportion between stress, τ and strain, γ in the Hookean element.

Newton model

In the Newton model the applied shear load, τ is linearly proportional to the shear strain rate as

$$\tau = \eta\dot{\gamma} \tag{6.2}$$

where τ is the applied shear load in Pa, η is the dynamic viscosity (Pa.s) and $\dot{\gamma}$ is the shear strain rate. If we consider a uniaxial loading with axial strain ε_{axial} the distortion γ can be related by

$$\gamma = (1+\nu)\varepsilon_{axial} \tag{6.3}$$

where ν is the poisson's ratio of the material. Then the axial stress can be given as

$$\sigma_{axial} = 2\eta(1+\nu)\dot{\varepsilon}_{axial} \tag{6.4}$$

Thus the axial strain at time, t can be evaluated by Equation (6.5) which shows that the creep strain is directly related to the applied load and inversely related to the dynamic viscosity value.

$$\varepsilon(t) = \frac{\sigma_{axial}}{2\eta(1+\nu)}t \tag{6.5}$$

Equation (6.5) can be described in a tensor form as

$$s_{ij} = 2\eta\dot{e}_{ij} \tag{6.6}$$

where s_{ij} is the deviatoric stress, $\dot{e}_{ij}$ is the deviatoric viscous strain rate and η is the dynamic viscosity of the material.

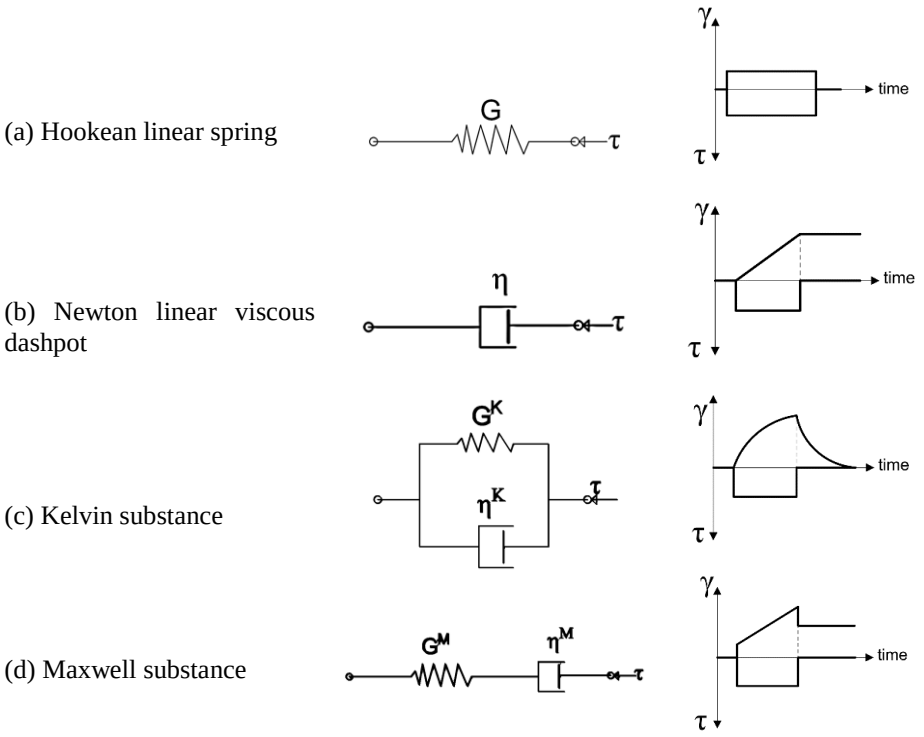

Figure 6.5: Summary of basic Rheological models, their schematic representations and time dependent responses

Maxwell model

In this model the spring element is connected in series to the dashpot to represent a Maxwell or elasto-viscous substance (Figure 6.5d). Suppose a Maxwell material with elastic property (bulk modulus *K*) and viscoelastic properties (dynamic viscosity η^M and shear modulus G^M) is subjected to a shear stress, τ , then the shear strain rate, $\dot{\gamma}$ can be evaluated as

$$\dot{\gamma} = \frac{\dot{\tau}}{G^M} + \frac{\tau}{\eta^M} \tag{6.7}$$

where γ is the total shear strain from both the spring and dashpot.

If an incremental axial σ_1 stress is imposed at time=0 and maintained thereafter, the axial strain ε_1 can be given as

$$\varepsilon_1 = \frac{\sigma_1}{9K} + \frac{\sigma_1}{3G^M} + \frac{\sigma_1 t}{3\eta^M} \tag{6.8}$$

Note that the term $\frac{\sigma_1}{9K} + \frac{\sigma_1}{3G^M}$ represents the elastic solution during the axial compression.

Moreover, Equation (6.8) describes the total axial strain ε_1 in a Maxwell substance which constitutes an instantaneous elastic response and a long-term viscous response controlled by the viscosity η^M parameter.

The Maxwell deviatoric strain rate $\dot{e}_{ij}^M$ can be defined interms of stress tensor as

$$\dot{e}_{ij}^M = \frac{\dot{s}_{ij}}{2G^M} + \frac{s_{ij}}{2\eta^M} \tag{6.9}$$

where s_{ij} is the deviatoric stress, G^M is the shear modulus and η^M is the Maxwell viscosity.

Kelvin Model

In the Kelvin model the spring and the dashpot are connected in parallel (Figure 6.5c), the total stress is the sum of stress carried by the spring and the dashpot. Consider a rock mass with elastic property in compression (bulk modulus K) and behaves as a Kelvin solid in shear with viscoelasticity properties (viscosity, η^K and shear modulus, G^K) is subjected to a shear stress increment, τ. Then the shear stress, τ can be given as

$$\tau = G^K \gamma + \eta^K \dot{\gamma} \tag{6.10}$$

Suppose a uniaxial creep test on a Kelvin body subjected to an incremental axial stress σ_1 at time t = 0 and maintained constant thereafter, the axial stain ε_1 can be evaluated as

$$\varepsilon_1 = \frac{\sigma_1}{9K} + \frac{\sigma_1}{3G^K}\left[1 - \exp\left(-G^K t / \eta^K\right)\right] \tag{6.11}$$

The kelvin model can describe the primary creep behavior (i.e. creep deformation with a decreasing strain rate).

The deviatoric Kelvin strain rate $\dot{e}_{ij}^{K}$ can be defined interms of stress tensor as

$$s_{ij} = 2\eta^{K}\dot{e}_{ij}^{K} + 2G^{K}e_{ij}^{K} \tag{6.12}$$

where s_{ij} is the deviatoric stress, G^{k} is the Kelvin shear modulus and η^{K} is the dynamic viscosity.

Burgers visco-elastic model

Burgers visco elastic model is formed by combining Kelvin and Maxwell components in series as shown in Figure 6.6.

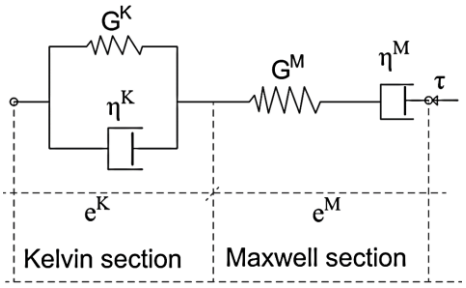

Figure 6.6: Burgers model representation

The creep strain rates can be described as the sum of Kelvin and Maxwell components

$$\dot{e}_{ij} = \dot{e}_{ij}^{K} + \dot{e}_{ij}^{M} \tag{6.13}$$

the Kelvin component is given by

$$s_{ij} = 2\eta^{K}\dot{e}_{ij}^{K} + 2G^{K}e_{ij}^{K} \tag{6.14}$$

and the Maxwell part is evaluated as

$$\dot{e}_{ij}^{M} = \frac{\dot{s}_{ij}}{2G^{M}} + \frac{s_{ij}}{2\eta^{M}} \tag{6.15}$$

where s_{ij} and e_{ij} refer to the deviatoric stress and strains respectively. And the superscripts ^{K}, ^{M} stands for Kelvin and Maxwell components respectively.

If a Burgers substance has elastic bulk modulus *K*, Kelvin component (dynamic viscosity η^K and shear modulus G^K) and Maxwell component (dynamic viscosity η^M and shear modulus G^M) that is initially unstrained is subjected to an incremental stress of σ_1 and maintained thereafter. The resulting axial strain, ε_1, which is the sum of instantaneous elastic strain, primary creep and secondary creep strain, can be evaluated as

$$\varepsilon_1 = \frac{2\sigma_1}{9K} + \frac{\sigma_1}{3G^M} + \frac{\sigma_1}{3\eta^M}t + \frac{\sigma_1}{3G^K}\left[1 - \exp\left(-\frac{G^K}{\eta^K}.t\right)\right] \tag{6.16}$$

Based on the above expression it is possible to obtain the creep parameters using numerical fitting from unconfined compression tests or triaxial tests. If we deduct the elastic solution from Equation (6.16) we will obtain the axial creep strain as

$$\varepsilon_1 - \varepsilon^{elastic} = \frac{2\sigma_1}{9K} + \frac{\sigma_1}{3G^M} + \frac{\sigma_1}{3\eta^M}t + \frac{\sigma_1}{3G^K}\left[1 - \exp\left(-\frac{G^K}{\eta^K}.t\right)\right] - \left[\frac{2\sigma_1}{9K} + \frac{\sigma_1}{3G^M}\right] \tag{6.17}$$

Thus

$$\varepsilon_a^{creep} = \frac{\sigma_1}{3\eta^M}t + \frac{\sigma_1}{3G^K} - \frac{\sigma_1}{3G^K}\exp\left(-\frac{G^K}{\eta^K}.t\right) \tag{6.18}$$

If we consider Equation (6.18), the axial stains in the creep curve asymptote to a line with a slope of $\sigma_1 / 3\eta^M$ for large creep times and the line has also intercept equal to $\sigma_1 / 3G^K$. Thus, the parameters η^M and G^K can be evaluated fitting the experimental data for a secondary creep.

If we now define, Δ as the distance between the creep curve and the asymptotic line for secondary creep we obtain

$$\ln(\Delta) = \ln\left(\frac{\sigma_1}{3G^K}\right) - \frac{G^K}{\eta^K}t \tag{6.19}$$

Then the parameter η^K can be evaluated from the slope of the $\ln(\Delta)$ vs time plot.

Visco-elasto-plastic model (CVISC)

In this model (CVISC in Itasca, 2011), the Burgers viscoelastic model acts in series with the plastic flow rule based on the Mohr-Coulomb yield criterion as shown in Figure 6.7. All the strain rate components (elastic,

plastic and viscous) are treated separately. This concept is different from the viscoplastic modeling approaches where viscoplastic strains are evaluated collectively. The main concept of the CVISC model is to split the deviatoric behavior from the volumetric behavior. Therefore, the volumetric behavior is elasto-plastic and is governed by elastic law and plastic flow rule. While the deviatoric behavior is visco-elasto-plastic governed by the Burgers model and by the same plastic flow rule. Thus, the viscoelastic strains are deviatoric and depend on the deviatoric stress while the plastic strains are both deviatoric and volumetric thus depend on σ_{ij} based on the chosen flow rule.

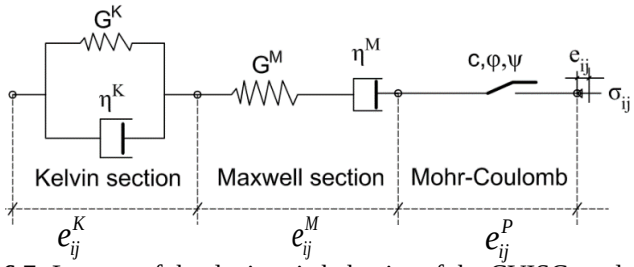

Figure 6.7: Lay out of the deviatoric behavior of the CVISC model

Thus, the stress and strain partitioning is provided in Equations (6.20)-(6.22). The constitutive laws of the deviatoric behavior of the three elements (Kelvin, Maxwell and Mohr–Coulomb) is formulated in Equations (6.23)-(6.25) respectively. While the volumetric behavior is presented in Equation (6.26).

$$\varepsilon_{vol} = \varepsilon_{kk} \quad \text{and} \quad \varepsilon_{vol} = \varepsilon_{vol}^{e} + \varepsilon_{vol}^{p} \tag{6.20}$$

$$e_{ij} = \varepsilon_{ij} - \delta_{ij}.\frac{\varepsilon_{vol}}{3} \quad \text{and} \quad \dot{e}_{ij} = \dot{e}_{ij}^{K} + \dot{e}_{ij}^{M} + \dot{e}_{ij}^{p} \tag{6.21}$$

$$s_{ij} = \sigma_{ij} - \delta_{ij}.p \quad \text{and} \quad \sigma_{o} = \frac{\sigma_{kk}}{3} \tag{6.22}$$

The viscoelastic strains, which constitute the Kelvin (superscript ^{K}) and Maxwell (superscript ^{M}) components in series can be evaluated as

$$\text{Kelvin section} \qquad s_{ij} = 2\eta^{K}\dot{e}_{ij}^{K} + 2G^{K}e_{ij}^{K} \tag{6.23}$$

$$\text{Maxwell section} \qquad \dot{e}_{ij}^{M} = \frac{\dot{s}_{ij}}{2G^{M}} + \frac{s_{ij}}{2\eta^{M}} \tag{6.24}$$

The plastic strains are governed by the general flow rule of plasticity and can be calculated as

$$\dot{e}_{ij}^{p} = \lambda \frac{\partial g}{\partial \sigma_{ij}} - \delta_{ij} \frac{\dot{\varepsilon}_{vol}^{p}}{3} \quad \text{with} \quad \dot{\varepsilon}_{vol}^{p} = \lambda \left[\frac{\partial g}{\partial \sigma_{11}} + \frac{\partial g}{\partial \sigma_{22}} + \frac{\partial g}{\partial \sigma_{33}} \right] \tag{6.25}$$

The volumetric behavior can be described as

$$\dot{\sigma}_{kk} = 3K \left(\dot{\varepsilon}_{vol} - \dot{\varepsilon}_{vol}^{p} \right) \tag{6.26}$$

In the above equations, the notations s_{ij} and e_{ij} are used for deviatoric stress and strain components respectively. σ_{kk} and ε_{kk} are the volumetric components of the stress and strain tensors. The superscripts K, M and P denote the Kelvin, Maxwell and Mohr-Coulomb plastic components. The variables with dot mark refer to their first differential with time. λ is the plastic multiplier, *g* is the plastic potential function which corresponds to a nonassociated flow rule given by similar function as that of Mohr-Coulomb failure function (Vermeer and De Borst, 1984). However, the shear potential function, *g* depends on dilation angle, ψ.

Moreover, the stress state should be enveloped by a failure criterion. Thus for the Mohr-Coulomb section, the yield function f and plastic potential function g are given by Equations (6.27) and (6.28).

$$f = \sigma_1 - \sigma_3 \frac{1+\sin(\varphi)}{1-\sin(\varphi)} + 2c\sqrt{\frac{1+\sin(\varphi)}{1-\sin(\varphi)}} \tag{6.27}$$

$$g = \sigma_1 - \sigma_3 \frac{1+\sin(\psi)}{1-\sin(\psi)} \tag{6.28}$$

where σ_1 and σ_3 are the major and minor principal stresses; *c*, φ and ψ are the cohesion, friction angle and dilation angle of the Mohr-Coulomb section respectively.

If the stress level is below the yield limit, the CVISC model is reduced to the Burgers substance. The parameters of the CVISC model can be derived from a numerical fitting of the creep test results (Bonini et al., 2009).

Previous study by Yu et al. (1999) discussed the creep behavior of soft rocks by employing a modified CVISC model. In the model the viscosity parameter is related to the stress level coefficient (i.e. stress-strength ratio) which is defined by $SSR = OA/OB$ as depicted in Figure 6.9. The

study showed that by incorporating the stress level dependent viscosity parameter, the creep behavior of a tunnel in a soft rock has been reasonably described. Figure 6.8 shows that Maxwell viscosity parameter (η_m) is dependent on the SSR as obtained from triaxial creep tests (Yu et al., 1999).

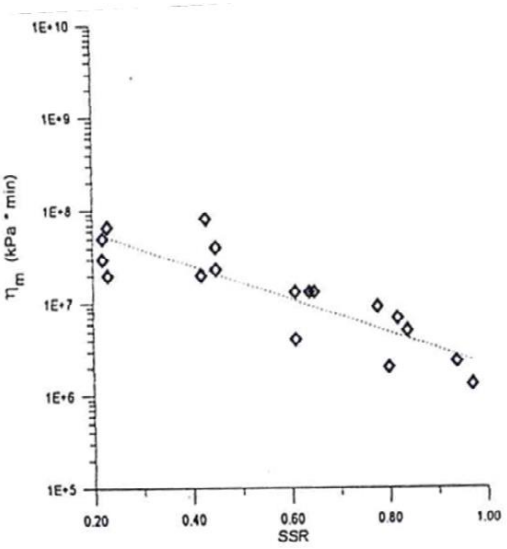

Figure 6.8: Relation between Maxwell viscosity parameter (η_m) with the stress-strength ratio SSR= A/B obtained from triaxial creep test (after Yu et al., 1999)

A similar study by Guan et al. (2008) applied the Burgers deterioration model based on the stress coefficient by modifying the basic CVISC model. The main assumption of the new model is that the cohesion, c and friction angle, φ decrease with time. And this loss of strength depends on the current stress state and a threshold value to initiate strength deterioration as illustrated in Equations (6.29)-(6.31).

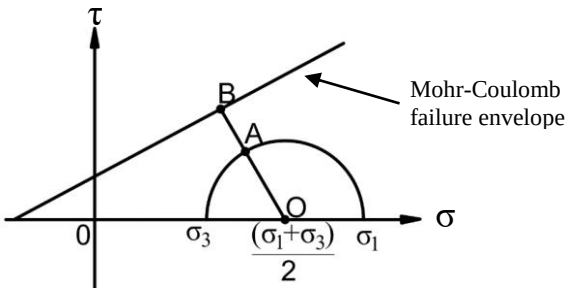

Figure 6.9: Schematic representation of the stress ratio or stress coefficient (after Guan et al., 2008)

$$\frac{dc}{dt} = -\omega_c * R \qquad (R \geq R_{thr}\ ;\ c \geq c_{res}) \qquad (6.29)$$

$$\frac{d\varphi}{dt} = -\omega_\varphi * R \qquad (R \geq R_{thr}\ ;\ \varphi \geq \varphi_{res}) \qquad (6.30)$$

$$R = \frac{\sigma_1 - \sigma_3}{2c\cos\varphi + (\sigma_1 + \sigma_3)\sin\varphi} \qquad (6.31)$$

where R is the stress coefficient which is defined as the distance from the current stress state to the Mohr-Coulomb failure envelope (Figure 6.9). ω_c and ω_φ are deterioration factors for the c and φ respectively. The rock strength deteriorates when R is greater than a given threshold value, R_{thr}. The parameters c_{res} and φ_{res} are residual cohesion and friction angle respectively that can be determined from triaxial tests (Guan et al., 2008).

6.3.2 Viscoplastic models using Perzyna's overstress theory

In this section, the elasto-viscoplastic creep models have been discussed based on the widely used Perzyna (1966) overstress concept. Unlike visco-elastic models, visco-plastic models show viscous behavior only in the plastic region. Contrary to the classical elasto-plasticity rule, the stress states in viscoplasticity theory can exceed the yield limit, which means that the consistency condition of the elastoplastic theory can be suppressed. Thus, the yield surface defines two regions in the effective stress space (Figure 6.10. The first region is an elastic one located inside the yield surface, $f(\sigma_{ij}) < 0$. In this region, only elastic deformations

occur which the Hooke's law governs. The second region is an elasto-viscoplastic that is found external to the yield surface, $f(\sigma_{ij}) > 0$. In this region, the strains are elasto-viscoplastic. Plastic and viscous deformations are often treated collectively. Therefore, the total strain rate is decomposed into two parts i.e. the elastic part and the viscoplastic component as shown in Equation (6.32). Moreover, the yield surface may harden or soften because of viscoplastic strains.

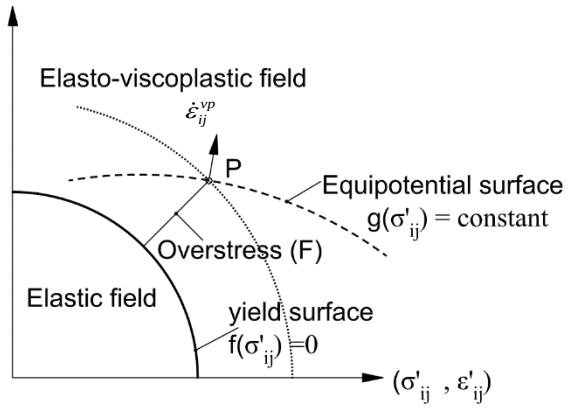

Figure 6.10: Elastic and elasto-viscoplastic regions in effective stress spaces of the Perzyna's overstress theory

$$\dot{\varepsilon}_{ij} = \dot{\varepsilon}_{ij}^{e} + \dot{\varepsilon}_{ij}^{vp} \tag{6.32}$$

where the subscript $\dot{\varepsilon}_{ij}$ is the total strain tensor, $\dot{\varepsilon}_{ij}^{e}$ and $\dot{\varepsilon}_{ij}^{vp}$ are the elastic and plastic components respectively.

The elastic component can be determined by the generalized Hooke's law of elasticity.

$$\dot{\varepsilon}_{ij}^{e} = C_{ijhk} * \dot{\sigma}'_{hk} \tag{6.33}$$

where C_{ijhk} is the elastic compliance tensor, which is independent of time and $\dot{\sigma}'_{hk}$ is the Cauchy effective stress rate tensor.

Using the classical theory of Perzyna (1963), the viscoplastic component can be defined as

$$\dot{\varepsilon}_{ij}^{vp} = \gamma . \langle \Phi(F) \rangle . \frac{\partial g}{\partial \sigma'_{ij}} \tag{6.34}$$

where the Macauly, $\langle\ \rangle$ controls the $\Phi(F)$ function as follows

$$\begin{aligned} \langle \Phi(F) \rangle &= 0 \qquad \text{if} \quad \Phi(\text{F}) < 0 \\ \langle \Phi(F) \rangle &= \Phi(F) \qquad \text{if} \quad \Phi(\text{F}) > 0 \end{aligned} \tag{6.35}$$

where γ is the fluidity parameter Φ(F) is viscous nucleus, F is the overstress function which represents the distance between the current stress state and the yield surface, while g is the viscoplastic potential and σ'_{ij} is the effective stress. The gradient to the plastic potential $(\partial g / \partial \sigma'_{ij})$ represents the direction of viscoplastic strain rate tensor. The overstress function influences its modulus by the viscous nucleus, Φ(F).

The viscous nucleus function can be defined by power or exponential functions (di Prisco and Imposimato, 1996, Fodil et al., 1997).

The deviatoric viscoplastic strain rate can be evaluated as

$$\dot{\varepsilon}_q^{vp} = \sqrt{\frac{2}{3} \dot{e}_{ij}^{vp} \dot{e}_{ij}^{vp}} \tag{6.36}$$

$$\dot{e}_{ij}^{vp} = \dot{\varepsilon}_{ij}^{vp} - \frac{1}{3} \delta_{ij} . \dot{\varepsilon}_{mm}^{vp} \tag{6.37}$$

where $\dot{e}_{ij}^{vp}$ is the rate of deviatoric viscoplastic strain tensor, δ_{ij} is Kronecker's delta, $\dot{\varepsilon}_{ij}^{vp}$ is the rate of the viscoplastic deformation tensor.

The elasto-visco-plastic model, which is depicted in Figure 6.11a, was implemented by Forlati et al. (2001) for the study of a deep-seated slope movement in a gneiss rock formation. In this model, the viscous component becomes active only when the applied stress exceeds the yield limit of the friction slider, otherwise under low stress levels the model exhibit an instantaneous deformation governed by the Hook spring. The viscous element has only deviatoric strains, which depend on the deviatoric stress while the friction element has both deviatoric and volumetric strain components.

The model shown in Figure 6.11a, could represent secondary and tertiary creep behavior of rock mass. However, the visco-elastic model cannot be obtained from this model formulation. In fact, as discussed by Sterpi and Gioda (2000), the visco-elastic Kelvin model which accounts for the primary creep can be connected to the visco-plastic Bingham model which collectively can represent primary, secondary and tertiary creep deformation (Figure 6.11b).

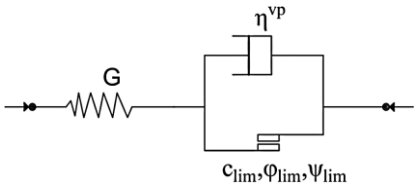

(a)

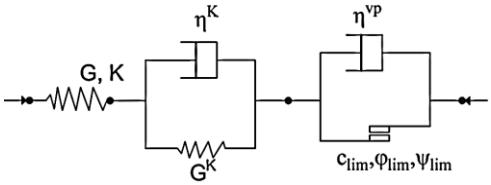

(b)

Figure 6.11: (a) Elasto-visco-plastic rheological model which accounts for secondary and tertiary creep deformation (after Forlati et al., 2001). (b) Visco-plastic model which accounts for primary, secondary and tertiary creep (after Sterpi and Gioda, 2009)

Previous study by Sterpi and Gioda (2009) also discussed the tertiary creep phase by taking in to account the peak and residual values of the Bingham parameters as a function of the deviatoric viscoplastic strains (Figure 6.12).

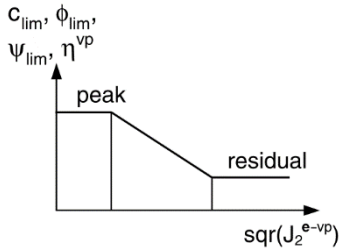

Figure 6.12: Variation of the visco-plastic parameters with the 2nd invariant of deviatoric visco-plastic strains (after Sterpi and Gioda, 2009)

In the Bingham model (Figure 6.13), similar to the overstress concept of viscoplastic theory, the flow of substances occurs when the applied shear stress exceeds the yield value. In other words, once the shear resistance is overcome, the velocity of the moving mass is controlled by the viscosity η^{vp} of the dashpot aligned parallel to the mass (Figure 6.13). Therefore, the Bingham model exhibits elastically below a yield stress limit and it behaves viscoplastically above the yield limit as discussed by several authors (Angeli et al., 1996, Van Asch et al., 2007, Conte and Troncone, 2011).

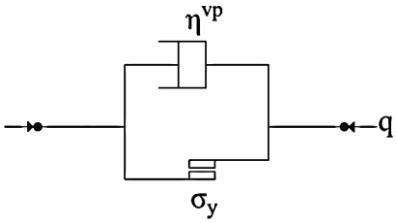

Figure 6.13: Bingham model

The overall resistance of a moving mass can be evaluated as the sum of the shear strength of the sliding surface and the viscous resistance of the soil, which is defined by analogy of fluid mechanics, both collectively, can be expressed as

$$\tau_f + \eta \frac{dV}{dz} \tag{6.38}$$

where η is the coefficient of viscosity which depends on material property (Pa.s), V is the velocity (m/s) and τ_f is the shear yield limit which is defined as

$$\tau_f = c' + \sigma' \tan(\varphi') \tag{6.39}$$

where c' and φ' represent residual shear strength parameters and for a slope undergoing antecedent movements the value of c' = 0 can be reasonable.

The viscoplastic model illustrated in Figure 6.14, proposed by Lemaitre and Chaboche (1990) was first introduced for rate sensitive plastic materials and it was latter applied for the study of time dependent behavior of rocks (Boidy, 2001, Boidy et al., 2002, Bonini et al., 2009). The model is formulated based on the concept of the Perzyna's overstress theory (1966). In the model, viscoplastic deformations occur only as a result of deviatoric stress. In other words, the viscoplastic deformations occur without inducing any volume changes. While the elastic deformations are limited to the isotropic state of stress.

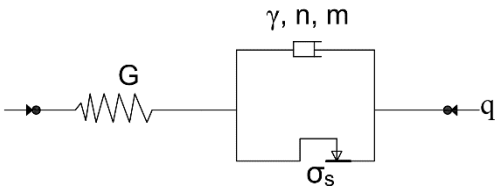

Figure 6.14: Lemaitre's viscoplastic model representation

Numerical compression creep test

A uniaxial numerical compression test has been carried out considering the parameters (axial load = 1MPa, Poisson's ratio = 0.25, deformation modulus = 1GPa). In the simulation, the influence of viscosity parameters Kelvin viscosity (η^K) and Maxwell viscosity (η^M) on the model behavior of the Burgers substance has been examined.

Figure 6.15a shows the effect of Kelvin viscosity, η^K on the calculated displacement keeping $\eta^M = 2.2x10^{15}$Pa.s, and the influence of the Maxwell viscosity, η^M can be referred as well from Figure 6.15b. Figure 6.15c illustrates the response of Burgers model to creep parameters, η^K and η^M.

It has been clearly understood that the Kelvin cell viscosity affects only the primary creep stage while the Maxwell cell viscosity controls the steady state creep or secondary creep behavior.

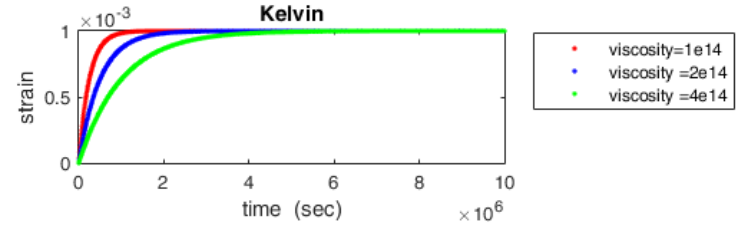

(a)

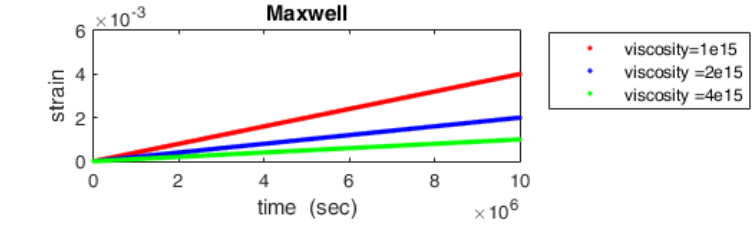

(b)

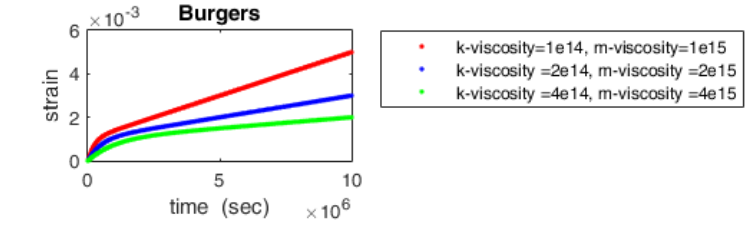

(c)

Figure 6.15: The influence of viscosity (Pa.s) on model response of a Burgers substance and its components during a uniaxial compression loading

6.4 Modeling the creep behavior of the slope

As discussed in Chapter 2, monitoring data analyses have shown that the slope movement is characterized by mainly a stationary creep type with some seasonal reactivation phases attributed to changes in rainfall and pore pressure regime. The aim of the following analyses is to describe the evolution of the ongoing slope movement, which is characterized by a constant velocity with the help of numerical modeling. In further analyses, the influence of increase of reservoir level or reduction of friction angle on the displacement velocity has been explored by employing viscoplastic model.

The time dependent behavior of the observed slope movement has been studied herein using creep models.

At first, it has been decided to consider creep behavior only to the slip surface and the transition zone (Figure 6.16). This can be justified by the presence of the clay-rich gouge in the slip surface, which could exhibit creeping behaviors. In addition, some inclinometer profiles in the toe part (Chapter 3) suggest the presence of a sheared zone with a localized deformation. Therefore, the moving mass has been assigned with the standard elasto-plastic model with Mohr-Coulomb failure criterion (Table 6.1 and Table 6.2).

In the first part, the standard CVISC model has been considered. In the second part of the modeling study, a viscoplastic model, which is formulated by extending the basic CVISC model, has been discussed. Comparisons of model results and model behavior will be presented too. The creep models have been implemented in a continuum approach via FLAC code in plane strain condition.

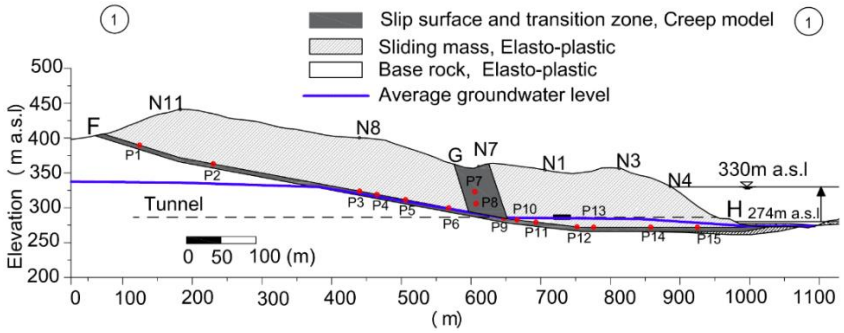

Figure 6.16: Location of points (P1---P15) along the basal slip surface used to examine the stress-path during a creep deformation

6.4.1 Modeling protocol

Concerning the pore pressure distribution inside the slope, the average groundwater level, which was evaluated previously by the flow analyses (Section 5.5), has been kept throughout the creep time The reservoir level is 274m a.s.l which represents the current average level of the dam.

Firstly stable mechanical equilibrium condition has been achieved by employing elasto-plastic analysis. Then the friction angle of the basal slip surface has been reduced from 10^o to 8.8^o, a bit higher than the collapse friction angle i.e. 8.45^o (Section 5.5). Up to this stage, the overall material model is elasto-plastic and equilibrium condition is maintained.

Then the creep model has been initiated only to the basal slip surface and the transition zone keeping the shear strength parameters constant throughout the creep time. Parameters considered in the CVISC model are reported in Table 6.1.

Then the creep analyses have been performed in order to reproduce the observed 20 years stationary slope movement. Latter the creep analyses have been extended for a longer time domain (i.e. up to. 100 years) in order to figure out the velocity trends for longer periods.

The stress-path during the creep deformation has been assessed by considering several control points (P1---P15) located in the upper, transition and lower parts of the basal slip surface (Figure 6.16). Stress redistribution during the creep deformation has also been examined.

Table 6.1: CVISC model parameters adopted for the slip surface and transition zone

Unit	K (GPa)	G^K (Pa)	G^M (Pa)	$*\eta^K$ (Pa.s)	$*\eta^M$ (Pa.s))	c (kPa)	φ (^{o})
Sliding surface	0.667	0.4	0.4	$2.2x10^{15}$	$2.2x10^{15}$	0	8.8
Transition zone	0.667	0.4	0.4	$2.2x10^{15}$	$2.2x10^{15}$	0	15

Table 6.2: Elasto-plastic model parameters applied for the sliding mass and base rock

Unit	K (GPa)	G (GPa)	c (kPa)	φ (^{o})
Upper sliding mass	3.3	1	300	35
Lower sliding mass	3.3	1	250	37
Base rock	7.2	3.1	500	40

6.4.2 Numerical results

With the help of preliminary analyses, it has been understood that the steady state creep behavior is dependent on the creep parameter, η^M. Therefore, the influence of creep parameter, η^M on the predicted displacements has been explored. Figure 6.17 illustrates that the secondary creep behavior is influenced by the viscosity (η^M) parameter. For instance, the displacement of N3 has decreased from 0.82m to 0.4m (i.e. by 50%) as the magnitude of the creep parameter; η^M has increased by 50% i.e. from $2x10^{15}$ to $4x10^{15}$ Pa.s. Similar results were obtained for other target points (N1 --- N11) which confirm that the stationary creep displacement is influenced proportionally with the creep parameter, η^M. The influence of the creep parameter η^K on the predicted displacement

was minimal which confirms that the model results are less sensitive to Kelvin viscosity.

In a separate analyses, comparison of displacement predicted by Burgers visco-elastic and CVISC model has been shown in Figure 6.18. In the analyses, value of $\eta^K = \eta^M = 2.2x10^{15}$ Pa.s. Obviously, the displacements predicted by the CVISC model are close to the observed displacements as compared to the visco-elastic model results.

Based on the previous preliminary model analyses, it has been understood that the viscosity parameter, $\eta^M = 2.2x10^{15}$ Pa.s has been implemented in the subsequent numerical analyses since it gives good estimation of the observed displacement trends (Figure 6.17).

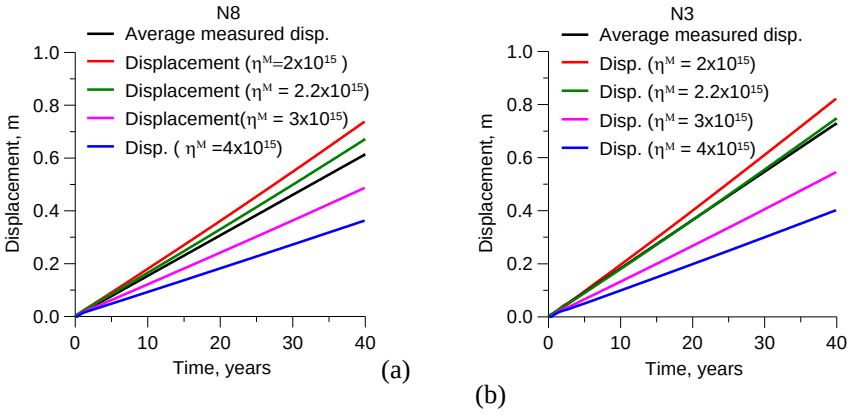

Figure 6.17: Influence of creep parameter η^M (Pa.s) of CVISC model on estimated displacement of targets (a) N8 and (b) N3

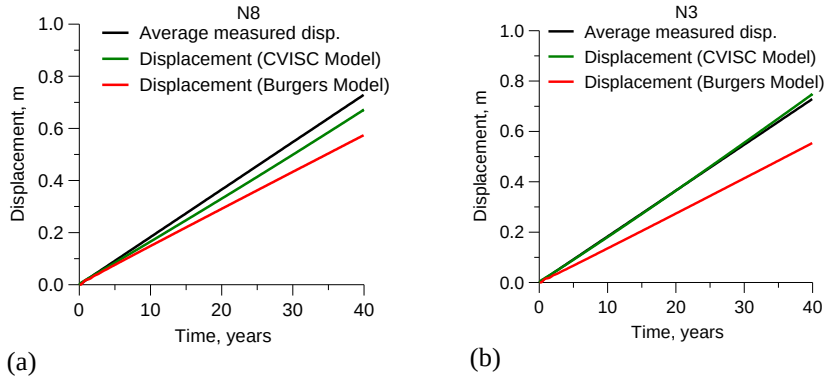

Figure 6.18: Comparison of model displacements obtained by Burgers and CVISC model

Stress-path

In order to determine the yield limit at the creeping zones, friction angles $\varphi=8.8^{o}$ and $\varphi=15^{o}$ have been considered respectively for the basal slip surface and the transition zone.

The yield limit condition is evaluated from

$$t = s'\sin(\varphi) + c'\cos(\varphi) \tag{6.40}$$

where s' (Pa) is the average effective stress and t (Pa) is resistance shear stress, φ (^{o}) is the friction angle and c (Pa) is the cohesion.

It is worthwhile to remind that in the previous elasto-plastic analyses some of the points, particularly located in the upper part of the slip surface have already reached close to the yield limit. The history of s-and t-stresses is shown in Figure 6.19. It seems that points located close to the transition zone (i.e. P9, P10, P12 and P13) shows some stress changes from their initial stress point, moreover P1 also shows a similar trend during the creep time.

Figure 6.20 and Figure 6.21 illustrated the stress path followed by the control points. During the creep deformation, points P1 and P2 remain in the yield line apart from limited stress changes. Similar results were evidenced from points P3, P4, P5 and P6. Points lying in the transition zone (P6 and P7) also exhibit limited stress changes and they remain in the elastic region. For the points, lying between the transition zone and flat basal slip surface (i.e. P9, P10, P11, and P12) the stress path is different from the points lying in the upper portion. Hence, P9 and P12 exhibit a reduction in stress while remaining on the yield line. Points P10 and P11 come back to the elastic region during the creep time from their previous yield point achieved during the first elasto-plastic analyses. P13 shows a relatively higher stress changes during creeping and it approaches the yield limit. P15 exhibits small stress changes and approaches to the yield line during the creep time while P14 shows a small stress changes but it comes back to the elastic region.

Using the Burgers visco-elastic model, the stress path has been also studied, and in contrast to the CVISC model, here the stress points can exceed the yield limit (Figure 6.21). It has been understood that points like P1, P9, P12 and P15 cross the yield limit in visco-elastic model. Points P10 and P13 experience relatively higher stress changes while remaining in the elastic region (Figure 6.21).

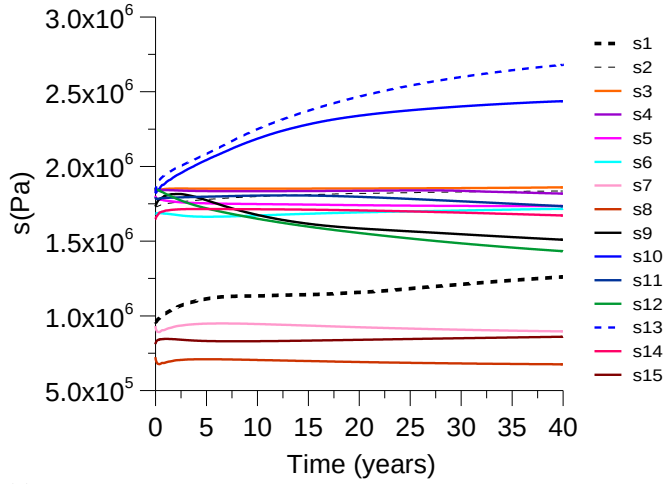

(a)

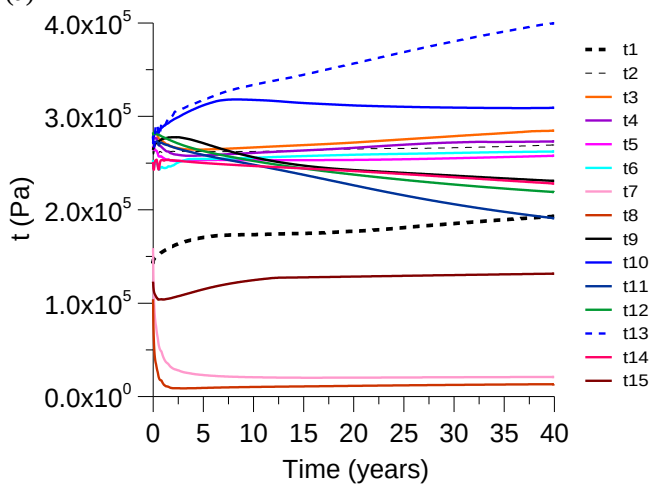

(b)

Figure 6.19. History of s- stress (a) and t- stress (b) during the creep deformation

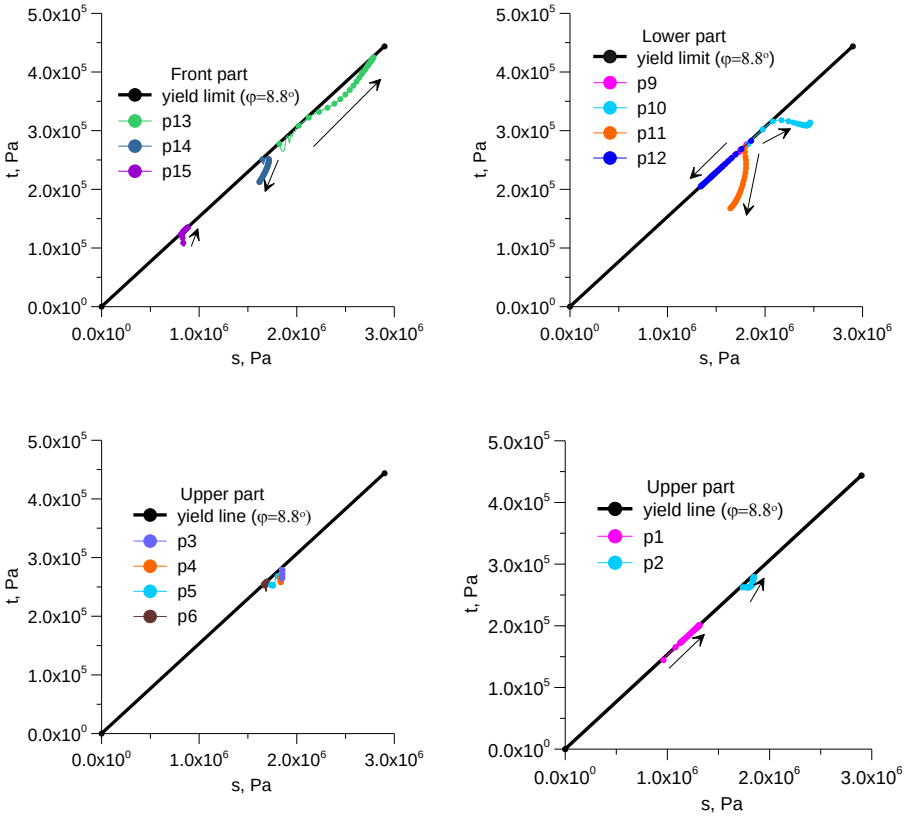

Figure 6.20: Stress-path of points (P1---P15) located on the basal slip surface during creep analyses by CVISC model. Note that the arrows indicate the stress-path followed by the points during the creep deformation

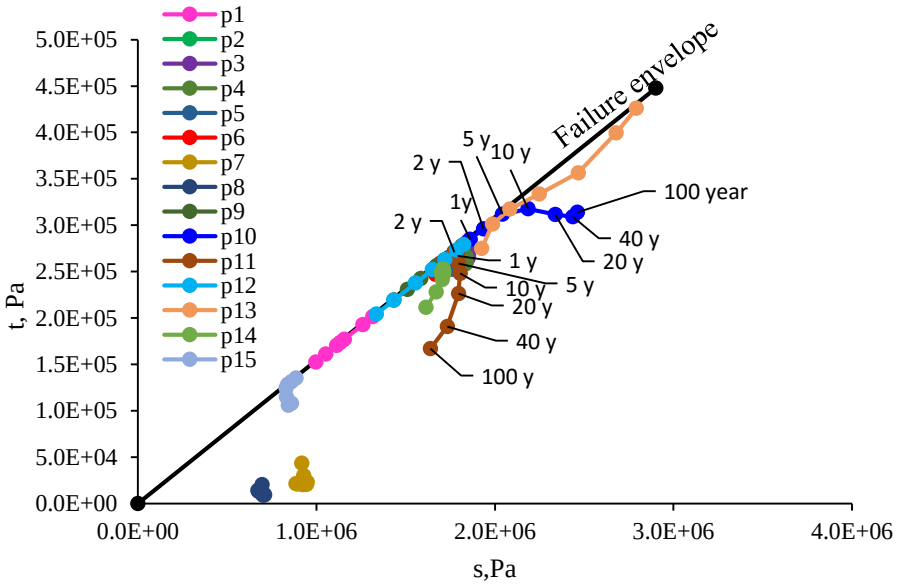

(a)

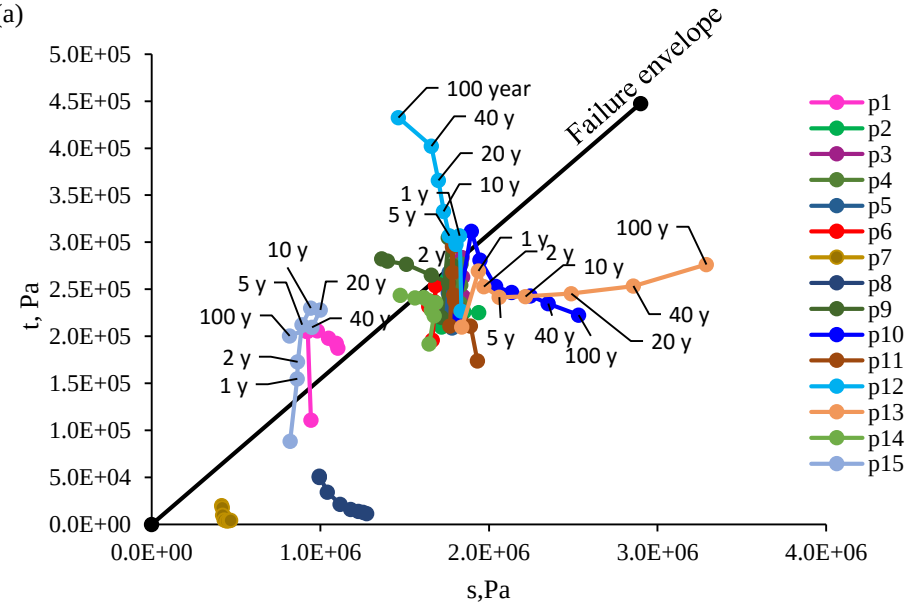

(b)

Figure 6.21: Stress-path of points located on the slip surface using CVISC model (a) and Burgers model (b)

Calculated displacement

It is worthwhile to recall herein the results of the statistical model (Section 2) implemented in order to approximate the observed displacement velocity (Figure 6.22).

The estimated average velocities by numerical modeling are compared with the corresponding average displacement velocities obtained using the linear regression of the measured displacements.

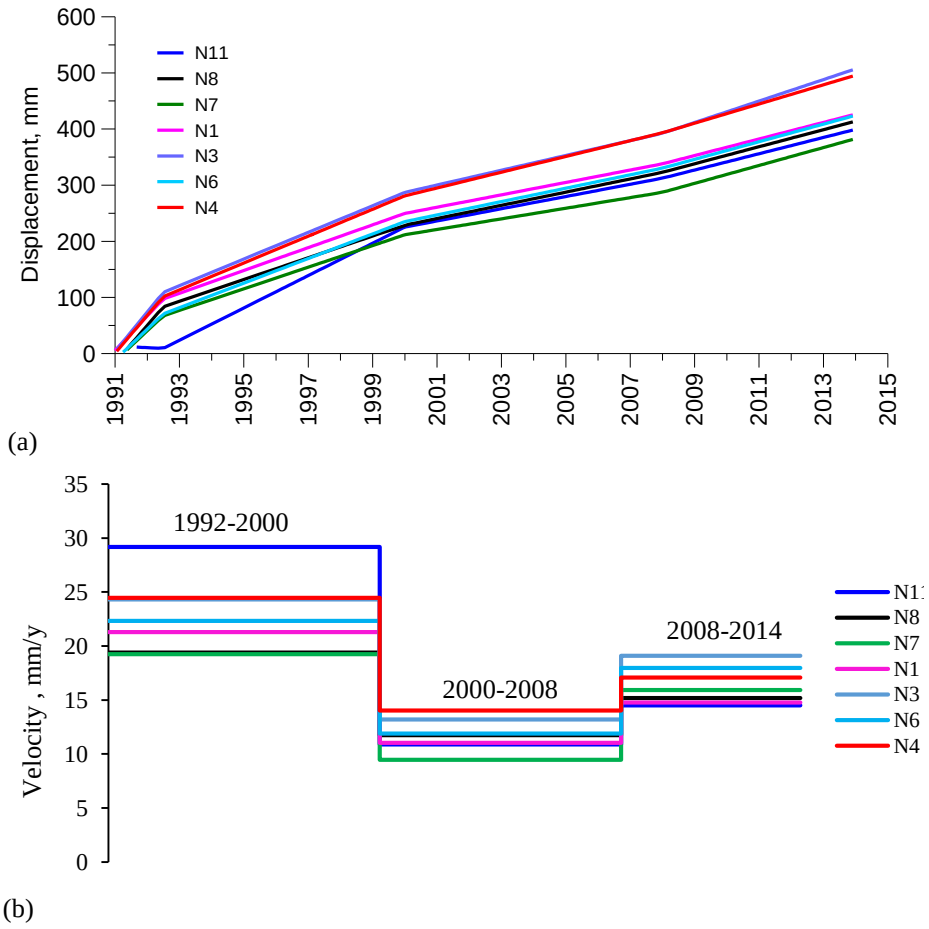

Figure 6.22: Displacement trend approximated by linear splines (a) and average velocities calculated considering three time intervals (b)

Figure 6.23 shows the velocity of targets points is found in between 15-20 mm/y. The velocity of N11, which is around 15mm /y, is quite close to the average velocity 14.5 mm/y observed during 2008-2014

period. The velocity of target points (N3, N4 and N6) located in the toe part are close to 20 mm/y (Figure 6.23) which is similar to the average velocity 17-19mm/y observed during 2008-2014 period.

Therefore, by adopting CVISC model, the observed steady state movement (i.e. constant velocity) has been reproduced reasonably for the assumed model parameters and boundary condition.

It is worthwhile to understand that the stress redistribution occurred along the basal slip surface during creep deformation has limited effect in changing the velocity magnitude.

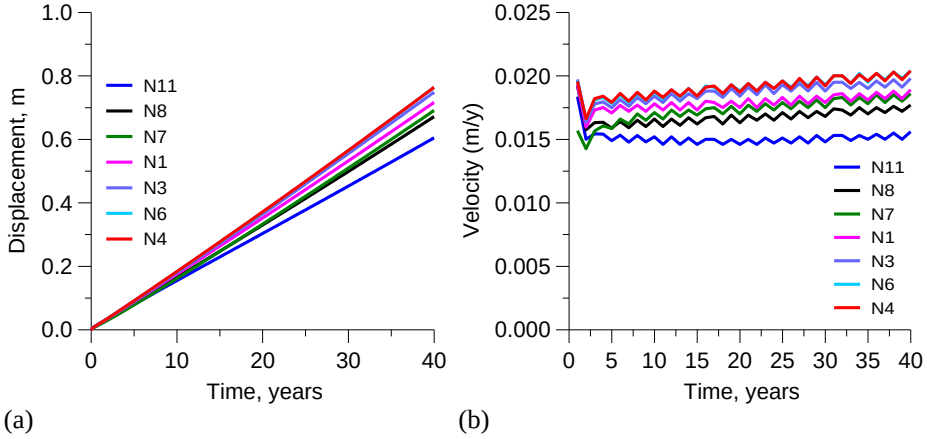

(a) (b)

Figure 6.23: Predicted displacements vs time (a), and corresponding velocities vs time during creep deformation (b)

Separate numerical analyses have been worked out in order to explore the influence of basal friction angle on the predicted model displacements. Moreover, it could be expected that the friction angle of the slip surface located in the upper less disturbed slope part would be higher. However in the creep analyses herein have been carried out assuming the basal friction angle equals to 10^o for the entire slip surface The creep parameter $\eta^M = 2.2x10^{15}$ Pa.s has been kept for creeping zones.

Figure 6.24 shows the estimated displacement corresponding to the assumed friction angles of the slip surface. As expected, the magnitude of displacement decreases, for instance for N3 by around 0.09m when a higher friction angle has been employed for the sliding surface. However, in this case the estimated displacement at point N8 is relatively better than before (i.e. when basal friction angle is 8.8^o). Moreover, the yearly calculated average velocity from the predicted displacements shows a slight decrement as it is shown in Figure 6.25.

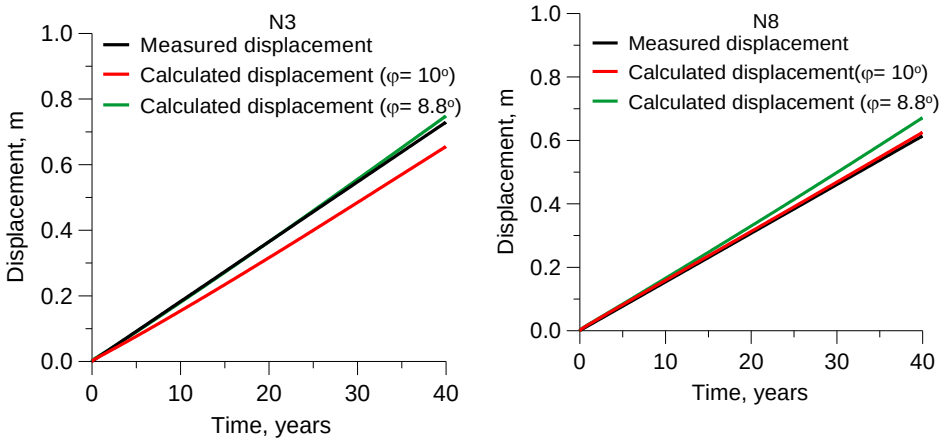

Figure 6.24: Influence of the basal friction angle on model estimation

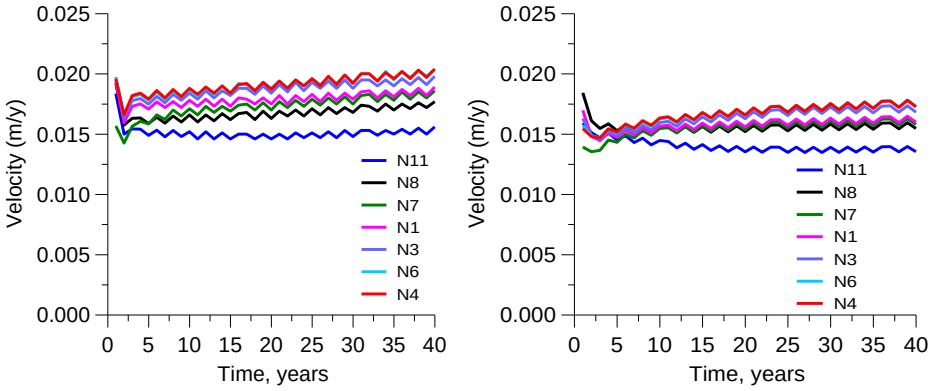

(a) (b)

Figure 6.25: Calculated yearly velocity when basal friction angle is equal to (a) 8.8° and (b) 10°

6.4.3 Creep analysis at different hydraulic boundary conditions

Since the previous creep analyses were performed considering the current average reservoir level of 274m a.s.l; therefore, it is worthwhile to extend the creep analyses by considering higher reservoir levels at the toe of the slope. Theses sets of analyses could give us some useful insights about the ongoing creep behavior of the movement when the dam will begin operation. The creep parameters reported in Table 6.1and Table 6.2 have been adopted.

At first, flow analyses have been carried out in order to obtain a reasonable pore pressure distribution corresponding to a given reservoir level.

Then keeping the computed pore pressure distribution from the previous flow calculation constant, then only mechanical (i.e. mainly creep) analyses have been carried out in the subsequent steps.

Figure 6.26 shows the stress-path comparisons at the considered hydraulic boundary conditions (i.e. at reservoir levels. 274, 295 and 330m a.s.l). The effective stress has decreased as we increase the reservoir level, however the stress state cannot be changed.

For instance, point P11, the effective stress has changed during the filling process, but the point remains in the elastic region. Similar results were confirmed in other points (Figure 6.26). Moreover, the displacement estimated by the model considering the above reservoir levels are almost similar. This is a consequence of limited stress changes induced by the filling of the dam.

In other situation, the creep calculations have been performed at two different water tables (i.e. minimum and average groundwater tables). Figure 6.27 illustrates the stress path during creep deformation at the two hydraulic conditions (minimum and average water tables).

It is apparent that if we draw the yield line taking friction angle of 8.8^{o}, stress states evaluated considering the average groundwater condition are close to the yield limit as compared to stress obtained from the minimum water table condition. Figure 6.28 shows the calculated displacement at the minimum and average water tables.

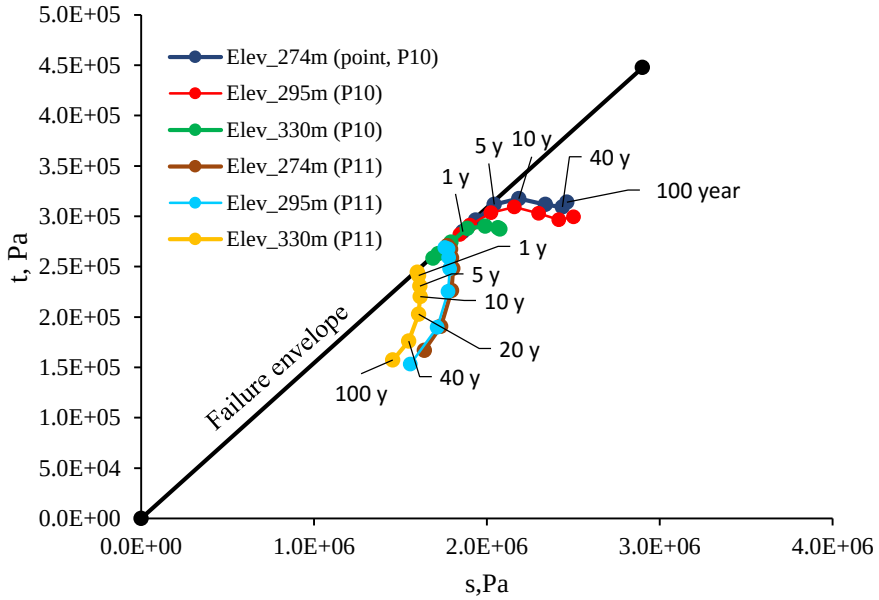

(a)

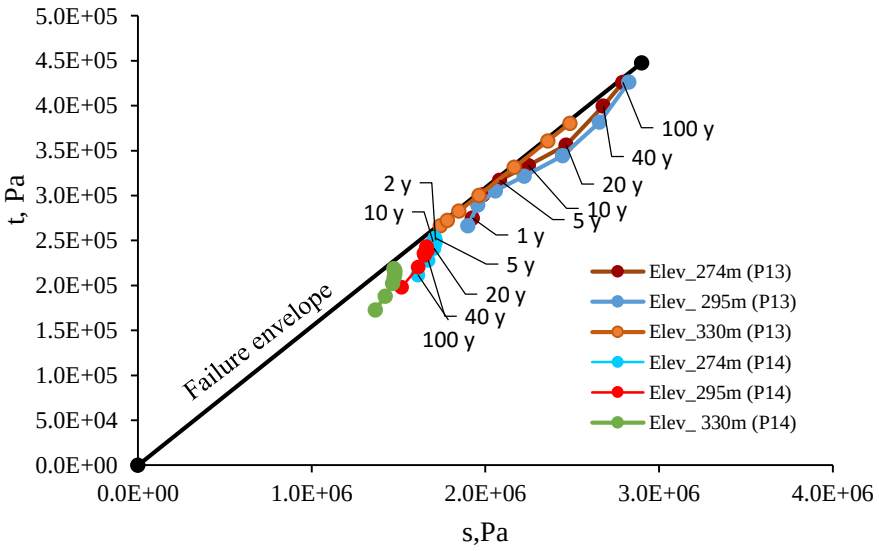

(b)

Figure 6.26: Influence of reservoir level on the stress-path of points located in middle part (a) and front part (b) of the basal sliding surface

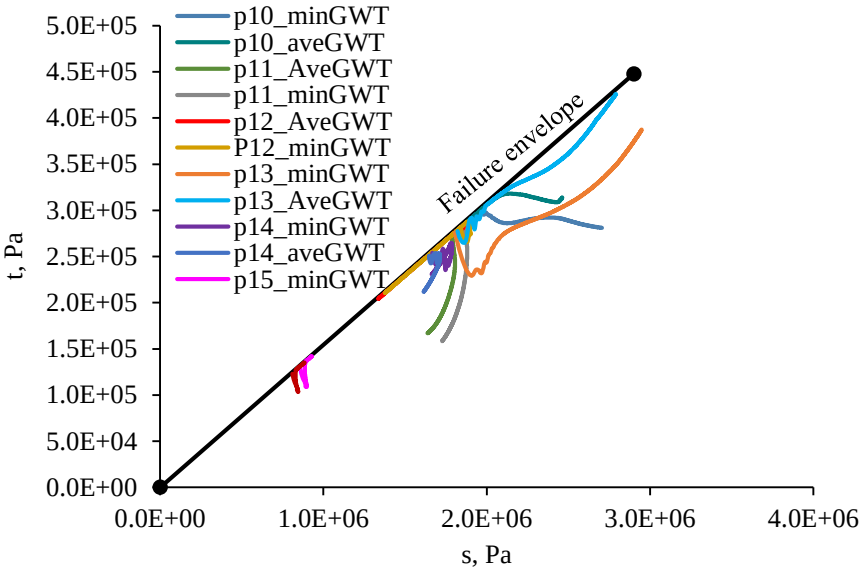

Figure 6.27: Stress path plots obtained from creep analyses carried out at the minimum and average groundwater tables (i.e. min.GWT or ave. GWT)

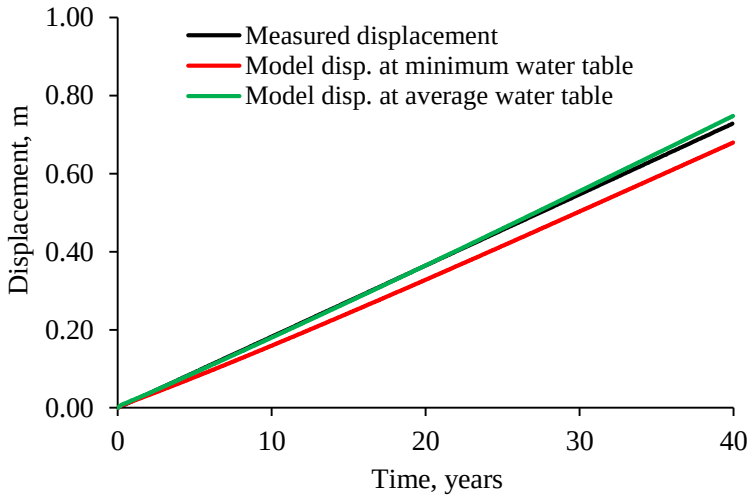

Figure 6.28: X-Displacement (N3) vs time evaluated at minimum and average groundwater table

6.4.4 Viscoplastic modeling of the slope movement

In this section, a viscoplastic model depicted in Figure 6.29 has been employed to describe the ongoing slope movement. This simple model with its Bingham component assists to describe the viscoplastic strains induced owing to excess stress beyond the yield limit. Thus, the Bingham component is active only when the stress level exceeds the yield limit, otherwise the model behaves like Burgers viscoelastic model. Conceptually this model (Figure 6.29) could also describe the tertiary creep by employing appropriate laws which allows the decay of shear strength of the plastic slider from peak to residual strength (Sterpi and Gioda, 2007). Previous studies (Wang et al., 2013, Wang et al., 2014) implemented a combined model of Kelvin, Maxell and Bingham units to discuss creep behaviors.

The value of creep parameter (η^{vp}) strongly controls the model behaviors; therefore, the velocity of the movement in the viscoplastic phases depends on this parameter. In the following analyses, the viscosity parameter $\eta^{vp} = 1x10^{14}$ Pa.s is assumed for the Bingham unit.

The model has been implemented in a continuum approach (FLAC code) using an internal programming language, FISH.

This new model helps to assess the velocity changes due to change of loading history (for instance, pore pressure increase due to sudden filling of the reservoir) or reduction of the material properties (i.e. in this case shear strength of the basal slip surface).

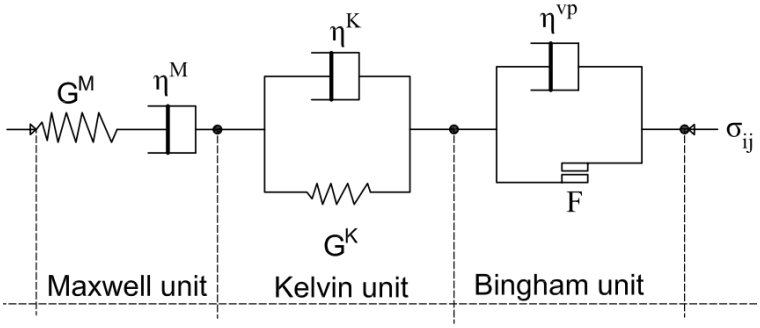

Figure 6.29: Lay out of the modified model used to describe viscoplastic responses

Model response to change of fluid boundary condition

With the intention of examining the model behavior owing to loading changes, pore pressure change due to sudden filling of the dam has been

considered. In the modeling procedure, first creep deformation has been evaluated until stationary displacement has been obtained (i.e. in this case a constant velocity is obtained after 5 years of creep time) and then an increase of reservoir level from the initial 274m to 330m a.s.l is imposed to the model.

Figure 6.30 depicts the displacement history evaluated when the reservoir level has been increased from 274m a.s.l to 330m a.s.l (maximum design level) during the creep time. A clear picture of velocity increase has been displayed at the moment when the reservoir level is increased (Figure 6.30). Similar results with relatively less velocity change have been obtained when the reservoir level is increased from 274m a.s.l to 296m a.s.l, which is actually the maximum observed reservoir level in the early (1991-92) filling of the dam.

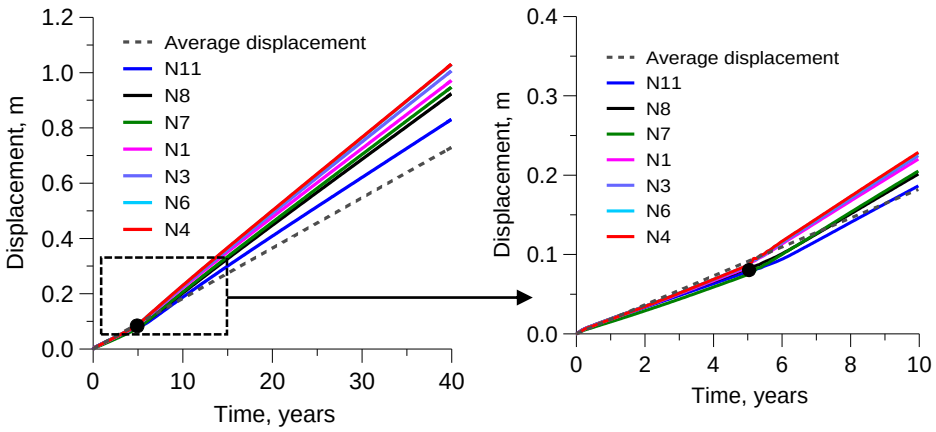

Figure 6.30: Horizontal displacement vs time showing the change in velocity when the reservoir level is increased to maximum design level 330m a.s.l. Note that the black dot shows that the creep time when the velocity changes

The stress path plots (Figure 6.31) can be referred to visualize the stress changes occurred when the reservoir level increase. Moreover, the history of s- stress plot (Figure 6.32) shows that the stress magnitude decreases as the reservoir level increases, obviously this arises due to the pore pressure increase. The s-stress at points P1 and P2 is not affected by the reservoir level increase (Figure 6.32).

A similar result has been found when the friction angle of the basal slip surface is reduced from 8.8 to 8.4^{o} (Figure 6.33).

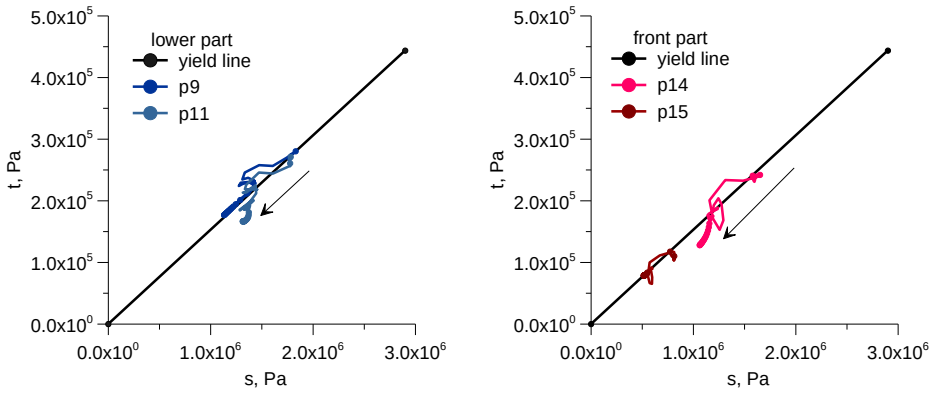

Figure 6.31: Stress-path obtained when the reservoir level has increased from 274m a.s.l to 330m a.s.l

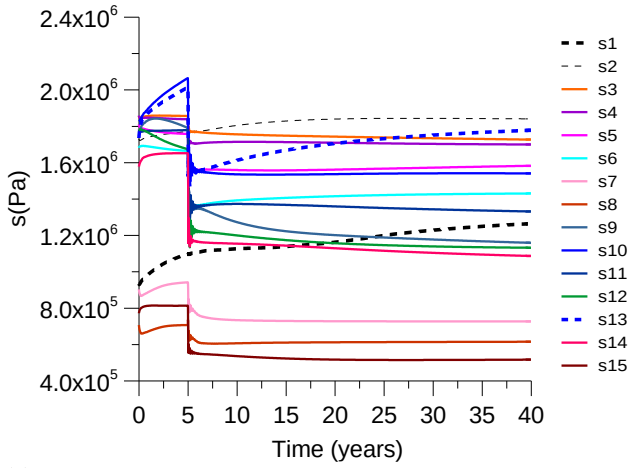

(a)

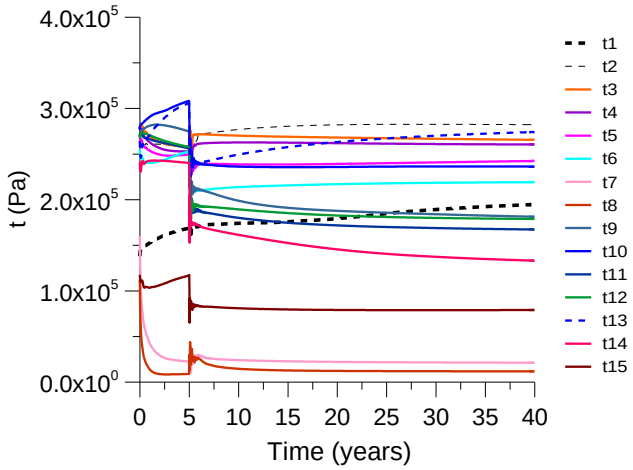

(b)

Figure 6.32. History of s-stress (a) and t-stress (b) during creep deformation

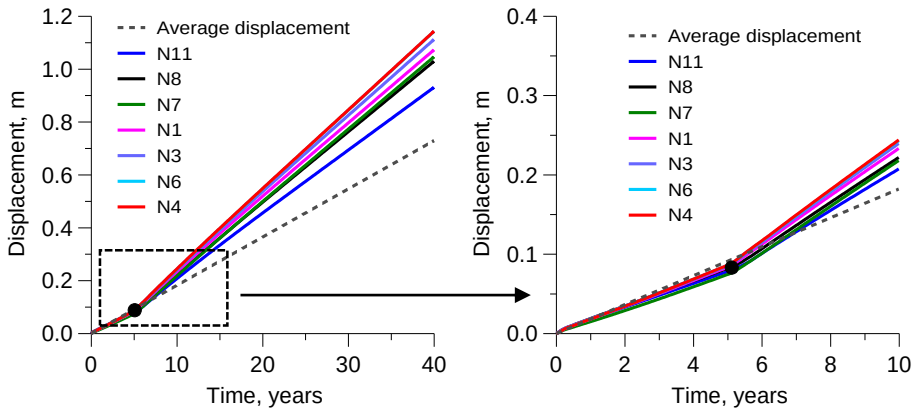

Figure 6.33: Horizontal displacement vs time. The black dot shows the point where the friction angle of the basal slip surface is reduced from 8.8 to 8.4°

6.4.5 Discontinuum modeling approach

In other aspect of modeling, the creep analysis has been extended by employing discontinuum model using UDEC code. As usual, in the discontinuum modeling, blocks are elastic and joints are elasto-plastic and obey Mohr-Coulomb yield criterion. While for the creeping zones (i.e. the slip surface and transition zones), CVISC model has been employed. Therefore, the creep behavior has been applied only to the

block materials (i.e. zones) not for joints. The creeping behavior of joint deformation is not considered and it is beyond the scope of this research. In the model, the creep parameter $\eta^M = 2.2x10^{15}$ Pa.s has been applied to the basal slip surface while for the transition zone $\eta^M = 2.2x10^{17}$ Pa.s has been considered in order to mobilize the observed rock mass deformation.

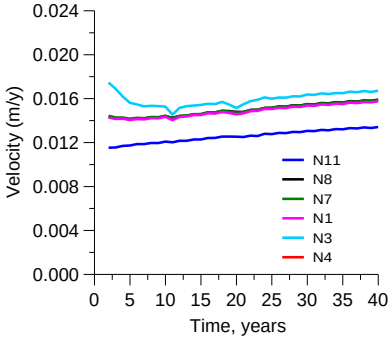

Figure 6.34. Velocities vs time (m/y) evaluated by the CVISC model using the discontinuum approach

The residual friction of the shear zone, which is 8.8º, has been kept and while for the transition zone, the friction angle is equal to 30º.

Basically the CVISC creep model implemented in the discontinuum approach gives almost identical behaviors like continuum model results. The constant velocity which is in the range of 12-16 mm/year has been depicted in Figure 6.34. Moreover, these velocities are lightly lower than the previous velocities estimated by the continuum model (16-20 mm/y) (Figure 6.23).

The creep analysis using the discontinuum model has been extended taking take in to account the influence of the remedial measure (i.e. a large rockfill embankment at the toe) on the steady state velocity. The results of these group of analyses will be presented in the next Chapter (Section 7.4).

6.5 Conclusions

This chapter has attempted to reproduce the observed stationary movement using appropriate rheological models. The CVISC model sufficiently describe the already understood constant velocity movement taking in to account the value of creep parameter $\eta^M = 2.2x10^{15}$Pa.s.

A user defined viscoplastic model has been applied too. This viscoplastic model has been employed to assess the model response due

to loading changes (in this case, reservoir level increase) or loss of friction angle of the basal surface. The new proposed model highlights that the steady state velocity can change as a consequence of reservoir level increase or shear strength loss of the basal slip surface throughout the creep time.

Chapter 7

7 Remedial measure: Rockfill embankment

7.1 Introduction

This chapter aims to assess the role of the proposed remedial measure (a large rockfill embankment at the toe of the slope) on the ongoing slope deformation.

In the first part, properties of rockfills have been revised from previous studies and particular attention has been paid to large-scale laboratory tests. Then a series of biaxial and uniaxial numerical tests have been carried out using DEM via UDEC code in order to assess the deformability and strength of rockfill.

Lastly, the influence of the rockfill embankment on the ongoing slope deformation has been examined, in particular its effect on joint shearing and horizontal displacements have been highlighted. In addition, creep analyses have been performed with CVISC model to assess the effect of the embankment on the steady state velocity.

7.2 Review of rockfill behavior from large scale triaxial tests

Rockfills have similar characteristics like granular materials and their behavior depends on shape of particles, gradation curve, internal friction between particles and relative density of granular medium. Moreover, Rockfills are applied in dam and embankment construction since they offer significant and reliable strength.

Representing the prototype rockfill with actual rockfill sizes and shapes in laboratory is limited. However, some large-scale triaxial tests were carried out by previous studies (Marachi et al., 1972, Charles and Watts, 1980, Indraratna et al., 1994, Varadarajan et al., 2003, Linero et al., 2007) for analyzing the deformation and strength of rockfills (Figure 7.1).

In triaxial testing, to reduce the influence of size on rockfill specimens, Marachi et al. (1972) suggested a minimum size ratio of 6. Previous study by Indraratna et al. (1994) discussed the behavior of Greywacke rockfill by using a large scale triaxial test which can accommodate specimen size of 300m diameter and 600m height by employing 100 to 600kPa confining pressures using the particle size ratio of 8 and 12.

Rockfills are subjected to deformations during compactions and filling of dams. Rockfills are characterized by high rate of particle breakage which is not possible for sands except for high stress levels, particularly materials like schist and shales are prone to breakage as compared to hard and tough lithologies for example limestone (Alonso et al., 2010).

Breakage depends on the size, shape of particles, and confining stress applied. Angular particles are more susceptible to breakage than round particles. This particle breakage by a high stress level usually leads to a more stable condition by rearranging the particles to stable position. A study by Indraratna et al. 1994 showed the particle size distribution before and after triaxial testing (Figure 7.2). Figure 7.3 shows the crushed stones during oedometer tests (Alonso et al., 2013).

Tests conducted by Marachi et al. (1972) on compressibility of cohesionless materials, large in size, including rockfills showed samples containing particles rounded in shape are less compressible. They substantiate Casagrande's (1965) conclusion where rockfill materials composed of well-graded and well-rounded particles are superior in their mechanical properties as compared to uniform, angular rockfill materials and thus are more suitable for use in high rockfill dams.

For a typical aggregate, compressibility is decreased by increasing the relative density. Compressibility is less for well-graded than for uniform graded particles. The angle of internal friction angle (φ) decreases with relative density as it is known that loose sands and gravels have less resistance to shear than in their dense state.

The individual particle resistance also plays important role in compressibility and shear strength of rockfills. When particles have higher resistance as compared to the confining stresses, dilation plays a great role in dense state. If particles have low resistance, they tend to break down and diminishing dilatancy and shear resistance of the rockfill. Previous studied by Ovalle et al. (2014) showed the particle size has inverse relation with the crushing strength of rockfill.

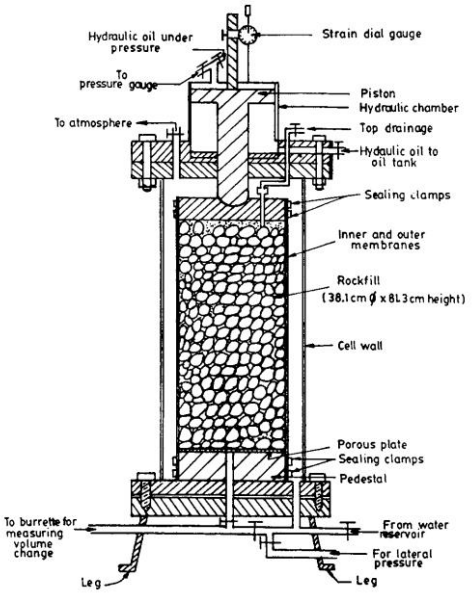

Figure 7.1: Triaxial cell for 381 mm diameter and 813 mm high specimen used by Varadarajan et al. (2003)

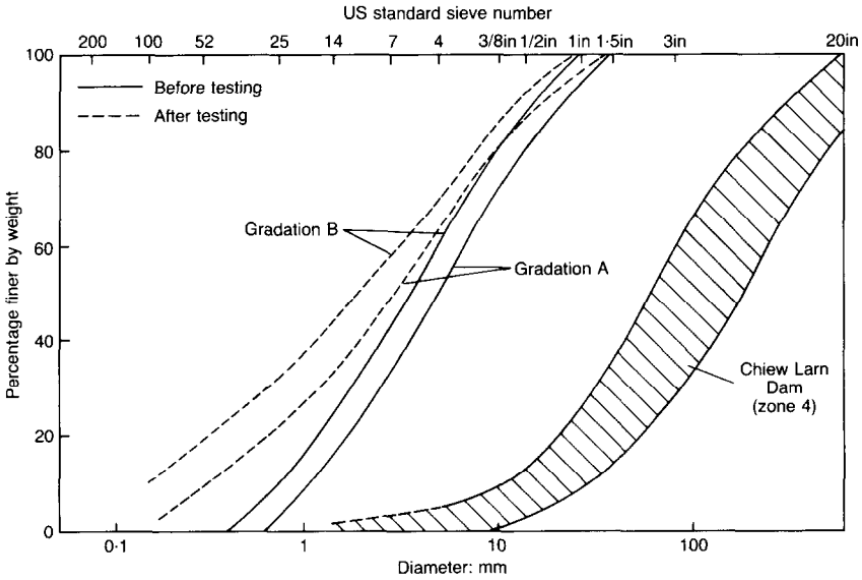

Figure 7.2: Particle size distribution of greywacke rockfill before and after triaxial testing (after Indraratna et al., 1994)

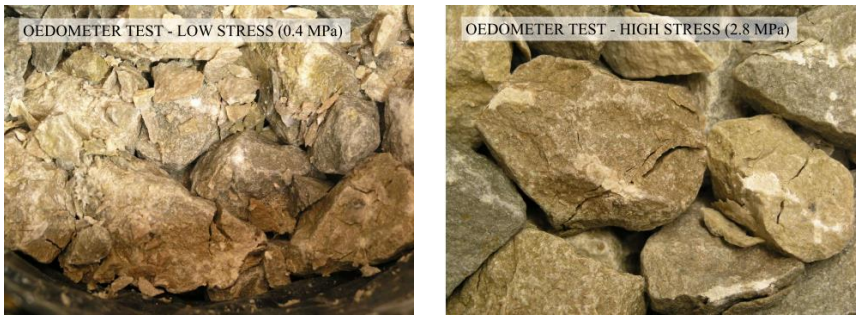

Figure 7.3: Crushed stones after oedometer tests conducted at low and high stress levels (adapted from Alonso et al., 2013)

The stress-strain behavior of rockfills as discussed by previous works (De Mello, 1977, Charles and Watts, 1980, Indraratna et al., 1994) is nonlinear, stress dependent and inelastic. The shear resistance of rockfill depends on the particle size distribution, shape, relative density, porosity and confining stress.

The effect of dilation at low normal stress level and crushing of angular particles at higher stress levels should be considered when triaxial results are analyzed with modeling predictions. The influence of particle crushing during compaction and shearing on the shear strength of rockfills is a complex phenomenon.

In triaxial compression tests, the friction angle is also affected by dilation effect in very low confining pressure and particle crushing at very high confining pressures which subsequently contribute for reduction of internal friction angle. At low confining pressure dilation increase the angle of internal friction and contributes to steep failure envelopes as is observed in dense sands (Charles and Watts, 1980). Moreover increasing confining pressure can have effects: reducing brittleness of the stress-strain curve, increasing strain to failure, and decreasing the dilation effect as shown in Figure 7.4. Charles and Watts (1980) remarked the influence of confining pressure on the shear strength of the rockfill using large-scale triaxial tests (Figure 7.5).

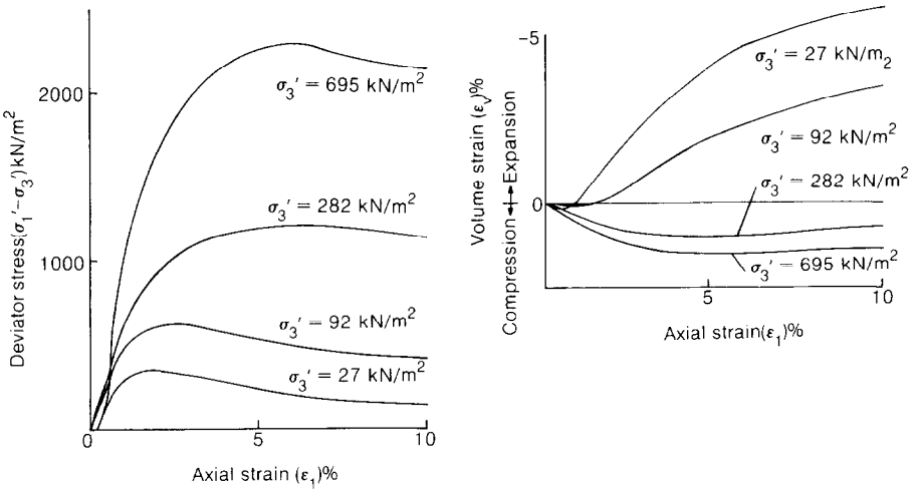

Figure 7.4: Drained triaxial compression tests on heavily compacted sandstone rockfill at various confining pressures (after Charles and Watts, 1980)

Donaghe and Cohen (1978) discussed strength and deformation of rockfill using large-scale triaxial testing. They showed the influence of gradation, confining pressure, relative density, and engineering property of aggregate particles on consolidated-drained strength and deformation behavior of gravely materials. Samples are subjected to confining pressure varying from 400kPa to 2.75 MPa. Unconfined compression strength of the specimens varies from 68 to 206 MPa. And maximum particle sizes considered in the analysis are around 76 mm, 51 mm, 25.4 mm, 12 mm and 6 mm. The study found that the axial strain at failure increases with increasing confining pressure for each gradation. The rate of change of stains decreases at high confining pressures. Moreover, the change in volumes of specimens at failure is positive (volume increase) at low confining pressure and negative (volume decrease) at high confining pressure where finer particles experience the greatest change in volume at each confining pressure.

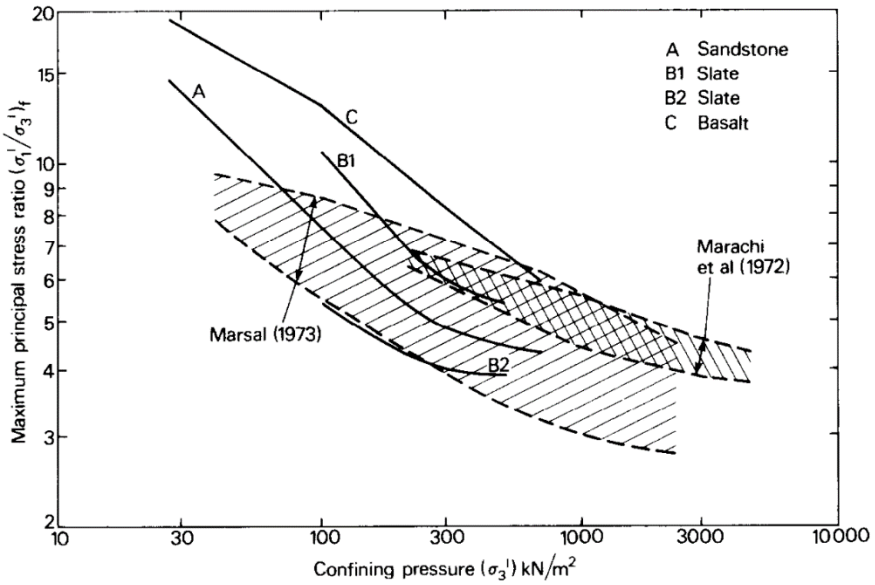

Figure 7.5: Influence of confining pressure on the maximum principal stress ratio (after Charles and Watts, 1980)

A similar study which was conducted by Williams and Walker (1983) on stability of mine waste rockfills. Their study showed evaluation of shear strength parameters of poor quality rockfills by employing large scale triaxial testing. The samples have average initial density of around 16 and 20 kN/m^3. The test was carried out by applying confining stress varying from 140 to 640 kPa. The triaxial samples were 150 mm diameter by 300 mm height. From their experimental findings, they concluded that the strength of waste rockfills depends on the particle size distribution of the waste rockfill. In good quality rockfill, the proportion of sand size or finer is less than 15% and about 25 to 35% cobble size or coarser, comprising fresh rock. While in poor quality rock fill, about 20% is sand size or finer and about 25% cobble size or coarser, comprising moderately to slightly weathered rock.

Williams and Walker (1983) showed that the internal friction angle decreased with maximum particle size and with confining pressure (Figure 7.6). Saturation significantly reduce the strength of initially loose material and the effect reduces with increasing the confining pressure. While the initial density has little influence on strength envelopes (Williams and Walker, 1983) (Figure 7.7).

Previous study conducted by Indraratna (1994) revealed the angle of friction for rockfill is affected by the size, shape, by degree of compaction, moisture content etc...

The design value for rockfills friction angle varies from 35°-40°. A review of several triaxial test on rockfills by Leps (1988) showed friction angle values between 35-40° for a stress level approximately between 0.1-1.0MPa.

Williams and Walker (1983) determined shear strength parameters (φ= 32° and c= 12kPa) for waste rockfill which are substantially lower than the reported rockfill strength parameters used for dam construction.

Garcia and Romo (2009) revised rockfill strength obtained by previous large-scale triaxial tests using cascade correlation networks.

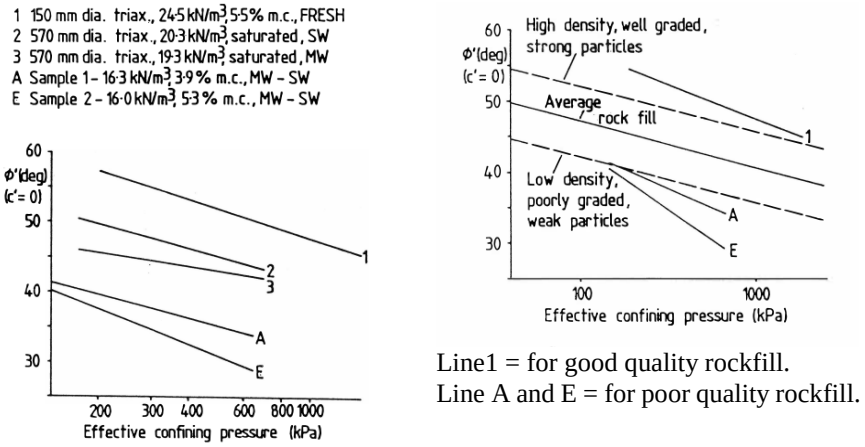

Figure 7.6: Effective friction angle (φ´) vs effective confining pressure (after Williams and Walker, 1983)

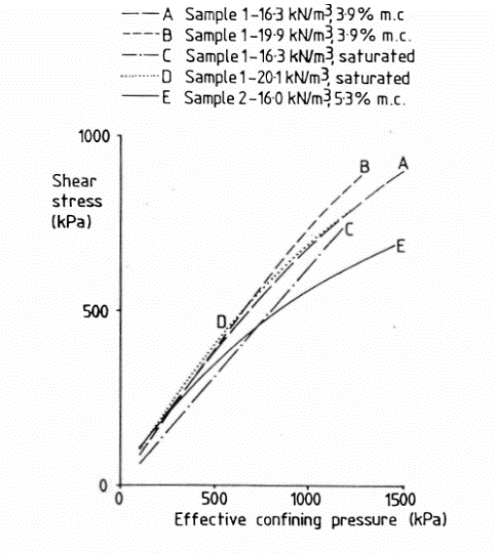

Figure 7.7: Effect of saturation and density on failure envelopes (after Williams and Walker, 1983)

Several authors (Lobo-Guerrero et al., 2005, Deluzarche and Cambou, 2006, Xu and Song, 2009) discussed the effect of particle shape, particle breakage on the overall behavior of the behaviors rockfill using DEM approaches. Obviously, numerical model results can be compared with the large-scale triaxial tests.

7.3 Numerical compression tests

With the aim of assessing the deformability and shear strength of a rockfill embankment, several numerical analyses have been carried out. The model results have not been compared with large-scale triaxial experiments. These exercises are only intended to understand the behavior of a rockfill model when subjected to biaxial compression load. Particularly in this research, it is crucial to assess the characteristics of the stabilizing rockfill embankment when subjected to compression load from the moving slope. Moreover, the behavior of the rockfill model should be isotropic, therefore, during modeling with DEM approach the jointing pattern take in to account this concept. For instance, the use of random joint pattern (e.g. voronoi polygons) can reproduce this concept.

The model is subjected to biaxial compression keeping low confining stresses between 100 to 1000kPa which are typically representative of the actual confining pressures in a rockfill. The model is axially loaded by

servo-controlled displacement rate of 0.2mm/cycle. Axial stresses and strains are calculated automatically by including user FISH functions to the code.

7.3.1 Modeling procedure

A 1x1m square model which consists of a random, irregular interconnected voronoi blocks or "granular materials" has been assumed for the rockfill model. The rockfill is represented as a blocky structure or "granular material" which is formed by defining voronoi seed value. Figure 7.8 illustrates the three models generated considering different sizes of the voronoi polygons.

The effect of block size on behavior of rockfill was assessed by using three block sizes (i.e. size of 0.08m, 0.04m and 0.02m which correspond to a size ratio of 12.5, 25 and 50 respectively). The ratio value has been calculated by dividing the model size to the size of voronoi polygons (Figure 7.8).

In the analysis, each block is zoned to make full deformability and characterized by purely elastic properties (E, ν). While joints have both elastic properties, joint normal stiffness (k_n), joint shear stiffness (k_s) and plastic parameters (joint friction angle, φ, and cohesion, c) as presented in Table 7.1. Joints obey Mohr-Coulomb yield criterion. Uniaxial and biaxial compression tests have been carried out in plane stain condition.

Table 7.1: Assumed mechanical properties for numerical compression tests

Young Modulus (blocks) E (GPa)	Poisson's ratio ν	Joint normal stiffness, k_n (GPa/m)	Joint shear stiffness k_s (GPa/m)	Joint friction angle φ* (°)
20	0.25	600	300	12

*Joint friction angle is varied in order to assess rockfill model strength properties.

The model is fixed at the bottom boundary which is similar to triaxial testing and subjected to lateral confining stress on the left and right boundaries (Figure 7.9). Then axial compression is applied by specifying boundary velocity at the top, and then calculations have been carried out for a given confining stress value to evaluate the peak axial load. The confining stresses vary from 100kPa to 1000kPa.

In order to minimize inertial effects similar to the standard servo-controlled laboratory tests, here it has been applied a FISH function to the UDEC code to maintain a servo-controlled loading condition by setting the limit values to the maximum and minimum unbalanced forces.

In the model analysis, the cohesion and friction angle of the joints are considered to control the uniaxial compression strength and shear strength parameters of the rockfill model. While the joint stiffness together with the bulk and shear moduli of the intact blocks (granular materials) are used to control the modulus of the rockfill model. The effect of pore pressure is not considered here. Previous study by Christianson et al. (2004) can give useful insights about UDEC simulation techniques.

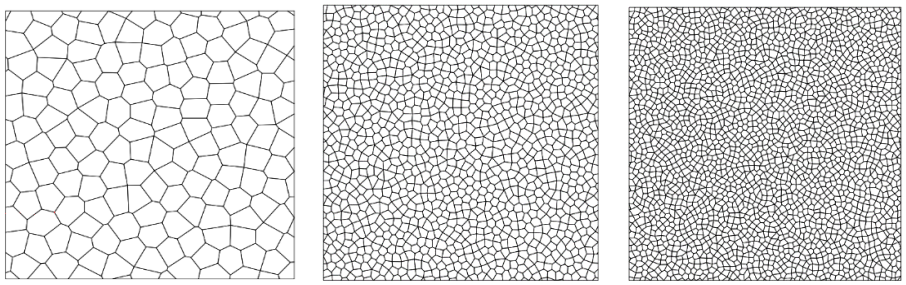

Figure 7.8: Models used for numerical compression analyses, formed using voronoi polygons (a) ratio = 12.5, (b) ratio = 35 and (c) ratio = 50. Note that the ratio is obtained by dividing the model size (1m) by the voronoi polygon "grains"size

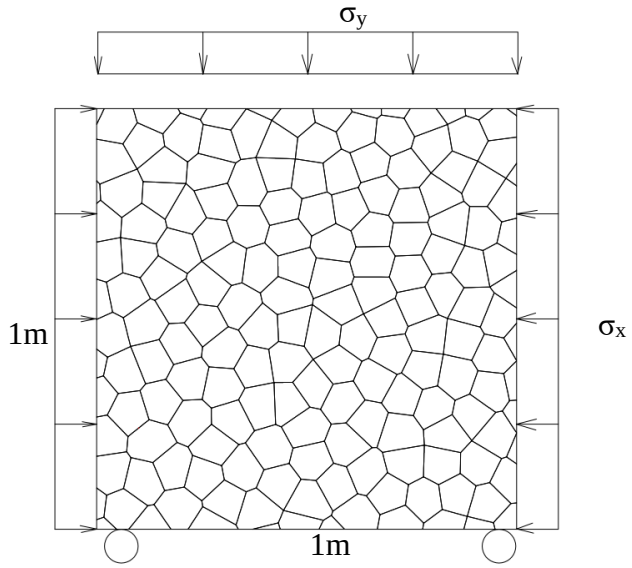

Figure 7.9: Boundary and loading conditions considered in the numerical modeling

7.3.2 Discussion of numerical results

The deviatoric stress vs axial strain curves has been illustrated in Figure 7.10, and the peak stress depends on the confining stress. Moreover, the initial tangent stiffness decreases with the confining stress. The peak stresses can be easily identified from the curves although there are some oscillations around the peak value. The axial strain is limited to 1.2% throughout the calculations, obviously this is due to the high stiffness parameters which are assigned for joints and intact blocks (Table 7.1). Simulations which were carried out with relatively lower stiffness values will be presented latter.

The peak friction angles which are evaluated using Equation (7.1) are listed in Table 7.2 considering models with size ratio of 35 and 50.

The peak friction angle is estimated from:

$$\varphi_p = \sin^{-1}\left(\frac{\frac{\sigma'_{1f}}{\sigma'_{3f}} - 1}{\frac{\sigma'_{1f}}{\sigma'_{3f}} + 1}\right) \tag{7.1}$$

where σ_{1f} and σ_{3f} are the principal stresses and φ_p is the peak friction angle.

The estimated friction angle increases when the confining stress reduces (Figure 7.11). In addition, the friction angle reduces with increasing size ratio, i.e. a higher friction angle is obtained when the size of voronoi polygons or "grains" are larger. The effect of block or "grain" size ratio on friction angle is not reasonable as expected from the behavior of rockfills. This implies that the effect of crushing of angular particles at high confining stresses couldn't be simulated by UDEC modeling since the code does not consider such effects.

As the confining stress increases from 100 to 1000kPa, the friction angle decreases from 64^o to 49^o for the model with size ratio of 35 and for the model with size ratio of 50, it decreases from 58^o to 40^o.

Table 7.3 illustrates the relationship between the assumed strength properties of the joint (φ, c) with the estimated rockfill model strength parameters (φ, c, and uniaxial compression strength, UCS).

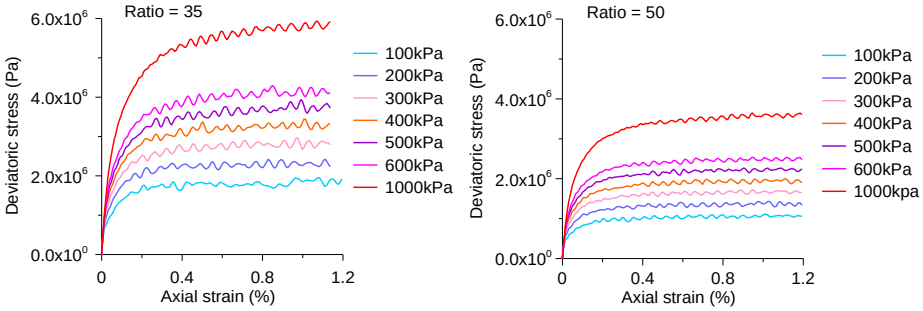

Figure 7.10: Stress- strain curves for rockfill model considering φ = 12° for joints

Table 7.2. Estimated friction angle of the rockfill model at various confining stresses

		σ_1/σ_3		φ(°)	
Test	σ_3(kPa)	ratio= 35	ratio= 50	ratio=35	ratio= 50
1	100	19	11.8	64	58
2	200	12.5	7.9	59	51
3	300	10.3	6.6	55	48
4	400	9.25	5.85	54	45
5	500	8.4	5.42	52	44
6	600	8	5.2	51	43
7	1000	7	4.6	49	40

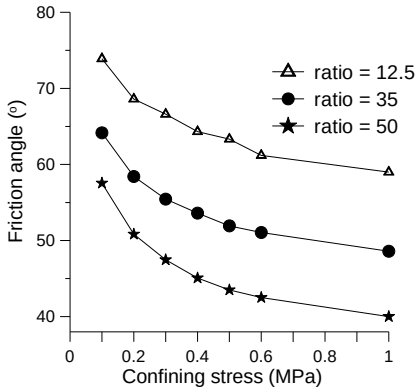

Figure 7.11: Friction angle vs confining pressure at different block size ratios

From the curves of principal stresses i.e. σ_1 vs σ_3 (see Figure 7.12), the shear strength parameters of the rockfill model have been estimated using a linear fit. The effect of block or "grain" sizes on strength envelopes in principal stress space is also shown in Figure 7.12.

Table 7.3: Rockfill model parameters estimated from joint properties considering block size ratio=50

Joint properties		Estimated parameters for the rockfill model		
φ(°)	c (MPa)	φ(°)	c(MPa)	UCS* (MPa)
12	0	35	0.23	0.89
14	0	37	0.24	0.98
15	0.001	33	0.41	1.51
16	0	42	0.17	0.76
27	0	51	1.08	6.01

*UCS is the unconfined compression strength.

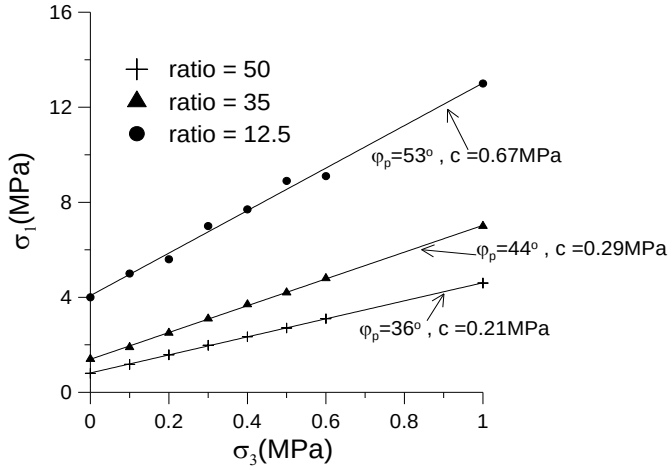

Figure 7.12: Strength envelopes (Mohr Coulomb) of the rockfill model for various block size models considering φ= 12° for joint friction angle

Influence of stiffness parameters

In this section, the influence joint and block stiffness on the deformation behavior of the model is discussed. Therefore, in the following simulations a relatively lower values of normal joint stiffness and the intact block Young's modulus have been employed as compared to values reported in Table 7.1.

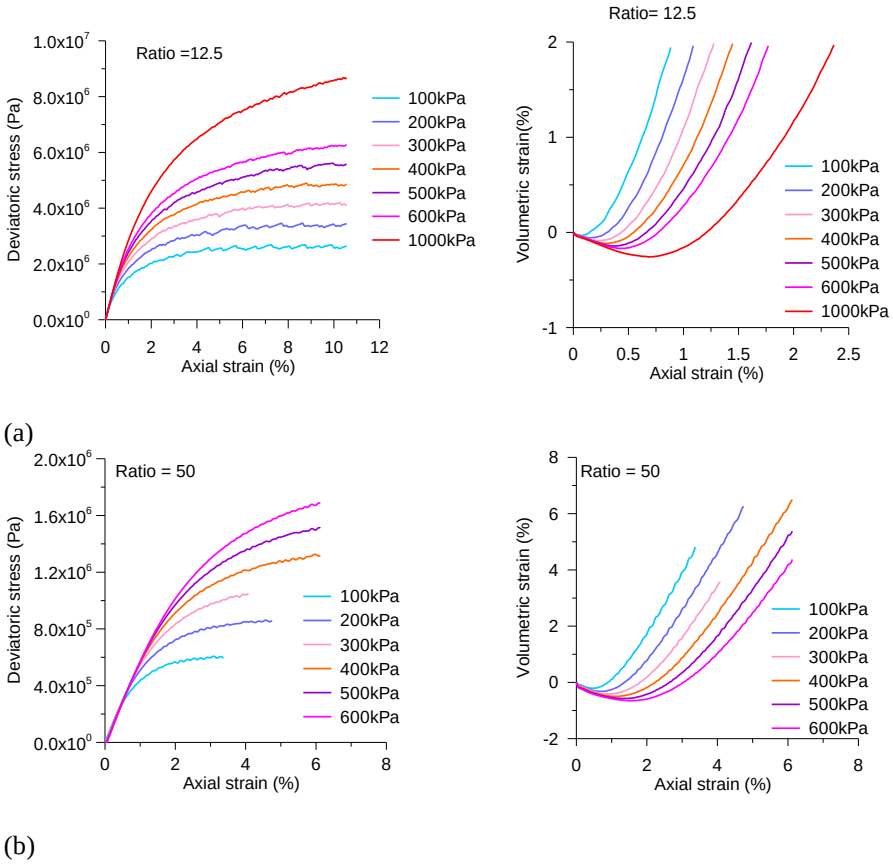

Figure 7.13: Stress-strain curves for rockfill model for block size ratio of 12.5 (a); and size ratio of 50 (b) taking in to account confining stresses between 100kPa to 1000kPa and stiffness properties, E=8GPa, k_n =6GPa

The stress-strain curves for large and small block size ratios show similar behavior as depicted in Figure 7.13. The maximum axial stress is lower when smaller blocks or "grains" size model is considered as compared to large blocks or "grains" size model. However, the volumetric strain is higher in smaller blocks size model as compared to large blocks size model (Figure 7.13).

Besides this, the calculation time for small blocks size model is quite long, therefore, the peak axial stresses are not fully achieved during the calculations especially for high confining stresses (Figure 7.13). Therefore, numerical results obtained using relatively large blocks model (i.e. size ratio of 12.5) have been discussed herein since computation time is relatively shorter.

As it has been presented in Table 7.4, the estimated internal friction angle, φ, increases when the confining stress decreases.

Table 7.4: Numerical results obtained using E=8GPa, k_n =6GPa using block size ratio = 12.5

Test	σ_3 (kPa)	σ_1/σ_3	φ (°)	ε_a (%)	ε_v (%)
1	100	27	68	4	23.5
2	200	18	63	6	36.5
3	300	14.7	61	7	42
4	400	13	59	8	47
5	500	12.2	58	9	52
6	600	11.35	57	10	57
7	1000	9.70	54	10.5	50

In further analyses, the influence of joint normal stiffness, k_n, on the model response has been assessed keeping E=8GPa for all the blocks. Figure 7.14 shows that the deviatoric stress decreases as the value of k_n decreases. Similarly, the volumetric strain increases when the joint stiffness decreases. The shear strength envelopes also showed differences with joint stiffness (Figure 7.15). From these results, it has been understood that the joint stiffness parameter controls both the strength and deformation behavior of the rockfill model.

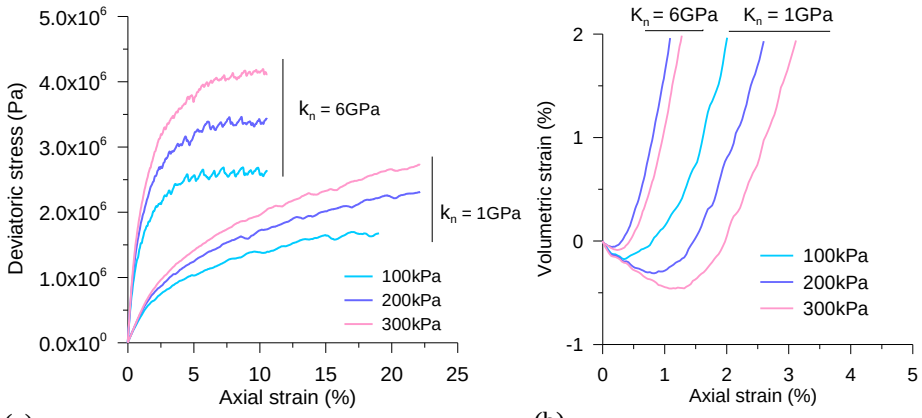

Figure 7.14: Stress – strain curves (a), and volumetric strain vs axial strain curves

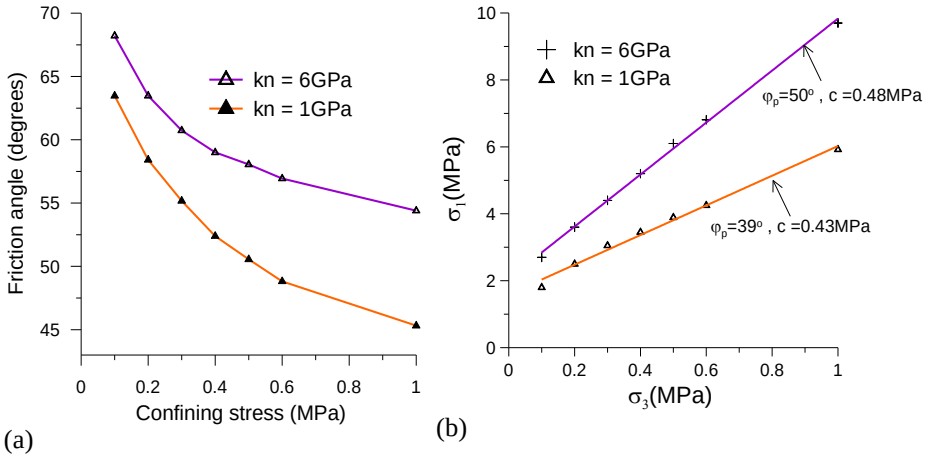

Figure 7.15: Friction angle vs confining stress curves (a), and failure envelopes in principal stress plane

Effect of block deformation modulus

Further analyses were also conducted to assess the influence of the elastic modulus of the blocks or "grains" on the model responses. Thus in the analyses, the value of k_n = 1GPa has been kept to the joints. Figure 7.16 depicts the stress–strain curves for different confining stress when E = 0.1GPa and E= 0.8GPa. Figure 7.17 shows that a relatively higher friction angle has been obtained when the value of E =0.8 GPa was considered as compared to when E=0.1GPa.

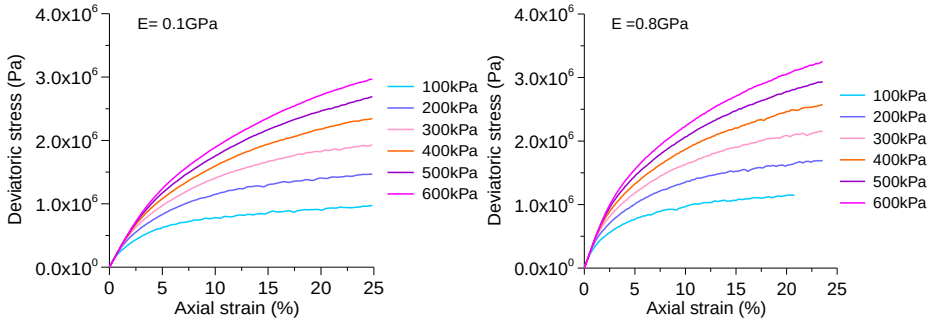

Figure 7.16: Stress-strain curves for numerical rockfill model when E= 0.1GPa and 0.8GPa

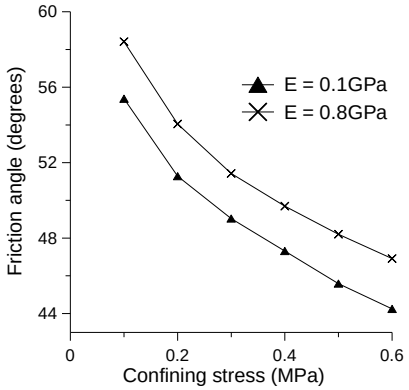

Figure 7.17: Friction angle vs confining stress curves at two different values of E

Non- linear failure envelope

The non-linear failure envelope for rockfills can be fitted by adopting empirical relation suggested by De Mello (1977) in Equation (7.2**)** for some of the numerical results. Figure 7.18 shows the strength envelop drawn by adopting the non-linear relation given by

$$\tau = A(\sigma_n)^b \qquad (7.2)$$

where A and b are empirical constants, σ_n, is normal stress and τ is the rockfill shear strength.

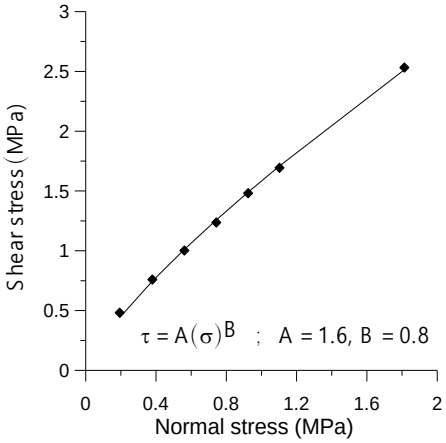

Figure 7.18: Strength envelope for rockfill model with block size ratio = 12.5

7.3.3 Comments

These numerical exercises can give us some useful insights about the strength and deformation behavior of rockfills. Numerical biaxial and uniaxial compression tests were performed via UDEC code in plane strain condition. The effect of confining pressure on the friction angle of the rockfill model has been presented. Besides this, the influence of joint stiffness, block modulus on deformation and strength of the model was studied. The shear strength of the model can be predicted from the assumed joint shear strength parameters (c, φ). It has been understood that models with large blocks, or coarser particles or "grains" yields higher strength as compared to smaller block model. The expected behavior of particle breakage particularly at high normal stresses cannot be modelled by UDEC. The computation time in smaller blocks size model (i.e. large number of blocks) is quite long, so few results have been presented from this type of model. The influence of pore pressure on the rockfill model behavior was not considered in these numerical tests.

7.4 Modeling slope-embankment interaction by DEM

From a practical point of view, a moving mass can be stabilized by constructing a restraint structure, for instance rockfill embankment or berm at the toe part.

In order to stabilize the moving slope in Chiascio valley, a rockfill embankment at the toe part, not yet realized, was proposed, but design works of the embankment have been completed (Figure 7.19). To understand the mechanical behavior of the rockfill materials large scale triaxial tests (dimension D=200mm and H=400mm) was employed on the rockfill materials. The friction angle, φ, between 39-44^{o} has been reported from the test result analyses.

To explore the mechanical effect of the toe restraint provided by embankment on the moving slope, a numerical modeling using a discontinuum approach has been realized (Figure 7.20). The slope-embankment interaction has been discussed by referring the model results (i.e. horizontal displacement and joint shearing).

Similar to the previous DEM models, block insides the embankment are elastic, while rockfill joints and the interface joint (Figure 7.21) are modelled as elasto-plastic obeying Mohr-Coulomb failure criterion (Table 7.5).

Table 7.5: Joint properties adopted in slope-embankment simulations

Description	Joint constitutive model	Friction angle φ (°)	Normal stiffness k_n (GPa/m)	Shear stiffness k_s (GPa/m)
Rockfill joints	Mohr-Coulomb	30	2.3	0.23
Interface joint	Mohr-Coulomb	27	2.3	0.23

This section highlights the benefits of the remedial measure using numerical modeling. The deformation mode and possible gain of safety factor has been presented. As it has been previously discussed in Chapter 4 of the slope modeling, the two joint patterns (i.e. staggered and persistent joint pattern) have been considered here too for the slope model. The embankment has been also represented by a blocky structure with random joint pattern (voronoi polygons) to get isotropic responses during mechanical interaction with the moving mass. The designed rockfill embankment is about 200m long and 41 m high.

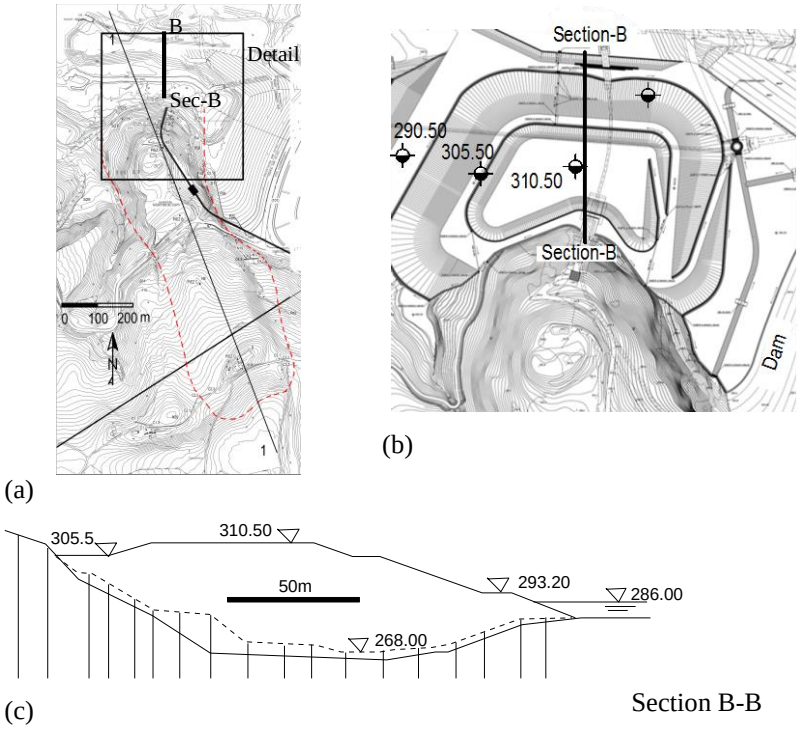

Figure 7.19: Map which show location of embankment (a); plan (b) and typical cross-section of the proposed stabilizing embankment (c)

In all analyses, average groundwater table has been considered inside the slope taking in to account the reservoir level of 274m a.s.l at the toe part. The usual basal shear strength reduction calculations have been carried out to examine the slope response to the toe restraint provided by the embankment.

The mobilized friction angle in the model with embankment is around $\varphi = 6.^{o}$ as compared to 7.6^{o}, when the model without rockfill embankment has been considered (Figure 7.22). This means that by looking only the change in mobilized friction angle (i.e. 1.6^{o}), the model with embankment requires about 20% lower friction angle to see large displacement increments as compared to the other model (no embankment case). Obviously, similar comparisons can be also made by just looking the corresponding model displacement magnitudes obtained at various basal friction angles during the strength reduction stages (Figure 7.22).

The applied remedial measure reduces significantly both the horizontal displacement and internal joint shearing especially in the toe part (Figure 7.23).

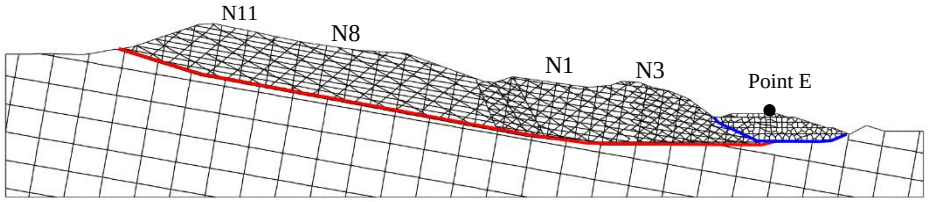

Figure 7.20: Model configuration established to represent slope-embankment interaction. Red line represents the basal slip surface while blue line stands for the interface joint between slope and embankment

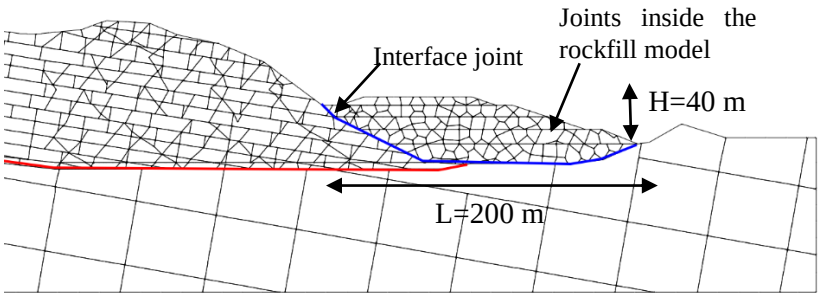

Figure 7.21: Detailed mode set up with the rockfill embankment

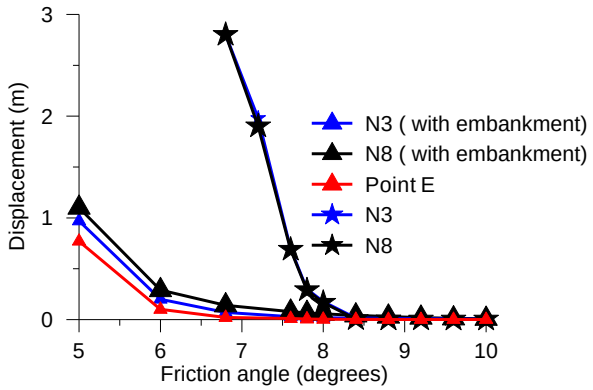

Figure 7.22: Horizontal displacement vs basal friction angle curves taking in to account the embankment or without the embankment

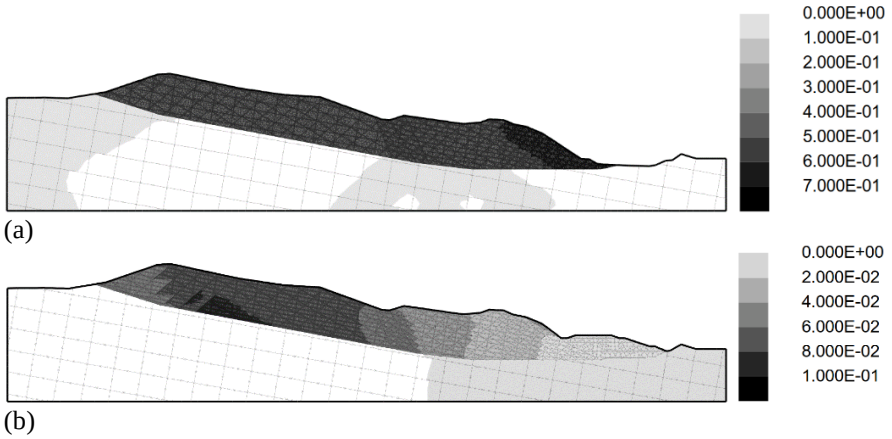

Figure 7.23: X-displacement contours (a) without embankment and (b) with embankment included in the model when the basal friction angle is 7.6°

7.4.1 Influence of stabilizing embankment on creep behavior

In this section, the role of the proposed stabilizing embankment on the creep behavior of the ongoing slope movement has been examined.

As it has been presented before in Section 6.7, the creep model (CVISC) is applied only to blocks located in the transition zone and basal slip surface (Figure 7.24). The Maxwell viscosity, η^M, = $2.2x10^{15}$ Pa.s has been implemented to the basal slip surface while for the transition zone η^M =$2.2x10^{17}$ Pa.s has been applied to reproduce the observed translational deformation behavior.

The predicted velocity has been compared with the previous modeling results which have been obtained without embankment (see Section 6.8). The friction angle of blocks located in the basal slip surface and in the transition portion is 8.8^{o} and 31^{o} respectively.

Figure 7.25 illustrates the estimated horizontal displacements and corresponding velocities by the model. It is worthwhile to note that the velocity of points N8 and N11, which are located in the upper part of the moving mass, experienced an increased velocity as compared to N3 and N4 located in the front part. The gradual stabilization effect of the embankment has been appreciated by observing the velocity of the movement at the upper (points N8, N11) and lower part (points N3, N4) during the creep movement. Therefore, the velocity of the lower part (N3, N4) has been reduced since the beginning of the creep analyses while the upper part (N8, N11) approaches to the lower velocity gradually (Figure 7.25b). The model displacement can be compared with the measured displacement values in Figure 7.26; obviously, the applied stabilizing embankment reduces significantly the displacement magnitudes, especially in the toe part (N3).

Moreover, the average velocity of all targets approaches to 0.008 m/y, which is half of the average velocity (i.e. 0.016m/y) obtained without applying the rockfill embankment (Figure 7.27).

Figure 7.28 depicts the deformed shape of the model at a creep time of 40 years, which shows the shear failures observed at the interface between the moving slope and inside the embankment body.

Previous studies (Gioda and Borgonovo, 2004, Corkum and Martin. 2004) remarked the effectiveness of toe berm in reducing the rate of slope deformation. A study by Puzrin and Schmid (2011) discussed the behavior of a constrained creeping slope, which tend to slow down approaching to final displacements or experiences passive failure behind the stabilizing structure followed by a post failure evolution of the moving mass. A study by Corkum and Martin (2004) also highlighted that toe berms significantly reduce the rate of slope displacement.

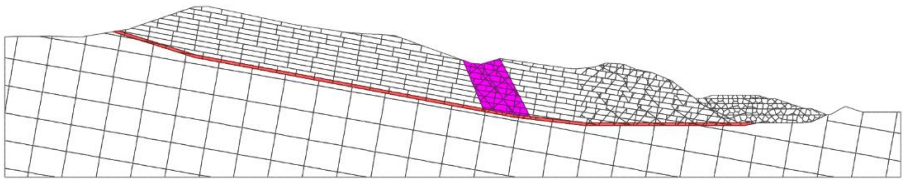

Figure 7.24: UDEC model set up including the rockfill embankment

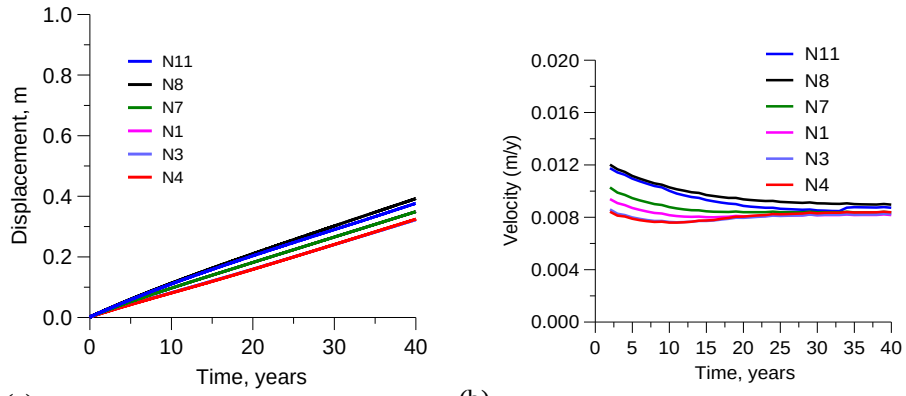

(a) (b)

Figure 7.25: Estimated horizontal displacement by CVISC model (a) and the corresponding velocities calculated from the displacements (b)

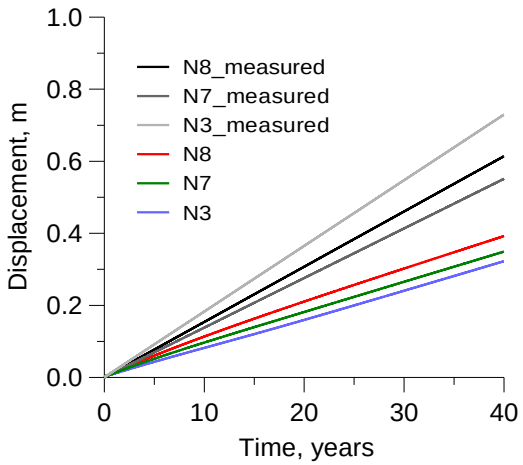

Figure 7.26: Estimated horizontal displacements by the model with rockfill embankment and the corresponding target displacements calculated using average velocity obtained from the observed target displacements linear regression approaches

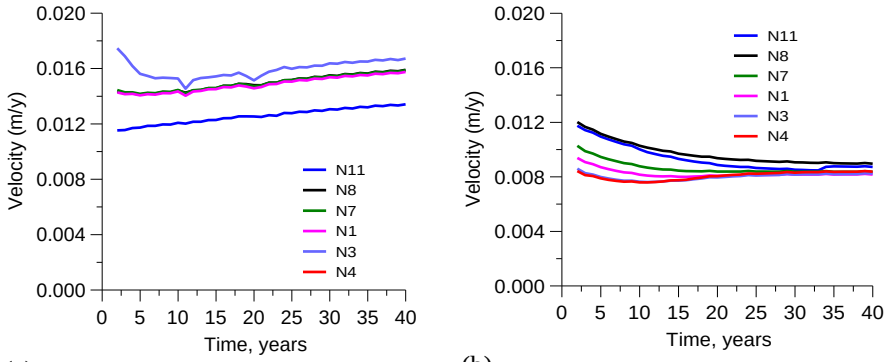

Figure 7.27: Comparison of average velocity estimated using CVISC model: (a) without rockfill embankment and (a) with rockfill embankment

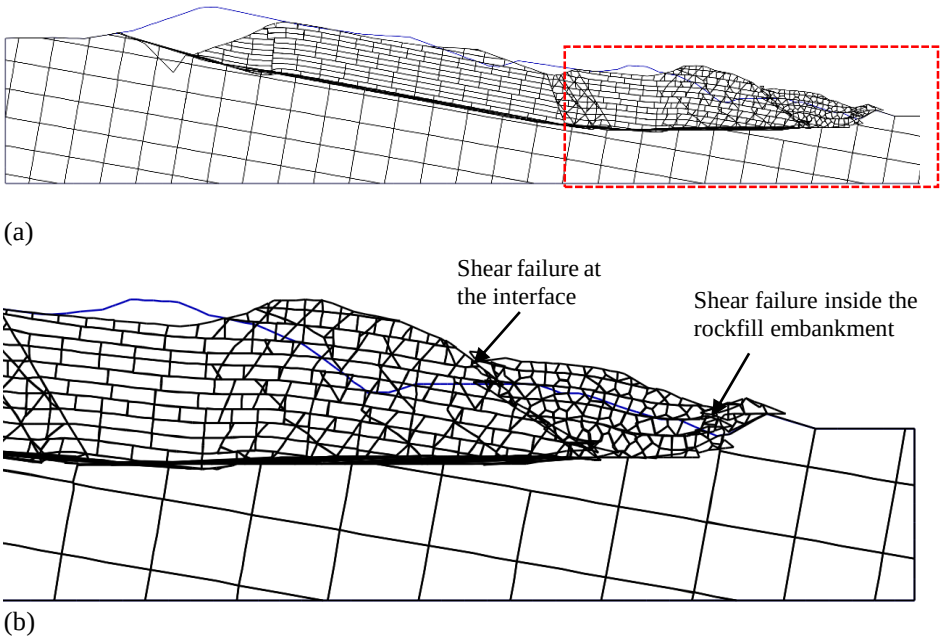

Figure 7.28: Deformed shape (x250) after 40 years of creep deformation (a) and portion of the deformed shape at the toe part (b)

7.5 Conclusions

On the basis of compression tests using DEM modeling, the strength and deformation behavior of the rockfills has been discussed. For instance,

the influence of the rock joint friction angle on the overall shear strength of the rockfill material has been highlighted.

The influence of the proposed remedial measure (a large rockfill embankment at the toe), not yet realized, on the slope deformation (shearing and horizontal displacement) and safety factor has been remarked. The remedial measure can reduce the ongoing average velocity by almost 50%, which is around 8 mm/y as compared to velocity 16 mm/y, evaluated without including the stabilizing embankment. However, these beneficial effects are also accompanied by diffuse yielding inside the stabilizing embankment and at the interface of the embankment with the moving slope.

Chapter 8

8 Summary, conclusion and reccomendation

8.1 Summary

This dissertation focuses on the study of a slow movement in a complex rock formation. The summary of the research is presented below:

- In order to understand the behavior of the ongoing slope movement, a rigorous analyses of the site investigation data which include geomorphological, geotechnical, piezometer readings and displacement monitoring has been carried out.

- With the help of DEM modeling, the observed deformation mode has been studied. The slope has been modelled as a blocky structure by introducing reasonable joints sets, bedding and sub-vertical joints. In the analyses, the influence of model structure (slip surface geometry, block scale and joint pattern) on the mobilized friction angle and deformation mode has been explored. In a further analyses the influence of pore pressure regime change on the mobilized friction angle of the slip surface has been studied too.

- Hydromechanical analyses have been carried out in order to examine the influence of pore pressure regime change on the slope behavior. Flow analyses have been carried out to estimate the observed piezometer readings using both continuum and discontinuum modeling approaches. The influence of the rock mass permeability and water infiltration on the pore pressure distribution has been studied. Further analyses have been performed to assess the influence of stepwise filling of the reservoir on the pore pressure distribution and slope deformation.

- The observed stationary movement has been modelled with visco-elastoplastic model. The ongoing stationary movement has been reproduced by the model. A new modified viscoplastic model has been considered too. This viscoplastic model has been

employed to assess velocity changes due to reservoir level increase or loss of friction angle.

- The influence of the proposed remedial measure (a large rockfill embankment at the toe) on the ongoing slope displacement and joint shearing has been highlighted. The rockfill has been modelled as a blocky structure via discontinuum model using random joints in order to obtain an isotropic response. Creep analyses have been carried out to assess the influence of the rockfill embankment on the steady state velocity.

8.2 Conclusions

The behavior of slope movement in a complex rock formation has been analyzed in detail. This thesis integrates the following main aspects and will be considered in the conclusion part.

- Analysis of site investigation.
- DEM modeling of the blocky structure.
- Hydromechanical analysis.
- Modeling time dependent behavior of the ongoing movement.
- Remedial measure (rockfill embankment).

8.2.1 Analysis of site investigation

The detailed data analysis shows that the ongoing movement is characterized by a stationary movement (constant velocity), also influenced by transient variation of pore pressure regime.

The rock mass is characterized by complex rock formation (Marly-arenaceous formations). Based on field investigations, the slope is characterized by different degree of fracturing: more disturbed toe part and less fractured upper part.

The shape of the slip surface has been reasonably traced on the base of inclinometer profiles and borehole loggings only in the toe part. While in the upper part, reasonable hypotheses have been established on the basis of the location of the damaged tunnel section and morphological aspects. This issue has been studied in detail with the help of DEM models.

The basal shearing zone is formed by tectonized clay gouge and is characterized by a mobilized strength close to the residual condition.

Extensive analyses of correlation between rainfall measurements and piezometer readings have been carried out. The results showed that the 3 months (90 days) cumulative rainfall is best correlated with piezometer levels. In further analyses, the 90 days cumulative rainfall exceeding the average value (i.e. excess rainfall) is reasonably correlated with the increase in piezometer level. Moreover, the peak displacement velocities (tunnel extensometer and target points) shows some reliable correlation with the three months cumulative excess rainfall and peak increase in piezometer levels for some periods.

By using statistical models, the observed displacement trend has been studied. By adopting a given standard model, the observed displacement trends of tunnel extensometer and targets points, located at various part of the slope, can be described well, which confirms that the ongoing movement is characterized by a monotonic movement.

The lateral boundary of the movement can be traced more confidently on the E side, on the base of the displacement measurements, while in the west side distinction between stable and unstable zone fades away. The current kinematics of the movement can be outlined as a compound mechanism in which a block system is sliding on a low inclination basal plane accompanied with inter-block deformation.

8.2.2 DEM modeling of the blocky structure

With the intention of exploring the observed slope deformation mode and mobilized friction angle of the slip surface, several DEM models have been established. The slope structure (block size, joint pattern and shape of the slip surface) has limited effect on the mobilized friction angle of the slip surface. The collapse limit obtained from the model analysis is close to the residual friction angle of the clay gouge. The staggered joint pattern experiences less joint shearing as compared to the persistent joint pattern. The translational movement accompanied by internal shearing at the transition zone and location of change of slip surface inclination characterize the overall deformation behavior of the slope. Moreover, the mobilized friction angle is less dependent on the change of groundwater table and reservoir level rise.

8.2.3 Hydromechanical analysis

Using the discontinuum modeling approach, the observed average and maximum piezometer levels have been estimated by employing steady state flow analyses considering reasonable joint properties (initial aperture, residual aperture and joint pattern). To account the effect of infiltration amount on the groundwater table, two approaches have been realized. In the first case, low boundary pore pressure (0.1-0.2kPa) have applied on the surface to trigger infiltration amount. While in the second case, inflow rate (in the order of $1x10^{-5}m^3/s$) have been applied to each boundary joints. The second approach gives reasonable groundwater profile as compared to the first one. It is worthwhile to remind that the applied total infiltration amount in the discontinuum model does not match with the expected infiltration amount in the field since the model considers only few of the actual joints.

A continuum model has been also applied to estimate the observed groundwater profiles considering reasonable rock mass permeability of slope regions (upper, lower and transition zones) and infiltration amount. Contrary to the discontinuum modeling, the applied infiltration which is estimated from the average rainfall by empirical methods can be related to the expected infiltration amount.

Further coupled hydromechanical analyses have been carried out considering the step wise filling of the reservoir. The displacement rate caused by each step increase of the reservoir level has been highlighted.

8.2.4 Modeling time dependent behavior

The observed stationary movement (constant velocity) can be described reasonably by employing visco-elastoplastic (CVISC) model to the creeping zones (i.e. transition zone and slip surface). A new modified viscoplastic model has been considered too. This new model allows to simulate the velocity change as a result of filling of the dam or strength reduction which cannot be discussed by the CVISC model. Moreover, in the new model the stress state can exceed the yield limit and the viscoplastic deformation strictly depends on the creep parameter, η^{vp}. If the stress state is below the yield limit, the model will be simplified to the standard Burgers viscoelastic model.

8.2.5 Remedial measure (rockfill embankment)

The proposed stabilizing embankment decreases the joint shearing and horizontal displacement particularly in the toe part. The rockfill embankment decreases by almost 50% the velocity of the movement. Moreover, the velocity in the front part (N4, N6) decreases immediately since the beginning of the calculation while in the upper part (N8, N11) the velocity decreases gradually to the same velocity (8 mm/y). However, these benefits are accompanied by shear failure at the interface location with the slope and inside the rockfill embankment.

8.3 Recommendations for future studies

- Since this study considers the modeling of the complex rock slope structure by employing a deterministic joint pattern, it would be more interesting to implement a stochastic generation of joint system which resembles the real situation (i.e. the complex joint orientation usually encountered in the field). In this way, the overall behavior of complex rock formation: e.g. rock mass permeability, hydromechanical behavior and mechanical deformation can be understood reasonably.

- Besides the Mohr –Coulomb joint model, it is recommended to consider the Barton-Bandis joint model to the rock joints for detail discussion of joint behaviors.

- The seepage process would be fully understood if a 3D model is developed in both continuum and discontinuum modeling approaches, in order to take in to account influence of lateral flows, slope morphology on the steady state groundwater profile.

- Since the new user defined model is basically implemented in a continuum model, it is more interesting to employ the same concept to the discontinuum model. That means by considering the creep behavior of a continuum material bounded by shearing joints.

- The influence of the large rockfill embankment at the toe would be understood better if a 3D model is developed taking in to

account the location and geometry of the proposed rockfill embankment.

- Moreover, the deformation behavior of slopes in a complex rock formation is still a challenging problem since it depends strictly on the situation of the case study (i.e. geomorphological, geotechnical, and boundary situation), so a research has to be continuously progressed with the help of field investigations, laboratory tests and numerical modeling.

Appendix A

In this appendix, the formulation of the new modified viscoplastic model has been presented. The main task of the new constitutive law in FLAC code is to update the new stress in each time step from the old stress tensor and strain increments.

The Mohr-Coulomb shear yield function, f_s, is given by

$$f_s = \sigma_1 - \sigma_3 N_\varphi + 2c\sqrt{N_\varphi} \tag{A.1}$$

$$\text{where} \quad N_\varphi = \frac{1+\sin(\varphi)}{1-\sin(\varphi)} \tag{A.2}$$

The shear potential function, g_s, which corresponds to the nonassociated flue rule is given by

$$g_s = \sigma_1 - \sigma_3 N_\psi \tag{A.3}$$

$$\text{where} \quad N_\psi = \frac{1+\sin(\psi)}{1-\sin(\psi)} \tag{A.4}$$

where σ_1 and σ_3 are the major and minor principal stresses; c, φ and ψ are the cohesion, friction angle and dilation angle of the Mohr-Coulomb section respectively.

If shear failure is detected, the viscoplastic strain rate $\dot{\varepsilon}_i^{vp}$ is given by

$$\dot{\varepsilon}_i^{vp} = \gamma \left\langle \Phi\left(f_s\right) \right\rangle \frac{\partial g_s}{\partial \sigma_i} \qquad \text{for i = 1, 2, 3} \tag{A.5}$$

where γ is the fluidity parameter and $\left\langle \Phi\left(f_s\right) \right\rangle$ is the viscous nucleus. Assuming the viscous nucleus is equal to $\left\langle f_s \right\rangle$ for simplicity. The brackets defined by Macaulay, $\langle\ \rangle$ control the function as follows.

$$\left\langle f_s \right\rangle = f_s \qquad \text{for} \quad f_s \le 0 \tag{A.6}$$

$$\left\langle f_s \right\rangle = 0 \qquad \text{for} \quad f_s > 0 \tag{A.7}$$

The new model allows to take in to account the viscoplastic strains when the stress state exceeds the yield limit. Therefore, the total strain for an element (i.e. with stress exceeding the failure strength) is given by the sum of elastic part (reversible), $\Delta\varepsilon_i^e$ and viscoplastic part (irreversible), $\Delta\varepsilon_i^{vp}$. The viscoplastic part includes both the plastic and viscous parts, which is given by Equation (A.5). Thus, the total strain, $\Delta\varepsilon_i$ is given by

$$\Delta\varepsilon_i = \Delta\varepsilon_i^e + \Delta\varepsilon_i^{vp} \qquad \text{for 1, 2 , 3} \qquad \text{(A.8)}$$

and if we write Equation (A.5) in the form of increment, it becomes

$$\Delta\varepsilon_i^{vp} = \gamma\Delta t \left\langle f_s \right\rangle \frac{\partial g_s}{\partial \sigma_i} \qquad \text{for 1, 2 , 3} \qquad \text{(A.9)}$$

where Δt is the timestep. If we put Equation (A.3) in Equation (A.9) and then substituting in Equation (A.8), we obtain for total strain increments as follows:

$$\begin{aligned} \Delta\varepsilon_1 &= \Delta\varepsilon_1^e + \gamma\Delta t \left\langle f_s \right\rangle \\ \Delta\varepsilon_2 &= \Delta\varepsilon_2^e \\ \Delta\varepsilon_3 &= \Delta\varepsilon_3^e + \gamma\Delta t \left\langle f_s \right\rangle \end{aligned} \qquad \text{(A.10)}$$

The stress increments (σ^N_i - σ^o_i) are related to the elastic strain increments by the elasticity equations as:

$$\begin{aligned} \sigma_1^N &= \sigma_1^o + A\Delta\varepsilon_1^e + B(\Delta\varepsilon_2^e + \Delta\varepsilon_3^e) \\ \sigma_2^N &= \sigma_2^o + A\Delta\varepsilon_2^e + B(\Delta\varepsilon_1^e + \Delta\varepsilon_3^e) \\ \sigma_3^N &= \sigma_3^o + A\Delta\varepsilon_3^e + B(\Delta\varepsilon_1^e + \Delta\varepsilon_2^e) \end{aligned} \qquad \text{(A.11)}$$

$$A = K + \frac{2}{3*a}$$
$$B = K - \frac{1}{3*a} \tag{A.12}$$

where

$$a = \frac{1}{2G^M} + \frac{\Delta t}{4}\left(\frac{1}{\eta^M} + \frac{1}{A\eta^K}\right)$$
$$b = \frac{1}{2G^M} - \frac{\Delta t}{4}\left(\frac{1}{\eta^M} + \frac{1}{A\eta^K}\right) \tag{A.13}$$

The initial estimate of new stresses before testing failure is also derived from the elastic relations as:

$$\begin{aligned}\sigma_1^I &= \sigma_1^o + A\Delta\varepsilon_1 + B(\Delta\varepsilon_2 + \Delta\varepsilon_3)\\ \sigma_2^I &= \sigma_2^o + A\Delta\varepsilon_2 + B(\Delta\varepsilon_1 + \Delta\varepsilon_3)\\ \sigma_3^I &= \sigma_3^o + A\Delta\varepsilon_3 + B(\Delta\varepsilon_1 + \Delta\varepsilon_2)\end{aligned} \tag{A.14}$$

Equation (A.14) can be rewritten as:

$$\begin{aligned}\sigma_1^o &= \sigma_1^I - A\Delta\varepsilon_1 - B(\Delta\varepsilon_2 + \Delta\varepsilon_3)\\ \sigma_2^o &= \sigma_2^I - A\Delta\varepsilon_2 - B(\Delta\varepsilon_1 + \Delta\varepsilon_3)\\ \sigma_3^o &= \sigma_3^I - A\Delta\varepsilon_3 - B(\Delta\varepsilon_1 + \Delta\varepsilon_2)\end{aligned} \tag{A.15}$$

If we substitute Equation (A.10) in Equation (A.15), we obtain,

$$\begin{aligned}\sigma_1^o &= \sigma_1^I - A\left[\Delta\varepsilon_1^e + \gamma\Delta t\left\langle f_s\right\rangle\right] - B\left[\Delta\varepsilon_2^e + \Delta\varepsilon_3^e - \gamma\Delta t\left\langle f_s\right\rangle N_\psi\right]\\ \sigma_2^o &= \sigma_2^I - A\Delta\varepsilon_2^e - B\left[\Delta\varepsilon_1^e + \Delta\varepsilon_3^e + \gamma\Delta t\left\langle f_s\right\rangle(1 - N\psi)\right]\\ \sigma_3^o &= \sigma_3^I - A\left[\Delta\varepsilon_3^e - \gamma\Delta t\left\langle f_s\right\rangle N_\psi\right] - B\left[\Delta\varepsilon_1^e + \Delta\varepsilon_2^e + \gamma\Delta t\left\langle f_s\right\rangle\right]\end{aligned} \tag{A.16}$$

Then if we insert Equation (A.16) in Equation (A.11), it gives

$$\begin{aligned}
\sigma_1^N &= \sigma_1^I - \gamma\Delta t\left\langle f_s\right\rangle\left[A - BN_\psi\right] \\
\sigma_2^N &= \sigma_2^I - B\gamma\Delta t\left\langle f_s\right\rangle\left[1 - N_\psi\right] \\
\sigma_3^N &= \sigma_3^I - \gamma\Delta t\left\langle f_s\right\rangle\left[B - AN_\psi\right]
\end{aligned} \tag{A.17}$$

Appendix B

In this appendix, the displacement vectors and deformed shapes of the inclinometers installed in the toe part are presented.

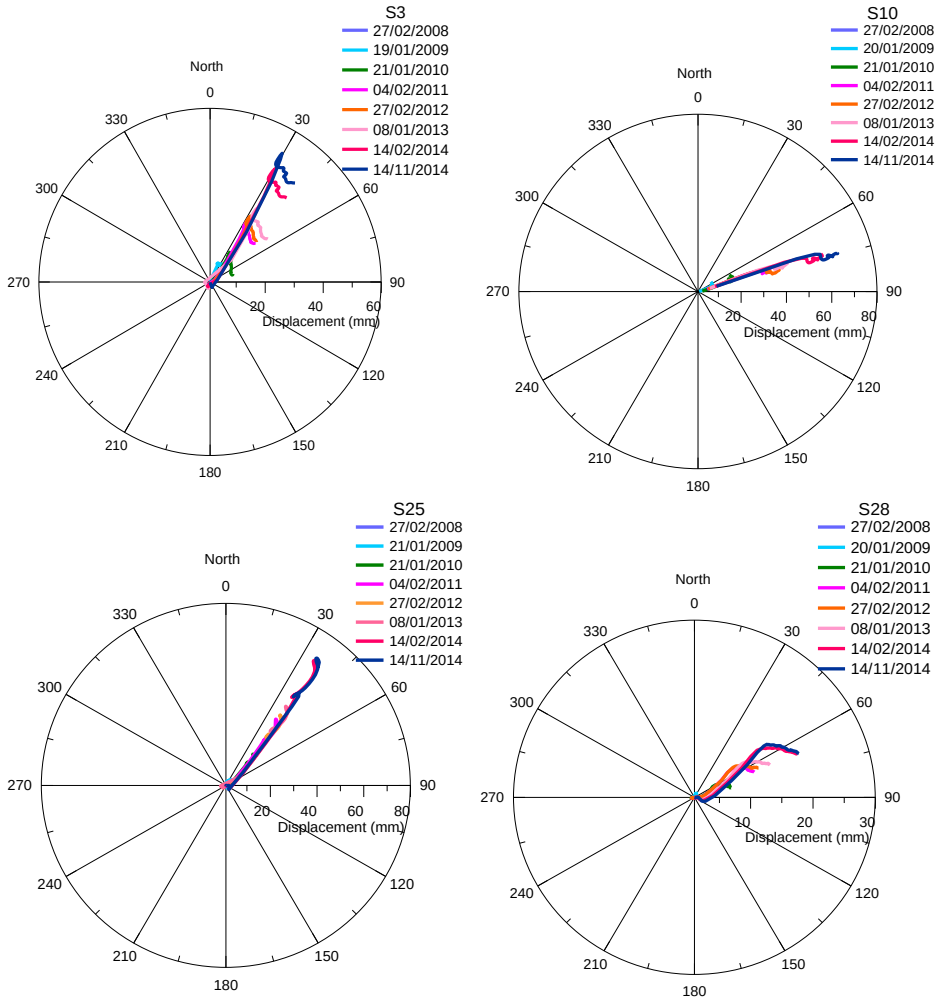

Figure A.1: Displacement vectors measured by inclinometers (S3, S10, S25 and S28)

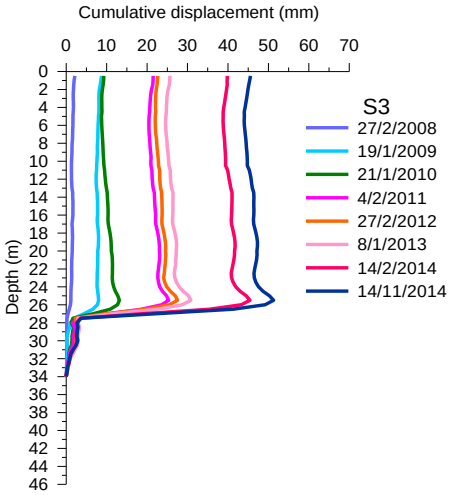
Cumulative displacement (mm)
Depth (m)
S3
27/2/2008
19/1/2009
21/1/2010
4/2/2011
27/2/2012
8/1/2013
14/2/2014
14/11/2014

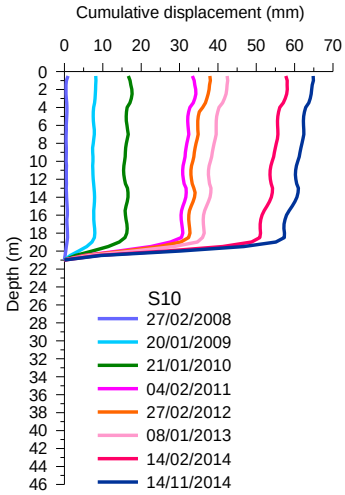
Cumulative displacement (mm)
Depth (m)
S10
27/02/2008
20/01/2009
21/01/2010
04/02/2011
27/02/2012
08/01/2013
14/02/2014
14/11/2014

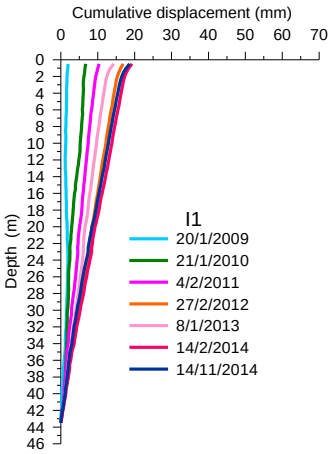
Cumulative displacement (mm)
Depth (m)
I1
20/1/2009
21/1/2010
4/2/2011
27/2/2012
8/1/2013
14/2/2014
14/11/2014

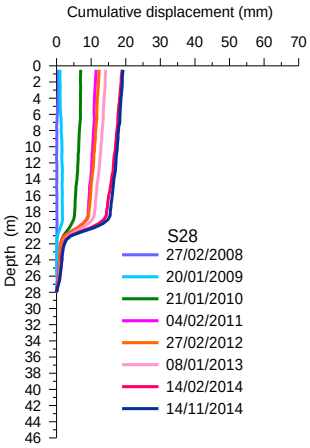
Cumulative displacement (mm)
Depth (m)
S28
27/02/2008
20/01/2009
21/01/2010
04/02/2011
27/02/2012
08/01/2013
14/02/2014
14/11/2014

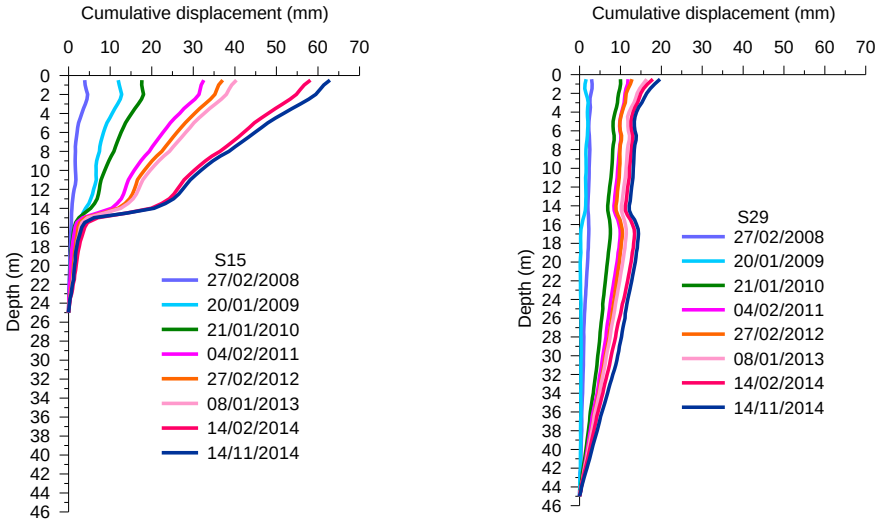

Figure A.2: Deformed shape of inclinometer profiles along depth

List of references

Alonso, E., Gens, A. and Lloret, A. (1993). The landslide of Cortes de Pallas, Spain; a case study. *Gèotechnique* **43**, 507-521.

Alonso, E. and Pinyol, N. M. (2014). Slope stability in slightly fissured claystones and marls. *Landslides*, doi: 10.1007/s10346-014-0526-5.

Alonso, E.E, Pinyol N and Puzrin, A.M. (2010). A constrained creeping landslide: Brattas-St. Moritz Landslide, Switzerland. In: *Geomechanics of failures advanced topics*. Springer, Berlin, pp 3–32.

Alonso, E., Gens, A. and Lloret, A. (1993). The landslide of Cortes de Pallas, Spain; a case study, *Geotechnique*, **43**, 507-521.

Alonso, E., Tapias, M., Gili, J. (2013). Particle crushing, scale effects and delayed behavior of rockfill a DEM investigation. *Alert Workshop. Degradation in geomaterials*.

Alonso, E., Cardoso, R. (2009). Behavior of materials for earth and rock fi ll dams: Perspective from unsaturated soil mechanics. *Front. Archit. Civ. Eng*, doi 10.1007/s11709-010-0013-6.

Angelucci, A., De rosa, E., Fierro, G., Gnaccolini, M., La monica, G. B., Martinis, B., Parea, G. C., Pescatore, T.,Rizzini, A. and Wezel, F. C. (1967). Sedimentological characteristics of some italian turbidites. *Geol. Rom*. **VI** pp 345-420.

Angeli, M.G., Gasparetto, P., Menotti, R.M., Pasuto, A. and Silvano, S. (1996). A visco-plastic model for slope analysis applied to a mudslide in Cortina d'Ampezzo, Italy. *Quat J Eng Geol* **29** (3), 233–240.

Assefa, S., Graziani, A and Lembo-Fazio, A. (2014). Analisi di uno scivolamento planare in una formazione marnoso-arenacea. *Incontro Annuale dei Ricercatori di Geotecnica -IARG Chieti e Pescara*, (in italian).

Assefa, S., Graziani, A. and Lembo-Fazio, A. (2015). A deep seated movement in a marly-arenaceous formation: analysis of slope deformation and pore pressure influence. IOP Conf. Series: *Earth and Environmental Science*, **26**, 012052, doi: 10.1088/1755-1315/26/1/012052.

Assefa, S.,Graziani, A. and Lembo-Fazio, A. (2016). Investigation on a slope movement in a complex rock formation: modeling of the deformation mode and remedial measures. *50th US Rock Mechanics/Geomechanics Symposium*, Houston, Texas, USA.

Assefa, S.,Graziani, A. and Lembo-Fazio, A. (2016). A slope movement in a complex rock formation: deformation measurements and DEM modelling. *Engineering Geology (*under revision*).*

Barton, N. and Choubey, V. (1977). The Shear Strength of Rock Joints in Theory and Practice. *Rock mechanics*, **10** 1-54.

Barton, N., Bandis, S. and Bakhtar, K. (1985). Strength, Deformation and Conductivity Coupling of Rock Joints. *Int.J. Rock Mech. Min. Sci. & Geomech. Abstr*, Vol **22** (3), 121-140.

Barton, N. (2002). Some new Q-value correlations to assist in site characterization and tunnel design. *International Journal of Rock Mechanics and Mining Sciences* **39**: 185–216.

Barton, N. (2007). *Rock Quality, Seismic Velocity, Attenuation and Anisotropy*. UK & The Netherlands: Taylor & Francis.

Bandis, S., Lumsden, A., and Barton, N. (1983). Fundamentals of Rock Joint Deformation. *Int.J. Rock Mech. Min. Sci. & Geomech. Abstr*, **20**(6), 249-268.

Bandis, S., Lumsden, A., and Barton, N. (1981). Experimental studies of Scale Effects on the Shear Behavior of Rock joints. *Int.J. Rock Mech. Min. Sci. & Geomech. Abstr*, **18,** 1-21.

Bandis, S. (1980). *Experimental studies of scale effects on shear strength, and deformation of rock joints*. Ph.d. Thesis, The University of Leeds.

Boon, C. W., Houlsby, G. T. and Utili, S. (2014). New insights into the 1963 Vajont slide using 2D and 3D distinct-element method analyses. *Gèotechnique* **64**, 800-816.

Brideau, M. A. and Stead, D. (2012). Evaluating Kinematic Controls on Planar Translational Slope Failure Mechanisms Using Three-Dimensional Distinct Element Modelling. *Geotech Geol Eng* **30**, 991–1011.

Baldovin, G. (1968). La resistenza a taglio delle rocce con alternanza di strati litologicamente eterogenei. *Rivista Italiana Geotecnica*, **4**: 170-181(in italian).

Barla, G., Bonini, M. and Cammarata, G. (2004). Stress and seepage analyses for a gravity dam on a jointed granitic rock mass. *In: Proceedings of the 1st international UDEC/3DEC symposium: numerical modeling of discrete materials in geotechnical engineering, civil engineering, and earth sciences, Bochum*, pp 263–268.

Barton, N. (2002). Some new Q-value correlations to assist in site characterization and tunnel design. *International Journal of Rock Mechanics and Mining Sciences* **39**: 185–216.

Barton, N. (2007). *Rock Quality, Seismic Velocity, Attenuation and Anisotropy*. UK & The Netherlands: Taylor & Francis.

Bonzanigo, L., Eberhardt, E. and Loew, S. (2001). Hydromechanical Factors Controlling the Creeping Campo Vallemaggia Landslide, Proceedings: *Landslides-Causes, Impacts and Countermeasures, Davos, Switzerland*, 13–22.

Bonzanigo, L., Eberhardt, E. and Loew, S. (2007). Long term investigation of a deep-seated creeping landslide in crystalline rock. Part I. Geological and hydro-mechanical factors controlling the Campo Vallemaggia landslide. *Canadian Geotechnical Journal*, **44**, 1157-1180.

Bretas, E.M., Lemos, J.V. and Lourenco, P.B. (2013). Hydromechanical Analysis of Masonry Gravity Dams and their Foundations. *Rock Mech Rock Eng*, **46**:327–339.

Bonzanigo, L., Eberhardt, E. and Loew, S. (2007). Long-term investigation of a deep- seated creeping landslide in crystalline rock Part I. *Can. Geotech J*, **44**, 1157-1180.

Barton, N., Kjaernsli, B. (1981). Shear strength of rockfill. *J. Geotech. Engng Div., Am. Soc. Cir. Engrs*, **107**, 873-91.

Boidy, E., Pellet, F. and Boulon, M. (2001). Numerical modeling of deep tunnels including time-dependent behaviour. In: Desai et al. (Eds.).*Computer Methods and Advances in Geomechanics*, Balkema, Rotterdam, 1663–1668.

Boidy, E., Bouvard, A. and Pellet, F. (2002). Back analysis of time-dependent behaviour of a test gallery in claystone. *Tunnelling and Underground Space Technology*, **17**, 415-424.

Boidy, E. (2002): Modélisation numérique du comportement différé des cavités souterraines. Ph.D. Thesis, Université Joseph Fourier, Grenoble, France.

Bonini, M., Debernardi, D., Barla, M. and Barla, G. (2009). The Mechanical Behaviour of Clay Shales and Implications on the Design of Tunnels. *Rock Mech Rock Engng*, **42**, 361–388.

Cai, M., Kaiser, P.K., Uno, H., Tasaka, Y. and Minami, M. (2004). Estimation of rock mass deformation modulus and strength of jointed hard rock masses using the GSI system. *International Journal of Rock Mechanics & Mining Sciences* **41**, 3–19.

Cappa, F., Guglielmi, Y., Soukatchoff, V.M., Mudry, J., Bertrand, C. and Charmoille, A. (2004). Hydromechanical modeling of a large moving rock slope inferred from slope levelling coupled to spring long-term

hydrochemical monitoring: example of the La Clapière landslide (Southern Alps, France). *Journal of Hydrology*, **291**, 67–90.

Cammarata, G., Fidelibus, C., Cravero, M. and Barla, G. (2007). The hydro-mechanically coupled response of rock fractures. *Rock Mech Rock Eng*, **40**(1):41–61.

Celluzzi, E., Graziani, A. and Lembo-Fazio, A. (2014). Analysis of a deep-seated slope movement in a marly- arenaceous formation. *Int. Conf. Eurock 2014 Vigo paper* **643**, 1-6.

Corominas, J., Moya, J., Ledesma, A., Lloret, A. and Gili, J. A. (2005). Prediction of ground displacements and velocities from groundwater level changes at the Vallcebre landslide (Eastern Pyrenees, Spain). *Landslides* 2: 83–96, doi: 10.1007/s10346-005-0049-1.

Conte, E., and Troncone, A. (2011). Analytical Method for Predicting the Mobility of Slow-Moving Landslides owing to Groundwater Fluctuations. *J. Geotech. Geoenviron. Eng*., **137**, 777-784.

Charles, J.A., Soares, M.M. (1984). Stability of compacted rockfill slopes. *Geotechnique*, **34**, 61-70.

Charles, J. A., Watts, K. S. (1980). The influence of confining pressure on the shear strength of compacted rockfill. *Geotechnique* **30**, No. 4,353-367.

Christianson, M.C., Board, M.P. and Rigby, D.B. (2004). UDEC simulation of Triaxial Testing of Lithophysal Tuff.

Corkum A.G. and C.D. Martin. (2004). Analysis of a rock slide stabilized with a toe-berm: a case study in British Columbia, Canada. *International Journal of Rock Mechanics & Mining Sciences* **41**: 1109-1121.

Chan Dave. H. (1999). Analysis and case histories of time-dependent movement of soils: An Informal workshop on slow movements monitoring and modeling, Italy. *Revisita italiana di geotecnica*.

Cruden, D.M.and Varnes, DJ. (1996) Investigation and Mitigation, in Turner, Keith A., and Schuster, Robert L., Landslides: investigation and mitigation, Transportation Research Board, *National Research Council*, *National Academy Press*, Special Report 247, p. 36-75.

Dawson, E., M., Roth, W., H. and Drescher, A. (1999). Slope stability analysis by strength reduction. *Gèotechnique* **49**(6), 835–840.

D'Elia, B., Picarelli, L., Leroueil, S. and Vaunat, J. (1998). Geotechnical characterisation of slope movements in structurally complex clay soils and stiff jointed clays. *Rivista Italiana Geotecnica,* **3,** 5-47.

Desai, C.S., Samtani N. and Vulliet L. (1995). Constitutive modeling and analysis of creeping slopes. J. Geotech. Engineering, **121**, 43-56.

D'Elia, B., Picarelli, L., Leroueil, S. and Vaunat, J. (1998). Geotechnical characterization of slope movements in structurally complex clay soils and stiff jointed clays. *Rivista Italiana Geotecnica*, **3**, 5-47.

di Prisco, C. and Imposimato, S. (1996). Time dependent mechanical behaviour of loose sands. *Mechanics of Cohesive-Frictional Materials*, **1**, 45-73.

De Mello V F B. (1977). Seventh Rankine Lecture: Reflections on design decisions of practical significance to embankment dams. *Géotechnique*, **27**(3): 279–356.

Donaghe, R.T., Cohen, M.W. (1978). Strength and deformation properties of rockfill. Soil and Pavement Laboratory, *U.S. Army Engineer Waterways Experiment Station*, Technical report S-78-1.

Deluzarche, R., Cambou, B. (2006). Discrete numerical modelling of rockfill dams. *Int. J. Numer. Anal. Meth. Geomech*, **30**:1075 – 1096.

Farinha, M. L. B., Lemos J. V. and Maranha das Neves E. (2012). Analysis of foundation sliding of an arch dam considering the hydromechanical behavior. *Front. Struct. Civ. Eng*., **6**(1): 35 – 43.

Fernández-Merodo, J. A., García-Davalillo, J. C., Herrera, G., Mira P. and Pastor, M. (2012). 2D viscoplastic finite element modelling of slow landslides: the Portalet case study (Spain). *Landslides*, doi: 10.1007/s10346-012-0370-4.

Fodil, A. Aloulou, A. and Hicher, P. (1997). Viscoplastic behaviour of soft clay. *Geotechnique*, **47,** No 3, 581-591.

Forlati F., Gioda, G., and Scavia C. (2001). Finite Element Analysis of a Deep-seated Slope Deformation. *Rock Mech. Rock Engng*, **34** (2), 135-159.

Grana, V. and Tommasi, P. (2013). A deep-seated slow movement controlled by structural setting in marly formations of Central Italy. *Landslides*, doi: 10.1007/s10346-013-0384-6.

Graziani, A., Rossini, C. and Rotonda, T. (2012). Characterization and DEM modelling of shear zones at a large dam foundation. *International Journal of Geomechanics*, **6**, 648-664.

Graziani, A., Rotonda, T. and Tommasi, P. (2009). Stability and deformation mode of a rock slide along interbeds reactivated by rainfall. *1st Italian Workshop on Landslides, Napoli* **1** 62-71.

Gabellani, S., Silvestro, F., Rudari, R. and Boni, G. (2008). General calibration methodology for a combined Horton-SCS infiltration scheme in flash flood modeling. *Nat. Hazards Earth Syst. Sci*., **8**, 1317–1327.

Guglielmi, Y., Cappa, F. and Binet, S. (2005). Coupling between hydrogeology and deformation of mountainous rock slopes: Insights from La Clapière area (Southern Alps, France), C. R. *Geoscience* **337**, 1154–1163.

Graziani, A., Rotonda,T. And Tommasi, P. (2009). Stability and deformation mode of a rock slide along interbeds reactivated by rainfall. Picarelli L. et al. (eds.), *1st Italian Workshop on Landslides, Napoli*, **1**, 62-71.

Grøneng, G., Lu, M., Nilsen, B., Jenssen, A. K. (2010). Modelling of time-dependent behavior of the basal sliding surface of the Åknes rockslide area in western Norway. *Engineering Geology*, **114**, 414–422.

Guan, Z., Jiang Y., Tanabashi, Y., and Huang, H. (2008). A new rheological model and its application in mountain tunneling. *Tunnelling and Underground Space Technology*, **23**, 292-299.

Gioda, G. and Borgonovo, G. (2004). Finite Element Modeling of the Time-Dependent Deformation of a Slope Bounding a Hydroelectric Reservoir. *International Journal of Geomechanics*, Vol **4**, No 4, 229–239.

Garcia, S. R., Romo, M. P. (2009). Rockfill Strength Evaluation Using Cascade Correlation Networks. *Geotech Geol Eng* **27**:289–304. Doi: 10.1007/s10706-008-9229-9.

Maugeri, M., Motta, E., and Raciti, E. (2006). Mathematical modelling of the landslide occurred at Gagliano Castelferrato (Italy). *Natural Hazards and Earth System Sciences*, **6**, 133–143.

Lembo Fazio, A., Ribacchi, R. and Sciotti, M. (1997). Slow deformation of high rock slopes and their influence on hydraulic structures. *Rivista Italiana di Geotecnica*.

Hoek, E. and Brown, ET. (1998). Practical estimates of rock mass strength. *Int J Rock Mech Min Sci* **34**, 1165–1186

Hoek, E., Marinos, P. and Benissi, M. (1998) Applicability of geological strength index (GSI) classification for very weak and sheared rock masses. The case of the Athens Schist Formation. *Bull Eng Geol Env* **57**, 151-160.

Hoek, E., Brown, E. T. (1980). *Underground Excavations in Rock*. London: Instn. Min. Metall.

Hammah, R. E., Yacoub, T. and Curran, J.H. (2009). Variation of failure mechanisms of slopes in jointed rock masses with changing scale. In:

Diederichs MS, Grasselli G (eds). *Third Canada-U.S. rock mechanics symposium*, Toronto, Canada, Paper 3956.

Hoek, E. and Diederichs, M.S. (2005). Empirical estimation of rock mass modulus. *International journal of Rock Mechanics and Mining Sciences*. doi:10.1016/j.ijrmms.2005.06.005.

Hatzor, Y.H. and Levin, M. (1997). The shear strength of clay-filled bedding planes in limestones back analysis of a slope failure on a phosphate mine, Israel. *Geotechnical and Geological Engineering* **15**, 263-282.

Indraratna, B., Haque, A. and Aziz, N. (1998). Laboratory modelling of shear behaviour of soft joints under constant normal stiffness conditions. *Geotechnical and Geological Engineering*, **16** 17–44.

Indraratna, B., Ranjith, P. G., Gale, W. (1999). Single phase water flow through rock fractures. *Geotechnical and Geological Engineering*, **17**: 211-240.

Indraratna, B. (1994). The effect of normal stress-friction angle relationship on the stability analysis of a rockfill dam. *Geotechnical and Geological Engineering*, 113-121.

Indraratna, I., Wijewardena, L.S.S., Balasubramaniam, A.S. (1993). Large-scale triaxial testing of Greywacke rockfill. *Geotechnique* **43**, No. 1, pp. 37-51.

Itasca Inc. (2011): UDEC-5 and FLAC-7 User's Manual Itasca Consulting Group Inc Minneapolis, USA.

Jeanne, P., Guglielmi, Y. and Cappa, F. (2013). Hydromechanical Hetrogeneities of a Mature Fault Zone: Impacts on Fluid Flow. *Groundwater*. Doi: 10.1111/gwat.12017.

Kulatilake, P. H. S. W. and Shu, B. (2015). Prediction of Rock Mass Deformations in Three Dimensions for a Part of an Open Pit Mine and Comparison with Field Deformation Monitoring Data. *Geotech Geol Eng* **33**:1551–1568.

Kveldsvik, V., Kaynia, A. M., Nadim, F., Bhasin, R., Nilsen, B.and Einstein, H. H. (2009). Dynamic distinct-element analysis of the 800 m high Åknes rock slope. *Int. J. Rock Mech. Mining Sci*.**46** (4), 686–698.

Lembo Fazio, A., Tommasi, P. and Ribacchi, R. (1990). Sheared bedding joints in rock engineering: Two case histories in Italy. *Proceedings on the international symposium on rock joints* Leon, Norway.83-90.

Lemaitre, J. and Chaboche, J. L (1990). *Mechanics of solid materials*. Cambridge University Press, Cambridge.

Lee, K.L., Seed. H.B. (1967a). Drained characteristics of sands. Journal of the soil mechanics and foundation division. ASCE.93. No .SM6, pp 117-14.

Leps, T.M. (1988). Rockfill dam design and analysis, Advanced Dam Engineering for Design Construction and Rehabilitation (Edited by R.B. Jansen), New York, Van Nostrand Reinhold, 368-87.

Linero, S., Palma, C., Apablaza, R. (2007). Geotechnical characterization of waste material in very high dumps with large-scale triaxial testing. *Proceedings, International Symposium on Rock Slope Stability in Open Pit Mining and Civil Engineering*, Perth, Australia. 1:59-76.

Lobo-Guerrero, S., Vallejo, L. E. (2005). Discrete Element Method Evaluation of Granular Crushing Under Direct Shear Test Conditions. *J. Geotech. Geoenviron. Eng.***131**:1295-1300.

Liao, Q.H. and Hencher, S.R. (1997). Numerical modelling of the hydro-mechanical behaviour of fractured rock masses. *Int. J. Rock Mech. & Min. Sci.* **34**:3-4, paper No.177.

Marachi, N.D., Chan, C.K., Seed, H.B. (1972). Evaluation of properties of rockfill materials. *J. Soil Mech. Fndn. Div., Am. Soc. Cir. Engrs*, **98**, 95-114.

Malan, D.F. (2002). Simulating the Time-dependent Behaviour of Excavations in Hard Rock. *Rock Mechanics and Rock Engineering*, **35** (4), 225–254.

Malan, D. F. (1998). An investigation into the identifcation and modelling of time-dependent behavior of deep level excavations in hard rock. PhD thesis, University of the Witwatersrand, Johannesburg, South Africa

Norton F. H. 1929. Creep of Steel at High Temperatures. New York: McGraw-Hill Book Company.

Ovalle, C., Frossard, E., Dano, C., Hu, W., Maiolino, S., Hicher, P-Y. (2014). The effect of size on the strength of coarse rock aggregates and large rockfill samples through experimental data. *Acta Mech* **225**, 2199–2216. Doi: 10.1007/s00707-014-1127-z.

Oberti, G., Bavestrello, F., Rossi, P. and Flamigni, F. (1986). Rock Mechanics Investigations, Design and Construction of the Ridracoli Dam. *Rock Mechanics and Rock Engineering*, **19**, 113-142.

Oberender, P. W. and Puzrin, A. M. (2016). Observation-guided constitutive modelling for creeping landslides. *Géotechnique* **66**, No. 3, 232–247.

Palmström A., (1995). RMi - *a rock mass characterization system for rock engineering purposes*. PhD thesis, University of Oslo, Norway.

Palmström, A. (2005). Measurements of and correlations between block size and rock quality designation (RQD). *Tunnelling and Underground Space Technology* **20**, 362-377.

Pisani, G., Castelli, M. and Scavia, C. (2010). Hydrogeological model and hydraulic behaviour of a large landslide in the Italian Western Alps. *Nat. Hazards Earth Syst. Sci*., **10**, 2391–2406.

Perzyna, P. (1966). Fundamental problems in viscoplasticity. *Advances in Applied Mechanics*, Vol. **9**. Academic Press, New York, 243–377.

Puzrin, A. M. and Schmid, A. (2011). Progressive failure of a constrained creeping landslide. *Proc. R. Soc. London* A **467**, 2444–2461.

Ribacchi, R., (1987). Rock mass deformability. Insitu tests, their interpretation and typical results in Italy. *2nd international symposium. Field measurements in Geomechanics* **1**, 171-192. Kobe.

Ribacchi, R. (1987). Rock mass deformability. Insitu tests, their interpretation and typical results in Italy. *2nd international symposium. Field measurements in Geomechanics*, **1**, 171-192. Kobe.

Ronchetti, F., Borgatti, L., Cervi, F., Gorgoni, C., Piccinini, L., Vincenzi, V. and Corsini, A. (2009). Groundwater processes in a complex landslide, northern Apennines, Italy. *Nat. Hazards Earth Syst. Sci*., **9**, 895–904.

Stavropoulou, M. (2014). Discontinuity frequency and block volume distribution in rock masses. *International journal of Rock Mechanics and Mining Sciences* **65**, 62-74.

Sterpi, D., and Gioda, G., (2000). A strain softening creep model for the time-dependent behavior of rocks. *Rivista italiana di geotecnica*.

Sterpi, D. and Gioda, G. (2009). Visco-Plastic Behaviour around Advancing Tunnels in Squeezing Rock. *Rock Mech Rock Engng*, **42**, 319–339.

Ter-Stepanian, G. (1963). On the long-term stability of slopes, Publ. No. 52, *Norwegian Geotech. Inst*., Oslo, Norway.

Turc, L. (1961). Estimation of irrigation water requirements, potential evapotranspiration: A simple climatic formula evolved up to date, *Annals of Agronomy*., **12**, 13–49.

Tommasi, P., Verrucci, L., Campedel, P., Veronese, L., Pettinelli, E. and Ribacchi, R. (2009). Buckling of high natural slopes: The case of Lavini di Marco (Trento-Italy). *Engineering Geology* **109**, 93–108.

United States Department of Agriculture, S. C. S. (1954). National Engineering Handbook, Section 4, *US Department of Agriculture*, Washington, DC.

Vyalov, S.S. Rheological fundamentals of soil mechanics. Developments in geotechnical engineering, vol **36**. Elsevier Science Publishers b.v.

Vulliet L. (1999). Modelling creeping slopes: Informal workshop on slow movements monitoring and modeling: *Rivista Italiana Geotecnica*, 71-76.

Vulliet, L. and Hutter, K. (1988). Some constitutive laws for creeping soil and for rate-dependent sliding at interfaces. In: Swoboda (ed) *Numerical methods in geomechanics (Innsbruck 1988)*. Balkema, Rotterdam, pp 495–502.

van Asch, T. W. J., Van Beek, L. P. H. and Bogaard, T. A. (2007). Problems in predicting the mobility of slow-moving landslides. *Eng. Geol.*, **91**, 46 – 55.

Vermer, P. A., and de Borst, R. (1984). Non-associated plasticity for soils, concrete and rock, *Heron*, vol **29**, no 3.

Varadarajan, A., Sharma, K. G., Venkatachalam, K., Gupta, A. K. (2003). Testing and Modeling Two Rockfill Materials. *J. Geotech. Geoenviron. Eng.***129**:206-218.

Witherspoon, P.A., Wang, J.S.Y., Iwai, K. and Gale, J.E. (1980): Validity of cubic law for fluid flow in deformable rock fracture. *Water Resour. Res.* **16**(6):1016–1024.

Wang, S., Qi, J., Yin, Z., Zhang, J. and Ma, W. (2014). A simple rheological element based creep model for frozen soils. *Cold Regions Science and Technology*, 106-107, 47-54.

Wang, S., Qi, J., and Yu, F., and Yao, X. (2013). A novel method for estimating settlement of embankments in cold regions. *Cold Regions Science and Technology*, **88**, 50-58.

Williams, D.J., Walker, L.K. (1983). Laboratory and field strength of mine waste rock. Research report No. CE 48. University of Queensland.

Xu, M., Song, E. (2009) Numerical simulation of the shear behavior of rockfills. *Computers and Geotechnics* **36**, 1259–1264.

Yerro, A., Pinyol, N.M. and Alonso, E.E. (2015). Internal Progressive Failure in Deep-Seated Landslides. *Rock Mech Rock Eng*, doi: 10.1007/s00603-015-0888-6.

Yu, C.W., Chern, J.C. and Snee, C.P.M. (1999). Physical modeling for creep parameters of soft rock. *Rock mechanics for industry, Amadei, Kranz, Scott and Smeallie (eds)*, Balkema, Rotterdam, ISBN 90 5809 0523.

Zangerl, C., Eberhardt, E. and Loew, S. (2003). Ground settlements above tunnels in fractured crystalline rock: numerical analysis of coupled hydromechanical mechanisms. *Hydrogeology Journal*, **11**:162-173.

Zangerl, C., Eberhardt, E. and Perzlmaier, S. (2010). Kinematic behaviour and velocity characteristics of a complex deep-seated crystalline rockslide system in relation to its interaction with a dam reservoir. *Eng. Geol*. **112**, 53-67.

Zhang, L. and Einstein, H.H. (2004). Using RQD to estimate the deformation modulus of rock masses. *International Journal of Rock Mechanics & Mining Sciences* **41**, 337-341.

Zhang, X., Sanderson, D.J., Harkness, R.M. and Last, N.C. (1996). Evaluation of the 2-D permeability tensor for fractured rock mass. *Int. J. Rock Mech. & Min. Sci*. **33**(1), 17–37.

Zhang, X. and Sanderson, D. J. (1996a). Effects of stress on the 2-D permeability tensor of natural fracture networks. *J. Geophys. Int*., **125**, 912-924.

Zhou, W., Ma, G., Chang, X., Zhou, C. (2013). Influence of Particle Shape on Behavior of Rockfill Using a Three-Dimensional Deformable DEM. *J. Eng. Mech.* **139**:1868-1873.